University of Southampton
School of Electronics and
Computer Science

Optimisation of the piezoelectric properties of thick-film piezoceramic devices

Russel Neil Torah

A thesis submitted for the degree

Doctor of Philosophy

Supervised by Prof. Neil M. White

May 2004

UNIVERSITY OF SOUTHAMPTON

ABSTRACT

FACULTY OF ENGINEERING AND APPLIED SCIENCE
SCHOOL OF ELECTRONICS AND COMPUTER SCIENCE

Doctor of Philosophy

OPTIMISATION OF THE PIEZOELECTRIC PROPERTIES OF THICK-FILM PIEZOCERAMIC DEVICES

By Russel Neil Torah

This thesis details the optimisation of the thick-film piezoelectric strain constant $d_{33,f}$ and the mechanical properties of thick-film Lead Zirconate Titanate (PZT) materials. The investigation focuses on the effects of the fabrication process parameters involved in thick-film screen-printing and the materials used.

Initial investigations examine the effect of powder milling on type PZT-5H powder supplied by Morgan Electro Ceramics Ltd. Ball milling, jet milling and attritor milling are studied in conjunction with the percentage of glass frit in the screen printable film. Subsequently, an investigation was conducted to improve the density of the fired film by blending ball and attritor milled powders together. The results showed that the optimum paste formulation is 18% attritor3, 72% ball milled PZT-5H and 10% CF7575 lead borosilicate glass powders. Following the formulation of the optimum paste, a study was conducted to identify the optimum furnace firing profile and polarisation process. The study showed that a peak firing temperature of 1000°C and poling at a temperature of 200°C for 5 minutes produced the optimum piezoelectric activity. The results show an increase in $d_{33,f}$ value from 18.5pC/N to 131pC/N. This represents a six-fold increase in piezoelectric activity in the fired films. The introduction of a multilayer structure of three individual PZT layers improved the $d_{33,f}$ coefficient to 325pC/N.

Finally, the thesis outlines current applications and collaborative work for the optimised film and details avenues for future work and further development of the PZT-5H thick-film.

Contents

List of Figures

List of Tables

Acknowledgements

I would like to say thank you to Dr Beeby and Professor White for answers to the endless questions, to Neil, Matt, Andy, John, Nick, Ed and Tom for their help with finding things and getting equipment to work and to Marc and Mike from Morgan Electro-ceramics for all their help with the many experiments. Last but not least a special thank you to Bryony and my family for keeping me going when it all seemed to be going wrong and listening to me go on and on when it was all going right.

Symbol definitions

A	Area (m^2)
t	Thickness (m)
D	Electric displacement
d	Piezoelectric charge constant (CN^{-1} or mV^{-1})
E	Applied electric field (Vm^{-1})
k	Coupling coefficient
i	Current (A)
Q	Charge (C)
σ	Charge density
ε	Permittivity (F/m)
S	Strain
T	Stress (Nm^{-2})
Y	Modulus of elasticity (Nm^{-2})
ρ	Poisson's ratio
wt%	Percentage weight
T_c	Curie temperature
K	Dielectric constant

Glossary of Terms

MEMS	Micro Electro-Mechanical Systems
PZT	Lead Zirconate Titanate
PT	Lead Titanate
PVDF	Polyvinylidene fluoride
SAW	Surface Acoustic Wave
SEM	Scanning Electron Microscope
AFM	Atomic Force Microscope
IR	Infrared
UV	Ultra-violet
EDX	Energy dispersive X-ray spectrometry
ANSYS	Commercial finite element analysis software
FEA	Finite element analysis
CAD	Computer aided design
Q-Factor	Quality factor
MPB	Morphotropic Phase Boundary

1 Introduction

1.1 Background

Credit for the discovery of the piezoelectric effect is given to Pierre and Jacques Curie who first reported the effect in 1880 [1]. They observed that certain crystalline materials became electrically polarised when subjected to a mechanical force. In addition, compression and tension on the crystal was shown to produce a charge of opposite polarity, proportional to the applied force. Conversely, it was discovered that if a polarised crystal were subjected to an electric field, a structural deformation would occur. These observations were defined as the piezoelectric effect and the inverse piezoelectric effect respectively. Piezo is derived from the Greek word piezein, meaning to press or squeeze where piezoelectricity is 'pressure electricity'.

The earliest experiments concerning piezoelectricity were conducted using Quartz and Rochelle salt as single crystal naturally occurring materials. It is also possible to manufacture a piezoelectric material using ceramics technology. During the 1940's, Waigner and Salomon developed Barium Titanate ($BaTiO_3$) as the first piezoceramic [2] and then in 1954 Jaffe discovered Lead Zirconate Titanate (PZT) solid solution as a viable piezoceramic [3]. These materials are mixed in powder form with a vehicle to form a paste or slurry. The mixture is then formed into a pattern and subsequently dried and fired thus creating a piezoelectric ceramic.

The materials used in piezoceramics are generally chemically inert and physically robust. In addition, they are cost effective to manufacture and provide a broad scope for applications. The composition of the ceramic can be tailored to the type of application and to specific dimensions and shape. The most widely used piezoceramics are currently those formed from a PZT composition as these exhibit greater sensitivity and operating temperatures (d_{33} of 150-600pC/N,

Curie temperature of 150-400°C) than the more traditional compositions such as Barium Titanate (d_{33} of 50-100pC/N, Curie temperature of 90-200°C). These properties make PZT piezoceramics an ideal choice for many sensor and actuator systems.

The voltage generated by the piezoelectric effect can range from milli-volts for miniature sensors to kilovolts for spark ignitor systems. The amount of charge produced depends on the processes and composition involved in the fabrication of the piezoelectric material. The inverse piezoelectric effect typically produces a strain of 1-2% in the desired actuation direction. The piezoelectric effect is used in applications such as force or displacement sensors, the inverse piezoelectric effect is used in precision actuator applications and in generating sonic and ultrasonic signals such as those used in sonar applications.

Research and development into the combination of piezoelectric materials and micro-mechanical devices has increased dramatically in recent years as fabrication techniques have improved. Layers of piezoelectric materials in combination with micromachined structures enable piezoelectric Micro-Electro-Mechanical Systems (MEMS) to address a wide range of applications. The application of piezoelectric layers to silicon substrates allows the combination of traditional microelectronic fabrication and state of the art micro-mechanical fabrication to develop fully integrated systems. The flexibility of deposition techniques [4] for piezoceramic materials (bulk adhesion, screen-printing, sol-gel, tape casting, sputtering) means that the sensor and actuator designs can be very complex whilst remaining cost effective and reducing the dimensions of the product.

The work presented in this thesis aims to improve the piezoelectric properties of a PZT layer that has been deposited using a screen-printing process. The screen-printing process is a simple and efficient deposition technique that is based upon the silk screen-printing process that has been used for hundreds of years to print designs on fabrics. The technique produces thick-film piezoceramics on a variety of substrates with a piezoelectric layer thickness of 10-200 microns.

These thick-film piezoelectric layers have been demonstrated with a range of sensor and actuator applications including strain gauges, pressure sensors, micro-pumps and accelerometers and these will be discussed in this thesis. Developing the existing materials to produce a greater piezoelectric response will enhance many existing applications and broaden the field of possible future applications.

This thesis has been funded by an EPSRC PhD studentship with financial and practical support from Morgan Electro Ceramics Ltd, an industrial company producing PZT powders and piezoceramic sensor and actuator solutions.

1.2 Scope of this Thesis

This thesis details the optimisation of the piezoelectric properties of screen-printed thick-film piezoceramics. A literature review covering the background of piezoceramics, deposition techniques and potential applications is provided to introduce the concepts and techniques behind the work performed in this thesis. Two methods for determining the piezoelectric properties of the film are evaluated and the limitations of each are considered.

Several PZT paste formulations are considered with various materials, powder sizes and preparation techniques evaluated to determine the optimum paste formulation for increased piezoelectric activity. In addition, the preparation and process parameters are optimised to further increase the piezoelectric activity of the film. Finally, a number of applications are demonstrated and future work identified to utilize the improvements made to the piezoelectric activity of the films.

A full break down of each of the chapters in this thesis is provided in the following section.

1.3 Structure of this Thesis

Chapter 1 provides an introduction to the research area of piezoelectric materials with an emphasis on screen-printable PZT films. A description of the scope and structure of the thesis is included and is concluded with a statement of novelty defining the areas of improvement contained within this thesis.

Chapter 2 discusses previous work and developments in the field of piezoelectric materials, processes and applications. The theory of piezoelectricity and the parameters associated with determining the piezoelectric properties of the material are defined. Following this is a review of the current developments in piezoelectric materials, substrate materials, and deposition techniques. Finally, there is a broad discussion of the applications associated with piezoelectric materials.

Chapter 3 defines the thick-film fabrication process, focusing on the materials used and the screen-printing equipment and process used throughout the thesis. The methods for mixing and printing the active material and conductor layers are described in detail along with the advantages and disadvantages associated with this deposition technique.

Chapter 4 evaluates two measurement techniques for defining the piezoelectric activity of the fired thick-films. The differences between the techniques are discussed and measurement comparisons described. This work identified a suitable method for measuring the d_{33} value for the thick-films, $d_{33,f}$, throughout the work contained within this thesis. In addition, a study of the clamping effect associated with the introduction of a substrate to the piezoceramic is included to assess the differences between the d_{33} values measured for bulk unclamped piezoceramics and thick-film piezoceramics deposited onto a substrate.

Chapter 5 examines the composition of the paste required in the screen-printing process. Focusing on the percentage of glass binder used within the paste and the novel step of evaluating the powder milling technique that is used to obtain

the PZT powder, the chapter details the results of this study and the effect this has on the piezoelectric properties of the film.

Chapter 6 uses the results contained in chapter 5 to further advance the optimisation of the piezoelectric properties by considering alternative electrode materials and studying the poling parameters used to induce piezoelectric properties in the film.

Chapter 7 considers the novel approach of combining the optimal powders from chapter 5 with the aim of producing higher piezoelectric response with a greater consistency and repeatability of results. Beginning with an evaluation of simple 2-Dimensional and 3-Dimensional modelling of the film structure, a start point is obtained for initial composition percentages for the paste. Four different powder combinations are assessed and the results are evaluated to determine the optimum paste composition.

Chapter 8 takes the optimum paste composition described in chapter 7 and details the identification of the optimum firing and poling process parameters. A study of the effect of firing temperature on the piezoelectric properties of the film is conducted. The temperature and number of firing cycles that the thick-film is subjected is studied and an alternative glass binder material is evaluated. In addition, the possibilities of co-firing specific layers of the thick-film structure are evaluated. The poling analysis includes an investigation of temperature, time and electric field strength effects on the piezoelectric properties of the film. The conclusions of this chapter assess the work covered in this thesis, with a stated optimal paste formulation and associated process parameters to achieve the highest piezoelectric activity levels.

Chapter 9 covers a range of measurements taken to obtain the characteristic values for the optimised PZT films. Details of experiments conducted to obtain these values are provided and a final table of defining characteristics is given.

Chapter 10 examines the increase in piezoelectric response with the introduction of second and third PZT layers with the use of series connected stacked

actuators. The chapter discusses the problems associated with multi-layered screen-printing and the various solutions available.

Chapter 11 provides an overview of the applications and research projects at the University of Southampton which have benefited from the optimisation work contained within this thesis.

Chapter 12 discusses the conclusions that have been drawn from the investigation into improving the piezoelectric properties of thick-film piezoceramics. Future work and avenues for study are also presented.

1.4 Statement of Novelty

The key novel contributions to the field of PZT thick-film development that are contained within this thesis are:

- A study of the substrate clamping effects on commercially available bulk PZT piezoceramics and the relation to thick-films (section 4.3).
- Evaluation of the main PZT powder milling processes and their influence on the quality of the screen printed thick-films (chapter 5).
- Improvement of piezoelectric activity with the combination of different powder sizes to improve the densification of thick-films (chapter 7).
- Optimisation of the process parameters for firing and poling of the improved PZT film (chapter 8)
- Demonstration of a wide range of applications for the newly developed optimal paste formulation (chapter 11).

2 Literature Review

2.1 Introduction

This chapter provides a discussion of piezoelectricity and the background theories and developments in the area of piezoceramics. The chapter begins with an overview of the definitions and properties associated with piezoelectricity. This leads to an identification of the three measurement methods required to determine the piezoelectric characteristics of a material. From here, the core topic areas concerning piezoceramics are discussed with related research.

These piezoceramic topic areas are:

- Piezoceramic materials, their associated properties and definitions.
- Deposition techniques required to produce piezoelectric layers.
- Substrate materials used for piezoelectric test structures.
- An overview of the range of applications for piezoceramics detailing current and future developments in the field.

2.2 Piezoelectricity

Pierre and Jacques Curie discovered the piezoelectric effect in the 1880's. It is a property exhibited by certain classes of crystalline material that generate an electrical charge when a force is applied and, conversely, a mechanical deformation when an electric field is applied [5,6,7]. Piezoelectricity differs from electrostriction because the reversal of the applied field reverses the direction of the resultant strain, whereas with electrostriction the induced strain is the same direction independent of the polarity of the applied field. Electrostriction is a property of all dielectric materials, however, the piezoelectric effect is only present in polar materials. Polar materials are crystal classes that exhibit a degree of polarisation under certain conditions, such as temperature change or an applied electric field. Only acentric polar materials

will exhibit the piezoelectric effect. A distinction is also made between a piezoelectric and a ferroelectric material. A piezoelectric material experiences a spontaneous polarisation effect which cannot be reversed, however, with a ferroelectric material this effect can be reversed and a polarisation of opposite polarity can be induced within the material with the application of a strong applied electric field.

2.2.1 Piezoelectric crystal structure

The piezoelectric effect occurs naturally in some crystalline materials and was first observed in Quartz and Rochelle salt. The distinction between these and other non-piezoelectric crystalline materials is that the atomic structure in a unit cell of a piezoelectric crystal does not possess a centre of symmetry. The non-symmetrical nature of the unit cell induces a dipole moment that results in an overall polarity to the crystal. In addition, the piezoelectric effect can be induced in some poly-crystalline ceramics (known as piezoceramics) with the application of an electric field; this process is known as poling. The first of these piezoceramics was barium titanate ($BaTiO_3$) but later experimentation by Hans Jaffe provided the discovery of strong and stable piezoelectric effects in lead zirconate titanate (PZT) solid solutions. PZT has since gone on to become the dominant piezoceramic material.

Piezoceramic materials have anisotropic properties and therefore do not have the same properties in all directions. Piezoceramic materials are typically polycrystalline ferroelectric materials and the most important piezoceramics crystallise in the perovskite crystal structure as shown in figure 2.1. These crystals contain three different ions of the form ABO_3. A small tetravalent atom, typically zirconium or titanium (B), is surrounded by a lattice of larger divalent atoms, typically lead or barium (A), and oxygen atoms (O).

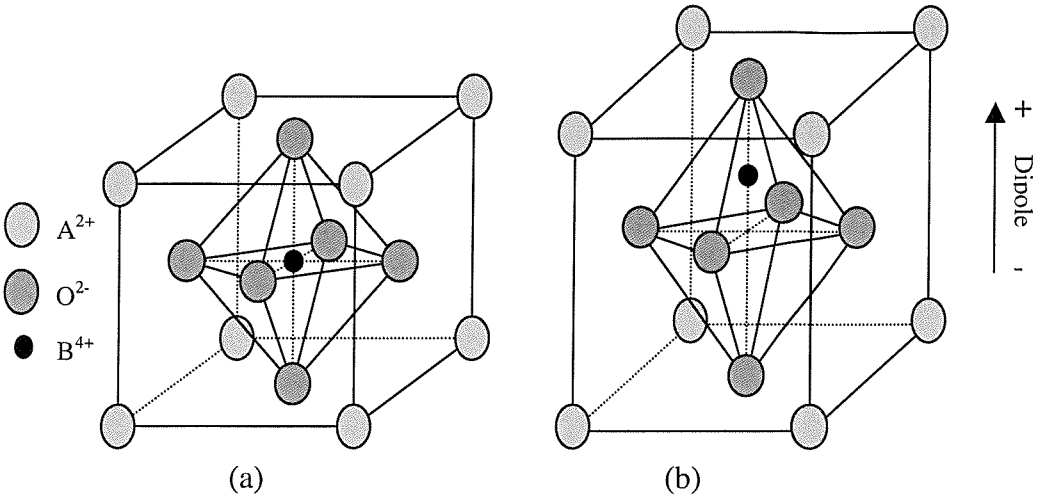

Figure 2.1: Perovskite crystal structure (a) cubic structure above the Curie temperature (b) tetragonal structure below the Curie temperature and has a dipole.

The crystal structure changes with temperature. Below a fixed temperature, known as the Curie temperature, the crystal exhibits piezoelectric activity. As the crystal temperature reaches the Curie temperature the crystal structure changes to a symmetrical cubic lattice and the ionic charges within the structure balance out thus removing the electric dipole of the crystal. Without the electric dipole the piezoelectric properties are lost.

2.2.2 Piezoelectric polarisation

The elementary cells of a piezoelectric crystal each have a built in electric dipole. These combine with neighbouring dipoles to form a region of local alignment known as a Weiss domain. The Weiss domain gives a net polarisation, the domains, however, are randomly distributed within the material.

In an ideal crystal, the Weiss domains would all combine to form a single large domain. However, commercially available piezoceramics are always polycrystalline. The polycrystalline structure creates a fragmented arrangement of smaller Weiss domains. These small Weiss domains are randomly oriented

and combine to create an electrically neutral sample as the vectors cancel each other out due to statistical distribution of directions.

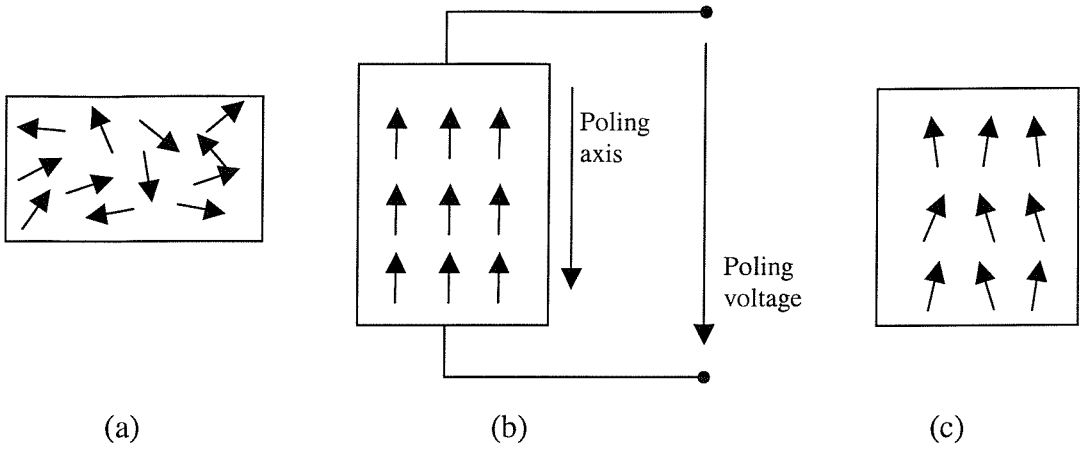

Figure 2.2: Electrical domain alignments

Whilst the domains are randomly oriented, figure 2.2(a), the material does not exhibit the piezoelectric effect or any overall polarisation. The domains must be aligned in a single direction in order for the material to become piezoelectric. This alignment is performed by the poling process.

The poling process involves the application of a large electric field to the material at just below the Curie temperature. Whilst this electric field is maintained, the domains are forced to switch and rotate into the desired direction, aligning themselves with the applied field, figure 2.2(b). This alignment also causes a change in the physical dimensions of the material.

The polarisation increases with electric field strength until it reaches a saturation point where no more polarisation can occur because all the domains are aligned [8]. As the field is reduced to zero, the domains moderately re-align but remain close to the desired alignment, as shown in figure 2.2(c). The result is a net polarisation that provides the piezoelectric material with a particular polarity. The material is said to have a remnant polarisation and this follows closely with that of magnetic hysteresis as shown in figure 2.3.

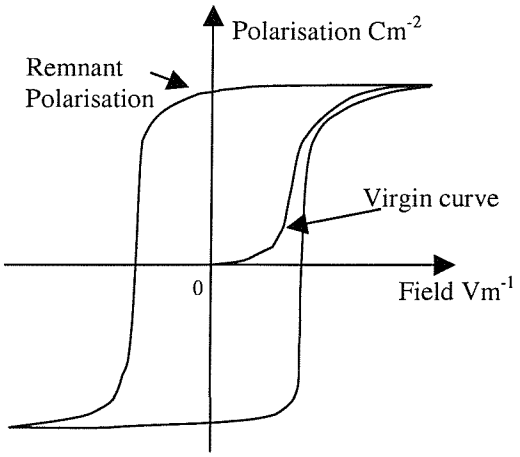

Figure 2.3: Typical polarisation hysteresis loop for a piezoceramic.

The volume of the piezoelectric material remains constant, so an increase or decrease in the sample dimensions will change others by the same amount.

2.2.3 Characteristic properties of piezoceramic materials

As stated previously, piezoceramics have anisotropic characteristics, thus, the properties of the material differ depending on which direction the measurements are taken. The anisotropic piezoelectric properties of the ceramic are defined by a system of symbols and notation [9]. This is related to the orientation of the ceramic and the direction of measurements and applied stresses/forces. The basis for this is shown in figure 2.4.

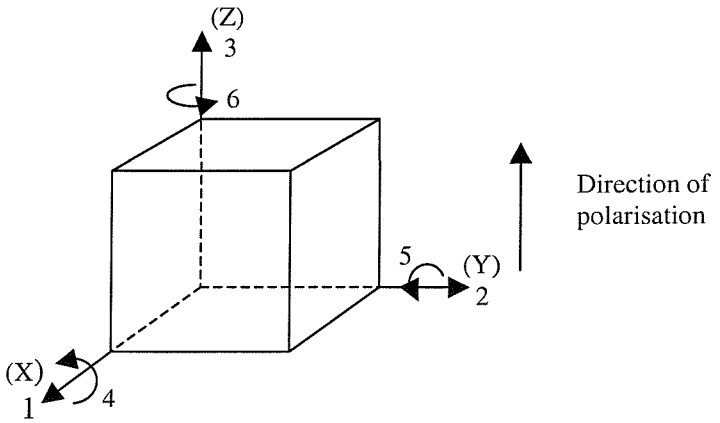

Figure 2.4: Notation of Axes

The level of piezoelectric activity of a material is defined by a series of constants used in conjunction with the axes notation. Most commonly used constant is the piezoelectric strain constant, d. This is often used because of the relative ease in which it can be measured compared to other piezo-coefficients.

$$d = \frac{\text{Strain developed}}{\text{Applied field}} \quad m/V \quad [2.1]$$

$$d = \frac{\text{Short circuit charge density}}{\text{Applied stress}} \quad C/N \quad [2.2]$$

Equations 2.1 and 2.2 show the two equations that relate the force and voltage to obtain the value of d. The results contained within this thesis focuses specifically on the characteristic value of d_{33}. The first subscript 3 indicates that the poling field is applied in direction 3, whilst the second indicates that the induced strain (or the applied stress) is in direction 3.

The following sets of equations are used to describe the characteristics of piezoceramics in more detail. These equations are known as the piezoelectric constitutive equations and are shown in their reduced suffix tensor form.

$$S_\alpha = s^E_{\alpha\beta} T_\beta + d_{i\alpha} E_i \qquad [2.3] \qquad D_i = d_{i\alpha} T_\alpha + \varepsilon^T_{ij} E_i \qquad [2.4]$$

$$E_i = -g_{i\alpha} T_\alpha + (\varepsilon^T_{ij})^{-1} D_j \quad [2.5] \qquad S_\alpha = s^D_{\alpha\beta} T_\beta + g_{i\alpha} D_i \qquad [2.6]$$

$$\alpha,\beta = 1,2,..6 \qquad i,j = 1,2,3$$

Where S = strain, D = electric displacement, E = electric field, T= stress, s = material compliance, ε = permittivity, d and g = piezoelectric strain constants. Where there is a superscript it means that the superscript value is constant, i.e. ε^T = permittivity at constant stress.

Equations 2.3, 2.4, 2.5 and 2.6 show the different electromechanical relationships involved in piezoceramics and are used in conjunction with

experimental and theoretical results to obtain the main characteristics of individual piezoceramics.

The electro-mechanical coupling coefficients, k, describe the efficiency with which the energy is converted within the material between electrical and mechanical forms in given directions. This is defined in equation 2.7 and 2.8 below.

$$k = \sqrt{\frac{\text{mechanical energy stored}}{\text{electrical energy applied}}} \quad [2.7]$$

$$k = \sqrt{\frac{\text{electrical energy stored}}{\text{mechanical energy applied}}} \quad [2.8]$$

In addition to this, k_p is defined as the planar coupling factor, which is typically used for radial mode of thin discs, and k_t is defined as the thickness mode coupling factor for a plate or disk.

Piezoceramics are used in a number of ultrasonic and other high frequency applications. Therefore the relative dielectric constant, K, and the dielectric loss tangent, tan δ, of the piezoceramic are often required.

The frequency constant, N, is the product of the resonant frequency and the controlling dimension. This property is important for frequency applications such as sonar and ultrasonic devices.

The piezoelectric properties of these materials will vary with age, stress and temperature. The change in the properties of the piezoceramic with time is known as the ageing rate and is dependant on the construction methods and the material type. This ageing means that manufacturers usually specify the constants of the device such as dielectric, piezoelectric and coupling for a specified time after poling. The changes in the material tend to be logarithmic with time, thus the material properties stabilise with age. The aging process is

accelerated by the amount of stress applied to the ceramic. Stress can be applied either by voltage or force. The higher the stress levels the faster the ageing. Temperature is a limiting factor with piezoceramics due to the Curie point. The application of stress can also lower the Curie temperature.

2.2.4 Measurement theory

The piezoelectric constant d_{33} is often used as the defining piezoelectric characteristic for improvements in piezoceramic technology. This value is significant because the majority of applications use planar technology where the electrodes are at the top and bottom of the application and thus the poling field and measurement direction are in axis 3. It is therefore important to measure d_{33} reliably and repeatably in order to confirm results obtained. For applications where the piezoelectric layer is mounted on a substrate the d_{33} value is often referred to as $d_{33,f}$ to indicate that the film is clamped by a substrate, section 4.3 covers this effect in more detail. There are three main methods of measuring d_{33}, the direct, indirect and resonant methods.

The direct method is a static method where a known force is applied to the ceramic sample and the piezoelectric charge generated is measured. This method uses equation 2.2 to find the value for d_{33}; the relation between the applied force and the voltage generated is shown in figure 2.5.

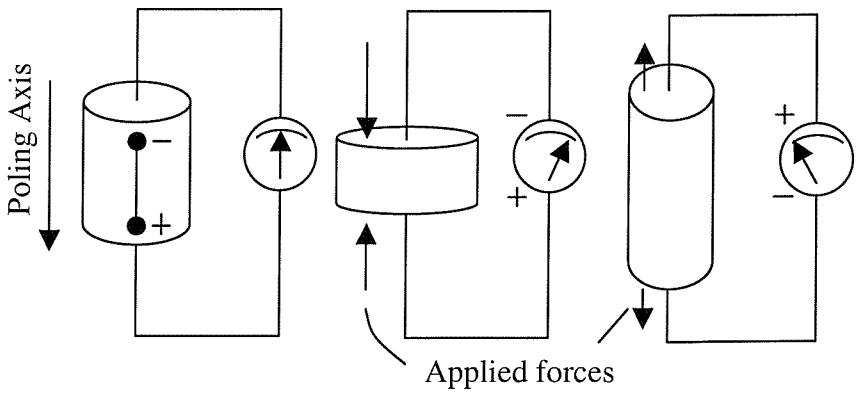

Figure 2.5: Relation between the applied force and charge generated.

Figure 2.5 shows that a compressive force applied along the poling axis will produce a voltage the same polarity as the ceramic element, and a tensile force will produce a voltage of opposite polarity. These effects are used in sensors and transducers for various applications. This method is the easiest to conduct because the voltage generated can be measured accurately with standard laboratory equipment. The majority of research papers use this method to measure d_{33} often using prototype measurement devices. A typical format involves the sample under test connected to a charge amplifier and then force applied or removed from the sample and the resulting charge being measured.

The indirect or converse method is also a static technique and is based on the relationship in equation 2.1. It involves an applied voltage to generate deformations in the dimensions of the ceramic that are much more difficult to measure than the direct method. Figure 2.6 below shows the relationship between the applied voltage and the resultant dimension change.

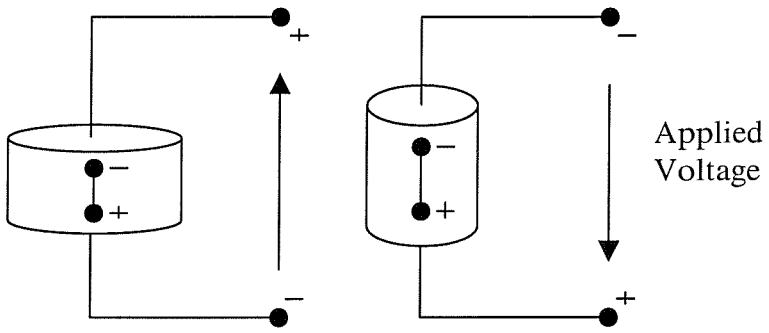

Figure 2.6: Relation between applied voltage and dimension change.

Figure 2.6 shows that an applied voltage of an opposite polarity will induce compression in the piezoelectric element and a voltage of the same polarity will induce an expansion along the poling axis. This property is used in acoustic and ultrasonic devices with an applied A.C. field. This method is rarely used in measurements due to the very small displacements in the devices, which are typically no greater than a few nanometres for the majority of MEMS devices.

The resonance technique [10] is a dynamic method used for obtaining an approximation of the value for d_{33} from the resonant frequency of the

piezoceramic. The equivalent circuit for the piezoceramic is shown in figure 2.7 below.

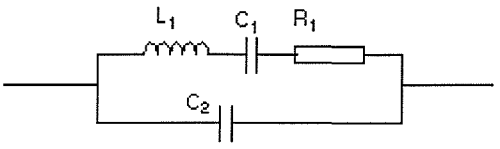

Figure 2.7: Equivalent circuit for a piezoceramic.

Figure 2.7 shows that the mechanical resonance of the device is represented by L_1, C_1 and R_1, and the electrodes of the device are represented by C_2. These components define the frequency response of the device which is shown with respect to the change in impedance levels in figure 2.8, it shows that if the vibration is electrically induced then the impedance falls to a minimum at resonance (f_m) and a maximum at what is known as anti-resonance (f_n).

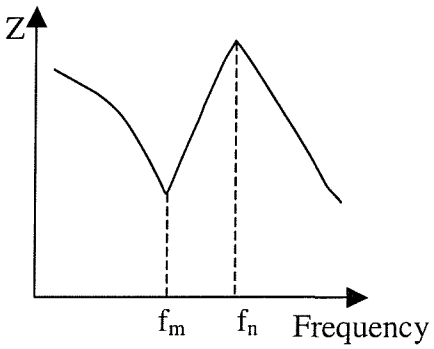

Figure 2.8: Impedance change with frequency.

This frequency value can be obtained by measuring the frequency at which the impedance is lowest and therefore the current is highest. This resonant frequency is related to the frequency constant N_{33} by equation 2.9.

$$f_m = \frac{N_{33}}{t} \qquad [2.9]$$

Where f_m = Resonance frequency.

N_{33} = Frequency constant in axis 3.

t = Thickness of ceramic.

Having obtained the frequency constant, equation 2.10 can be used to find d_{33}.

$$f_m = \frac{N_{33}}{d_{33}V} \Rightarrow d_{33} = \frac{N_{33}}{f_m V} \qquad [2.10]$$

Where V = Peak voltage at resonance.

This resonance technique is rarely used to measure the d_{33} value because of anomalies in the measured impedance as the frequency is increased. In addition, it is considered to be unsuitable for piezoceramics deposited on a substrate. This is due to the dominance of the substrate on the measured resonant frequencies and is therefore rarely used.

2.3 Piezoceramic materials

Piezoceramic materials are typically defined as either hard or soft ceramics. Hard ceramics have high mechanical quality factor (Q), low dielectric constant, low loss factor and are less susceptible to depolarisation. Soft and Hard PZT materials are obtained by adding dopant materials to the standard PZT composition. Donor dopant materials, such as niobium, or acceptor dopant materials, such as nickel, are used to obtain Soft and Hard PZT respectively. Hard ceramics are typically used in high power transducer applications such as sonar. Soft ceramics generally have a low mechanical Q factor, high dielectric constants and usually higher charge sensitivity than hard ceramics. Soft ceramics are used with low power sensor and actuator systems where sensitivity is an essential design factor. Industrial studies [11] have shown that PZT-5H formulation, a soft ceramic, provides the most sensitive composition in terms of electrical and mechanical responses.

2.3.1 Bulk piezoceramics

Most piezoceramic manufacturers develop what are termed 'bulk' devices, pressed ceramic structures fabricated from a combination of bulk piezoceramic

materials. This manufacturing process involves the use of a high temperature (1100-1700°C) sintering process to fabricate a solid poly-crystalline structure.

As stated previously, although there are many different piezoelectric materials, (e.g. Quartz, Barium Titanate, Lithium Niobate, and Lead titanate) the most commonly used piezoceramic is Lead Zirconate Titanate (PZT). This material is available in various formulations that are defined by the manufacturing process and the chemical composition of the material type. PZT piezoceramics produce the optimum piezoelectric activity when the composition lies near the Morphotropic Phase Boundary (MPB) [12]. The MPB is a boundary that separates the tetragonal and rhombohedral ferroelectric phases. PZT compositions that lie on the MPB are said to have both of these phases coexisting, which allows for a greater number of polarisation directions and improved results from the polarisation process [13]. These materials exhibit different mechanical and piezoelectric properties as shown in table 2-1.

Characteristic	**Bulk material type**			
	PZT4D	**PZT5A**	**PZT5H**	**PT2**
d_{33} (pC/N)	315	374	593	68
d_{31} (pC/N)	-135	-171	-274	-3
T_c (°C)	320	365	195	255
k_p	0.57	0.6	0.65	<0.02
k_T	0.675	0.71	0.75	0.54
N_p (Hz-m)	2180	1960	1965	2870
K^T_{33} ($x10^{-15}$)	1300	1700	3400	210

Table 2-1: Typical values for Bulk Lead Zirconate Titanate and Lead Titanate materials.

Another piezoceramic given in table 2-1 is Lead Titanate (PT). Lead Titanate is used because it has a high Curie temperature and low dielectric constant; this makes the material useful in high frequency and high temperature applications.

One of the problems associated with PZT and PT based ceramics is the difficulty with sintering, which can make the resulting ceramics fragile. The high sintering temperatures required result in the lead content of the ceramic being more mobile. This often causes evaporation of the lead, leading to an imbalance in the stoichiometry of the material, which can be a factor in reducing the piezoelectric activity of the ceramic. The lead loss can be avoided by firing the ceramics in a lead rich atmosphere to reduce lead evaporation or by reducing the firing temperature.

A particular problem with PT ceramics is that the high degree of lattice anisotropy makes the fired ceramic fragile when cooled. Studies by Chu et al [14] have considered the use of Calcium (Ca) or Samarium (Sm) in lead titanate ceramics to reduce the lattice anisotropy and increase the density of the piezoceramic. Their study used Sm, Manganese (Mn) and Ca with lead titanate, fired in a lead oxide atmosphere to maintain lead levels to compensate for losses in the sintering process. The results showed that an increase in Ca and Sm additives would increase the dielectric constant and reduce lattice anisotropy. The optimum percentage was found to be Ca at 13-15 mol%; this gave the piezoceramic a coupling factor k_T of 0.57 which is claimed to be sufficient for high temperature and high frequency applications. There are no specific figures given for the piezoelectric properties of the material so it is not possible to assess the impact these results have on any practical applications.

2.3.2 Thick and thin-film piezoceramics

As research and industrial developments tend towards miniaturisation of sensors and actuators, the requirement for smaller and more intricate designs increases. The high temperature and moulding pressures associated with bulk piezoceramics do not lend themselves easily to MEMS integration. Therefore, it was necessary to develop alternative techniques to combine piezoceramics and MEMS devices. These techniques can be classified as thick-film, typically 10-200μm thick [15], and thin-film, <1-10μm thick [16], piezoceramics.

Bulk ceramics are typically attached to a specific transducer structure using mechanical or adhesive bonding. However, piezoceramic films are deposited directly on to a substrate using one of a number of different deposition techniques discussed in section 2.4. Most piezoceramics films are fired at lower temperatures, 500-1000°C. This is not sufficiently high to obtain sintering between the bulk PZT materials and a sintering aid is often required to form a bonding matrix. The most common sintering aid for thick-film materials is a liquid phase glass, typically lead oxide (Pb-O) or lead borosilicate (Pb-Zn-B) with a melting point around 400°C. However, a number of alternative materials such as polymer-based binders have been developed that can be cured in air or temperatures below 200°C. Thin-film deposition techniques often rely on the chemical composition of the film to cause crystallisation of the film at specific annealing temperatures.

A study by Corker et al has considered the introduction of a sintering aid combining Cu_2O and PbO [17]. This work attempts to achieve similar levels of sintering to bulk devices whilst maintaining the lower firing temperature of 800°C. The study used Pz26-type PZT pressed pellets and a range of firing temperatures from 700°C to 950°C. The results showed good densification levels compared to the bulk Pz26. The optimum properties at low temperatures were achieved using 3 wt.% of the sintering aid, fired at 850°C. However, it was also noted that with 5 wt.% the firing temperature could be reduced to 800°C without a serious loss of performance. This study was conducted using bulk devices but the implication for thick-film technology is important as the results show that it is possible to improve density using an appropriate sintering aid.

2.4 Piezoelectric Layer Deposition Techniques

To use the piezoelectric layer in sensor and actuator applications it needs to be deposited on to a substrate. The substrate can either be a functional part of the device or simply a mounting for the finish product. A number of alternative techniques for depositing piezoelectric films have been established. The main

focus is to achieve a film that is free from cracks, is of uniform thickness and has good mechanical density.

2.4.1 Screen printing

Thick-film screen-printing, first reported by Baudry in 1987 [18], is attractive in MEMS applications because it is possible to print various patterns on a variety of substrate materials and therefore opens a broader range of possible applications than the traditional construction techniques such as pressing and extrusion [19].

Screen-printing is an effective and inexpensive method for producing the desired film geometry on the surface of the substrate. The technique is based on the same principles as t-shirt screen-printing. The screen design is etched on to a wire mesh using a photo-resistive etch which leaves only the desired pattern. The printable material is then placed on the screen and a squeegee drags the material across the design. As the squeegee passes over, the material is forced through the mesh and a deposit is left on the substrate under the screen in the desired pattern and the screen snaps back. The process is ideal for mass production with the ability to produce films of 10-200μm in one print whilst other deposition and printing techniques can require many hours of processing to achieve the same thickness. Limitations of conventional screen-printing are feature size and geometry with a minimum line width and space around 100-150 microns.

Recent work by Robertson et al has developed a thin stainless steel foil into which the required pattern is etched called the μ -Screen [20]. This custom etched mesh is mounted in a conventional screen frame and is therefore compatible with current printers this also alleviates problems with screen flexibility. The μ -Screen provides a higher resolution, 50μm line width, and edge definition than current fine line technology. The technology is not limited to squared off designs, curved lines and circular pads can also be produced easily on the mesh. Figure 2.9 shows a close up of the underside of an etched foil screen.

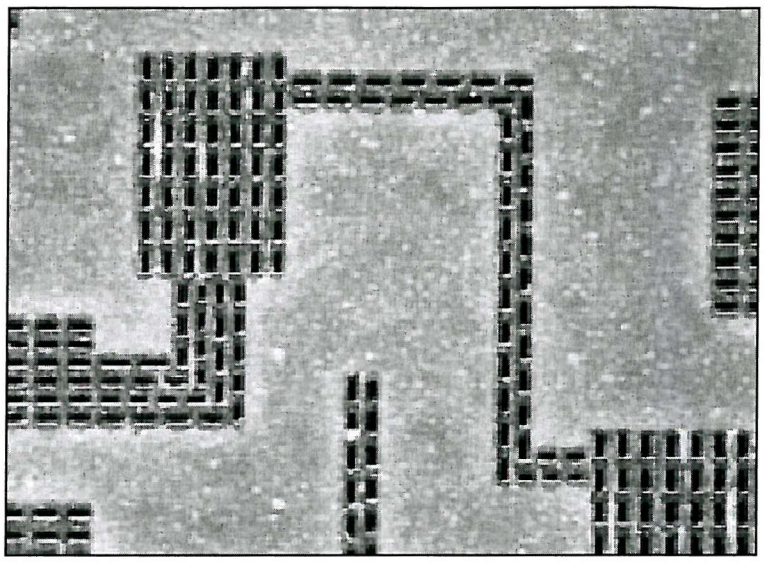

Figure 2.9: Close up of the underside of an etched foil screen. Holes are etched only where printing is required.

Work by Moilanen et al. has considered ways to reduce the amount of print cycles required for multilayer actuators. A new screen-printing technique known as double-paste printing was developed [21]. The technique maximises the efficiency of the printing process by only requiring only a single screen to be aligned and a squeegee blade that is divided into two sections. The screen is loaded with the electrode and piezoceramic pastes that the blade divides. When the printer is activated the blade passes over the screen and deposits the piezoceramic paste on one side of the substrate with the electrode on the other. For each subsequent print the substrate is rotated through 90° and a specific section of the substrate is covered whilst the screen remains in place. The printing is performed in a pre-determined sequence ensuring that the layers are built up in the correct order and the screen is designed with this in mind. With normal screen-printing, the screen must be cleaned before each new print to remove the possibility of contamination. It is claimed by the authors that this new printing method does not suffer the same problem because the piezoceramic screen apertures are designed to approach the actuator surface at different angles as the squeegee passes over the screen. This method will not work for all designs but where the system can be adapted it will be very beneficial to reducing costs in the mass production of multilayer stacked sensors and actuators.

The work contained within this thesis focuses on the use of screen-printed thick-films. Therefore, screen-printing and associated processing are described in more detail in chapter 3.

2.4.2 The Sol-Gel process

In general, thick-films are defined as films of 10-200μm. Some applications, however, require thin-films that are typically in the 1-10μm range. The Sol-Gel technique is usually known as a thin film technique but has seen increasing applications in thick-film devices [22]. Sol-Gel involves the transition of a mainly non-crystalline liquid solution, the sol, into a solid phase, the gel. Preparation of the sol involves the use of inorganic metal salts or metal organic components. This preparation subjects the materials to a series of hydrolysis and polymerisation reactions to form the suspension. The sol can then be processed further to make ceramic materials in various forms. This typically involves the formation of thin-films on a substrate by spin or dip coating. When the sol is cast it will form a wet gel, this is then converted into a dense ceramic with further drying and heat treatment.

Fabrication of Sol-Gel films above 10μm often leads to cracks in the film which leads to poor piezoelectric and mechanical properties. The advantage of this process, however, is the increased density of the films. This increased density of Sol-Gel films has lead to developments of composite Sol-Gel and screen-printed films. The studies are aimed at increasing the density of the typically porous thick-films by the application of a subsequent Sol-Gel film to fill the interstices in the film.

Work by Kim et al. [23] has seen the development of a composite technique for increasing the piezoelectric activity of a screen-printed PZT thick-film. A PZT paste was screen-printed on to a silicon substrate leading to a final film thickness of 20-40μm. A number of drying and burnout stages were used to remove the organic binder from the film. Subsequently, a Sol-Gel PZT solution was applied

to the dried thick-film PZT layer. The composite film was then sintered using temperatures of 700, 800 and 900°C to observe the effects of firing temperature on the film and substrate. The fired films were then polarised at 130°C for 15 minutes with an applied field of 10MV/m. SEM micrographs of the films show that the sol-gel treatment improved the density of the films although they were still porous. The 800°C firing profile produced the optimum results, the measured $d_{33,f}$ value was increased from around 75 to 177-200 pC/N with the application of a Sol. Above 800°C, the bottom electrode was shown to deteriorate which allowed diffusion of lead oxide between the PZT layer and the substrate. This diffusion results in a reaction in the substrate that removes the possibility of further microfabrication in the substrate and therefore reduces the number of applications available.

A similar development by Corker et al. [24] has seen the fabrication of thick-films using a composite of a ferroelectric powder and an organo-metallic sol. The solution was made using a Ferro Pz26 PZT powder mixed with the sol, a Kenrich KR55 dispersant and 5wt.% liquid phase sintering aid. The film was deposited onto KOVAR and platinised silicon substrates using spin coating at 2000rpm for 25 seconds. The films were dried on a hotplate at 450°C for 15 seconds. This process was repeated to build up a composite layer thickness between 8 and 40μm. The films were fired at 710°C for 30-45 minutes in an argon atmosphere. After firing, the films were polarised for 2 minutes at 90°C with an applied field of 4MV/m. Measured $d_{33,f}$ values of 50pC/N were achieved with these films. The results showed that the film density was higher than that achieved with conventional thick-films. However, it was noted that the films are denser close to the substrate than they are at the top of the film. This is considered to be due to a number of factors. These include; the sintering aid sinking within the film, the organic vehicle burnout during sintering resulting in pores and a similar effect caused by lead evaporation during firing.

2.4.3 Lithography

Investigations into new possibilities for thick-film deposition have included the use of microstereo lithography (μSL) as a viable deposition technique for piezoelectric thick-films [25]. Jiang et al. fabricated PZT thick-films on silicon substrates using the μSL apparatus. The μSL apparatus consists of precision computer controlled x-y-x stages, a blade with a precision micrometer and an argon laser with its beam delivery system. The UV curable PZT suspension consisted of ball milled PZT powder, UV curable monomer, photo-initiator, solvent and dispersant. The precision blade section of the apparatus was used to spread the PZT suspension layer uniformly with controlled thickness across the substrate. Subsequently, the film was solidified then patterned with UV laser exposures. The wafer was rinsed with isopropyl alcohol and deionised water to remove the unpolymerised PZT. After drying, and a process of curing and annealing, a final platinum electrode was sputtered on as a top electrode. The UV laser beam can focus at 1-2μm to obtain high-resolution designs. Complex 3D structures can be fabricated within a few hours with synchronised x-y beam scanning and z motion, layer by layer. Crack-free PZT films with thickness ranging from 50-130μm were achieved.

The highest claimed $d_{33,f}$ obtained was 100pC/N, which showed that PZT films could be effectively deposited on silicon in this manner and could also be integrated into further microfabrication process' on the substrate, giving this method an advantage for reduced costs and increased complexity and precision for MEMS. The disadvantage of this system is that each device must be processed individually on each substrate, thus not lending itself to low-cost, high volume, batch fabrication applications.

2.4.4 Anodic bonding

Studies have also been conducted to bond bulk PZT layers on to silicon substrates using anodic bonding [26]. This has the advantage of reducing reactions in the substrate due to the firing process whilst not loosing any

piezoelectric properties of the bulk PZT device. The process involved a glass layer deposited on the silicon substrate that was then placed on a hot plate. The substrate is subsequently heated to a bonding temperature between 350-500°C, a PZT layer and an aluminium electrode were then deposited. The hot plate formed the anode; the cathode connecting to the top electrode of the PZT layer, a DC bonding voltage was then applied. The equipment configuration is shown in figure 2.10.

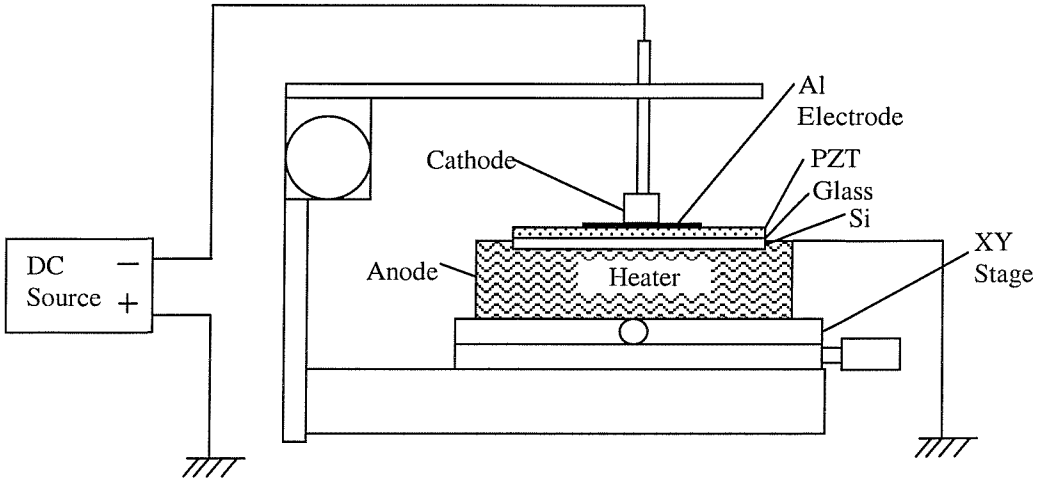

Figure 2.10: Anodic bonding equipment, Tanaka et al. [26].

The results showed that at 500°C with an applied voltage of 300V, a good bond was achieved after 20mins. Further experiments showed that the bonding temperature could be reduced to below 400°C with increased applied voltage or through the use of longer heating times.

This process has the advantage that the PZT layer used is bulk material and will therefore have higher piezoelectric properties. However, it is a more complex process requiring thermal expansion matching to ensure a suitable bond, thus limiting the compatible materials. The use of a bulk PZT also means that the device pattern is limited compared to the screen-printing approach and will require subsequent machining thus limiting its applications.

2.4.5 Hydrothermal deposition

The hydrothermal technique developed by Shimura et al. is a thin-film technique designed for depositing a PZT layer on a titanium substrate [27]. The hydrothermal technique utilises the chemical reaction between a titanium base metal and high temperature dissolved ions. The technique requires a nucleation process followed by a crystal growth process. A solution containing lead, zirconate and potassium hydroxide (KOH) is prepared and applied to the titanium electrode in an autoclave. The nucleation process results in an adhesive force between the titanium substrate and the deposited film. The crystal growth process then builds up the thickness of the layer with the chemical composition being controlled by the contents of the solution. The reaction takes 48 hours which makes it far more time consuming than screen-printing. However, it has been discovered that the crystal becomes polarised during the crystal growth process, the authors hypothesise that this is due to the chemical reaction being in the polarisation direction but a more detailed explanation is not currently available.

The hydrothermal film is reported to have a d_{31} of –90pC/N but subsequent repetitions of the process by Morita et al. [28] have produced a d_{31} –25pC/N which compared with other thin-films would seem a more realistic figure.

2.4.6 Sputtering

Sputtering is a thin-film technique that can produce a PZT film thickness in the micron range [29]. The technique involves bombarding a target to eject the surface atoms or molecules and then attract them to a substrate to form a deposited layer. A typical sputter technique uses hot pressed discs of PZT for the target material. The disc is placed in a vacuum chamber with the desired substrate. The PZT disc is then bombarded with argon ions and are deflected around the chamber. The substrate is either heated or polarised to attract the PZT molecules which then land on the substrate. The PZT condenses and forms a thin-film piezoelectric layer on the substrate.

2.5 Substrate Materials

Bulk ceramic devices are typically discs or rectangular shapes because the moulding and pressing processes used are often not suitable for small intricate designs without incurring large costs. This means the thickness of these devices tends to be in the hundreds of microns to millimetres range. Thick and thin-film devices, however, have typical thickness in the tens of microns range. The films are deposited on to a substrate to provide structural integrity to the films as they are dried and fired. The substrate therefore becomes part of the overall device structure.

2.5.1 Alumina substrate

Typical PZT thick-film devices use alumina substrates since they are inexpensive and offer good adhesion for the printed layers whilst being rigid enough to reduce the influence on the active device due to bending moments, covered in section 4.3. Alumina is hermetic so moisture is not able to seep in and reduce the quality of the prints during firing. In addition, the alumina has a thermal expansion coefficient that is closely matched to most thick-film inks.

2.5.2 Silicon Substrates

Investigations concerning the use of silicon substrates to integrate the PZT sensors directly with the electronic circuitry have produced significant results for the increase in MEMS applications including resonators, accelerometers and micro-pumps. [30,31,32]. However, lead diffusing into the silicon substrate during firing is a significant problem for MEMS applications. Work by Maas et al. evaluated the use of a screen-printed Heraeus IP211 barrier layer [33]. The results showed that there was no lead diffusion into the substrate and that the lead diffused into the barrier layer did not change its insulating characteristics. The authors therefore concluded that the electrodes and further thick-film devices could be printed on to the barrier layer without short-circuiting. This is a significant result because one of the limiting factors of using silicon substrates is

the reaction caused by lead diffusion from the PZT film. A reduction in this lead diffusion enables further micro machining of the silicon substrate. Therefore, an increased number and range of potential applications may be realised on silicon substrates that can integrate further electronics and mechanical structures to reduce costs and application dimensions.

Chen et al developed an ultrasonic transducer consisting of a PZT film printed on to a silicon micro-machined system [34]. The films that were produced were screen-printed using Ultrasonic Powders Inc. PZT501A material with a 4wt.% glass frit content, fired at 850°C ensured no blistering of the bottom electrode. However, SEM micrographs showed the low firing temperature resulted in the presence of residual porosity in the films. This work showed that it was possible to print crack free PZT films onto silicon substrates; measurements showed that a maximum $d_{33,f}$ of 50pC/N for the films was obtained.

2.5.3 Glass substrate

Current studies have highlighted the future possibilities for glass as a substrate [35] for use in optoelectronic circuits such as optocouplers or isolation amplifiers. These studies involved polymer-based thick-film conductors and resistors due to the limits of low temperature firing with a glass substrate. The study has shown that hybrid thick-film circuits are a viable area for development, with future possibilities for piezoelectric thick-films being incorporated into optoelectronic systems.

2.5.4 Piezoelectric substrate

Some sensor designs use the piezoelectric material as the substrate. Surface Acoustic Wave (SAW) devices are often designed to use a piezoelectric substrate [36]. The SAW devices are fabricated on piezoelectric materials such as Quartz, Lithium Niobate ($LiNbO_3$) and Lithium Tantalate ($LiTaO_3$) which provide excellent temperature stability due to their high Curie temperatures and high

electro-mechanical coupling coefficients making them ideal for high frequency applications, typically 10MHz to 2GHz.

In addition to these traditional materials, more recent work has considered bulk PZT. A pressure sensor, developed by Huang and Cheng, uses a bulk PZT substrate with the sensor layers deposited above [37]. An insulating layer of SiO_2 is sputtered on to the bulk PZT and this is then placed within the probe structure for use as a pressure sensor.

2.6 Alternative piezoelectric materials

The range of applications for MEMS devices is increasing rapidly. Therefore, designers require new piezoelectric materials to support these developments. Traditional materials and deposition techniques described in sections 2.3 and 2.4 are restricted to applications with a flat and reasonably rigid surface. This section describes examples of the ongoing work to develop new piezoelectric materials and the deposition techniques developed alongside them.

2.6.1 Polymer-based piezoelectric films

Interesting developments in polymer materials have recently lead to their increasing use in thick-film devices [38,39]. Polymer devices have the advantage of having simple fabrication techniques, low cost and most significantly, the ability to be deposited on a wider range of substrates. The methods of depositing polymer films can include; spinning or casting, screen printing, electrochemical polymerisation and vacuum deposition.

The most common piezoelectric polymer in current sensor and actuator applications is polyvinylidene fluoride (PVDF) [40]. The devices using piezoelectric polymers are similar to standard cermet films but with greater flexibility in design and processing. The films can be cured at lower temperatures (100-250°C) and poled at lower voltages in comparison to standard cermet films. This enables these films to be compatible with plastic substrates as

well as other materials with low resistance or melting points. Current PVDF films have low Curie temperatures of around 80°C and comparatively low piezoelectric constants, with a measured $d_{33,f}$ of 24pC/N [40].

Further studies by Papakostas et al [41] have considered the use of polymer binders in thick-film pastes. This replaces the standard glass frit binding material in an effort to lower the processing temperatures. The experiments used PZT5H powder and Ronascreen Green OPSR 500 polymer. Three pastes were analysed, 90, 85 and 75wt.% PZT powder with their respective amounts of polymer paste. These pastes were printed on to an alumina substrate with a capacitor structure of two electrode layers with the test paste in between. The bottom electrode was a standard cermet silver/palladium ESL 9635-A paste used for convenience in the experiment. The top electrode was a standard silver polymer ESL 1107-S paste.

The PZT/Polymer layer was printed and then dried in an IR drier at 140°C for 10 minutes, this partially cures the polymer. The samples were cured under a polarising field for 1 hour, with a selection of samples poled for 24 hours. Poling/Curing was conducted at 130°C with an applied field of 3MV/m.

The results showed the 85wt.% concentration to give the best results, with a $d_{33,f}$ of 15 pC/N. The results also indicated that the poling time does not result in a significant improvement in $d_{33,f}$ and this allows for poling to be concurrent with curing. This is a low figure for $d_{33,f}$ and the measurement method used is not very accurate. The low $d_{33,f}$ value is thought to be influenced by the lack of a high temperature firing process for the PZT powder, thus the stoichiometry of the material remains in the pre-fired state and not at the morphotropic phase boundary where the optimum piezoelectric properties occur.

2.6.2 Piezoelectric paints

Piezoelectric paints are an area of increasing interest as manufacturers seek sensors with more direct interaction with the surface they are mounted upon. It

is important that these materials have no adverse effects or require changes to the existing mechanical structure and material. Work by Egusa and Iwasawa has investigated piezoelectric paints [42] using PZT ceramic powder as a pigment and an epoxy resin as a binder. The paint films obtained were between 25 and 300μm thick having been cured at room temperature or 150°C on aluminium substrates. This work has proved the viability of piezoelectric paints for applications such as vibration sensors and acoustic emission sensors.

Novel work by Hale and Tuck has seen the development of a strain sensor using a PZT based lacquer spray [43]. The effectiveness of a piezoelectric paint is largely dependant on the amount of piezoelectric powder loading. The research identified a lacquer by 'LeFranc et Bourgeois' as a suitable resin binder which could contain a 75wt% of PZT whilst maintaining a blemish-free finish. Paints with 80wt% concentration of PZT were also realised. However, it was only possible to apply these with a brush, this produced films with an uneven surface and susceptibility to short circuits. The painted films use a steel substrate as a bottom electrode, with a vapour deposited gold for the top electrode. Experimental results showed that poling for 1 hour at 600V produced the optimum piezoelectric properties. The strain sensors have produced output voltages in excess of 200mV, however, it is stated by the authors that repeatability between sensors is limited and further work is focused on developing a repeatable fabrication process.

2.6.3 Piezo-composite materials

Figure 2.11 shows a diagram for the general types of piezo-composite available. However, most designers define the combination of a piezoelectric ceramic and a non-piezoelectric polymer as a piezo-composite [44,45].

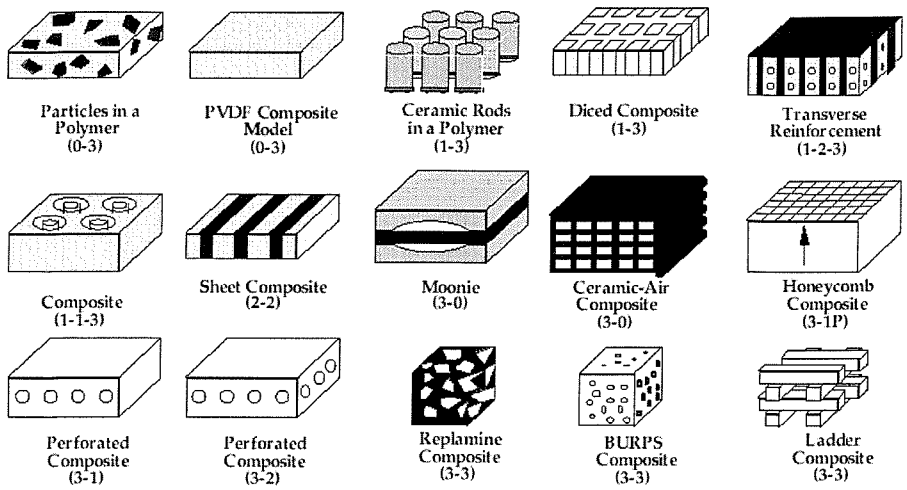

Figure 2.11: Schematic showing piezoelectric composites with different connectivity, A. Safari [45].

The most common form of piezocomposite consists of PZT rods in a polymer, often referred to as a 1-3 Composite. These 1-3 Composites are typically constructed by bundling together the PZT rods and then casting a polymer around them, once dried the composite disk is just sliced off. An alternative fabrication technique involves cutting grooves into a bulk ceramic and then casting the polymer in-between, once dried the base of the PZT rods is removed leaving the desired 1-3 piezocomposite. The fabrication technique is limited by the fragility of the PZT rods and is typically limited to rod diameters of ~50 microns. In addition, the machining required to remove the base and polish the piezocomposite disk can result in damage due to the problem of machining a brittle ceramic and a flexible polymer simultaneously.

The piezocomposites are ideal for medical ultrasound application because they provide high electromechanical coupling, due to the compact nature of the fabrication, and an acoustic impedance close to that of body tissue, due to the flexible polymer. In addition, the rod composite geometry can be designed to focus the ultrasonic waves to further enhance medical imaging applications.

2.7 Applications of piezoelectric materials

This section provides an overview of common applications for piezoelectric materials. The most familiar application for a piezoelectric material is that of the

Quartz time base for use in clocks and other timepieces. Marrison and Horton demonstrated the Quartz crystal clock [46] for the first time in 1927, since then, the invention has developed uses in various modern day applications such as computers, calculators, digital watches and mobile phones. Industrial and military applications for piezoelectric materials typically involve ultrasonic and sonar devices with large-scale bulk devices providing the signal strength required for long distance communication and detection [47,48]. Recent manufacturing developments such as screen-printing, thin-film sputtering and sol-gel have been used successfully to combine piezoelectric materials and complex MEMS designs from accelerometers to micro-pumps.

2.7.1 Acoustic and Sonar applications

Traditional applications for piezoceramics include the field of ultrasonics and in particular for sonar devices, with bulk and thick film devices being used in transducers. One such application is that of flextensional piezoceramic transducers for underwater acoustics applications [49]. These devices are typically based on very thin bulk ceramics. However, as technology advances the introduction of thick film devices would increase their resolution and accuracy, thus, increased control over micro movement without the inaccuracy of mechanically moving parts.

Acoustic wave sensors are highly sensitive and are most commonly found in the telecommunications industry. However, recent developments have seen an increase in applications such as chemical, humidity, vapour, temperature and mass sensors [36]. Traditional designs are etched directly on to a piezoelectric substrate such as quartz and lithium tantalate.

Work by White and Ko has evaluated the use of a thick-film acoustic wave design [50]. The use of thick-film technology allows for a reduction in costs due to the less labour intensive processes associated with screen-printing. The design was printed on a 96% alumina substrate using a PZT-5H type

piezoelectric layer with silver palladium electrodes both deposited using the screen-printing process. Figure 2.12 shows the layout of the design.

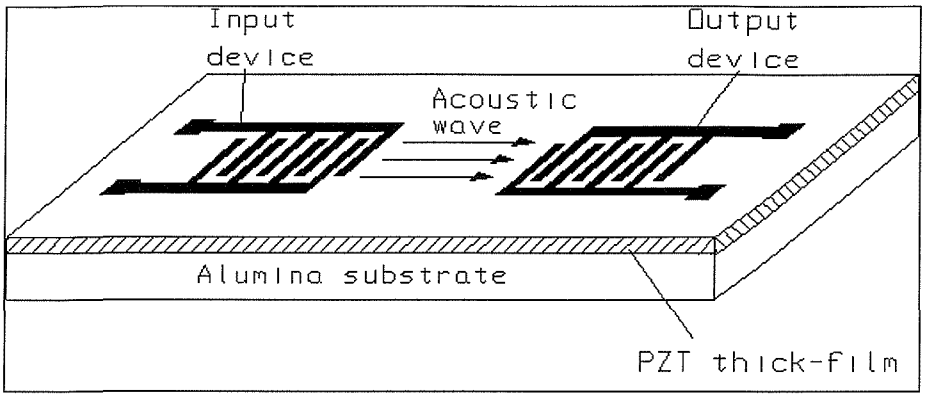

Figure 2.12: Thick-film acoustic wave sensor, White et al, [50].

The device operates by applying an alternating voltage at the input which gives rise to an acoustic wave in the structure due to the piezoelectric effect. This wave propagates to the output electrode providing a detectable signal due to the inverse piezoelectric effect. The devices were tested to observe the effects of strain on the resonant frequency. The resonant frequency was measured and then a mass was applied to the centre of the beam, any changes in the resonant frequency were recorded. The results showed a linear characteristic for the devices and a suitable response for use in applications such as torque, pressure and low magnitude force measurement.

2.7.2 Accelerometers

As the piezoelectric and mechanical properties associated with thick-film technology improves, applications become more varied. One area of current research is accelerometers and their use in the automotive, industrial and laboratory fields. Accelerometers can use different effects such as piezoelectric, piezoresistive and variable capacitance methods. Devices using piezoelectric effects have higher bandwidths because of their intrinsic material stiffness but are more susceptible to temperature changes and drift due to charge build up and ageing of the materials.

Studies by Crescini et al have developed a thermally compensated thick film accelerometer [51]. The paper shows that the use of two sensing elements printed on either side of the substrate in a plane capacitor structure allows for the reduction in thermal drift. By connecting the two piezoelectric elements in series and packaging the sensing elements and the electronics close together, it is possible to reduce the effects of the extra charge generated with increase in temperature. However, this requires the manufacturing limits of the devices to be as close to a perfect match as possible. The two devices are polarised in the same axis, but with opposite polarity. This means that any thermal drift in one device will be the opposite polarity in the other and therefore cancels out. Figure 2.13 shows a schematic of the device.

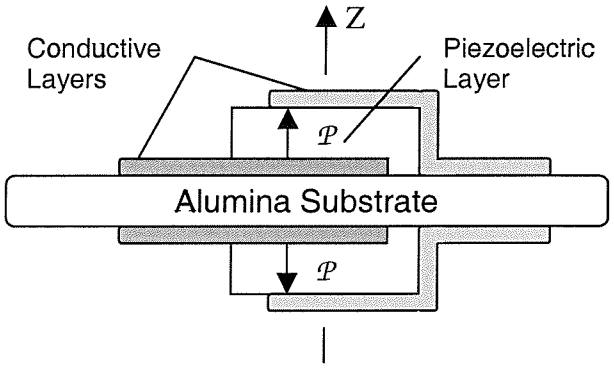

Figure 2.13: Cross sectional view of the accelerometer sensing part. Crescini et al [51].

By removing the inertial mass, the high frequency cut off of the device is determined only by the resonance properties of the alumina substrate that the devices have been printed on, the elastic properties of the case or the bonding techniques used. The printed films were 40-50μm thick, with a $d_{33,f}$ coefficient of around 180 pC/N when poled at 3 MV/m.

An accelerometer design by Beeby et al combines a silicon micromachined structure with screen-printed thick-film PZT layers [52]. The accelerometer is a deflection based system with a central inertial mass suspended by four beams, the beams are located at each corner of the mass and are covered with a

piezoelectric element. Figure 2.14 shows an aerial view of the accelerometer design.

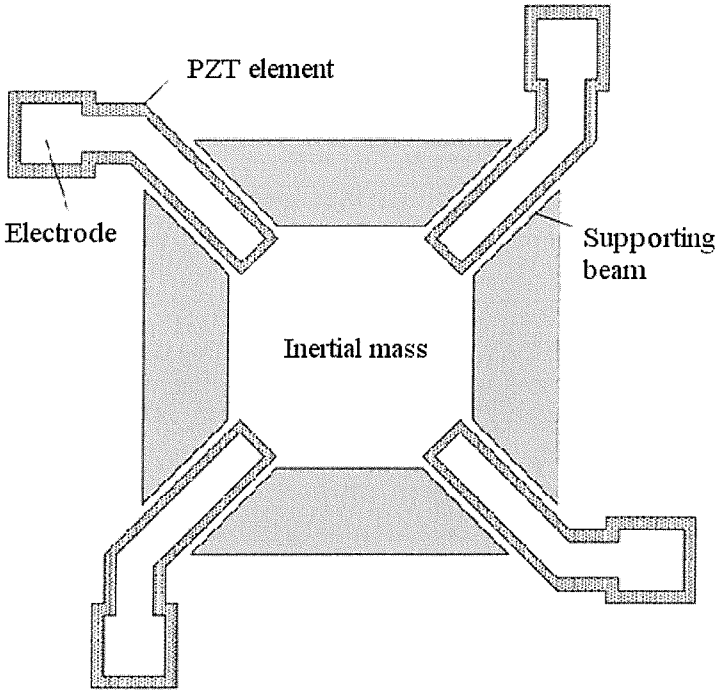

Figure 2.14: Diagram of accelerometer. Inertial mass 4mm^2; beam 975μm long. 750μm wide; piezo element 900μm long, 600μm wide; top electrode 800μm long, 420μm wide. Beeby et al [52].

The piezoelectric element is printed in a capacitive structure with a bottom and top electrode sandwiching the PZT layer. The novelty of this design is that the screen-printing of the cermet layers is performed prior to the etching of the silicon. This approach enables the use of the more cost effective screen-printing deposition technique where previously the forces involved in printing would damage the etched structure. The piezoelectric elements act as sensors to detect the deflections of the inertial mass, the optimum detection position was determined using the ANSYS™ finite element (FE) analysis software package. In addition, the piezoelectric elements are used as actuators to perform a self-test diagnostic on the device, which, with the aid of a microprocessor, can determine the resonant frequency of the device and confirm the operation of the piezoelectric elements [53].

2.7.3 Stress and Strain Sensors

Capacitive strain sensors are an innovative area of investigation for thick film devices. Previous implementations have involved air as the dielectric between two plates, where the change in geometry results in a change in capacitance. Arshak et al have investigated the use of PZT and polyvinylidene fluoride PVDF dielectrics [54] fabricated on alumina substrates. As a strain is induced on the sensor, the thick film dielectric is deformed; this causes a change in capacitance. It has been found that the capacitance increases proportionally with the increase in strain, this is known as the piezocapacitive effect. The sensitivity to strain of a certain material is known as the gauge factor (GF), it is defined as the ratio of change in resistance and material strain due to an applied stress. The results have shown that both the PZT and PVDF films show good linearity and have a good gauge factor, 6 and 3.5 respectively, in comparison to commercially available devices, 2 [55]. They also exhibit greater sensitivity and it is claimed that with external circuitry this is increased by a factor of 10.

2.7.4 Piezoelectric bimorph actuators

The deformation that occurs when an electric field is applied to a piezoceramic is essential in MEMS using bimorphs. One such bimorph application has been studied by Yoo et al to be used as part of a cooling fan for electronic devices [56].

Typical cooling fans are of the rotary type with electronic motors that produce undesirable electromagnetic noise. The advantages of this bimorph structure design are reduced electromagnetic noise and reduced power consumption compared to existing motor designs; both are essential design factors for modern electronics. Four designs, shown in figure 2.15, were evaluated using aluminium, phosphor bronze and brass for the vibrating plate. The most effective design was shown to be a phosphor bronze vibrating plate with a pressed bulk PZT-5 piezoelectric element on each side, design (c) in figure 2.15.

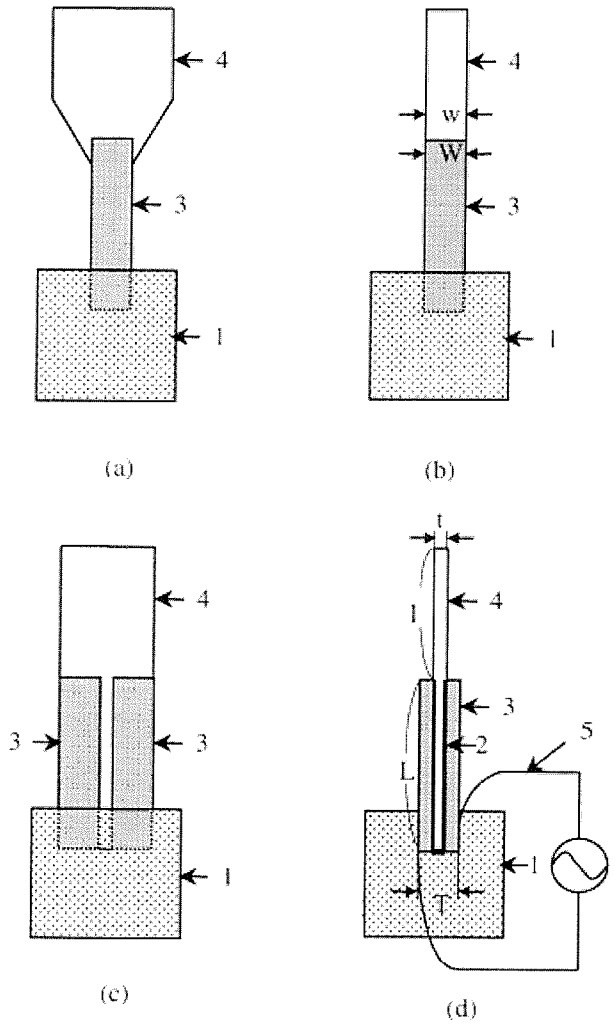

Figure 2.15: Designs of the piezoelectric fans. Different parts are labelled as the following: 1, base support; 2, elastic adhesive; 3, ceramic bimorph; 4, metal vibrating plate; 5, AC voltage circuit. Yoo et al. [56].

The optimum design had a measured d_{31} of –173 pC/N, giving a wind speed of 3.1m/s showing promise for future developments.

Friend et al have also incorporated the bimorph actuation technique in their design for a piezoelectric linear actuator [57]. The design uses a multiple array of piezoelectric bimorphs, again using a thin phosphor bronze plate with PZT on either side. The principles of the design and associated motion are shown in figure 2.16.

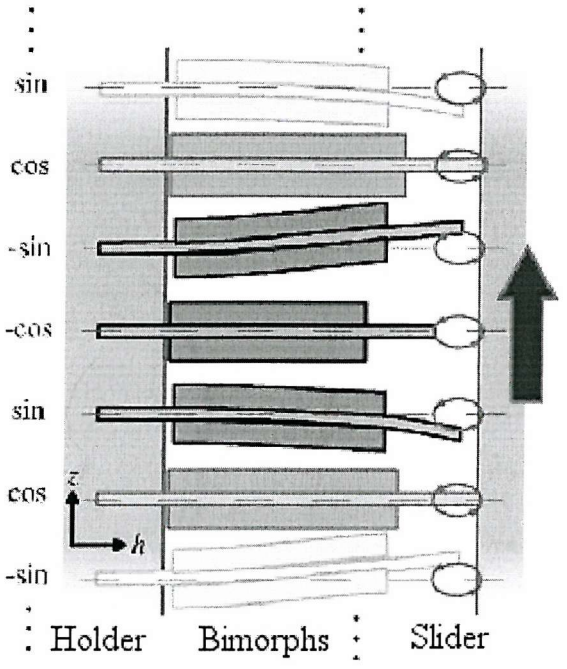

Figure 2.16: Layout and principle of motion for multiple bimorph linear actuator. Friend et al. [57].

The PZT used is a bulk ceramic, Taiheyo type-NA, that was attached using an epoxy adhesive. Four bimorphs were mounted in parallel on an aluminium plate with the actuation end being placed on a bakelite plate to test the strength and speed of the linear movement. A linear velocity of 18.1cm/s and 150mN of force was obtained.

2.7.5 Ultrasonic motors

Recent work has considered the use of a piezoelectric actuator as part of a transducer to convert ultrasonic vibrations to rotary motion in the form of an ultrasonic motor. The advantage of the ultrasonic motor compared to the traditional electromagnetic design is that the component parts, rotor and stator, are solid structures instead of wire wound coils. There are a wide range of ultrasonic motor designs each using different principles of converting ultrasonic vibrations to rotary movement [58,59,60,61].

An ultrasonic motor design by Hu et al. has looked at the feasibility of using piezoelectric actuators to levitate the rotor [62]. Two Langevin PZT transducers

(BLT) are attached to a ring shaped stator with a ring shaped rotor inside the stator, separated by a 0.05mm air gap shown in figure 2.17.

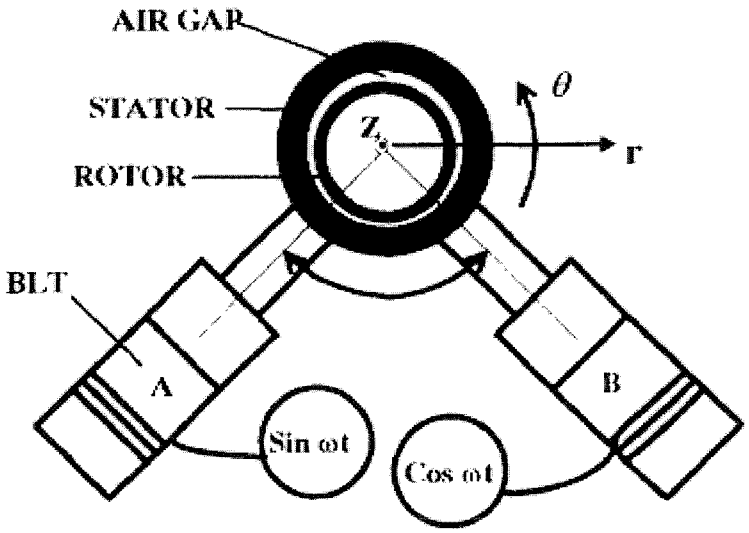

Figure 2.17: Ultrasonic levitated motor design. Hu et al. [62].

The transducers vibrate to excite a travelling wave in the structure that results in the rotor levitating and then being driven by the flexural ultrasonic vibrations. The paper reports that the motor has a revolution speed that exceeds 3200rpm. The Langevin transducers use bulk ceramic technology, this is a potentially prohibitive factor for integration within a MEMS device where minimum feature size is required.

Dexterous robot arms, manipulators and endoscopes are some of the areas that the development of ultrasonic motors is concerned with. Takemura et al. have developed a multi degree of freedom (DOF) ultrasonic motor with a small CCD (Charge Coupled Device) camera mounted on the tip [63]. The motor uses a column design for the stator, which is then vibrated in three modes using piezoelectric ceramic plates. Driving the column into specific bending modes causes the spherical rotor, mounted on top of the column, to rotate using frictional forces. This design uses pre-fired bulk ceramic plates that are screwed together. Although the design requires complex construction, the motor requires no gears and provides full multi-directional control for the CCD camera on the tip providing the design with potential applications in the medical and industrial maintenance industries.

Similar column designs have been developed using thin-film piezoelectric layers deposited hydrothermally [27]. Developed from a bulk device equivalent by Kurosawa et al. [64], the design has been changed to incorporate a thin-film PZT layer and reduce the size of the motor to 1.4mm diameter with a 5mm long stator [65,28]. A thin-film PZT layer, 12μm, was deposited on to a titanium stator using hydrothermal deposition. The rotor is made of stainless steel and is held in place using by a spring at the top of the cylinder. The contact area between the stator and rotor is conical and spherical respectively; this configuration provides enough contact for the rotor to be moved by frictional forces. The PZT layer is printed in four equidistant electrode patterns along the length of the cylinder. Each electrode is electrically excited in turn with a 90° phase shift. Using the indirect piezoelectric effect a travelling wave on the top and bottom surfaces causes the rotor to rotate, the principle of the motion is shown in figure 2.18.

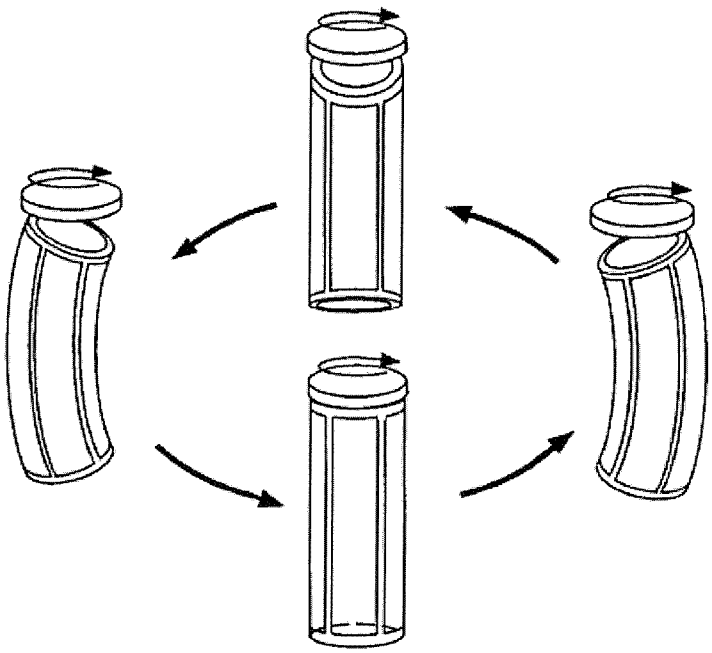

Figure 2.18: Principle of the cylindrical ultrasonic motor. Morita et al [65].

The research has demonstrated a working micro ultrasonic motor that has a reversible revolution direction and a maximum output torque of 0.67μNm.

Work by Aoyagi et al has seen the development of a thick-film screen-printed multi-degree of freedom ultrasonic motor [66,67]. The electrode and PZT layers are deposited on to a 96% alumina substrate using the screen-printing technique. The electrodes are arranged in such a way that the piezoelectric elements can drive the substrate into three specific resonance modes, defined as B_{30}, B_{03} and B_{22}. An alumina column is attached to the middle of the substrate on the opposite side to the electrodes with a metal sphere on top as the rotor. When an A.C field is applied to the electrodes at the appropriate voltage and frequency, the substrate is driven into a vibrational mode, the column moves accordingly and frictional forces move the rotor. The vibration modes can be combined to induce movement of the sphere in specific directions thus allowing the sphere multi-degrees of freedom. The PZT 5H-type used in the motor gave a measured d_{31} of –33pC/N compared to the bulk value of –274pC/N. This reduction in d_{31} meant that a relatively large voltage of 200V needed to be applied to obtain a sufficient level of excitation. Improvements in the piezoelectric properties of thick-film PZT-5H could potentially lower the excitation voltage required or provide greater control for the existing voltage. This supposition is explored in more detail, with particular relevance to the work contained in this thesis, in section 11.6. The very basic construction techniques required for this motor make it ideal for mass production in areas such as medical applications where cost is a large factor.

2.7.6 Multilayer stacked actuators

Related developments in actuator technology have shown that multilayer structures can be constructed using thick film screen-printing processes more efficiently than conventional stacked actuators. The layers can be printed to the desired shape and fired in a furnace to complete the design as a single element where before, the individual layers would be assembled and bonded separately.

Current studies have shown that multilayer actuators using piezoelectric layers can provide higher accuracy, displacement and lower production costs than typical devices. Zhu et al [68,69] have researched possible implementations

involving a screen-printed PZT paste with 5wt.% lead oxide as a binder on an alumina substrate. Using a sandwich layer fabrication technique, one PZT layer is screen-printed then an electrode before the next PZT layer, building up 7-15 layers depending on the sample. Also observed was the grain size for the PZT layers after firing along with the d_{31}, showing a 4μm grain size to give the greatest value of –101pC/N for d_{31} with 11 layer devices. The study showed that a great number of laminated layers were not a prerequisite of a large actuator displacement and therefore production costs could be reduced with the increased precision for such applications as computer hard disk driver actuators. Their results also showed that higher sintering temperatures increased the average grain size, which resulted in increased piezoelectric coefficients.

2.7.7 Micro-Pumps and Liquid/gas sensors

A MEMS micro-pump is another application that benefits from piezoelectric actuation [70]. These consist of an etched membrane on a silicon substrate, with a PZT actuator moving the diaphragm. One such device, shown in figure 2.19, consists of two silicon wafers with cantilever valves etched into the top and bottom wafer then both bonded together.

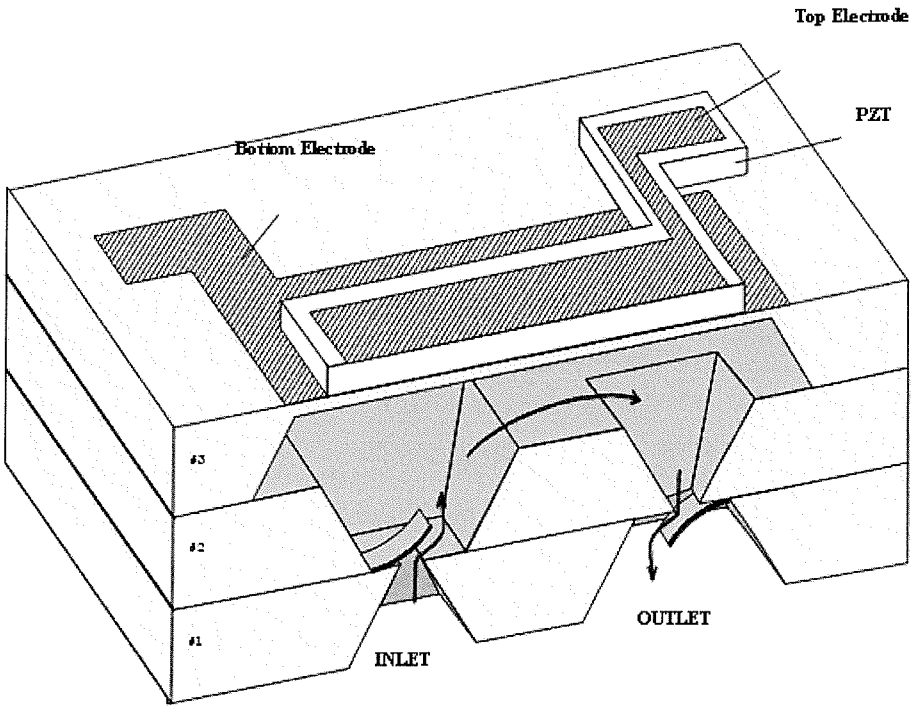

Figure 2.19: Flow and pressures within the micro pump, Koch et al. [20]

A silicon nitride/silicon dioxide double layer was deposited on silicon and then patterned with a standard KOH etch to form a membrane. This left a cavity between the two structures. The PZT layer was then printed on the membrane as an actuator to oscillate the membrane. As the diaphragm moves it causes a volume displacement, which results in a flow through the cavity. The valves are orientated in such a way that the flow is unidirectional.

This pump design was simulated using ANSYS and FLOW3D and verified by the device. The simulations showed that a pump rate of 400μl/min is achievable and therefore is practical for medical drug dispensing or other sample collection applications.

Possibilities for thick-film PZT technology to be used in the fabrication of gas sensors have also been studied [71]. In general the devices work by the use of ultrasonic resonance of gas flowing through a cavity cell, with a specific change in the gas resulting in a change in the resonant frequency that can therefore be detected electronically. The advantage of using PZT films for this application is the wide range of design possibilities for the devices. A lower temperature coefficient that PZT films exhibit over the conventional quartz crystal devices is also advantageous in this field.

2.8 Conclusions

This chapter has reviewed a number of current piezoelectric materials and deposition techniques. The chapter has emphasised work related to thick-film PZT materials and the screen-printing deposition technique. The current level of piezoelectric activity claimed to have been achieved in these areas have been highlighted. The review has shown that there is scope for improvement both in the mechanical and piezoelectric properties of the films.

A number of the most common applications that feature piezoelectric materials have been discussed in detail. The techniques used to fabricate the devices and the problems associated with these has been discussed.

The scope for optimisation of PZT screen-printed thick-films is large. The number of applications that would benefit from an increase in the piezoelectric properties, using the same raw materials, gives a large impetus for continued work in this area.

3 Thick-film piezoelectric material processing

3.1 Introduction

This chapter of the thesis describes the standard thick-film process used at the University of Southampton. This process is used throughout this project to fabricate screen-printed PZT thick-film layers. The chapter begins with an overview of the thick-film screen-printing process parameters required, with emphasis on the materials that will be used in this study. Each stage of the thick-film process is then discussed in detail for the standard process and those specific to this thesis. These stages are:

- Screen design.
- Mixing the powders to form a thixotropic paste.
- Printing the paste with a screen-printer.
- Drying the printed films.
- Firing the films in a furnace.
- Poling process.

The section also covers any problems associated with each stage of the process and details any compromises made. In addition, where required, a discussion of any future changes that could be made to each process stage.

3.2 Piezoceramic thick-film screen printing process

The thick-film screen-printing fabrication process is based upon that used for fabric printing for hundreds of years. The process involves a specific material being deposited on an underlying substrate using a patterned screen. The advantage of a screen-printed film is that it can be used to deposit complex

patterns. In addition, the process can often be combined with existing micro-machining techniques to reduce costs [72].

3.2.1 Screen design

The pattern to be deposited on the substrate is defined by the screen. The majority of the screen is covered with an emulsion, the patterned areas are left clear so that the paste can pass through the screen on to the substrate below.

The pattern is designed using the LEdit™ computer aided design (CAD) software. A screen must be designed for each of the desired layers, this makes CAD very beneficial as it is possible to observe all the layers together and plan the printing order correctly. For more complex designs, it is often advantageous to use alignment aids such as squares or crosses. Using these aids enables the operator to align intricate designs using just a simple square away from the main pattern.

The screen consists of a metal frame with a patterned steel or polyester stretched mesh. The size of the frame limits the size of the design as in order to print the screen must be able to flex and it cannot flex where it is attached to the frame. The choice of mesh size determines the maximum resolution of the design. A mesh with a mesh count of 125/cm (125 wires per cm) will give an aperture resolution of ~50 microns which allows a realisable features size of 150-200 microns.

The pattern is achieved by coating the mesh in a photosensitive emulsion; this passes through the entire mesh to ensure a sharp print contact to the substrate. The screen mesh is then exposed to an ultra violet (UV) light through an image of the desired pattern. The UV light polymerises the emulsion in all areas except those of the desired pattern, the screen is then washed to dissolve the patterned parts. This process leaves the desired pattern etched into the mesh leaving the exposed areas for the paste to pass through during printing.

3.2.2 Thixotropic screen-printable paste formulation

The PZT paste consists of a percentage weight of PZT powder, a liquid phase sintering aid, such as lead borosilicate, and an organic binder, such as pine oil. It is important to balance the amount of PZT and glass frit correctly. Increasing the percentage of glass frit will lead to a stronger mechanical bond but will reduce the piezoelectric powder loading.

The organic binder is required to make a thixotropic paste that will pass easily through the screen in the printing process but will retain the shape of the printed pattern when the screen is removed. Excessive pine oil will result in a smeared print and reduced definition of the printed geometry whilst a lack of pine oil will result in an uneven print and can also lead to screen damage.

Investigations concerning the use of dispersants in PZT films as a means of optimising the particle distribution have been conducted. To improve the quality of the printed films it is essential that the paste spreads evenly on the substrate. Dispersants act to create the repulsive forces between the particles, thus reducing clumping and increasing the homogeneity of the film.

In the case of thick-film piezoceramics, work by Thiele and Setter [73] has studied various dispersants and their effects on the rheology of thick-film pastes. Their experiments looked at eight commercially available dispersants with a Sensor Technology BM500 PZT powder. One sample set had no dispersant as a reference. Once the optimum dispersant was found, a set of four samples was examined to determine what effect the order of component additions had on the viscosity of the paste. In addition to this, two bulk samples, one with dispersant added and one without were prepared. This was to test the effect that the dispersant had on the electrical properties. Rheological and optical microscopy measurements of the fired film surfaces showed the benefits of using a dispersant in the thick-film ink formulations. A decrease of 40% in mean surface roughness was observed for the film containing the dispersant compared with the sample containing none. The results showed that a phosphate ester oligomer was the optimum dispersant. This dispersant allowed for an increase of PZT loading

in the paste from 75 wt.% to 80 wt.%, whilst reducing the amount of terpineol solvent by 25%. This increase in PZT weight, whilst maintaining viscosity, is an important benefit as it allows for a thicker layer for given screen-printing conditions and more controlled drying process. The addition of only 0.1 wt.% of this dispersant results in dramatic decreases in viscosity (2.42 Pa.s to 0.22 Pa.s), which allows for a higher concentration of solids. This improves the micro-structural homogeneity. The bulk experiment showed that the dispersant has no adverse effects upon the dielectric and piezoelectric properties, giving a d_{33} of 320 pC/N for bulk samples of BM500 PZT powder with or without the dispersant.

3.2.3 Printing thick-film pastes

The next stage in the process is the printing of the design on to the substrate. The same method applies to all materials with just the individual settings on the printer changing. The desired screen is placed within the printer and a suitable amount of the printable paste is deposited on the screen. The amount of paste must be sufficient to cover the entire screen when the print stroke is complete, if there is too much or too little material then the print quality will be poor. The substrate is typically attached to a moveable chuck using a vacuum. The chuck allows for the substrate to be handled outside of the printing mechanism, when the print begins the chuck will automatically position the substrate under the screen.

For the initial print it is necessary to cover the substrate with plastic or tape to mask it from the printed material. This masking technique is used to precisely align the substrate with the screen pattern and allows for adjustment of the screen alignment. It is important to wipe the mask clean before each subsequent alignment check. Once the alignment is satisfactory, the masking layer can be removed. It is important that the mask is easy to remove without disturbing the substrate or the subsequent prints will be misaligned.

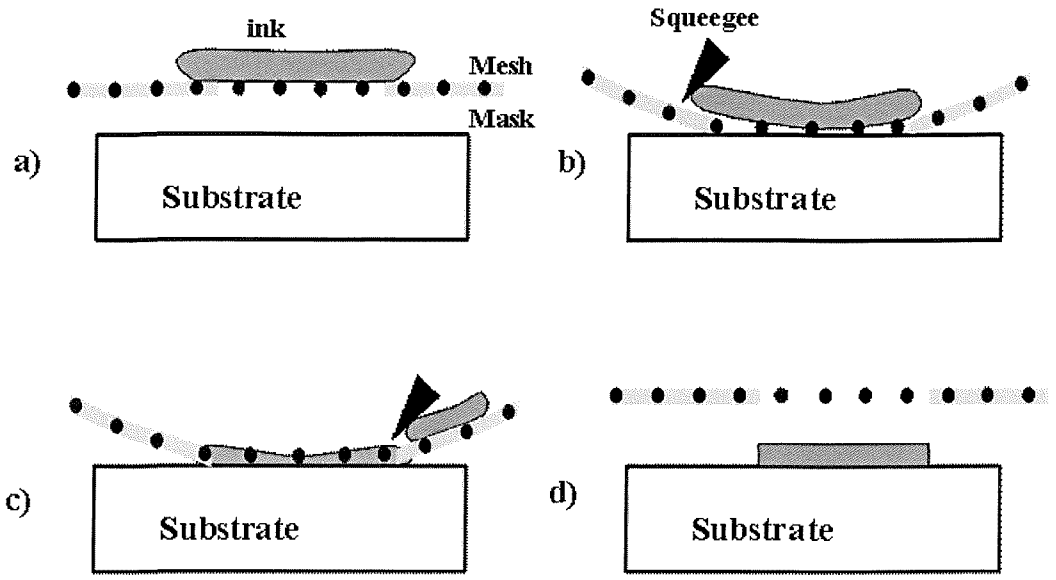

Figure 3.1: Process steps for screen-printing.

Figure 3.1 shows the four stages of the printing process. The ink is spread across the screen by a flood blade ready for printing (a). A polyurethane squeegee then forces the screen down on to the substrate as it begins the print stroke (b). The squeegee is then drawn across the screen, forcing the ink through the etched sections of the mask and removing the excess ink (c). Finally, at the end of the print stroke, the pressure of the squeegee is removed and the screen springs back into the start position leaving the ink deposited on the substrate in the desired pattern (d).

The printing pressure must be set sufficiently high to produce high quality prints. Insufficient pressure will lead to poor contact between the screen and substrate. This reduces the definition of the printed geometry and can result in a spreading of the material on to the underside of the screen. If the pressure is set too high the paste can be spread too thinly across the design as the squeegee blade becomes deformed across the pattern and removes too much paste. Also, excessive pressure can result in damage to the substrate or the screen.

The gap size is defined as the space between the substrate and the underside of the screen. If this gap size is too large then the transfer of paste is poor and can lead to a build up of material which will reduce the consistency of future prints

in the same batch. If the gap size is too small then the print will be smeared as the substrate is withdrawn from the printer.

The printing process allows a number of layers to be printed in sequence on top of the previous layers. The printing pressure and the gap between the screen and the substrate control the thickness of the printed layer. Therefore, for subsequent printed layers it is necessary to increase the gap size to ensure the screen can spring back without smearing the print.

3.2.4 Drying the printed films

The PZT films and the cermet conductive pastes both use an organic binder to aid in the printing process. Once printed, it is necessary to remove the excess organic vehicle to prepare the printed films for the firing process.

If the organic vehicle is not removed during the drying stage, the high furnace temperatures can result in rapid heating and boiling of the vehicle within the paste. This boiling of the vehicle can result in voids within the film and warping of the printed geometry. As the printed layer passes through the furnace the warped surface is fired and causes further cracks and voids within the film. However, if too much of the organic vehicle is burnt off during the drying phase the printed film will become powdery. This can result in a distortion of the printed design and with a reduced adhesion to the substrate the printed layer could detach completely during firing.

The excess organic vehicle is typically removed using an infrared drier (typically 100-200°C) but can often be incorporated into the firing process. A typical thick-film process uses a belt furnace for the firing stage and is therefore limited by the number of temperature stages. Therefore, it is it more efficient to perform the drying stage externally before firing.

3.2.5 Firing of the films

Thick-film piezoceramics require lower firing temperatures to ensure compatibility with other micro machining processes and their associated materials. The lower firing temperatures require the PZT film to contain a bonding matrix material, typically a glass frit. The bonding matrix material reduces the amount of active piezoelectric material in the film and will not provide the same comprehensive bond between the piezoelectric particles as bulk sintering. Due to this reduced structural bond, the mechanical coupling within the film will be reduced and as such the piezoelectric properties will be further reduced. It is for these reasons that thick-film piezoceramics are typically an order of magnitude smaller in terms of piezoelectric response compared to bulk piezoceramics.

With PZT based cermet films it is desirable to have a peak firing temperature sufficient to melt the glass frit. It is important to use a sufficient firing temperature to enable material bonding, however, care must be taken to avoid burning off the constituent parts of the powder and therefore reducing the piezoelectric properties. Typically, temperatures between 700°C and 1000°C are sufficient to create a liquid phase for the glass enabling an appropriate bonding matrix [74]. Temperatures over 800°C cause the lead to evaporate which is typically lost in the atmosphere but can diffuse into the substrate. Problems of lead loss are often balanced by firing in a lead rich atmosphere or in lead walled caskets. Powder manufacturers also balance the stoichiometry of their powder to match the firing process. For example, before firing the powder will often be loaded with more lead than required thus achieving the correct stoichiometric balance after firing.

Because of the lower temperatures used, there is typically limited sintering between the bulk particles of the film. Therefore, when the literature refers to sintering it will typically be referring to the sintering of the binder material and the quality of the bond between the binder and bulk materials.

Studies have been conducted into the firing profile for piezoelectric thick-film layers on silicon [75] although the results are applicable to thick-films in general. The study fired Morgan Electro Ceramics Ltd. PZT-5H films over a range of temperatures from 750°C to 1000°C and firing times between 1-8 hours. The results showed that films at the low firing temperature of 750°C exhibited poor sintering and low adhesion to the substrate. Above 800°C samples showed acceptable adhesion and sintering. The samples fired at 800°C and 850°C produced $d_{33,f}$ measurements of 101 and 109pC/N respectively. However, the maximum results were obtained from the 1000°C samples fired for one hour that produced 169pC/N. This increase in $d_{33,f}$ is due to the increased sintering of the film at the higher firing temperature and the closer stoichiometric match to that of the bulk device. The higher temperature, however, induced greater reaction in the silicon substrate. These reactions in the silicon prevent further micro-machining after the deposition of the film.

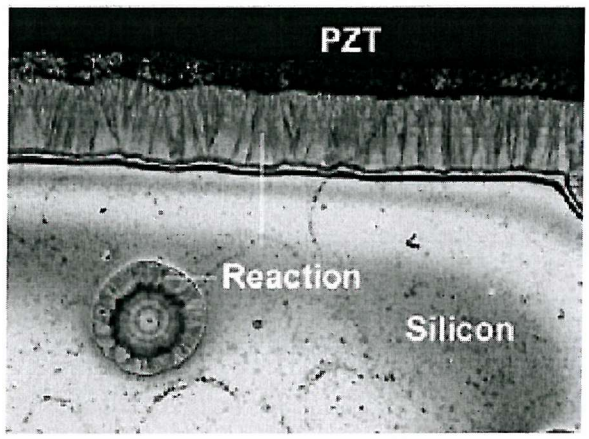

(a)

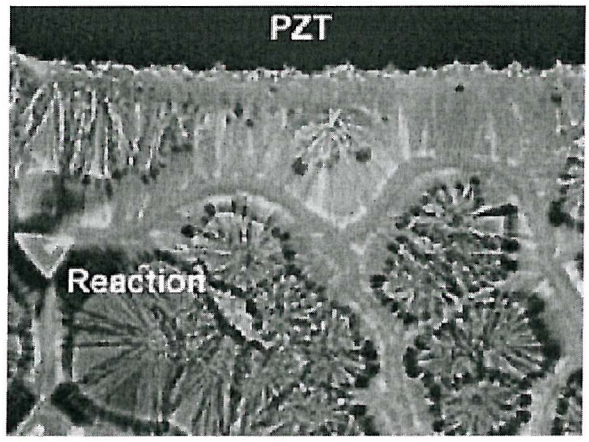

(b)

Figure 3.2: Reaction profile SEM micrographs of wafers fired at (a) 800°C and (b) 1000°C.

Figure 3.2 shows SEM micrographs of the reaction in the silicon substrate at 800°C and 1000°C. The study concluded that the optimum profile is 800°C for 8 hours, in cases where the reaction needs to be minimised to enable subsequent processing.

A further problem with high temperature firing is that of electrode migration. This is a particular problem with silver based cermet films where the electrode material migrates into the PZT layer. This is typically associated with the high temperatures used in the firing process but can also be caused by stress on the materials, humidity and the application of large voltages. This effect can reduce the properties of the PZT layer and in extreme cases result in a short circuit. It is therefore important to match the electrode materials to the application and process that is being used.

3.2.6 Standard thick-film quality tests

Following the furnace firing process, it is necessary to conduct a number of qualitative tests. Initial visual observations of the film are conducted to confirm that the geometry of the design is intact and the materials have not been removed during firing. After visual confirmation, there are two standard tests that are used within the screen-printing industry, these are the scratch test and tape test.

The scratch test involves the use of a metal blade or scribe. The test is an attempt to remove the thick-film from the substrate, or previous printed level, to provide an indication of the adhesion levels of the film. The greater the force required to remove a portion of the film, the greater the adhesion and fired quality of the film. A good quality film will typically only be left with a mark on the surface. The test is potentially destructive and it is therefore important to consider which sample the test is conducted upon.

The tape test involves a strip of lightly adhesive tape placed on the surface of the fired films. The tape is pressed down on to the substrate and then removed. If

the fired film has low levels of sintering and bonding then material particles will be seen within the adhesive tape. If the film has fired correctly then there should be very little residue left on the tape, the ideal would be no residue.

3.2.7 Polarisation process

Thick-film piezoelectric materials, like their bulk counterparts, have no remnant polarisation after firing and therefore the piezoelectric properties must be induced by poling. The polarisation process involves heating the printed film to a specific temperature either close to or above the Curie temperature using a hot plate or oil bath. Once at the desired temperature, an electric field is applied to polarise the film. The electric field strength is determined by the thickness of the film and should be sufficiently high to cause polarisation but not too high that dielectric breakdown occurs. In practice, a test sample from the batch is used to determine the field strength. The electric field is applied and increased until dielectric breakdown occurs. For the remaining samples, a field of 90% of this breakdown value is used.

The electric field is maintained for a set poling time. The level of polarisation is increased over time to a saturation point, where possible a poling time of 24 hours or more should be used but for most practical applications a poling time of 3-30 minutes is used. The poling voltage is maintained throughout this poling time. At the end of the poling time the temperature of the film is reduced to room temperature whilst maintaining the applied electric field. Once room temperature is reached, the applied field is removed and the material is polarised.

Studies have been conducted into the optimum poling conditions for PZT based thick films [76] looking at the poling time, temperature and poling voltage. The experiments studied two types of paste formulations, both using a Ferroperm type 27 PZT powder; one set with 3wt.% lead oxide binder the other with lead borosilicate binder. The films were printed using standard screen-printing techniques and using gold cermet electrodes.

Three PZT layers were deposited and fired sequentially at 950°C in order to produce suitably thick films, in the order of 100μm. The samples were split into batches and a range of poling voltages from 0.5 to 4.5 MV/m, durations of 5minutes to 24hours and temperatures ranging from 75-150°C were used and then the results correlated. The results gave a clear indication that the value for d_{33} increases with the duration of the poling and that devices poled at higher temperatures provided the same d_{33} values at shorter times than samples poled at lower temperatures. The results also showed that the d_{33} is only marginally improved when the poling field increases beyond 2.5MV/m.

These results are significant because they show that the d_{33} coefficient of the samples is increased with a higher poling temperature and a longer poling time, but also that poling fields greater than 2.5MV/m had less significant effect on the results. The experiment also showed that the lead borosilicate samples gave better d_{33} values and also allowed for greater poling voltages before dielectric breakdown. The maximum values for $d_{33,f}$ obtained from the samples was approximately 225 pC/N, which is around 60% of the bulk value stated in the paper for the material used, 375 pC/N. However, the bulk value given for Ferroperm type 27 PZT by the manufacturer is 425pC/N [77], which means the results are closer to 50% of the bulk d_{33} value.

Whilst these values appear to be close to the bulk values for type 27 PZT the measurements taken may not accurately reflect the actual d_{33} value of the samples. The measurement technique does not compensate for the influence of the bending moments in the substrate and is also not very repeatable.

3.2.8 Summary

This section has covered the individual stages involved in screen-printing thick-film devices. Details have been given of the processes involved and the potential improvements and developments to these systems for use throughout this thesis. The descriptions of screen design, paste mixing, the printing process and quality tests apply to all printed materials, the drying, firing and poling are more specific

to the material type. Therefore, the next stage is to identify the variations in the processes specific to the University of Southampton standard thick-film process and in particular the variations developed for this thesis.

3.3 Thick-film process parameters used for this study

The initial process parameters required to fabricate a thick-film PZT layer were obtained from previous investigations at Southampton University [75,76]. The PZT paste formulations consisting of Morgan Electro Ceramics Ltd. PZT-5H powder, a terpineol solvent (ESL 400) and a lead borosilicate glass binder (Ferroperm CF7575) provide an adequate starting point for this investigation.

Throughout the initial stages of this study, the process parameters have been precisely controlled to observe any trends in the results. Therefore, the piezoelectric properties will not be optimised. This is discussed in more detail in chapter 6 where a number of process parameters are investigated to maximise the piezoelectric properties of the films.

3.3.1 Paste mixing

The PZT paste is formed by mixing PZT and glass powders with a standard terpineol thick-film organic vehicle (ESL 400) thereby forming a thixotropic paste. Typically, lower glass content pastes (1-5%) require ~5ml of pine oil, whilst an increase in glass content (>10%) and smaller particle size (<1μm) powders require ~10ml of pine oil. The thixotropic nature of the paste will vary at different stages during the printing process. This enables it to pass through the screen during the printing phase and retain the printed geometry during the drying phase.

The paste is mixed in a container using a spatula. Once mixed, it is transferred to a laboratory scale triple roll mill. The paste was then collected in a clean container and stored ready for printing. The use of a triple roll mill is an important factor in obtaining a consistent, repeatable paste since it evenly

distributes the glass amongst the PZT. The triple roll mill gives the paste a smooth texture that is ideal for the printing process. The powder mixing was conducted in the Southampton University Microelectronics Centre class 100 clean room. Mixing in a clean room helps to further reduce any inconsistencies in the pastes due to dust and other contaminants.

3.3.2 Printing on alumina substrates

The pastes are printed on a Coors ADS 96R 96% alumina substrate [78] using a DEK 1750 screen-printer. Alumina is a suitable substrate material for test patterns as it is relatively cheap, provides good adhesion for the printed pastes and provides a sturdy platform for subsequent measurements and testing. This material has been used in commercial thick-film hybrid applications and is therefore known to be compatible with a wide range of thick-film pastes. The material properties for the alumina substrates are shown in table 3-1 below.

Property	ADS 96R Alumina
Density	3750kg/m^3
Young's Modulus	331GPa
Poisson's Ratio	0.25
Thermal coefficient of expansion (20-1000°C)	8.2x10^{-6}/°C

Table 3-1: Material properties of ADS 96R Alumina substrate

The substrates are laser scored to create six equally sized columns. The substrate can easily be snapped along the score lines, which can be done before or after firing. This enables the splitting of substrates so that a set of samples can be printed together but then dried or fired individually where required.

3.3.3 Screen design

The prototype design is a planar capacitor structure shown in figure 3.3. This structure was chosen because it is suitable for easy measurement of $d_{33,f}$ as discussed in section 2.2.4. Three electrode materials have been used in the investigations: ESL 9633B silver/palladium, ESL 1110-S silver polymer and ESL 8836 gold thick-film pastes.

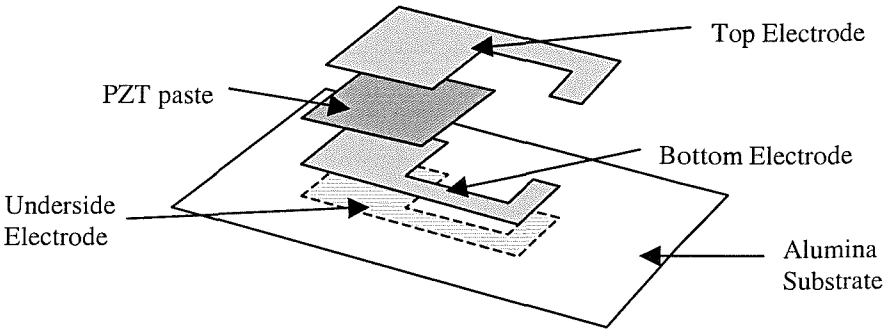

Figure 3.3 Typical layout for a single piezoelectric device used.

Each material layer has an individual screen design. For measuring $d_{33,f}$ on the Take-Control piezometer (discussed in chapter 4.2) it was necessary to add an underside electrode to the substrates. This was performed by printing the top electrode screen design on the underside of the substrate. The printing process was performed in the Southampton University Microelectronics Centre class 100 clean room

The screen design produces 18 devices per substrate. The substrates are laser-scribed to facilitate separation of the devices. Three devices (one column) were removed per printing batch for later observation with the scanning electron microscope (SEM). Figure 3.4 shows a completed substrate.

The PZT layer is a square with dimensions of 1.1cm by 1.1cm. The substrates used are 102mm by 102mm with an average thickness of 635μm.

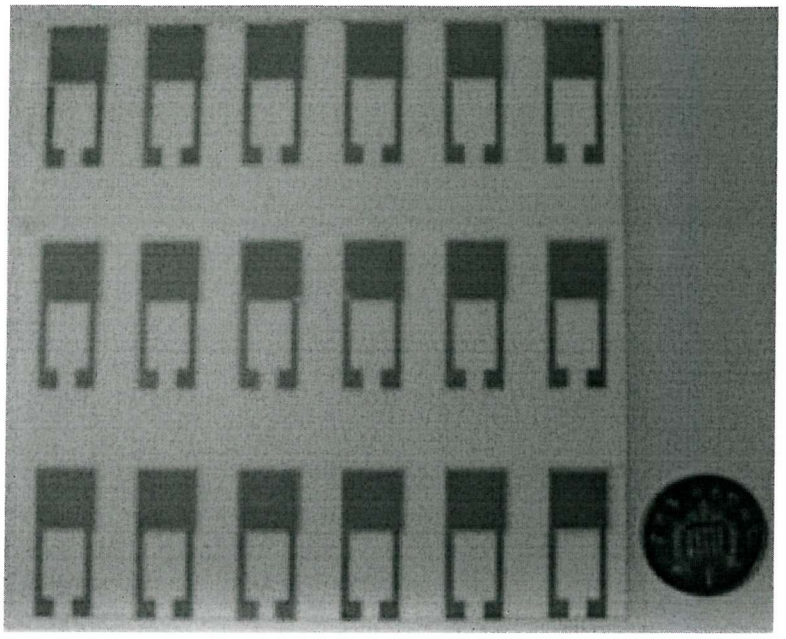

Figure 3.4: Layout of the printed devices

3.3.4 Drying and firing process

After printing, the thick-film layers were allowed to settle for 10 minutes before being dried in a DEK 1209 IR drier at 140°C for 10 minutes. The settling time allows for the printed paste to relax which can remove the impression of the screen mesh in the print. The IR drier is used to evaporate the majority of the organic carrier used in the screen printable pastes, leaving a solid but unsintered film prior to the firing process. This is a key step and is essential in ensuring a good quality fired film.

Once dried, the films are subsequently fired on a thick-film belt furnace. A typical furnace profile, known as Dupont 60, is shown in table 3-2. This profile has been previously identified as suitable for use in firing PZT and electrode materials [76]. Each furnace stage is 5 minutes 40 seconds long.

Stage	1	2	3	4	5	6
Temp (°C)	350	600	885	883	890	870

Table 3-2: Dupont 60 furnace firing profile.

Upon removal from the furnace, two standard thick-film tests were conducted to check the film quality. These were the scratch and tape test covered in section 3.2.6. In addition, the films were visually inspected to ensure there were no smudges or anomalies.

Once a layer has been fired, the next layer can be printed on top. The substrate is covered with tape and then a few trial prints are made to align the next screen to the previous layer. Once aligned, the next layer is printed with sufficient print passes to gain an even covering of the paste over the print area.

The underside electrode was printed then dried, subsequently the bottom electrode was printed and dried. Both layers were then co-fired to save time.

It was found that one fired layer of PZT was insufficient to prevent the devices short-circuiting. Therefore, all subsequent PZT layers were printed, dried and then another PZT layer printed and dried directly on top. These two dried PZT layers were subsequently co-fired. Unless otherwise stated, this printing method is considered to be a single PZT layer throughout the thesis. This problem is further explored in section 6.2.1

Following the firing of the PZT layer, the top electrode was printed. Because the PZT layer was thick, the gap size was increased and the top electrode would often require 2-3 print passes. This ensured a continuous conductive path over the step from the top of the PZT layer to the substrate. This top electrode was then dried and fired in the same manner as the other layers.

3.3.5 Poling process

Before applying the polarisation field, it is important to determine the suitability of the films for polarisation. The suitability for poling is confirmed using a Fluke 73 digital multi-meter (DMM) to determine the resistance of the films. An ideal film should have a high resistance, above 5MΩ. Any device that produces

a low resistance or a short-circuit can be considered to be defective and not included in the poling process. These defections are a result of poor print coverage, possible contamination or electrode material migration.

To enable comparison between devices they were all poled with a field of 4MV/m applied across the electrodes. Previous studies [76] have shown that whilst the devices can sustain higher field strengths than this, this is a reasonable optimum value.

The calculation of the applied voltage required to maintain this field strength assumed a uniform thickness of the PZT layer across the substrate. In practice, this would not be the case. However, for continuity and ease of experimentation, the thickness of the top left sample for each substrate was measured and from this the voltage calculated using equation 3.1.

$$\text{Field Strength} = \frac{\text{applied voltage}}{\text{PZT thickness}} \Rightarrow$$

$$4\text{x}10^{6}\,\text{x}(\text{PZT thickness}) = \text{applied voltage} \quad [3.1]$$

Once the poling voltage was determined, each of the devices on the substrate was connected in parallel. All the top electrodes were connected to the ground connection on the poling rig with all the bottom electrodes connected to the live connection. This is good practice because it means that the any external electrical interference will be grounded.

The substrate being poled was placed on a hot plate and heated to 150°C. The voltage was applied gradually until the desired electric field strength was achieved. Initially, the samples were poled for 30 minutes at this temperature. At the end of the polarisation time, the substrate was allowed to cool for a further 30 minutes. Once the substrate had cooled the electric field was removed. Subsequent tests showed that by using a fan to assist in the cooling process the cooling time could be reduced to 5 minutes with no reduction in piezoelectric properties.

3.3.6 Post processing

Once the samples were poled, it was necessary to prepare them for use with the measuring rig, discussed in chapter 4. The devices on each substrate were labelled and then the columns were separated along the score lines. The columns were then scribed to enable measurement of each individual device. To make the devices compatible with the PM35 Piezometer, described in chapter 4, it was necessary to connect the bottom electrode of the device with the underside electrode. This connection was made using a silver conductive paint (Electrolube 03B) which was applied to the substrate and then cured for 10 minutes in air. This provided a low resistance, <1Ω, connection between the two electrodes that showed no reduction in measurements compared to a soldered wire. All measurements were taken 24 hours from the end of the polarisation process unless otherwise stated. This delay in measurement allows for the material values to settle to more consistent levels as the dipoles experience a degree of re-alignment and the material properties change.

3.3.7 Summary

This section has highlighted the changes to the standard thick-film process that have been incorporated within this study. The printing methods and parameters used describe the initial stages of the study and are used as the platform for other developments in the printing order, process and parameters. The further improvements and developments in the later stages of the study are discussed in detail in the following chapters.

3.4 Conclusions

This chapter has described the details of the thick-film screen-printing process and the current process used at the University of Southampton. The review of the process has shown that there has been very little work in the area of powder composition, milling and particle size and their effect on the piezoelectric properties. The levels of glass frit used in the sintering process and the optimum

formulation have not been fully investigated and depend mainly on the principle that the best results are achieved with the lowest amount possible.

There has only been minimal research in the area of processing the films. This includes the type of electrode materials, the furnace profiles and, in particular, the optimum poling parameters for the completed devices.

The chapter has shown that there is a broad scope for improvement of the piezoelectric activity of screen-printed PZT-5H thick-films. The remainder of this thesis will focus on the main areas in which the piezoelectric activity of the material can be improved. These areas are:

- PZT milling process.
- Paste composition, percentages of glass and PZT.
- Increasing the density of the PZT layer.
- Furnace firing profile.
- Electrode materials.
- Polarisation process, time, temperature and field strength.
- Print structure, i.e. multiple PZT layers.

4 Evaluation of $d_{33,f}$ measurement techniques

4.1 Introduction

The poling process induces piezoelectric behaviour into the thick-film material. To determine the level of piezoelectric activity within the poled film and to evaluate the effect of any changes in composition or processing, it is necessary to measure the piezoelectric properties of the film. This thesis focuses on the thick-film piezoelectric strain constant $d_{33,f}$ as a property that best describes the level of piezoelectric activity. Therefore, to evaluate any improvements in the films it is necessary to obtain a measurement technique that will provide consistent and repeatable results.

This chapter evaluates two available $d_{33,f}$ measurement systems with their relevant merits, ending with a critique of the two systems for their use in this study. Finally conclusions are made and a system chosen for all future $d_{33,f}$ measurements for this study.

4.2 Piezoelectric constant, $d_{33,f}$, measurement comparisons

There are a number of alternative techniques for measuring the piezoelectric strain constant d_{33}, discussed in section 2.2.4. The most common technique is the direct method, applying a force to the piezoceramic and measuring the charge generated, often called the Berlincourt method. Alternatives, using the indirect method, include the use of interferometers or atomic force microscopy to measure the displacement of the film when a voltage is applied [79]. The indirect method typically provides a more accurate representation of the materials performance in a practical application. However, the measurements can be susceptible to background vibrations and environmental noise and are typically unsuitable for batch measurement. Conversely, commercially available 'Berlincourt' piezometers are simple to operate and are typically used in batch

processing. Care must be taken when using the direct method to minimise the effect of substrate bending on the measured $d_{33,f}$, this is discussed in more detail in section 4.3.

The observation of any significant change in the $d_{33,f}$ value requires the ability to accurately measure the difference that each change in PZT formulation makes to the piezoelectric activity of the film. A comparison of the available measurement options, the Take-Control piezometer [80] and the University of Southampton d_{33} measurement rig [81], was therefore conducted. The criterion of this evaluation was the establishment of a repeatable measurement technique that would be suitable for the volume of devices to be measured, whilst maintaining sufficient accuracy.

4.2.1 Take-Control PM35 Piezometer

The Take-Control PM35 piezometer is designed primarily to measure the d_{33} constant for bulk piezoceramics and not thick film devices. However, with consideration of the substrate bending it can be used for measuring thick-film samples. The piezometer is a dynamic measurement technique and works by subjecting the sample under test to an oscillating force applied by an electromagnetic transducer. This force is preset to 0.1N and the charge generated by the sample is measured through a differential amplifier in order to determine the d_{33} coefficient.

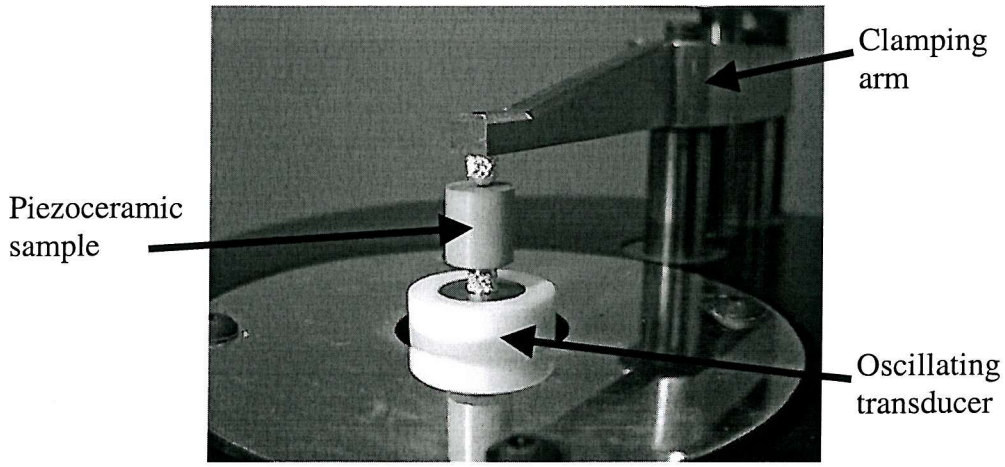

Figure 4.1: The Take-Control PM35 piezometer [80].

Figure 4.1 shows the PM35 piezometer with a bulk sample under test. The sample is placed between the two points of the oscillating transducer and the clamping arm. The sample must only be clamped to the point at which contact is made and the sample cannot move freely. A difference in measured d_{33} of 5% has been reported if the sample is over or under-tightened [82].

The thick-film devices under test were modified with a connection to the underside electrode of the test piezometer to measure the d_{33} of the sample, as discussed in section 3.3.3. All measurements were taken using a frequency setting of 97Hz because the documentation indicates that this value minimises electrical interference.

4.2.2 University of Southampton d_{33} measurement system

A similar measurement system for determining d_{33} was developed at the University of Southampton (UoS). This method measures the charge generated by the device under test when a fixed load is removed [81]. The equipment consists of a Precisa 1600C electronic weighing scales to measure the force on the device when it is removed, a charge amplifier to amplify the charge produced by the device and a storage oscilloscope as shown in figure 4.2.

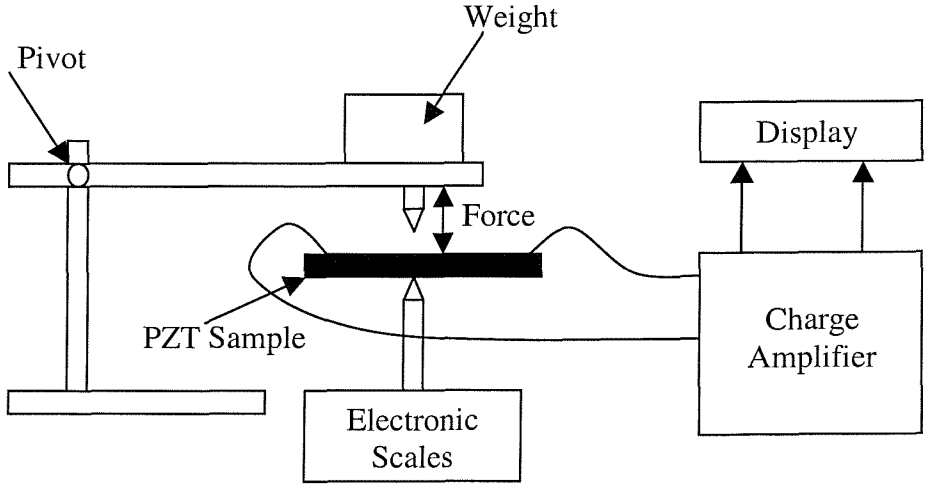

Figure 4.2: University of Southampton d_{33} measurement rig.

The system is a static method, one reading is obtained each time the weight is removed from the sample under test. It is considered that this method will produce higher d_{33} and $d_{33,f}$ values compared to the PM35 piezometer. This is because the piezoceramic is able to return to the pre-stressed dimensional height when the load is released. Therefore, a greater strain, and consequently a greater charge, will be generated than with the dynamic method PM35 where the piezoceramic is rapidly compressed and uncompressed over time. Typically 15 measurements were taken per device then an average value recorded. The formula to calculate the d_{33} from the voltage output and the mass measured by the scales is shown in equation 4.1.

$$d_{33} = \frac{\text{Coulombs}}{\text{Newton}} \rightarrow \frac{\text{Amp setting} \bullet \text{V}}{9.81 \bullet \text{g} \bullet 10^{-3}} \qquad [4.1]$$

Where,

Amp setting = amplitude setting on the charge amplifier.

V = the recorded output voltage difference.

g = mass in grams measured using scales.

d_{33} = the piezoelectric constant.

The charge amplifier was typically set to 200×10^{-12} C/V meaning that one volt on the output was equivalent to 200 pC.

4.2.3 Experimental procedure and results

Five PZT-5H type thick-film devices and two bulk devices, PZT-4D and PZT-5A, supplied by Morgan Electro Ceramics Ltd. were measured using both methods. The thick-film samples were made from a batch of PZT-5H powder and 5% by weight of CF7575 lead borosilicate glass used in previous studies [81]. These powders were mixed outside of the clean room with no milling of the paste. The devices were poled with a 4MV/m electric field.

PM35 Piezometer

The samples were measured using the PM35 piezometer measurements first and their d_{33} values were recorded. An average over six readings per sample was recorded. The results are shown in table 4-1 below.

Device	Piezometer $d_{33}/d_{33,f}$ (pC/N)
4D Bulk	314.2
5A Bulk	378.6
Thick Film Sample 1	11.8
Thick Film Sample 2	15.0
Thick Film Sample 3	20.0
Thick Film Sample 4	25.6
Thick Film Sample 5	13.4

Table 4-1: $d_{33}/d_{33,f}$ measurements using Take-Control piezometer

UoS measurement system

The samples were subsequently measured using the UoS measurement system, 15 measurements were taken per bulk sample and 20 measurements per thick-film sample due to a wide variance in measurements. Table 4-2 below shows the d_{33} results obtained from the UoS measuring system.

Sample	UoS system $d_{33}/d_{33,f}$ (pC/N)
4D Bulk	258.2
5A Bulk	454.1
Thick Film Sample 2	17.9
Thick Film Sample 3	20.2
Thick Film Sample 4	28.2
Thick Film Sample 5	17.5

Table 4-2: $d_{33}/d_{33,f}$ measurements using UoS measurement system.

The percentage differences between the two measurement methods for each sample can be seen in table 4-3 below.

Sample	Piezometer (pC/N)	University (pC/N)	Percentage difference
4D Bulk	314.2	258.2	-17.8%
5A Bulk	378.6	454.1	19.9%
Thick Film Sample 2	15.0	17.9	19.3%
Thick Film Sample 3	20.0	20.2	1%
Thick Film Sample 4	25.6	28.2	10.2%
Thick Film Sample 5	13.4	17.5	30.6%

Table 4-3: Comparison of $d_{33}/d_{33,f}$ measurements.

To determine the consistency between measurements for each measurement system, the percentage standard deviation was calculated. The percentage standard deviations of the individual measurements made for each device are shown in table 4-4. These were calculated using the Excel spreadsheet command STDEVP. This command gives the standard deviation of the full population of the results and is the recommended calculation tool for this type of sample set.

Sample	Piezometer standard deviation (%)	UoS standard deviation (%)
4D Bulk	2.2	2.6
5A Bulk	2.3	9
Thick Film Sample 2	7.7	20
Thick Film Sample 3	6.5	17.3
Thick Film Sample 4	6.7	14.6
Thick Film Sample 5	14.1	21.4

Table 4-4: Comparison of standard deviations per measurement of $d_{33}/d_{33,f}$ for each device.

4.2.4 Discussion of results

The results confirm the advantages and disadvantages of the two measurement systems. The PM35 piezometer produces the most consistent results (average 8.7% deviation compared to 18.3% for UoS) whilst the UoS system produces the highest $d_{33,f}$ values (average 21pC/N compared to 18.5pC/N for PM35). The reasons for the lower $d_{33,f}$ values observed when using the PM35 compared to the UoS system are believed to be due to the reduced relaxation time between measurements. The UoS static method produced $d_{33,f}$ values 15.3%, on average, higher than the dynamic PM35 method.

The PM35 piezometer is easier to operate and provides greater repeatability between measurements of the same sample. This is an essential factor when attempting to observe trends in the piezoelectric properties of the films between material and process changes. Therefore, it was decided that all future measurements throughout the thesis would be performed using the PM35 piezometer.

In addition to the measurement comparisons, this study has provided the initial data concerning the current level of the piezoelectric activity achieved with PZT-5H thick-films. The PM35 results show the average value of $d_{33,f}$ for the thick-film devices is 18.5pC/N, with a percentage standard deviation for the batch of 26%. These results show there is a broad scope for improvement both in terms of piezoelectric activity and repeatability between samples of the same batch.

4.3 Substrate clamping effects

The results in section 4.2.3 have shown that the $d_{33,f}$ values measured are far lower than the stated value of d_{33}=593pC/N for bulk PZT-5H. Optimum piezoelectric behaviour is obtained when the piezoceramic is unconstrained in all directions. Thick-film piezoelectric elements, however, are rigidly clamped on one face to a substrate. This constraint limits the movement of the PZT layer as it attempts to expand or contract when a force or voltage is applied. Previous

work [83,84,85] has investigated the internal stresses and boundary conditions for thin-film ferroelectrics but has not directly related these effects to bulk devices and the reduction in piezoelectric properties observed. This section conducts an experimental comparison of both constrained and unconstrained bulk PZT-5H samples and relates the analysis to thick-film piezoelectric layers. The results are compared with theoretical analysis presented in previous studies [86,87,88] to determine the amount by which the clamping effect reduces the effective $d_{33,f}$ coefficient of the printed PZT layer.

4.3.1 Theoretical evaluation of clamping effects

The direct and indirect method of measuring the piezoelectric coefficient are obtained from the relationships between charge, induced strain and induced stress on the piezoceramic [10]. Equations 4.2 and 4.3 are defined as the piezoelectric constitutive equations.

$$S_\alpha = s^E_{\alpha\beta} T_\beta + d_{i\alpha} E_i \quad [4.2] \qquad D_i = d_{i\alpha} T_\alpha + \varepsilon^T_{ij} E_j \quad [4.3]$$
$$\alpha,\beta = 1,2,..6 \qquad i,j = 1,2,3$$

Where S, T, D and E are strain, stress (Nm^{-2}), electric displacement (Cm^{-2}) and electric field (Vm^{-1}), and s, d and ε are compliance (m^2N^{-1}), piezoelectric constant (Cm^{-1}) and dielectric constant (Fm^{-1}) respectively. The superscript ^{E} and ^{T} indicate a constant electric field and constant stress respectively.

The overall strain on the device, given in equation 4.2, can be obtained by applying a force to the PZT and inducing a strain or by applying an electric field and creating a strain. Thus equation 4.2 is derived from the sum of the mechanically induced strain and the electrically induced strain.

The electric displacement D is defined by equation 4.3 and is equivalent to the charge developed by the piezoelectric properties of the ceramic and the capacitive effect due to the device having a capacitive structure of two electrodes and a dielectric.

Appendix A shows how these equations can be presented in their matrix form to derive equations for strain and electric displacement. The resulting direct and indirect equations for d_{33} can be derived with consideration of the boundary conditions affecting this result with the sample attached to a substrate. From these equations it is possible to derive a thick film $d_{33,f}$ equation that considers the effect of the substrate clamping on the deflection of the piezoceramic, equation 4.4.

$$\left(\frac{D_3}{T_3}\right)_E = d_{33,f} = d_{33} + 2d_{31}\left(\frac{-\left(\frac{\nu_{sub}}{Y_{sub}}\right) - s_{13}^E}{(s_{11}^E + s_{12}^E)}\right) \qquad [4.4]$$

Equation 4.4 gives the $d_{33,f}$ that would be measured as a result of the substrate clamping effects where ν_{sub} is Poisson's ratio and Y_{sub} is Young's modulus. Because d_{31} is a negative coefficient, the equation shows that the clamping causes restriction in the lateral plane of the device by restricting expansion when a force is applied.

The values for PZT-5H were obtained from Morgan Electro Ceramics and Efunda [11,89]. The values of Poisson's ratio and Young's modulus for the alumina substrate were obtained from Hybrid Laser-tech Ltd [78].

$$\nu_{sub} = 0.25 \qquad Y_{sub} = 331\text{GPa}$$

$$s_{11}^E = 16.4 \times 10^{-12}\text{m}^2\text{N}^{-1}$$
$$s_{12}^E = -4.78 \times 10^{-12}\text{m}^2\text{N}^{-1}$$
$$s_{13}^E = -8.45 \times 10^{-12}\text{m}^2\text{N}^{-1}$$

Substituting these values into equation 4.4 gives equation 4.5.

$$d_{33,f} = d_{33} + 1.33d_{31} \qquad [4.5]$$

From the Morgan Electro Ceramics data book, the typical values for d_{33} and d_{31} are 593pC/N and –274pC/N respectively. Therefore the typical measured $d_{33,f}$ values for thick film PZT-5H material should be approximately 227.76pC/N. This is a relatively simple equation and does not consider the shear effects, other bending modes or any clamping effects the top electrode may have if it is also attached to the substrate.

4.3.2 Practical measurement of the clamping effects

Thick-film samples cannot be used to demonstrate equation 4.4 because it is impractical to remove the devices from the substrate for direct measurement of d_{33}. Therefore, thin bulk samples from Morgan Electro Ceramics product range were attached to a substrate to observe the effects on the measured d_{33}.

Five metalised bulk 5H-type PZT discs (average thickness 220μm and 9.6mm diameter) were obtained from Morgan Electro Ceramics and their d_{33} coefficient measured. These were fully processed bulk piezoceramics that had been previously fired and poled by Morgan Electro Ceramics. The 5 discs were de-poled by heating them above the Curie temperature and then re-poled at Morgan Electro Ceramics factory using a proprietary poling process. The d_{33} value was then measured for each disc, this provided a reference point for the unclamped disc. The bulk samples were then bonded to a 0.64mm thick 96% alumina substrate. An ESL 9633B silver-palladium electrode was printed on the substrates and the bulk discs placed on the wet printed pastes. The samples were dried in a DEK 1209 IR drier and fired with an 890°C peak temperature furnace profile. The silver-palladium film provides an electrical connection to the base of the disc and simultaneously ensures a rigid bond to the substrate. The plane view of the assembled samples is shown in figure 4.3.

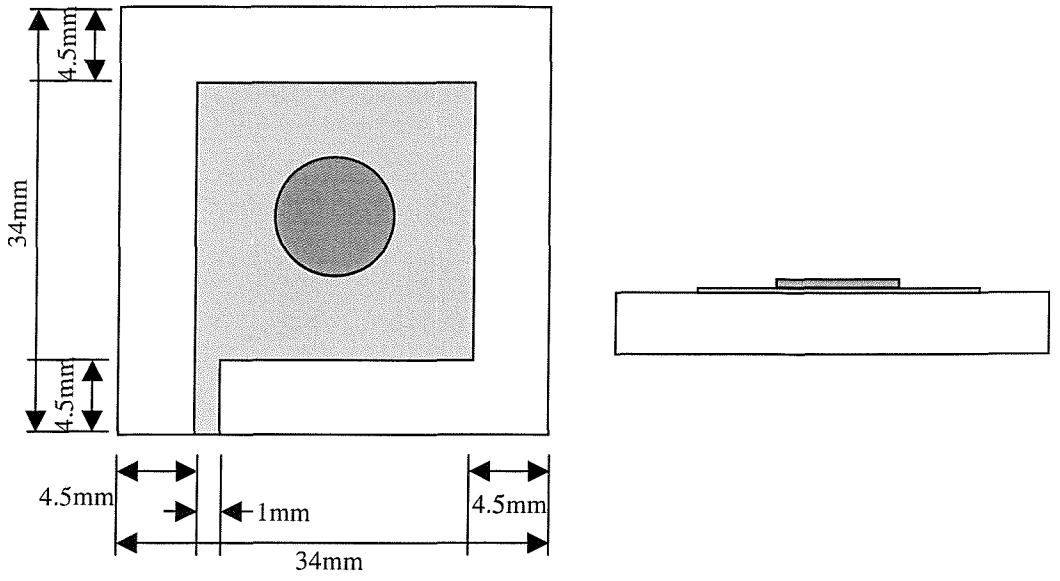

Figure 4.3: Sample design layout for substrate, electrode and PZT disc.

Because the furnace temperature is above the Curie temperature of 5H-type PZT, it was necessary to re-pole the discs once fired. The samples were re-poled at Morgan Electro Ceramics factory with identical parameters as used pre-firing to ensure consistency with the poling level and decay time, therefore enabling a direct comparison between the unclamped and clamped d_{33}. In addition it ensures that any reduction in d_{33} will be known to be due to the clamping effects rather than the device not obtaining polarisation saturation which would also result in a lower d_{33}. The d_{33} values before and after clamping were measured using a Take Control PM35 piezometer, 5 measurements were taken for each sample with a frequency setting of 97Hz.

4.3.3 Results

The thickness measurements and the applied voltage for each sample are shown in table 4-5. The results obtained are shown in figure 4.4 and depict a comparison between the theoretical values given by equation 4.4 and those measured values using the Take Control PM35 piezometer.

Sample	Thickness	Measured Bulk d_{33} (pC/N)	Theory d_{33} (pC/N)	Measured Clamped d_{33} (pC/N)	Calculated d_{31} (pC/N)
5H-1	226μm	543.6	211	124.6	-251
5H-2	216μm	520.4	202	122.4	-240
5H-3	214μm	559.4	217	153.8	-258
5H-4	196μm	479.4	186	164.4	-221
5H-5	222μm	539.8	209	125.6	-249

Table 4-5: Theoretical and measured d_{33} results

The values used for d_{31} in equation 4.5 were calculated as a ratio of the data sheet value for d_{31} compared to the measured value of d_{33}. This assumes the d_{33} and d_{31} would have changed proportionally. The theoretical value for $d_{33,f}$ was calculated using equation 4.5 with the value for d_{33} being the measured bulk device.

Figure 4.4 shows a comparison between the unclamped bulk devices, theoretical values given by equation 4.5 and the measured values once the disc was attached to the substrate and re-poled. These results show an average unclamped d_{33} of 529pC/N and an average clamped value, $d_{33,f}$, of 138pC/N giving a 74% reduction.

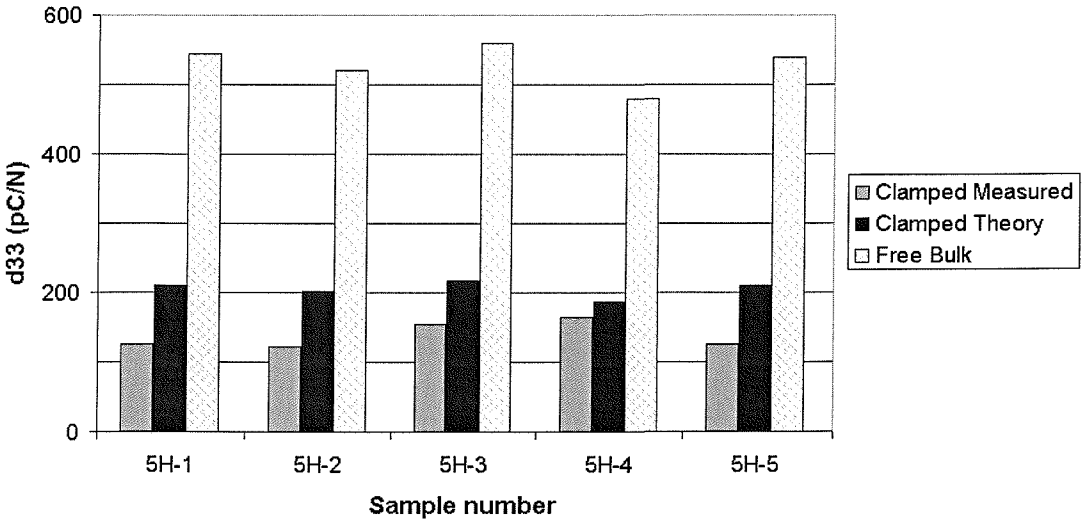

Figure 4.4: Comparison of theoretical and measured values for clamped d_{33}.

4.3.4 Discussion of results

Table 4-5 and figure 4.4 show that clamping a piezoceramic to a substrate reduces measured d_{33}. The clamped 5H samples have ~32% lower measured d_{33} than the theoretical values obtained from equation 4.5. This further reduction of d_{33} could be attributed to the lead loss experienced by the PZT layer when fired in the belt furnace. However, the firing temperature was only slightly above that at which lead migration occurs and therefore unlikely to have a large influence on the stoichiometry of the bulk device. This would indicate that any change in the domain structure of the bulk device would be minimal but could be a factor in the extra reduction observed.

Another contributing factor is that, despite the poling parameters before and after clamping being identical, the effect of the applied poling field after clamping is reduced. The electric dipoles within the ceramic cannot align to the same degree as an unclamped bulk ceramic when the poling field is applied because the associated deformation of the device is restricted by the substrate. This effect means that the polarisation saturation point in the bulk device is reduced, thus causing an overall reduction in the piezoelectric activity. Another possible source for error is that the theoretical calculation ignores the shear effects within the film structure, which in practice could be introducing a further negative effect on the measured piezoelectric activity. Reductions in d_{33} due to grain size or size related domain structure transitions [90,91] are believed to be minimal because the bulk disc was already fully sintered before being clamped to the substrate, as evidenced by the high d_{33} measurements before clamping.

4.4 Conclusions

Section 4.3 has confirmed that the addition of a substrate to a piezoceramic has significant effects on the measured d_{33} value, $d_{33,f}$. The clamping effect equation, equation 4.5, has been shown to be valid with the measured results showing a significant reduction in d_{33} as predicted. For the bulk PZT-5H devices, a reduction of average values from 529pC/N to 139pC/N was observed. This

gives an approximate reduction of 74% in measured d_{33} when a substrate is required. This result is significant because it provides an indication for the maximum achievable $d_{33,f}$ for a particular PZT type and substrate combination. This is important when considering which powder and process combinations to use when designing devices for a particular application. This is of direct relevance to work on thick-film devices where the measured $d_{33,f}$ value is considerably lower than the d_{33} value of bulk devices. These results give an estimation of the proportion of the reduction due to the clamping effect and that due to processing and material differences between bulk and thick-film devices.

The result from equation 4.5 suggests the maximum achievable $d_{33,f}$, when using an alumina substrate, would be 227.76pC/N. This value provides an aim for the development of the current piezoelectric level of 18.5pC/N. The thick-film PZT-5H will not be able to achieve a $d_{33,f}$ as high as the theory suggests because of the reduced firing temperatures and the absence of bulk sintering. However, the difference in current and theoretical values shows there is a broad scope for improvement.

To validate any improvements in the $d_{33,f}$ value it is important to obtain a reliable measurement procedure. Table 4-4 shows that the $d_{33,f}$ results obtained from the Take-Control piezometer have a lower standard deviation than those obtained from the University of Southampton d_{33} measurement rig. With average standard deviations of 8.7% and 18.3% respectively for the thick-film devices between measurements. In addition, the advantage of the PM35 piezometer is the speed and ease in which multiple measurements can be obtained compared with the UoS system.

The PM35 piezometer provides consistent and repeatable results. Therefore, it will be used to identify trends in the $d_{33,f}$ coefficient for the different materials in the next stage of the research.

5 Optimisation of $d_{33,f}$: effects of milling type and percentage of glass frit

5.1 Introduction

This chapter covers the initial stages of the investigation into improving the $d_{33,f}$ values given in chapter 4. The results in chapter 4 showed that the maximum $d_{33,f}$ from the original PZT-5H samples had an average $d_{33,f}$ value of 18.5 pC/N and a standard deviation of 26% between samples. The next stage in the study is aimed at increasing the average $d_{33,f}$ value, and reducing the standard deviation.

Further development of thick-film PZT-5H devices requires a study of the main components of the paste that forms the thick-film ceramics.
These are:

- The percentages of lead, zirconate and titanate that form the PZT compound.
- The particle size and milling process of the PZT compound.
- The percentage of glass frit.
- The quantity of vehicle used to form suitably viscous paste.

The composition of the PZT-5H powder is controlled by Morgan Electro Ceramics. Changes in this composition are beyond the scope of this thesis. Therefore, the particle size, milling process and the percentage of glass were the focus of this study. Whilst investigating these parameters it was essential the printing and poling remained consistent to confirm any trends in the results. At this stage of the study, the devices were all dried, fired and later poled using the same process parameters.

It is important to note that when describing the firing process the PZT layer does not experience sintering comparable to an equivalent bulk PZT device.

However, in this study, sintering is defined as the sintering of the glass particles and the bonding matrix formed with the PZT particles.

5.2 Powder milling process

The initial experiments were conducted using PZT 5H powders of the same $PbZr_xTi_{1-x}O_3$ composition (where x is a propriety figure of Morgan Electro Ceramics Ltd.). The particle size is determined by the process in which the PZT compound is milled. In this case Ball milled, Jet milled, Attritor Milled once and Attritor milled three times [92] have been investigated.

Ball milling process

The ball milling process involves the PZT materials being mixed in a slurry and tumbled or shaken with a suitable milling media such as sand, steel, zirconia or alumina in a horizontally rotating mill. This process is defined as a soft process due to the nature and speed of the mill and results in smooth particles.

Jet milling process

Jet milling involves the powder being inserted into the mill at a controlled rate where it is introduced to high-pressure jets of air. As the powder travels in the air stream, the particles collide and wear against themselves in an abrasive process. The mill is constructed in such a way that when the particles have been sufficiently reduced in size they drop out of the mill. This process produces fine particles but they exhibit uneven edges in comparison to the ball milled powder.

Attritor milling process

Attritor milling is a similar process to ball milling but instead of the mill itself rotating it has a vertical shaft that rotates inside. It is used both to reduce the size of the existing particles and primarily to produce a more uniform size distribution. It is standard practice to feed the resultant milled powder back into

the mill to achieve a tighter distribution. This investigation has evaluated powders that have been attritor milled once and three times. These are subsequently denoted as attritor1 and attritor3 respectively.

5.2.1 Particle size distribution

All particle distributions were measured using a Malvern Mastersizer X [93] at Morgan Electro Ceramics. This instrument uses Low Angle Laser Light Scattering (LALLS) or laser diffraction. A Helium-Neon (HeNe) laser is used in conjunction with a Fourier lens to detect the light scattered by the powder particles in a solution. A change in particle size affects the amount of light diffraction. This data is then correlated to produce a particle size distribution for the powder sample.

The four PZT-5H powders: ball, jet, attritor1 and attritor3 milled were measured using the Mastersizer. The resulting particle distributions are shown in figure 5.1. The powder distributions give an average particle size of 2, 4.3, 1.2 and 1μm respectively.

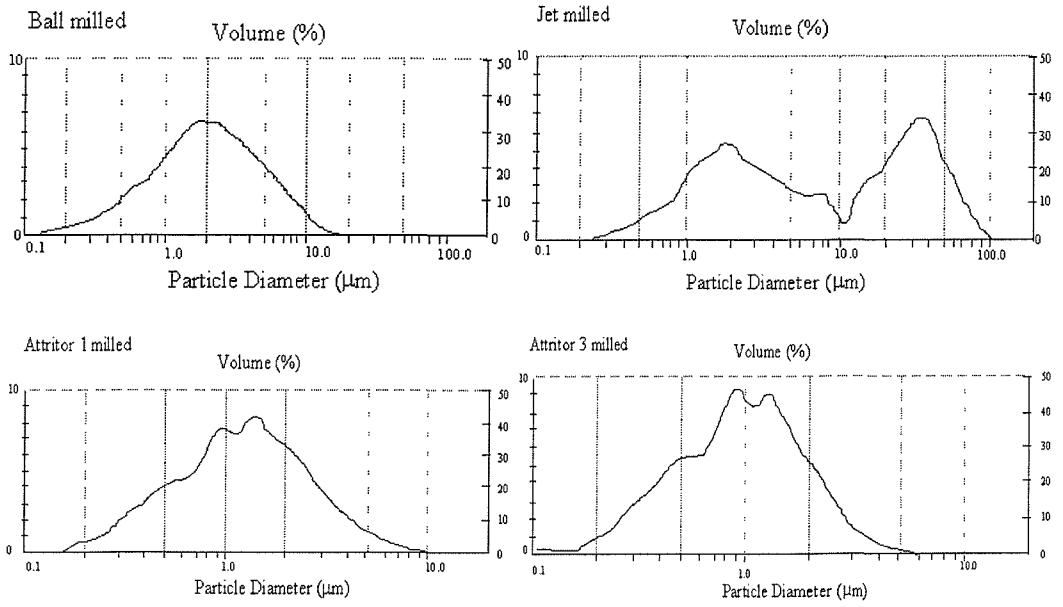

Figure 5.1: Particle size distributions for ball, jet, attritor1 and attritor3 milled powders respectively.

Ferro CF7575 lead borosilicate glass was selected as the binder for this study. The glass frit is commonly used in commercial thick-film pastes and has a suitable devitrifying temperature for the firing profile, Dupont60, used at this stage of the study. The core values of CF7575 are given in table 5-1 below.

Property	Ferro CF7575
Devitrifying temperature	460°C
Softening point	370°C
Thermal coefficient of expansion	$8.9*10^{-6}$/°C
Density	6200kg/m^3

Table 5-1: Core properties of Ferro CF7575 glass frit.

Figure 5.2 shows the particle size distribution for the CF7575 glass frit. The graph shows an average particle size of 10.2μm.

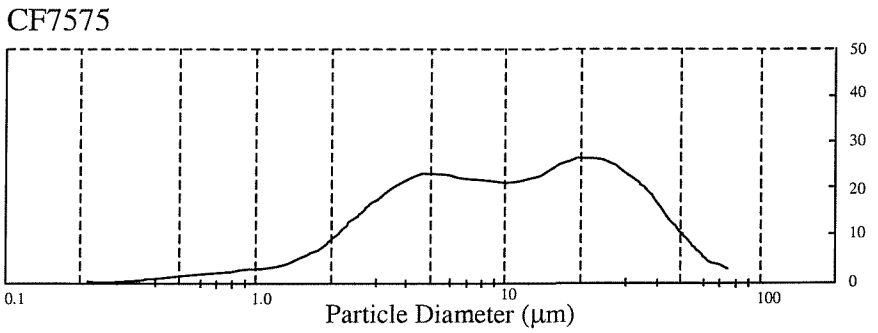

Figure 5.2: Particle size distribution for CF7575 lead borosilicate glass.

5.3 Percentage of Glass frit

The CF7575 glass frit is a binding matrix in the thick-film process. During firing, the glass melts and forms a bond with the PZT particles upon cooling. If the glass content is too low then the film will be poorly sintered and the mechanical quality of the film will be weak, thus reducing $d_{33,f}$. If the glass content is too high, the piezoelectric properties of the fired film will be reduced

because the amount of active material in the film is reduced. Therefore, it is beneficial to determine the minimum amount of glass content that will produce the highest piezoelectric response. However, sufficient glass must be added to ensure adequate sintering and good mechanical coupling of the film.

This study investigated 5%, 10%, 15% and 20% percentage weights of CF7575 lead borosilicate glass. The glass percentages will combine with the four milled powder types to give a range of 16 different batches from which to observe any change in piezoelectric activities. The piezoelectric activity of these batches will provide an indication of the optimum percentages of glass and the effects of the powder milling process. Table 5-2 shows the set of batches. Each batch consisting of 20g of PZT and glass combination, the details of which are shown below.

PZT-5H milling process	**Label**	**Percentage of lead borosilicate CF7575 (glass frit)**							
		5%		**10%**		**15%**		**20%**	
		PZT	Glass	PZT	Glass	PZT	Glass	PZT	Glass
Ball Milled	B	19g	1g	18g	2g	17g	3g	16g	4g
Jet Milled	J	19g	1g	18g	2g	17g	3g	16g	4g
Attritor milled	Att1	19g	1g	18g	2g	17g	3g	16g	4g
Attritor milled 3 times	Att3	19g	1g	18g	2g	17g	3g	16g	4g

Table 5-2: Pastes and their percentage components for initial tests.

Table 5-2 also introduces the notation that will henceforth be used to describe each batch and devices from the batch. The label defines the milling type used, B, J, Att1, Att3 define ball, jet, attritor and attritor3 milled powders respectively. The percentage of glass used will be a prefix, for example a 15% by weight jet milled batch will be 15J, device 12 from this batch will be 15J(12). This notation is for the individual devices, for the batch the notation would be '15%

Jet', which defines the batch of jet milled powders with 15% content by weight of CF7575 glass.

Three more examples:

5% glass with attritor milled 3 times powder, device number 7 will be: 5Att3(7).
20% glass with ball milled powder, device number 20 will be: 20B(20).
15% glass with attritor milled 3 times powder batch will be: 15% Att3

5.4 Processing

The processing of each of the powder combinations into pastes and subsequent screen-printing of the devices was conducted as described in section 3.3. All layers were fired with the Dupont60 furnace profile, table 3-2.

Each device in this study used ESL 9633B silver/palladium electrodes. This cermet paste is low migration silver and is a more cost effective material for the volume of samples required. For an industrial process gold would be used for the electrodes to remove the possibility of metal migration into the PZT layer.

The thickness values were measured for each device and they were subsequently poled with an applied field of 4MV/m, for 30 minutes at 150°C. Once the poling process is finished it was necessary to prepare the devices for the measurement process. As discussed in section 3.3.3, an extra underside electrode was printed for all devices to provide compatibility with the PM35 piezometer. Once all the substrates were broken into individual devices the bottom electrode was connected to the underside electrode. This connection was initially a wire soldered between the two electrodes but later a silver conductive paint (Electrolube 03B) was used. The connection was painted on and cured in air for 10 minutes. This reduced the overall processing time of the samples significantly with no observed reduction in measured $d_{33,f}$.

A marking system on each substrate sample was used, shown in figure 5.3. This system was used in conjunction with that described in section 5.3. The number system was included on the samples where one column was removed in the clean room. This meant that a comparison of results by substrate position could still be made for these substrates.

13	14	15	16	17	18
7	8	9	10	11	12
1	2	3	4	5	6

Figure 5.3: Device number orientation on the substrate.

5.5 Measurement results

The $d_{33,f}$ measurements were conducted using the PM35 piezometer. Each device was measured in turn, with time allowed for settling. Five measurements were recorded per device and the average $d_{33,f}$ value was calculated. The measurements were taken as consistently as possible, with the devices placed in the centre of the two measurement electrodes and identical pressure applied per device.

Due to losses in the printing process, poling and post processing the average batch had 26 devices from a potential 33. These losses were mainly due to substrate damage in transit and during the scribing procedure. However, these produced enough measurements to establish confidence in the results and to identify any trends that occurred.

Figure 5.4 shows the data obtained from two substrates of each of the ball milled pastes. The graph indicates the individual device number that corresponds to figure 5.3.

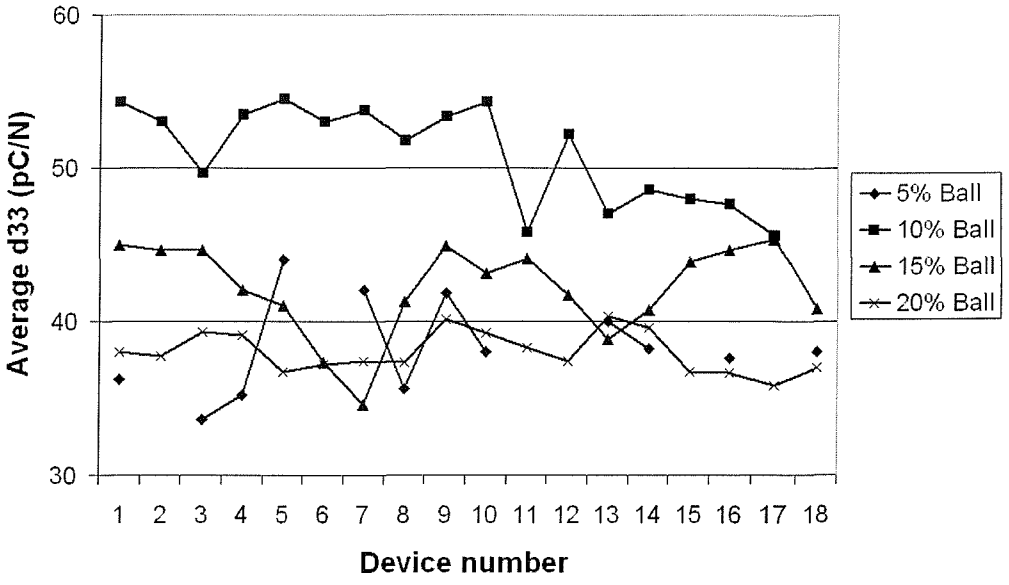

Figure 5.4: Average $d_{33,f}$ for ball milled powder with different percentages of glass frit.

Identical data sets were obtained for each of the batch types and can be found in Appendix B. These results are correlated into a single average between the two substrates printed for each batch. Figure 5.5 shows the average $d_{33,f}$ values calculated using all the obtained results.

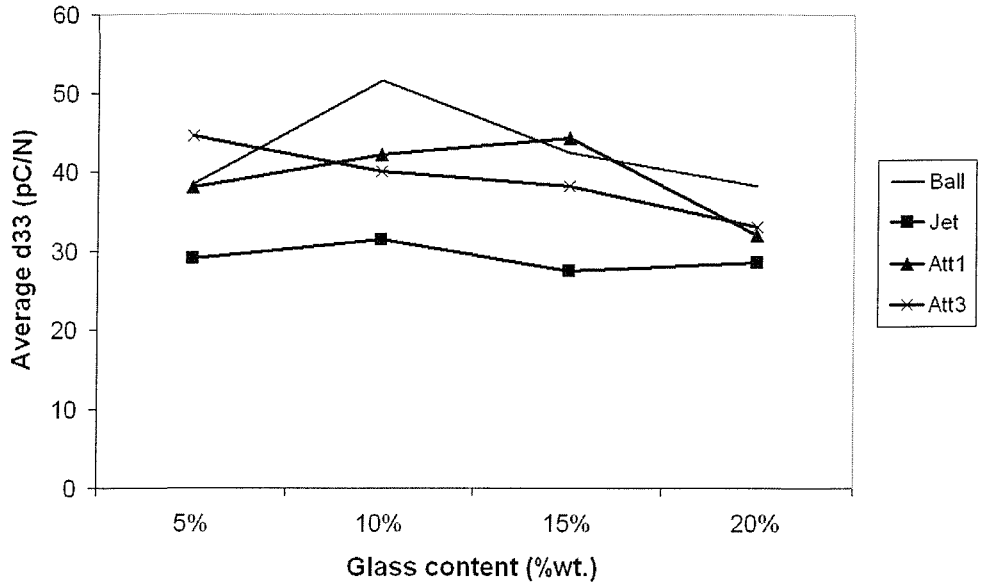

Figure 5.5: Comparison of the average $d_{33,f}$ per batch type.

To observe the effects of the glass and milling process on the repeatability of the pastes the standard deviation was calculated. The standard deviation was calculated using the STDEVP function in Excel for each of the batches and subsequently calculated as a percentage of the average. The results are shown in figure 5.6 below.

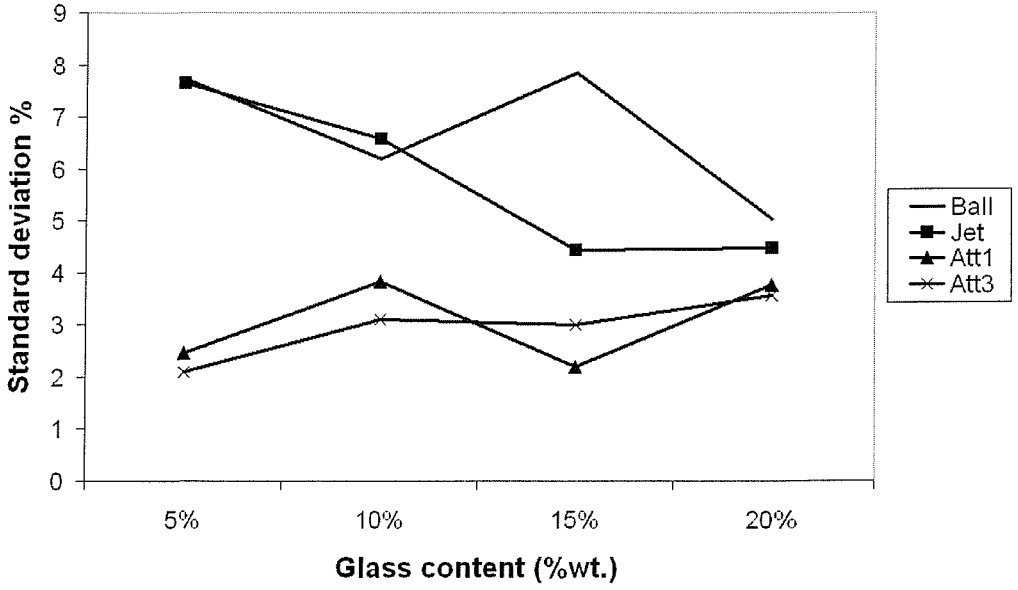

Figure 5.6: Standard deviation of $d_{33,f}$ values for the different milling types

Table 5-3 shows the thickness of the PZT layers for all the substrates, the (1) and (2) indicate the substrate number, however, there is no processing difference between them. All samples were measured using a Mitutoyo293 micrometer.

PZT-5H milling type	Percentage of lead borosilicate (glass frit)			
	5%	10%	15%	20%
Ball Milled	52μm	(1) 57μm	(1) 55μm	(1) 51μm
		(2) 70μm	(2) 51μm	(2) 52μm
Jet Milled	(1) 40μm	(1) 29μm	(1) 23μm	(1) 37μm
	(2) 35μm	(2) 30μm	(2) 28μm	(2) 41μm
Attritor milled	(1) 43μm	(1) 51μm	(1) 36μm	(1) 33μm
	(2) 43μm	(2) 44μm	(2) 37μm	(2) 32μm
Attritor milled three times	(1) 44μm	(1) 38μm	(1) 31μm	(1) 38μm
	(2) 46μm	(2) 40μm	(2) 41μm	(2) 36μm

Table 5-3: PZT film thickness for all the substrates.

5.6 Discussion of results

The results from figure 5.5 and 5.6 show the influence of the glass content on the average $d_{33,f}$ value and enable a comparison between the powder milling types. The consistency shown by the results in figure 5.6 indicate an improvement on previous devices with repeatable values for each sample.

The results show an improvement in the repeatability of the pastes, both substrates for each batch type have produced similar values. This would suggest that with tighter controls, achievable in commercial processes, the repeatability could be further improved. Mixing the pastes in clean room conditions and the use of a triple roll mill has contributed to further homogenisation of the paste. The increased homogeneity of the pastes allows for smoother, more even prints which improves the quality of the fired films. Table 5-3 has shown that the majority of the substrates exhibited an average of less than 4μm difference in

thickness compared to the other substrate of its type. These measurements confirm the repeatability of the printing process between substrates.

Figure 5.4 and the data sets in appendix B show that the $d_{33,f}$ values are consistent across the substrate. This indicates that the position of the device on the substrate does not have a significant effect on the $d_{33,f}$ values; these results support the claim of the repeatability of the printing process.

The highest $d_{33,f}$ values were obtained using 10% by weight of CF7575 combined with 90% ball milled PZT-5H (10% ball), giving an average $d_{33,f}$ of 51.5pC/N. However, the most consistent results were obtained using 5% by weight of CF7575 and 95% attritor3 milled PZT-5H (5% attritor3), giving a standard deviation of 2.1% between samples. Figure 5.7 and 5.8 show SEM micrographs of a 10% ball and 5% attritor3 PZT layer respectively. They are both cross-sectional micrographs of the PZT layer at the same magnification indicating the size and quality of the films.

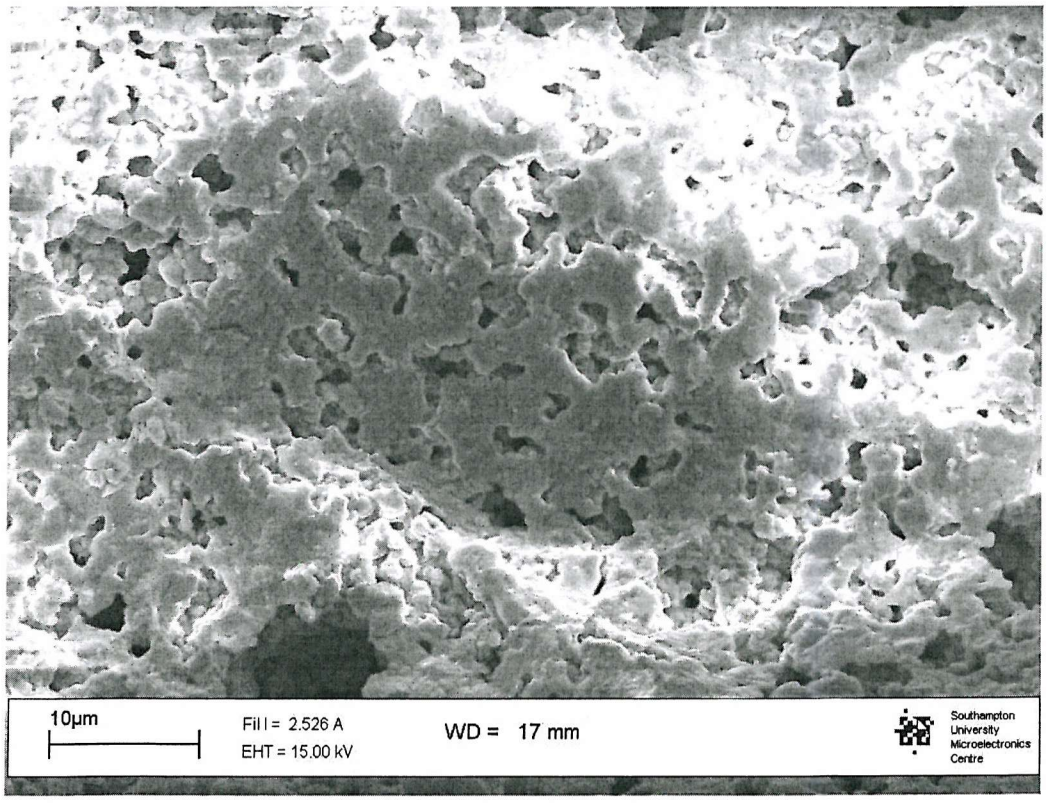

Figure 5.7: 10% ball cross sectional PZT Layer.

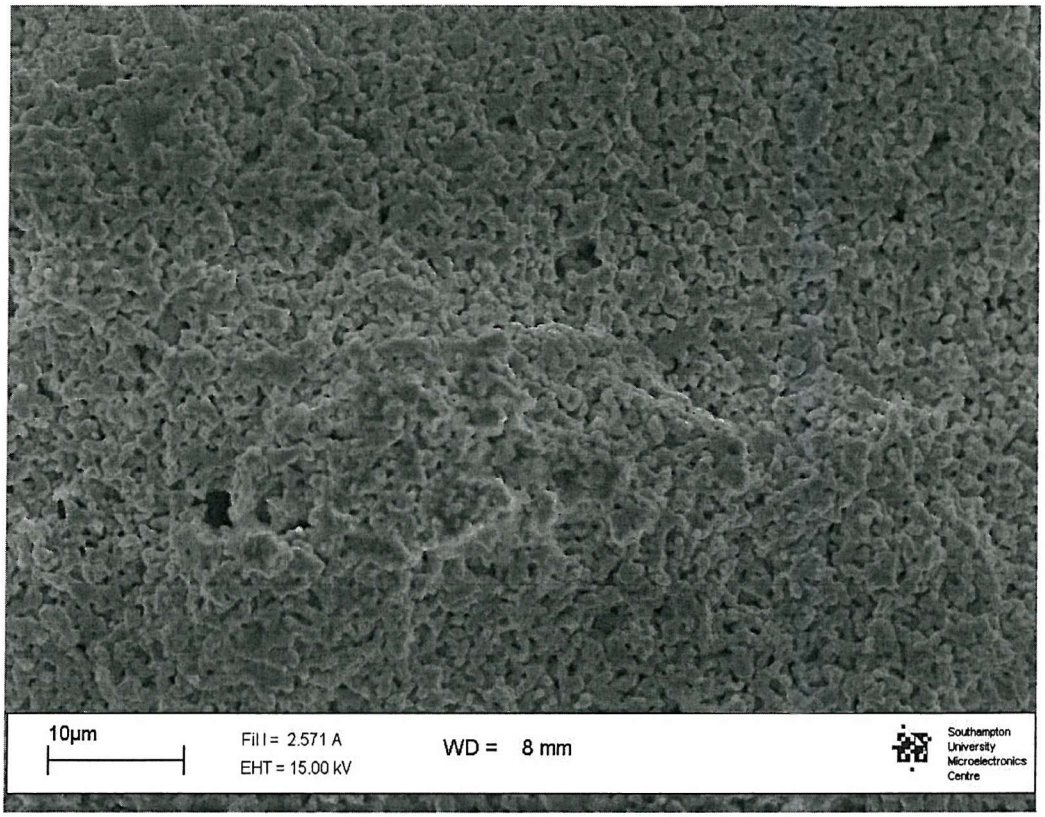

Figure 5.8: 5% attritor3 cross sectional PZT Layer.

Figure 5.7 shows that the ball milled film is well sintered but contains some larger voids which gives the film increased porosity compared to its bulk counterpart. This will be a contributing factor to the reduced mechanical coupling in the film that results in lower piezoelectric activity. Figure 5.8 indicates that the attritor films have good mechanical density but that the sintering is relatively poor. This is thought to be because of the low temperatures used and the size of the glass particles available. The CF7575 has an average particle size of 10.18µm, it is believed that as this melts within the film it contributes towards the large voids observed within the films.

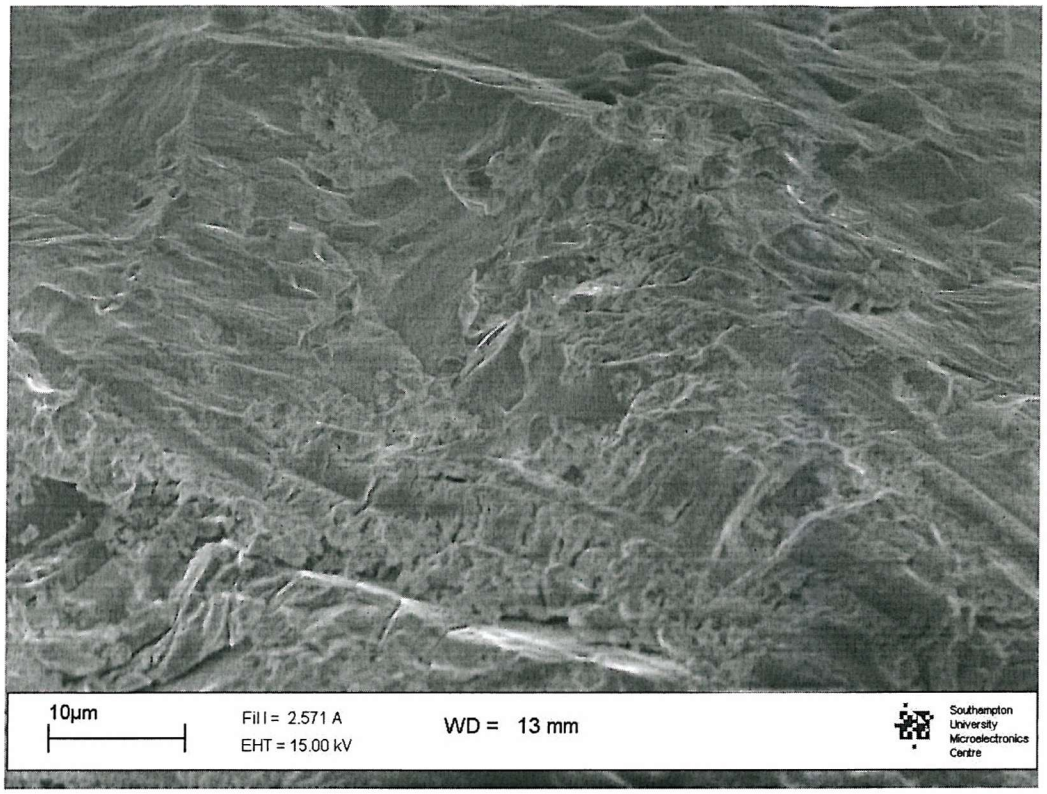

Figure 5.9: Bulk 5H PZT sample

Figure 5.9 is a cross sectional look at the PZT layer for a bulk sample of 5H material from Morgan Electro Ceramics product range. Figure 5.9 shows that the level of sintering for a bulk sample is much greater than the thick-film equivalent. The increased density of the film is a result of the bulk sintering that occurs with Morgan Electro Ceramics proprietary high temperature firing process. In addition, because the temperatures are high enough to cause bulk sintering, the films do not require a glass sintering aid and therefore further improve the piezoelectric powder loading.

5.7 Conclusions

The results obtained in this chapter have revealed a trend for each of the milling batches. Each milling type and glass percentage has produced a peak value.

The ball milled samples produced the highest $d_{33,f}$ values but the largest deviation from the mean. This result is compliant with the theory discussed in section 2.2.1. The larger particles have larger grain boundaries and therefore

should provide higher piezoelectric constants. However, the larger particle size also leaves larger voids in the fired film and a less homogeneous structure. Therefore, there is a greater difference in piezoelectric properties between devices.

The attritor milled samples have produced promising results. The piezoelectric properties observed are very consistent compared with other milling processes and the original devices from section 4.4. This consistency is explained by the smaller particle size and tighter particle size distribution observed in the powder. This produces improved density and homogeneity in the films. Therefore, the fired films are more consistent whilst maintaining good mechanical coupling which improves the piezoelectric response.

The jet milled powders have produced the most unexpected results. With consideration of the production and measurement errors, the average $d_{33,f}$ values for the four jet milled batches have produced similar piezoelectric response. Therefore, the results indicate that the piezoelectric properties are independent of glass content. It is considered that due to the rough nature of the jet milled particles, the lack of homogeneity in the films reduces the influence of the glass content.

The optimum $d_{33,f}$ average, 51.5 pC/N, is produced by the ball milled batch with 10wt.% glass frit. The highest $d_{33,f}$ value achieved by the same batch was 58.4 pC/N. This compares favourably to the results from chapter 4 which show an average value of 18.5pC/N for the original samples. This shows a 178% increase in measured $d_{33,f}$ although this is still lower than the predicted optimum of 227.76pC/N. The standard deviation for the 10% ball samples was 6.2%, which is a significant improvement on the original samples deviation of 26% (section 4.2.4). However, the lowest deviation was produced by the 5% attritor3 samples, 2.1%, with an average $d_{33,f}$ of 44.5pC/N.

6 Optimisation of $d_{33,f}$: Electrode materials and poling parameters

6.1 Introduction

This chapter covers a range of further optimisations and investigations building on the results obtained in chapter 5.

Silver migration is a well-known characteristic of silver thick-film materials. The migration of silver into the PZT layer has adverse effects on the piezoelectric properties of thick-films. The first section of this chapter evaluates a silver polymer electrode material that can potentially reduce this migration. These experiments also aim to reduce the problems associated with lead lost due to evaporation during the firing process. Part of this work considers a lowering of the furnace firing temperature. In addition, a set of substrates are fired using the bulk PZT-5H firing profile at a Morgan Electro Ceramics factory.

The second half of the chapter investigates the effects of the poling field on the current material and the decay in piezoelectric activity experienced over time. Finally, a comparison is made between the poling regime used in this thesis and that used for bulk devices by Morgan Electro Ceramics Ltd.

6.2 Electrode materials

As discussed in chapters 3 and 5, silver/palladium electrodes were used for all the prototype devices because it is cost-effective. However, the disadvantage of using this electrode material is the migration of the silver into the PZT layer during the firing process, discussed in section 3.2.5. This migration can encourage short circuits and reduce the piezoelectric properties of the film. The reduced distance between the conductive materials requires lower applied poling fields to ensure dielectric breakdown does not occur. As a consequence, the

amount of dipole alignment and remnant polarisation within the material is reduced.

Another disadvantage of the silver/palladium electrodes is the requirement of an additional firing cycle. Because the electrode is deposited on the previously fired PZT layer, the PZT layer is also subjected to an additional firing cycle. This additional firing cycle leads to further lead evaporation in the PZT film. The increased lead evaporation alters the stoichiometry of the film and potentially reduces the piezoelectric properties of the film.

To remove this additional firing cycle on the PZT layer, a low curing temperature silver polymer electrode was investigated. ESL 1110-S silver polymer thick-film paste was selected due to its low curing temperature of 200°C. In addition, the possibility of reducing the firing temperatures was also explored.

6.2.1 Experimental plan and processing

An alternative to reducing the number of firing cycles the PZT endures, is to lower the firing temperature of the PZT layer. This will reduce the level of lead evaporation during firing. However, the disadvantage is that the degree of sintering at lower temperatures and the adhesion between the film and substrate will be reduced. A lower peak firing temperature of 750°C was selected as sufficient to melt the glass frit but low enough to avoid lead evaporation. The 750PK firing profile is shown in table 6-1

Stage	1	2	3	4	5	6
Temp (°C)	330	550	750	750	550	350

Table 6-1: 750PK furnace firing profile

The results in chapter 5 have shown that the paste with 10wt.% CF7575 and 90wt.% ball milled PZT-5H produced the highest $d_{33,f}$ values. Therefore two substrates of this type were printed and dried using the standard process

described in this thesis. The underside and bottom electrodes for the substrates were silver/palladium and fired using the Dupont60 profile (table 3-2) before the PZT layer was printed.

Once the PZT layer was printed, the two substrates were cleaved in half. One half fired using the dupont60 profile and one half fired using the 750PK profile. Section 3.3.4 discussed the need for a second PZT layer because of short-circuits occurring with a single layer. This is believed to be due to the migration of silver into the PZT layer during firing. To test this hypothesis, one half of each substrate was only printed with a single PZT layer and subsequently fired. Both single and double printed PZT films were fired with a dupont60 profile and the 750PK furnace profile. Table 6-2 contains the experimental plan. The batch labels, with associated furnace profile, number of PZT layers and the electrode materials used, are shown.

Batch label	Firing profile	Number of printed PZT layers	Electrode materials used
750(s)	750PK	Single	Silver/palladium bottom – Silver poly top
750(d)	750PK	Double	Silver/palladium bottom – Silver poly top
Dup(s)	Dupont60	Single	Silver/palladium bottom – Silver poly top
Dup(d)	Dupont60	Double	Silver/palladium bottom – Silver poly top

Table 6-2: Process details for devices in electrode experiments.

The silver polymer top electrode was printed using the standard process. After being allowed to settle for 10 minutes the film was then dried in the IR drier at 130°C for 10 minutes and then cured in the IR drier for 1 hour at 200°C. The silver polymer layer produces a less uniform print compared to the cermet film equivalent. Therefore, it was difficult to determine the thickness of the PZT layers as precisely.

6.2.2 Poling and results

Once fired, the devices were poled with a 4MV/m field at a temperature of 150°C for 10 minutes. The $d_{33,f}$ value was subsequently measured using the PM35 piezometer and an average over 5 measurements was recorded. Table 6-3 shows the results obtained for the devices poled successfully. The suffix number indicates the position on the substrate as defined in figure 5.3

Sample	Thickness (μm)	Field (MV/m)	Average $d_{33,f}$ (pC/N)
750(s)1	37	4	33
750(d)1	45	4	33.4
Dup(s)1	35	short-circuit	N/a
Dup(d)1	50	4	64.2

Table 6-3: Average $d_{33,f}$ results for electrode experiment devices.

Comparing the results in table 6-3 with those from chapter 5 it is clear that the polymer silver electrode improves the $d_{33,f}$. To confirm these results, three more devices from the Dup(d) batch were poled with the results shown in table 6-4.

Sample	Field (MV/m)	Average $d_{33,f}$ (pC/N)
Dup(d)1	4	64.2
Dup(d)2	Short-circuit	N/a
Dup(d)5	4	62
Dup(d)8	4	69.2

Table 6-4: Average $d_{33,f}$ results for Dupont60 double PZT layer devices.

Table 6-4 indicates that the results are repeatable across the substrate and show an average $d_{33,f}$ for 10% ball milled samples with a polymer top electrode as 65.1 pC/N compared with the all silver/palladium electrodes average $d_{33,f}$ of 51.5 pC/N.

6.2.3 Discussion of results and conclusions

The investigations using a polymer top electrode has supported the hypothesis that reducing the number of firing cycles that the PZT layer sustains will improve piezoelectric properties. The single PZT layer fired at 750°C did not experience short-circuiting whilst the PZT layer fired at 890°C did. This result suggests that the silver migration from the bottom electrode during firing of the PZT layer is significant and exacerbated with an increase in temperature. It is possible that the higher temperature results in more pinhole interstices within the film that allows short-circuits to occur. The burn off of the organic vehicle could create these pinholes. With a double PZT layer print the second layer fills these pinholes and the distance between the electrode layers is increased.

The results show that using a polymer top electrode increases the average $d_{33,f}$ from 51.5pC/N to 65.1pC/N. The supposition that reducing the number of firing cycles and silver migration would increase the piezoelectric activity of the material has been confirmed. The increase in piezoelectric activity is believed to be due to the stoichiometry of the film remaining closer to the morphotropic phase boundary where the optimal piezoelectric properties lie. In addition, the lower Young's modulus associated with a polymer compared to the fired cermet film is thought to reduce the clamping effect on the PZT layer. However, the influence of the top electrode on the clamping effect will be much lower than from the substrate. This reduction in clamping is because the electrode does not encapsulate the PZT layer and is coupled to the substrate in a reduced area compared to the PZT layer. This suggests that the effect of silver migration is significant and that the combination of silver migration and extra firing cycle will reduce the $d_{33,f}$ value further. Therefore, for an optimised material attempts must be made to reduce or remove these factors.

The results from the 750PK firing profile show that while a reduced number of firing cycles is advantageous, a sufficiently high firing temperature is still required. The reduction in $d_{33,f}$ is believed to be because of the reduced sintering of the glass frit and mechanical adhesion within the film. In addition, it is

believed that insufficient lead will be evaporated to balance the stoichiometry of the film to the optimum percentages for PZT-5H.

6.3 Bulk device firing temperatures

The results from section 6.2.2 show that using lower firing temperatures will not improve the piezoelectric properties of the film. Bulk PZT samples are typically fired at 1100 -1500°C, significantly higher than the dupont60 profile peak temperature of 890°C. The bulk firing profile allows sintering to occur between the PZT powder particles. The lower Dupont60 firing temperatures require a glass frit to create a bond between the PZT particles.

To attempt a direct comparison between the bulk and thick-film materials, two substrates of screen-printed thick-film material were fired using a bulk material furnace. The bulk material furnace was situated at Morgan Electro Ceramics Thornhill factory. The firing profile used is propriety information of Morgan Electro Ceramics. However, it was known to be identical to that used to fire bulk PZT-5H materials.

Two thick-film PZT pastes were screen-printed on to 96% alumina substrates using the standard printing process. One paste contained 10wt.% CF7575 glass and 90wt.% ball milled PZT-5H, the other contained 100wt.% ball milled PZT-5H powder with no glass content. The 100% ball milled powder was used because it is the most direct equivalent to the bulk PZT-5H material. Standard silver/palladium bottom and underside electrodes were printed, dried and fired on the substrates. Subsequently, the two PZT pastes were printed, dried and then a second layer printed and dried on top. The substrates were then stored using clean room boxes and transported to the Morgan Electro Ceramics factory. The two substrates were then fired in the bulk furnace in a lead container that is designed to reduce lead loss in bulk samples.

6.3.1 Results and conclusions

Figure 6.1 shows the two substrates after firing in the bulk furnace. The melting point of the alumina substrates and the silver/palladium is ~1700°C and ~1400°C respectively. However, the combination of the lead container and the high temperatures resulted in extensive warping in the two substrates.

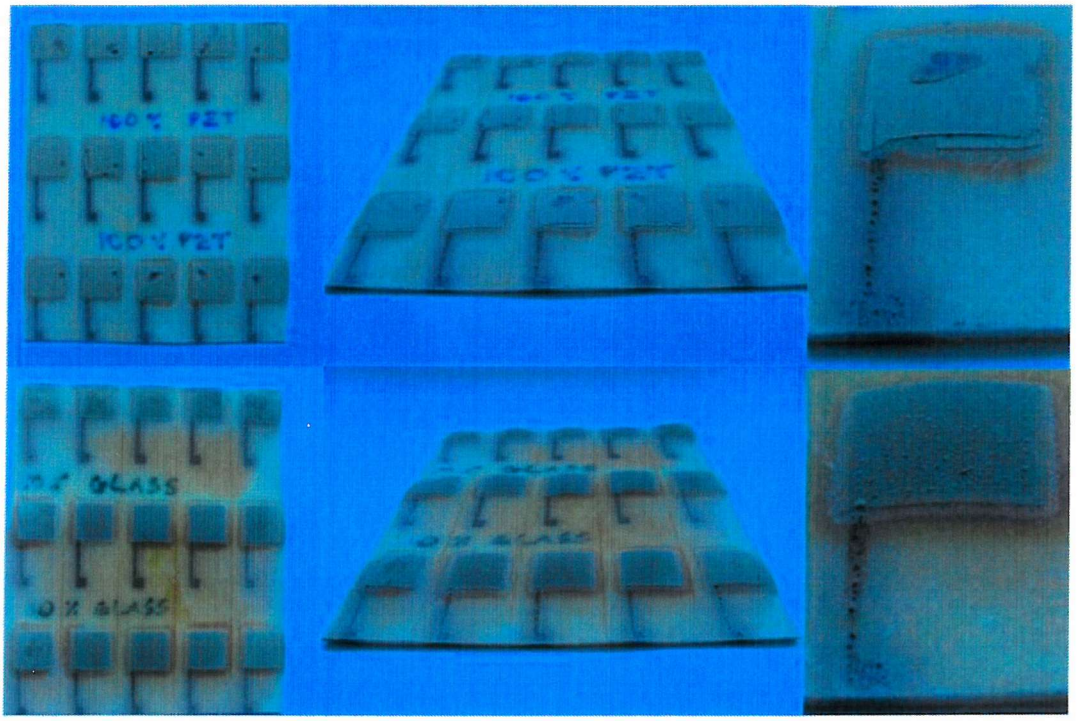

Figure 6.1: Bulk fired sample substrates

The silver/palladium electrodes have diffused into the alumina due to the high temperatures. The high temperature process has softened the alumina. This softening has allowed the various thermal coefficients of expansion for each of the materials to cause warping of the substrate.

The PZT layer exhibits high levels of adhesion in areas where the warping has not damaged it extensively. This would suggest that the high temperatures have provided satisfactory levels of sintering. However, the warping and damage to the substrates make them unsuitable for further processing. They results do indicate that the PZT layer can be fired at bulk temperatures after being screen-printed. Further work is required to improve the method in which the substrates

can be fired to produce practical results. However, due to time constraints and availability of equipment this work is beyond the scope of this thesis.

6.4 Poling optimisation

Chapter 5 outlined the requirement of a standard process for each of the batches produced so that trends in the results would be identifiable. It was recognised that the poling parameters were not the optimum for each batch but a practical standard level. Therefore, it was decided to observe the effects of the applied field on one device from the optimum 10% ball batch. In addition, the level of decay on the polarisation level was observed. A more detailed study of the complete poling parameters is conducted in chapter 8 once the optimal paste formulation has been achieved.

6.4.1 Applied poling field investigation

To determine the effects of the applied poling field on piezoelectric activity, one device from the batch 10% ball was re-poled over a range of poling fields. A device from the 10% ball batch (10B9) was chosen and poled in steps of 0.5MV/m until dielectric breakdown occurred. A poling temperature of 150°C and a poling time of 30 minutes was used for each polarisation step. The $d_{33,f}$ value was measured using the PM35 piezometer and an average of 5 readings was recorded. After each measurement the device was placed on a hotplate and heated to 200°C to de-polarise it.

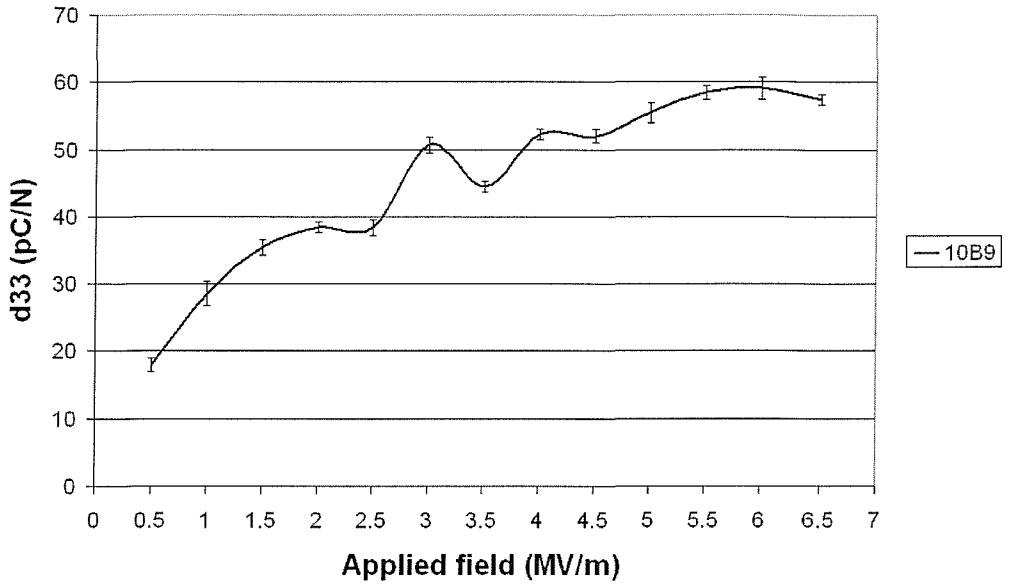

Figure 6.2: Comparison of applied field to average $d_{33,f}$ value

Figure 6.2 shows that there is an almost 50% increase in $d_{33,f}$ between 2.5MV/m and 5.5MV/m but beyond this point the field tends to have a reduced effect as the sample reaches its maximum dipole alignment, discussed in section 2.2.2. Device 10B9 produced a $d_{33,f}$ of 52.8pC/N from previous work, this was increased to a maximum $d_{33,f}$ of 59pC/N with a 6MV/m applied poling field. This represents a 12% increase in measured $d_{33,f}$ value. The results confirm that it is important to apply the maximum practical poling field to achieve the optimum polarisation and piezoelectric activity in the film.

6.4.2 Poling using Morgan Electro Ceramics factory conditions

A set of devices were poled in a Techne oil bath using Morgan Electro Ceramics Ltd factory conditions for bulk PZT-5H material. This process was conducted with the maximum field that could be applied before breakdown occurred, 30MV/m, for 3 minutes at a proprietary temperature. The standard poling process at the University of Southampton is 30 minutes poling time at 150°C with a 4MV/m applied electric field, this process is conducted in air.

Device	Standard poling process, average $d_{33,f}$ (pC/N)	Morgan Electro Ceramics poling process, average $d_{33,f}$ (pC/N)
10B2	49.4	31.2
10B4	55.6	30.8
10B5	55.2	31
10B17	45.6	29.4

Table 6-5: Comparison of $d_{33,f}$ values for different poling processes.

The results obtained in table 6-5 indicate that the higher field has reduced the measured $d_{33,f}$ values. However, the process for the bulk samples is significantly shorter than the standard poling process and previous studies [76] have shown that the poling time can have the same significance as the poling voltage.

6.4.3 Decay experiment

After poling, the dipoles suffer a moderate re-alignment until settling to a constant polarisation value as discussed in section 2.2.2. This re-alignment of the dipoles can be accelerated by mechanical stress but will occur naturally over time regardless of any external forces.

A study was conducting to observe the decay in piezoelectric properties of a thick-film device over a number of weeks. One device (10B8) was selected from the 10% ball batch from section 5.5. The device was re-poled with a 4MV/m applied electric field at 150°C for 30 minutes. The $d_{33,f}$ value of the device was subsequently measured using the PM35 piezometer directly after poling and over a range of 70 days. Five measurements were taken each time and an average $d_{33,f}$ recorded. In addition, a bulk PZT reference sample used to calibrate the piezometer was measured each time. This helped reduce measurement errors and ensure any change in $d_{33,f}$ was a result of polarisation decay. The results of this decay experiment are shown in figure 6.3 below

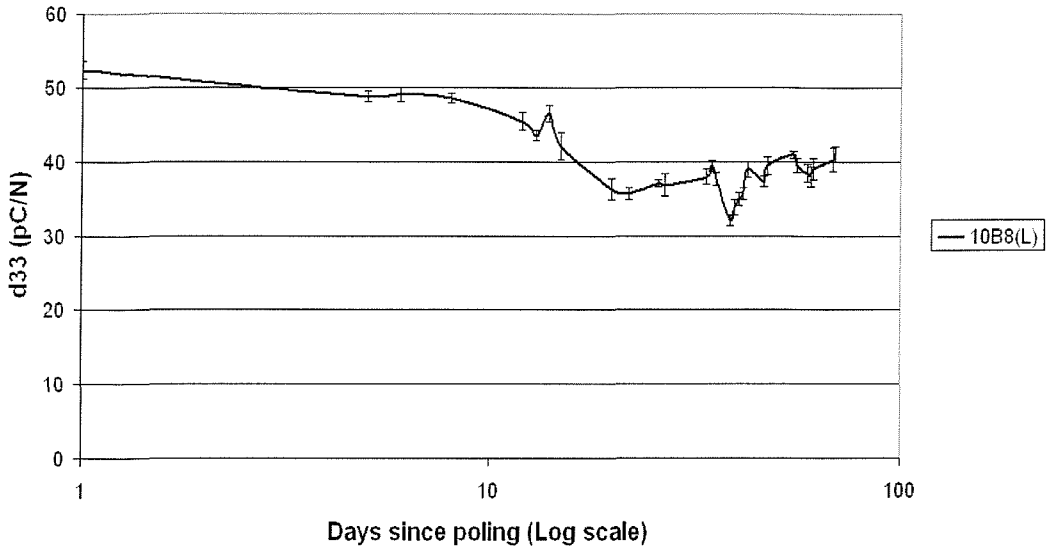

Figure 6.3: Decay of average $d_{33,f}$ value over time.

The results show that the device exhibited decay in piezoelectric polarisation for approximately 25 days as expected. Beyond 25 days the $d_{33,f}$ value settled to a virtually constant value. The 10B8 device decayed from 52.4pC/N to approximately 42pC/N. This represents a decay in piezoelectric activity of approximately 20%.

6.4.4 Conclusions

This range of investigations into the poling voltages and conditions has indicated that a significant proportion of the $d_{33,f}$ optimisation can be obtained from the poling parameters alone. The tests conducted under Morgan Electro Ceramics factory conditions and the re-poling experiments indicate that if the higher voltages could be maintained for a longer poling time the $d_{33,f}$ could be improved.

The time decay experiment demonstrated that the piezoelectric activity of the material will decay over time. This is due to minor re-alignment of the electric dipoles within the film to their pre-poled state. The 20% reduction observed is approximately twice that observed with bulk PZT-5H devices [5]. It is believed the additional re-alignment experienced by thick-film PZT-5H compared to the

bulk equivalent is due to two factors. The first is that the reduced sintering levels of the film result in smaller domain sizes in the films and therefore the level of polarisation is reduced. The smaller domains have a reduced dipole moment and therefore the electrical force maintaining alignment is reduced. Finally, the clamping effect of the substrate and electrode layers provides a greater restriction on the deformation of the film during the poling process. This results in a reduced amount of dipole alignment and a greater stress on the film structure which will reduce the piezoelectric properties of the material.

7 Optimisation of $d_{33,f}$: Mixed powder types

7.1 Introduction

The results achieved in chapter 5 show that the ball milled devices with 10% glass provide the optimum piezoelectric coefficients. However, the SEM micrographs of the PZT layer show that the films exhibit a good degree of glass sintering but the film density is of a lower quality than the attritor milled devices.

This chapter considers two methods for improving the density of the fired thick-film PZT-5H material. These are:

- Vacuum drying of existing PZT pastes.
- Combination of large and small powder particles.

Studies are conducted to evaluate vacuum drying of the current thick-film batches and the combination of different PZT powder particle sizes in the thick-film paste. It is proposed that the vacuum drying will exert external pressure on the film and should improve the density. Following this, theories concerning the combination of different powder particle sizes are discussed. It is proposed that by combining large and small particle sizes the interstices observed in the micrographs can be reduced, thus increasing the density of the fired films. Finally, an evaluation of the paste composition work is conducted and an optimum paste formulation decided.

7.2 Film densification

To achieve the maximum piezoelectric properties for thick-film PZT materials it is essential to increase the density of the film. The increase in density allows for improved mechanical coupling of the film and therefore an improved $d_{33,f}$. The improvement in $d_{33,f}$ is because the applied force has improved coupling to the

piezoelectric particles within the film matrix. This means that each particle is deformed to a greater extent and therefore produces a higher charge output.

Increasing the density of the film can be achieved by several methods, either by combining different processes or materials [23] or by compressing the films after printing, either during drying or firing [94].

Work by Dorey et al. [95] develops the composite technique developed by Corker et al, discussed in section 2.4.2 [24]. The technique combines a standard ferroelectric powder with the organo-metallic sol used in the sol-gel process. This composite film has an increased thickness compared to those fabricated using the sol-gel process and an improved film density compared to those formed using screen-printing techniques. The composite layer was deposited on a platinised silicon substrate using the same spin coating technique as before. However, in this study an additional sol infiltration was conducted after the film was dried, for each deposited composite layer. Once the required number of composite layers had been deposited, the film was fired at 710°C for 30 minutes. After firing, Cr-Au electrodes were evaporated on the films, which were then poled at 200°C for 5 minutes and an applied field of 8MV/m. The results show that the sol infiltration steps increased the observed density of the film, which increased the relative permittivity of the films. An increase in measured $d_{33,f}$ was observed when a single infiltration step was used. However, subsequent infiltrations had a reduced effect, although an increase was observed, as the optimum density of the film was approached. The paper does not state if the poling parameters used were the optimum. It is possible that the increased density and permittivity of the film would allow for an increase in applied poling field before breakdown occurs, thus further improving piezoelectric activity of the material.

The study showed that the average $d_{33,f}$ for the film was increased from 35pC/N to 62pC/N with the use of sol infiltration and an improved sintering aid. This suggests that densification of the films can have a significant impact on the piezoelectric activity of thick-films and is an important area of study.

7.3 Vacuum drying

The SEM micrographs in section 5.5 show the PZT-5H layer has increased porosity compared to the bulk equivalent. The bulk process can involve the use of, for example, isostatic presses to manufacture the size and shape of device required. However, the screen-printing process does not introduce any external pressure on the printed paste as it settles on the substrate. Therefore, the effect of a vacuum on a screen-printed substrate was investigated to observe any increase in film density.

7.3.1 Experimental procedure

Two substrates were screen-printed with a PZT paste composition of 10% CF7575 and 90% ball milled PZT-5H. After printing, one substrate was dried in a vacuum chamber with $2x10^{-4}$ mbar of pressure at 190°C for 10 min with the other dried in an IR drier with the same settings. The two substrates were then fired in the belt furnace using the Dupont60 furnace profile. Top electrodes were not printed on these substrates because the aim of the experiment was to observe any changes in the density of the PZT layer.

7.3.2 Results and conclusion

After firing, a sample from each substrate was removed for observation within the SEM. Figure 7.1 and 7.2 below show the SEM micrographs of the non-vacuum and vacuum dried samples respectively.

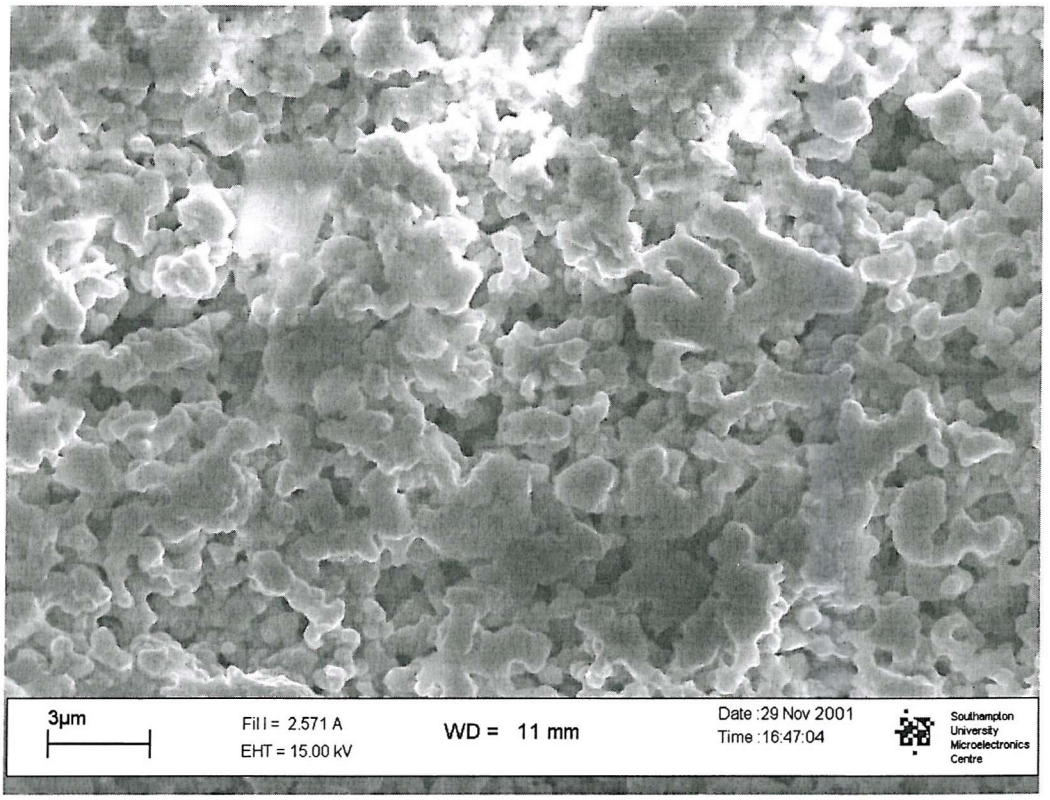

Figure 7.1: PZT layer of thick-film dried in IR drier.

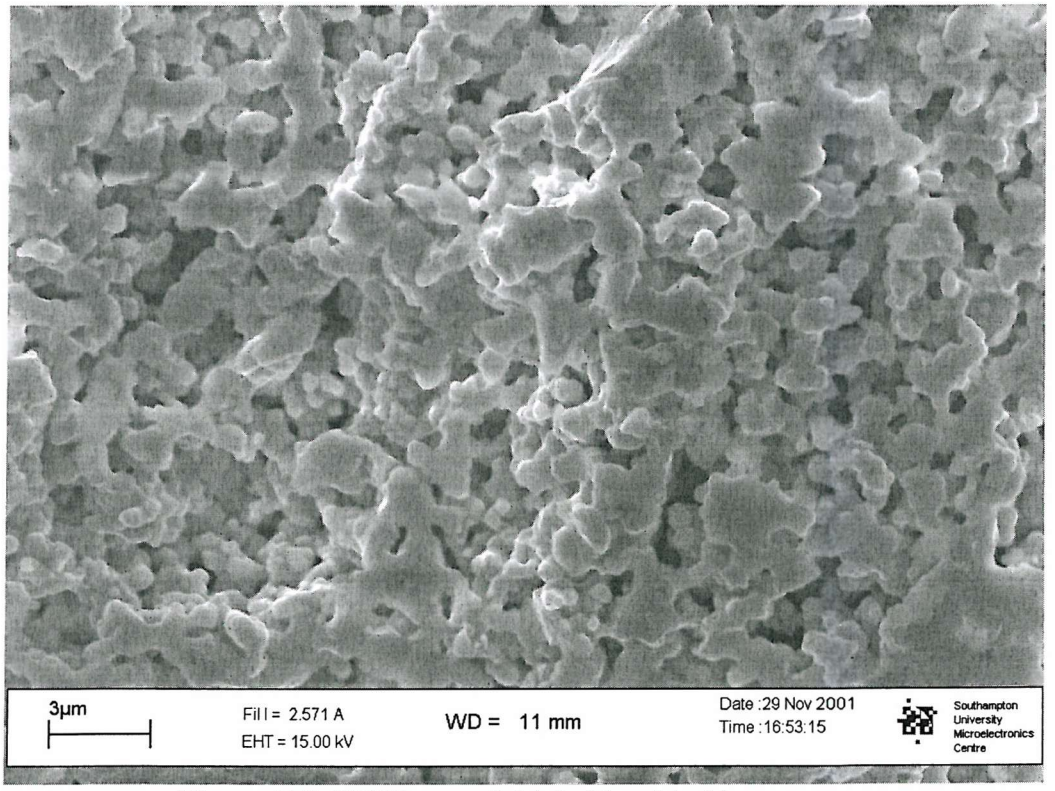

Figure 7.2: PZT layer of thick-film dried in a vacuum.

Figure 7.1 and 7.2 are cross-sectional micrographs of the PZT layer at the same magnification indicating the density of the films.

The SEM micrographs show no significant increase in the density of the film from this simple experiment. However, the use of more sophisticated techniques, such as hot isostatic pressing may yield more encouraging results. This work is beyond the equipment available and the scope of this thesis. However, cooperation with a commercial company may be possible for future work in this area.

7.4 Powder combinations

Following the vacuum experiment and the work in chapter 5 [96,97], the next stage in the development of improved $d_{33,f}$ values considered the combination of ball milled and attritor3 milled powders. It is proposed that the combination of PZT powder sizes should contribute towards an increased PZT layer density. The larger particle size associated with the ball milled powder results in increased piezoelectric responses. Therefore, it was important to maintain the ball milled particle as the dominant particle within any powder combination. The attritor3 particles can be used to fill any voids between the ball milled particles, thus resulting in an increased film density and improving its mechanical coupling and piezoelectric properties. Hence, it was anticipated that by combining these two powders, we would obtain the high $d_{33,f}$ values associated with ball milled powder and the consistency achieved with attritor3 powders.

The paste therefore consists of a combination of ball milled, attritor3 milled and Ferro CF7575 lead borosilicate glass. The analysis of such particle sizes is especially important since the films are fired at lower temperatures than the bulk equivalent. This is sufficient to melt the glass but minimal sintering of the actual PZT particles occurs as discussed previously.

7.4.1 Modelling of the film

To determine sensible ratios of ball and attritor3 milled powders, an analysis of the particle distribution was first carried out. This analysis would also identify the optimum attritor particle size in order to maximize film density. The analysis provides a simplistic model of the practical particle distribution. However, it is suitable to determine initial particle size values and percentage weights for the study.

It was first necessary to simplify the mathematical model for the PZT layer structure to a 2-dimensional representation of the particle distribution. A ball milled particle is the central particle in the lattice and the interstice between these are filled with smaller attritor milled PZT particles, shown in figure 7.3.

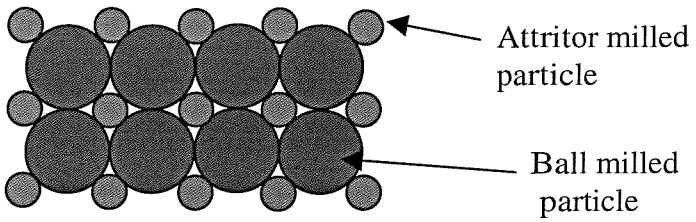

Figure 7.3: Ideal 2-d particle distribution.

This model assumes all the glass will melt in the processing and form a perfect bonding matrix surrounding the particles. In this study it was decided to use a fixed percentage of glass, 10% by weight, since the results in chapter 5 show this to be the optimum. Therefore, the optimum size of the attritor particles and their ratio by weight were the only factors that needed to be determined.

Assumptions of the model:

- Full control of the particle dimensions is possible.
- The glass content will not affect the size of the smaller particle.
- All the glass will melt to form a bond between the two particle sizes.
- The particles will form a perfect structure indicated in figure 7.3.
- That the optimum solution fills the interstice surrounding the central particle.

- The particles are round.

In practice none of these assumptions are possible but they are reasonable approximations of the practical conditions.

7.5 Ideal Calculations

The mean particle size for the ball milled PZT powder was measured to be 2μm, see section 5.2.1 [96]. Assuming the smaller circles from figure 7.3 to be attritor milled PZT, the maximum attritor particle can be calculated using figure 7.4.

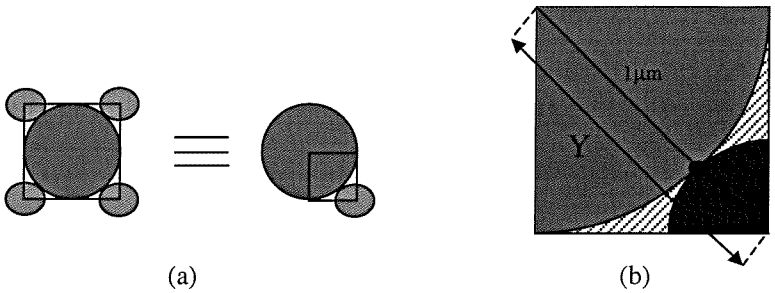

Figure 7.4: Equivalent diagram for calculations.

Figure 7.4(a) shows how the model can be reduced to the equivalent of one large and one small particle. Figure 7.4(b) can be used to derive the maximum radius of the small particle in order to fit within our model.

$$a = \sqrt{b^2 + c^2} \text{ [7.1]} \qquad A_c = \pi r^2 \text{ [7.2]} \qquad A_s = a \times a \text{ [7.3]}$$

Equations 7.1, 7.2 and 7.3 give Pythagoras theorem, the area of a circle and the area of a square respectively. Using these equations and figure 7.4(b) we can calculate the maximum diameter of the smaller particle.

$$Y = \sqrt{1^2 + 1^2} = 1.414\mu m$$
$$X = Y - 1\mu m \text{ (from figure 7.4(b))}$$
$$X = 0.414\mu m$$

Having obtained the radius, the maximum diameter of an attritor particle is 0.83μm. To determine how much of the area of the lattice from figure 7.3 will be filled, the combined area of the two particles must be calculated. The percentage of the area filled can be calculated using equation 7.4 in conjunction with equations 7.2 and 7.3.

$$\text{Percentage area filled} = \frac{\text{area of circles}}{\text{area of square}} \text{x } 100 \quad [7.4]$$

$$= \frac{[(\pi \times 1^2) + (\pi \times 0.414^2)]}{(2 \times 2)} = \frac{(3.14 + 0.54)}{4} = 92\%$$

Therefore, this configuration fills 92% of the area, which is the maximum achievable with two particle sizes. The remaining area is assumed to be filled by the glass as it melts during the firing process to bind the PZT particles.

To convert these particle sizes into percentage weights for the paste formulation it is necessary to calculate the weight of each particle. For this model it is assumed all the particles will be a perfect sphere, therefore the volume of the sphere and the material density can be used.

Equation 7.5 and 7.6 show the formula for the volume of a sphere and for mass, when the volume and density are known, respectively.

$$V_{sp} = \frac{4\pi r^3}{3} \quad [7.5] \qquad \text{mass} = \text{volume} \times \text{density} \quad [7.6]$$

To determine the weight ratio it is necessary to determine the mass of one particle. This value can then be used to extrapolate the ratio of particle numbers required using figure 7.4(a). Using equation 7.5 the volume of the two particles can be determined.

Where V_{Ball} and V_{Att} are the volumes of the PZT ball and attritor milled particles respectively:

$$V_{Ball} = 4.19\mu m^3$$
$$V_{Att} = 0.297\mu m^3$$

Using the density values shown in table 7-1:

$$\text{mass of ball particle} = 4.19\mu m^3 \times 7.45x10^{-12} g/\mu m^3 = 31.2x10^{-12} g$$
$$\text{mass of attritor particle} = 0.297\mu m^3 \times 7.45x10^{-12} g/\mu m^3 = 2.21x10^{-12} g$$

This calculation provides the mass of a single particle. Therefore, this value can be used to extrapolate the ratio of particle numbers required and their respective mass. Therefore, for a 1:1 ratio of ball to attritor milled particles, indicated by figure 7.4(a), we require 14.1 times more ball than attritor milled powder by weight. Assuming 10% by weight of CF7575 glass this equates to the values given in table 7-1.

Powder Type	Density ($g/\mu m^3$)	Percentage Weight
Ball milled PZT	7.45×10^{-12}	84%
Attritor milled PZT	7.45×10^{-12}	6%
CF7575 Lead Borosilicate	6.20×10^{-12}	10%

Table 7-1: Optimum powder combinations for ideal particle sizes.

These powder combinations do not relate directly to the practical situation. This is because the model is 2D and does not completely fill the interstice around the ball milled particle.

The remaining area, checked zone in figure 7.4(b), can be calculated to give the total area that needs to be filled. If we assume that our calculated diameter for the attritor milled powder can be used and will fill that entire volume.

Using equations 6.2 and 6.3 and figure 7.4(b) the area between the ball particles can be converted to a ratio of the area filled by the attritor particle:

$$\frac{\text{unfilled area}}{\text{area of att particle}} = \frac{A_s - A_{Ball}}{A_{Att}}$$

$$= \frac{4 - 3.141}{0.538} = 1.6$$

Maximum particle ratio = 1.6(Att) : 1(Ball)

This result shows that to fill the entire area between the ball particles we require 1.6 attritor particles. The particle mass calculations can be used to convert this ratio of particle numbers to a ratio by weight. Thus the optimum weight ratio, assuming that the attritor particles could be made small enough to fill the area between the ball particles, would be 8.8:1 ball to attritor milled powder by weight. The problem with this calculation is that it uses non integer values of particle numbers. However, this is supported by the supposition that in the practical case the powder contains a distribution particle sizes and therefore a number of these could be equivalent in size to 0.6 of a full sized particle.

7.6 Second model

Having considered the model in figure 7.3 it is necessary to look at an alternative configuration given in figure 7.5.

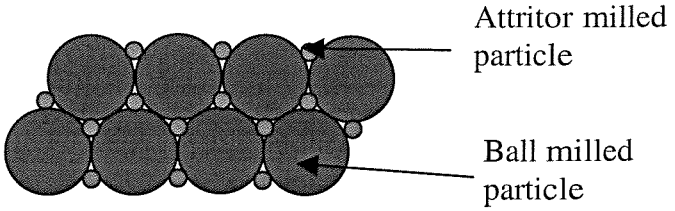

Figure 7.5: Ideal 2-d particle configuration for model 2.

This configuration requires a smaller attritor particle as the arrangement of ball particles is much more compact, however the number of particles required has increased. Each ball milled particle now has six surrounding attritor particles. However, these are shared between three ball particles so it is the equivalent ratio of two attritor particles to every one ball particle.

The size of this attritor particle can be calculated by reducing the model to an equivalent triangular area given in figure 7.6.

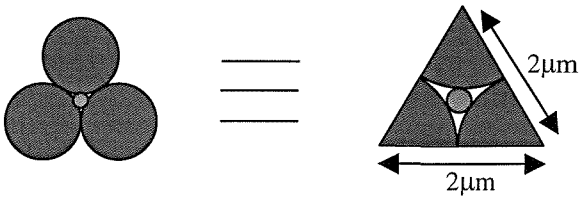

Figure 7.6: Equivalent diagram for model 2 particle size calculations.

Using figure 7.6, the attritor particle size can be calculated. Using trigonometry the centre point of the triangle can be calculated, and from here the diameter available between the 3 ball particles can be determined.

$$\text{Maximum diameter} = \text{distance between centre point and ball particle}$$

$$\cos 30° = \frac{1}{1+x} \Rightarrow x = 0.15\mu m \text{ radius}$$

$$\text{diameter for attritor particle} = 0.3\mu m$$

$$\text{mass of attritor particle} = \left(\frac{4\pi(0.15)^3}{3}\right)\mu m^3 \times 7.45x10^{-12} g/\mu m^3 = 0.105x10^{-12} g$$

Figure 7.5 shows that by using this size particle we would require a particle ratio of 2 attritor particles for each ball milled particle. Using the same method as before the weight ratio can be calculated to be 148.6:1 of ball to attritor milled powder by weight.

Powder Type	Density ($g/\mu m^3$)	Percentage Weight
Ball milled PZT	7.45×10^{-12}	89.4%
Attritor milled PZT	7.45×10^{-12}	0.6%
CF7575 Lead Borosilicate	6.20×10^{-12}	10%

Table 7-2: Optimum powder combinations for model 2.

Calculating the ratio between the particle area and the remaining area between the 3 ball particles, gives the following:

$$\frac{\text{area of triangle - area of ball particle}}{\text{area of attritor particle}} = \frac{\left(1.73\mu m^2 - \frac{\pi}{2}\mu m^2\right)}{\pi(0.15\mu m)^2} = \frac{0.16\mu m^2}{0.075\mu m^2} = 2.15$$

So therefore, the area equivalent to 2.15 attritor particles can fill the interstice between the ball particles, although figure 7.5 shows would not be the case in the ideal model. This equates to 4.3 attritor particles for each ball particle, by weight this is a ratio of 69.1:1 ball milled to attritor milled powder.

A summary of these four results for the two 2D models is given in table 7-3.

Powder Type	Density ($g/\mu m^3$)	Model 1 Percentage Weight (optimum size)	Model 1 Percentage Weight (optimum area)	Model 2 Percentage Weight (optimum size)	Model 2 Percentage Weight (optimum area)
Ball milled PZT	7.45×10^{-12}	84%	81%	89.4%	88.7%
Attritor milled PZT	7.45×10^{-12}	6%	9%	0.6%	1.3%
CF7575 Lead Borosilicate	6.20×10^{-12}	10%	10%	10%	10%

Table 7-3: Percentage weights of materials for each model.

The results in table 7-3 provide an indication of the optimum powder combination but are still based upon ideal values and an ideal model for each powder.

7.7 3D equivalent models

Following on from the 2D models it is necessary to calculate any effects of using 3D equivalent of the models.

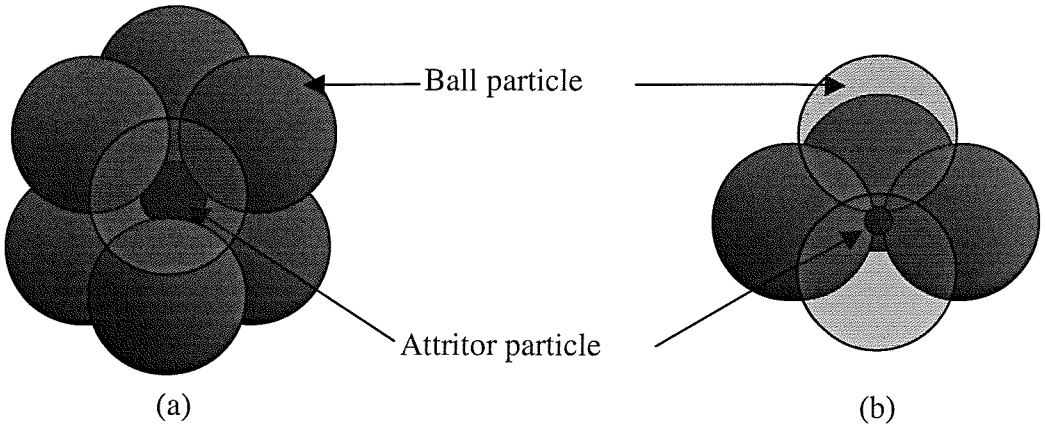

Figure 7.7: 3D equivalent of the 2D models.

Figure 7.7(a) and (b) show the equivalent 3D picture of model 1 and 2 respectively. Figure 7.7(b) shows the same base layer as 7.7(a) but the next layer of ball particles begins in the centre of the four ball particles, the attritor particle lies at the centre of these five particles. From these pictures and using the volume of a sphere from equation 6.6 it is possible to determine the volume remaining between the ball particles, and how much of that volume is filled by the attritor particle.

7.7.1 3D calculations for model 1

The volume between the ball particles can be equated to a corner of each sphere inside a box volume joining the centre points of each of the surrounding ball particles. Thus, the remaining volume can be determined by subtracting the 8 corner pieces from the box volume.

$$\text{Volume of box - Volume of sphere} = \text{Gap Volume}$$

$$2^3 - \frac{4\pi(1)^3}{3} = 3.81\mu m^3$$

$$\text{Volume of } 0.83\mu m \text{ diameter attritor particle} = 0.297\mu m^3$$

$$\text{Number of attritor particles to fill the gap} = \frac{3.81\mu m^3}{0.297\mu m^3} = 12.7$$

This shows that the volume equivalent of 12.7 attritor particles could fill the remaining interstice between the ball particles. Using the particle density and volumes this equates to a weight ratio of 1.11:1 ball to attritor milled powder.

7.7.2 3D calculations for model 2

This calculation is also based on the 2D calculations but uses a triangular prism shape between the centre points of 5 ball particles. Using figure 7.6 and 7.7 this can be equated to the equivalent of half a ball particle within the prism, from here we can calculate the remaining volume.

$$\text{Volume of prism} - \frac{\text{Volume of sphere}}{2} = \text{Volume of interstice}$$

$$2\text{x}1.73 - \frac{2\pi(1)^3}{3} = 1.365\mu\text{m}^3$$

$$\text{Volume of } 0.3\mu\text{m diameter attritor particle} = 0.014\mu\text{m}^3$$

$$\text{Number of attritor particles to fill the gap} = \frac{1.365\mu\text{m}^3}{0.014\mu\text{m}^3} = 97.5$$

This shows that for model 2, the volume equivalent of 97.5 attritor particles with 0.3μm diameter could fill the interstice between the ball particles. Using the particle density and volumes, and remembering that for model 2 there is the equivalent of two interstices per ball particle, this equates to a weight ratio of 1.52:1 ball to attritor milled powder.

7.8 Discussion of results

Both the 3D equivalents of the 2D models show an increase in the number of attritor particles that can fit between the ball particles. This is to be expected because of the spherical nature of the model. Table 7-4 gives a list of the percentages of each material that would be required with each of the models.

Powder Type	3D - Model 1 Percentage Weight (optimum volume)	3D - Model 2 Percentage Weight (optimum volume)
Ball milled PZT	47.5%	54.3%
Attritor milled PZT	42.5%	35.7%
CF7575 Lead Borosilicate	10%	10%

Table 7-4: Powder percentages for 3D models.

These percentages show an increase in the amount of attritor powder required in order to fill the volume surrounding the ball particles compared to the 2D model based only on the areas and optimum particle size.

These ideal models are only guides for the practical experiments because they are based upon a number of assumptions that would not match practical reality. They are also based upon the calculation that the volume of the attritor particle can fit into the interstice surrounding the ball particle completely. To determine the exact number of attritor particles that could fill the volume without being molten, would require complex calculations that, given the assumptions made and the approximate nature of this analysis, are not justified.

7.9 Practical calculations

The ideal models have shown that the attritor particle should be 0.83μm and 0.3μm diameter for model 1 and 2 respectively. However, for the practical experiments the attritor powder available was attritor3 powder, this had an average particle size of 1μm.

diameter for attritor3 particle = 1μm

$\text{Area} = \pi\,(0.5\mu\text{m})^2 = 0.79\mu\text{m}^2$

$$\text{mass of attritor particle} = \left(\frac{4\pi(0.5)^3}{3}\right)\mu\text{m}^3 \times 7.45\text{x}10^{-12}\,\text{g}/\mu\text{m}^3 = 3.9\text{x}10^{-12}\,\text{g}$$

Using the particle number and volume calculations from the previous section but substituting the real value for the attritor3 particle instead of the optimum value, the results in Table 7-5 and Table 7-6 were obtained.

Powder Type	Model 1 Percentage Weight (practical size)	Model 1 Percentage Weight (practical area)	Model 2 Percentage Weight (practical size)	Model 2 Percentage Weight (practical area)
Weight ratio Ball:Att3	8:1	7.3:1	4:1	20:1
Ball milled PZT	80%	79%	72%	86%
Attritor3 milled PZT	10%	11%	18%	4%
CF7575 Lead Borosilicate	10%	10%	10%	10%

Table 7-5: Percentage weights of materials for each 2D model using practical powder size.

Powder Type	Model 1 Percentage Weight (optimum volume)	Model 2 Percentage Weight (optimum volume)
Weight ratio Ball:Att3	1.1:1	1.5:1
Ball milled PZT	47%	54%
Attritor milled PZT	43%	36%
CF7575 Lead Borosilicate	10%	10%

Table 7-6: Percentage weights of materials for 3D models using practical powder size.

7.10 Discussion of results

The practical results for the paste compositions in table 7-5 and table 7-6 are very similar to the ideal values given in table 7-3 and table 7-4. These composition values provide a start point for an experimental plan to determine the optimum proportion of ball and attritor3 milled powder. Differences that occur in the results for the area based model 2 are due to the practical value for the attritor particle, 1μm, being much larger than the calculated ideal, 0.3μm. Both the 3D models would indicate that a weight ratio close to 1:1 would produce the optimum film density. The 2D models estimate the optimum composition to lie between 4:1 and 8:1 by weight of ball and attritor milled powder.

7.11 Experimental work

Having obtained a starting point for the work from the ideal calculations it was necessary to decide on the experimental values for each powder. Following the theoretical results that indicate the solution lies between 1:1 and 8:1 by weight it was decided to calculate the weight ratios for an integer number of attritor particles.

Weight ratios of 8:1, 4:1, 2.6:1 and 2:1 were tried which equates to 1, 2, 3 and 4 attritor3 particles per ball particle respectively; the percentage calculation results are shown in table 7-7.

Paste	Attritor3 percentage weight	Ball percentage weight	CF7575 percentage weight
8:1	10%	80%	10%
4:1	18%	72%	10%
2.6:1	25%	65%	10%
2:1	30%	60%	10%

Table 7-7: Experimental powder combination weight percentages.

7.11.1 Processing

From the values in table 7-7 the batches were mixed and then printed as described previously on a 96% alumina substrate with ESL 9633B silver/palladium electrodes. The PZT layer consisted of two prints, the first print was dried in the IR drier with the second printed directly on top and dried. Both layers were then co-fired in the belt furnace using the Dupont60 furnace profile. Two substrates per batch were printed, with one column from each substrate removed in the clean room for analysis in the SEM.

Once fired, the devices were poled at 150°C with an electric field applied for 30 minutes. The substrate with the 4:1 batch produced a higher layer thickness than usual. Therefore, the maximum achievable electric poling field with our equipment was 3MV/m. To maintain consistency the electric field applied to the other samples was reduced to this value.

In addition to this, a substrate of the 4:1 and 8:1 pastes were printed and fired as normal but then an ESL-110S silver polymer top electrode was printed instead of the silver/palladium. This silver polymer layer was cured for an hour at 200°C as described previously in section 6.2.1.

7.11.2 Experimental results

After poling, the $d_{33,f}$ coefficient of each device was measured using the PM35 piezometer. Five readings were taken on each device and an average recorded, shown in figure 7.8.

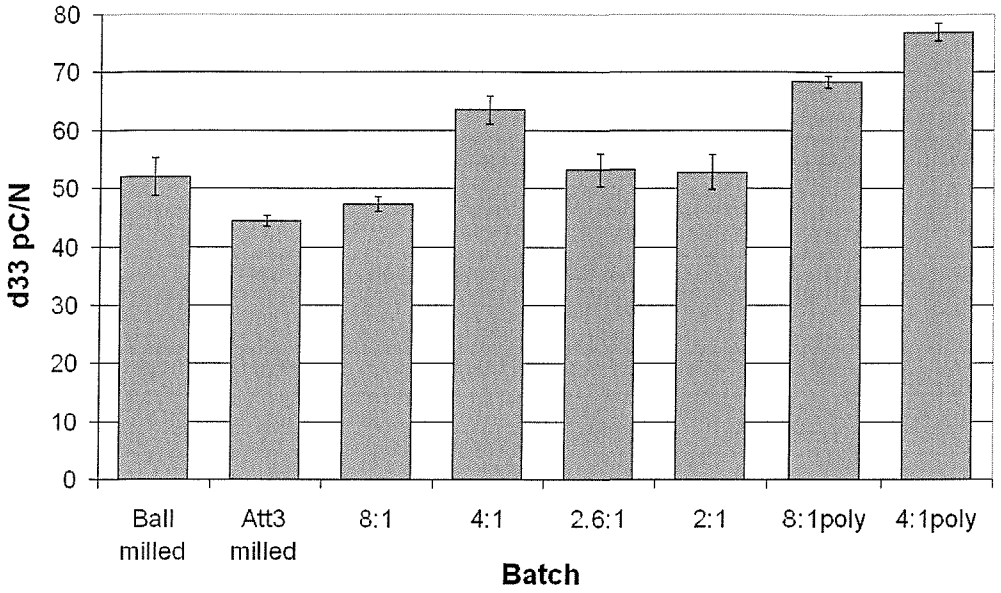

Figure 7.8: Average $d_{33,f}$ results for powder combination experiments.

The films with a polymer top electrode are labelled 8:1poly and 4:1poly. Also included for comparative purposes are the average $d_{33,f}$ results obtained for the 10% ball milled and 5% attritor3 milled films from previous work.

In addition to the $d_{33,f}$ results, figure 7.9 shows the percentage standard deviation associated with each paste batch to demonstrate the consistency of each batch. Included in this data set are the results from previous work for 10% ball and 5% attritor3 films as before.

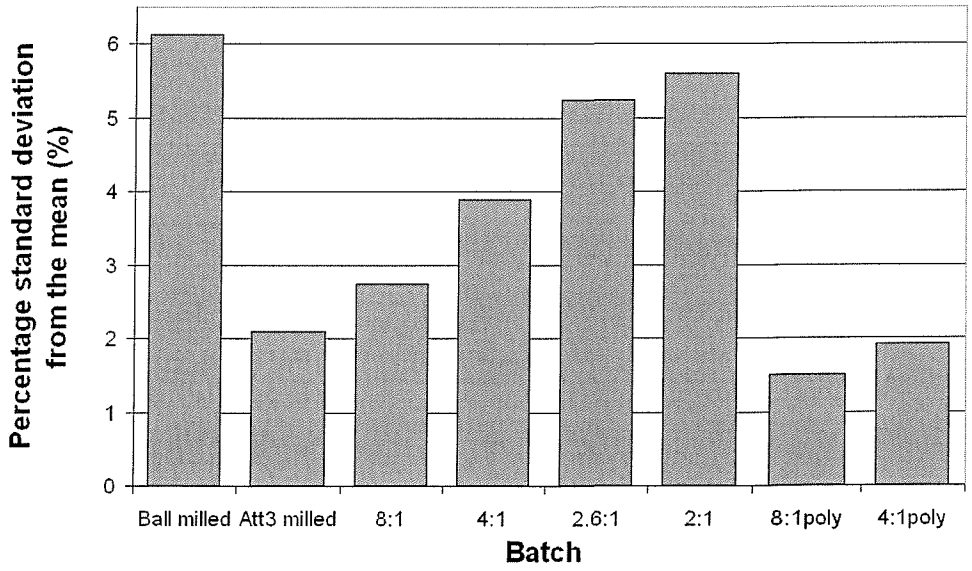

Figure 7.9: Percentage standard deviation for each paste formulation.

SEM micrographs

Figures 7.10 and 7.11 show the SEM micrographs of the 8:1, 4:1 Ball:Att3 sample PZT layers respectively. The samples are unpolished at this stage but the micrographs still give an indication of the density of the PZT layers.

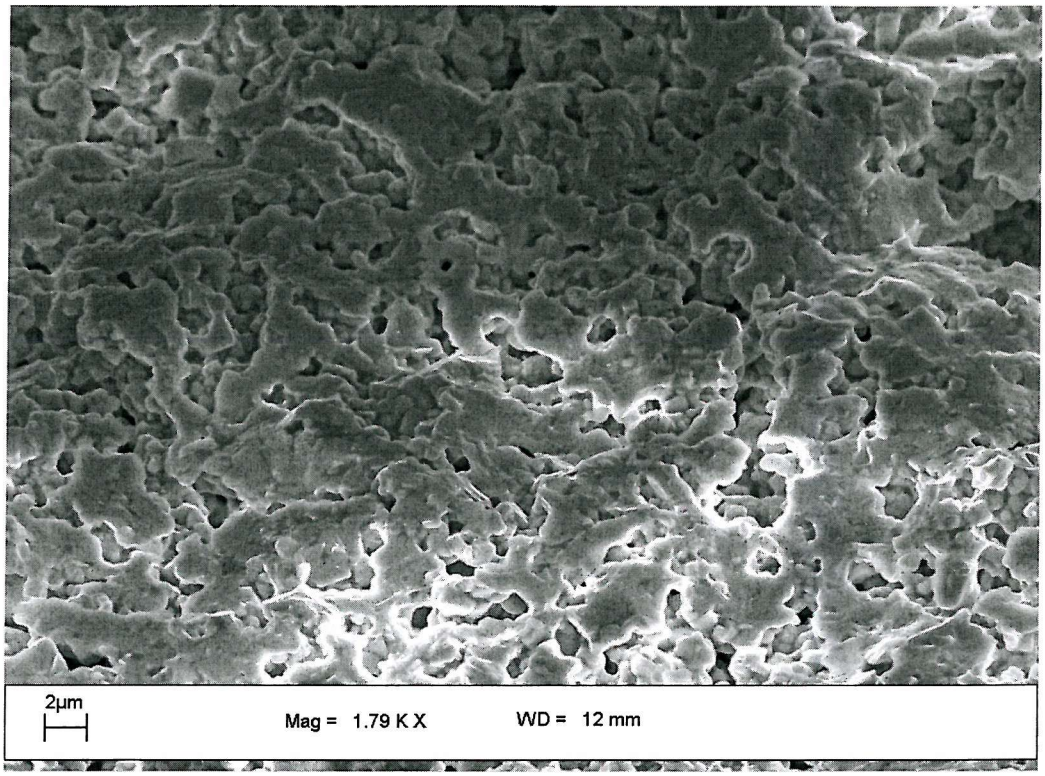

Figure 7.10: 8:1 Ball:Att3 sample PZT layer.

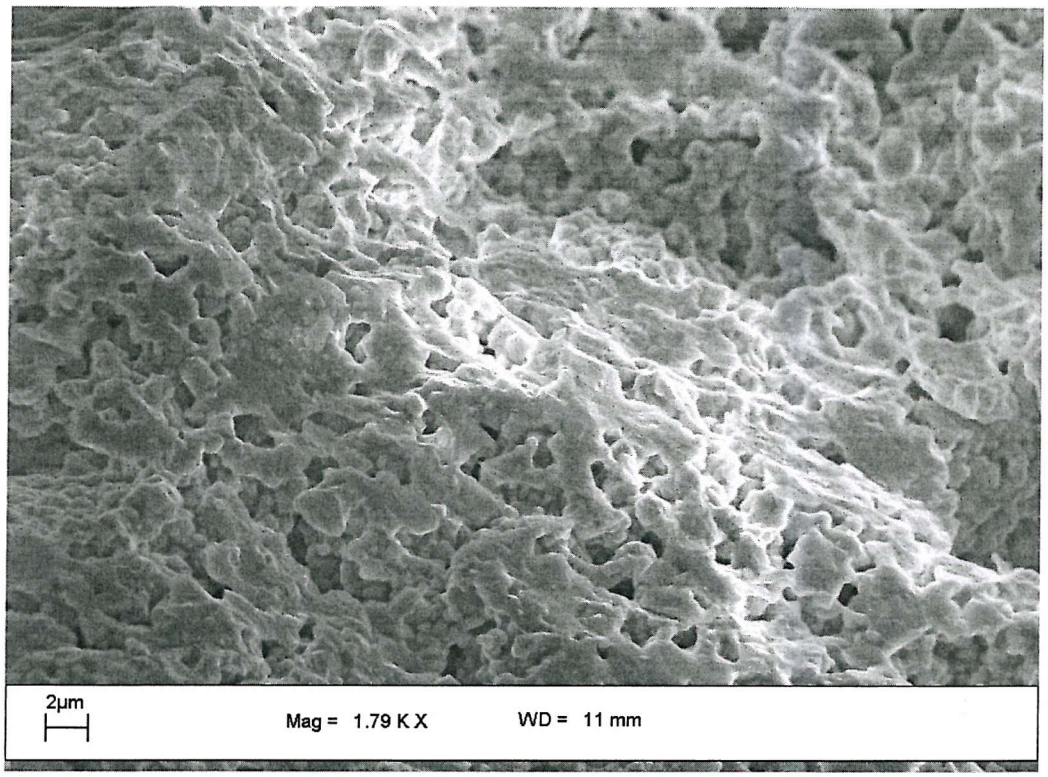

Figure 7.11: 4:1 Ball:Att3 sample PZT layer.

The SEM micrograph of the 4:1 ball to attritor3 PZT layer shows an improvement in film density over the standard ball samples although not as good as the att3 sample shown in figure 5.8. It appears that the level of sintering between the PZT particles is still low but that the glass bonding matrix and the combination of powders has produced a relatively dense film with reduced interstices.

7.12 Discussion of results

The results have shown that blending the ball milled powder with the attritor3 powder produces an increase in the piezoelectric activity of the film. Figure 7.8 suggests that the number of smaller particles added to the paste has a saturating effect beyond ratios of 2.6:1 as the interstices within the matrix have been already filled. This result agrees reasonably closely with the models and indicates that model 2 is the closest approximation to the experimental results.

The original 10% ball milled PZT paste demonstrated a $d_{33,f}$ of 51.5pC/N. This optimisation study has produced a highest average $d_{33,f}$ value of 63.5pC/N. This

$d_{33,f}$ value was obtained with a paste composition of 4:1 by weight of ball to attritor3 milled powder. This was further increased to 77pC/N when a polymer top electrode was introduced to the structure. The polymer top electrode removes the requirement for additional firing of the piezoelectric film. The extra firing results in additional lead loss and hence reduced piezoelectric behaviour. These developments represent an increase of 23.3% and 49.5% respectively.

The percentage standard deviation of the 4:1 devices was 3.9%. The most consistent batch from the previous work was the 5% attritor3 device exhibiting a 2.1% deviation. However, this is still an improvement compared to the original 10% ball milled devices that had a standard deviation of 6.1%. This deviation is improved to 1.9% with the introduction of a polymer top electrode and represents a consistency higher than the 5% attritor3 devices. However, fewer samples were fabricated and measured to obtain this value.

7.13 Conclusions

The combination of 4:1 by weight of ball milled to attritor milled powder (i.e. 18% attritor3, 72% ball and 10% CF7575 powders) produces the highest $d_{33,f}$ coefficient with an average measured value of 63.5pC/N. This result agrees reasonably closely with the models and shows that the practical model 2 from table 7-5 provides the optimum values for $d_{33,f}$.

The results confirm that the combination of small and large particles does increase the $d_{33,f}$ of the film and justifies the investigation. It has also shown that the consistency of the results can be increased in comparison to the ball milled devices, although they are not as consistent as the attritor3 devices.

This investigation has provided further increases in the $d_{33,f}$ values, 65.1pC/N to 77pC/N with polymer top electrode, and the consistency and repeatability of the paste formulation, 6.1% reduced to 3.9% deviation. The 4:1 combination is the optimum paste formulation for the thick-film PZT-5H determined by the work in this thesis. An increase in piezoelectric activity from an original $d_{33,f}$ of 18.5pC/N to 65.1pC/N has been achieved with this material.

8 Optimisation of $d_{33,f}$: Processing for final paste formulation

8.1 Introduction

This chapter discusses methods of optimising the piezoelectric activity of the final material composition decided in chapter 7, (18wt.% attritor3, 72wt.% ball, 10wt.% CF7575). The chapter focuses on two areas that have the greatest effect on the piezoelectric activity of the thick-film, these are:

- Firing temperature.
- Poling parameters.

The first half of the chapter discusses the effect of the firing temperature on the optimised paste composition. In addition, it builds upon the conclusions from chapter 6, which revealed an increase in $d_{33,f}$ when the number of firing cycles was reduced, by attempting to co-fire the PZT layer and top electrode.

The second half of the chapter details an investigation into the effects of the poling parameters on the piezoelectric activity of the optimised paste composition. Specifically, the poling time and temperature are studied with a view to reducing the overall poling time to ensure greater compatibility with commercial applications.

Finally, having achieved the optimum paste formulation, electrode materials, firing profile and poling parameters, a table of the characteristic values of the optimised PZT-5H thick-film devices are compared with those of the bulk PZT-5H equivalent.

8.2 Firing profile investigation

To produce a thick-film piezoceramic it is necessary to fire the film at a sufficiently high temperature to cause the glass bonding matrix to melt. However, as the temperature increases, the likelihood of lead evaporation from the material is increased and the film becomes more susceptible to metal migration from the electrode layers. It is therefore necessary to obtain a balance between high firing temperatures, low lead evaporation and low electrode migration.

One possible solution is co-firing. Co-firing involves two or more layers of electrode and PZT layer being fired together. This reduces the number of firing cycles the PZT layers endures and also reduces the overall process time significantly. The problems with co-firing are typically a result of differing thermal coefficients of expansion in the materials. This can lead to a poor bond between the materials and deformation of the printed geometry. In extreme cases the layers can separate completely.

In addition, a new glass binder was evaluated as part of this study. Ferro EG2928 is an alternative lead borosilicate glass recommended by Ferro for use as a glass binder in PZT thick-films.

Property	Ferro EG2928
Devitrifying temperature	490°C
Softening point	470°C
Thermal coefficient of expansion	$6*10^{-6}$/°C
Density	5260kg/m^3

Table 8-1: Core Properties of Ferro EG2928

Table 8-1 shows the core properties of EG2928. Potentially, with a higher softening point and lower thermal coefficient of expansion EG2928 could help to

increase the density of the fired films. The density would increase because the film would maintain the printed geometry for longer during the firing process and potentially form a more suitable bonding matrix.

8.2.1 Firing Profiles

The initial work in this study evaluates three alternative furnace firing profiles by comparing the $d_{33,f}$ values of the fired thick-film material. The standard thick-film firing profile used throughout this thesis is the Dupont 60 furnace profile. The Dupont60 profile was used as a benchmark from which to extrapolate temperature values for a 750°C and a 1000°C peak temperature firing profile. These profiles are henceforth denoted RNT750 and RNT1000 respectively. These profiles are given in table 8-2, each stage is 5mins 40 seconds long.

	Profile temperatures (°C)		
Stage	**RNT750**	**Dupont60**	**RNT1000**
1	295	350	393
2	506	600	674
3	746	885	994
4	744	883	992
5	750	890	1000
6	733	870	978

Table 8-2: Furnace firing profiles for RNT750, Dupont60 and RNT1000.

These furnace profiles were chosen to investigate the effects of changing the peak temperature but maintaining the same shape of the original Dupont60 profile. The Dupont60 profile is maintained as a reference point. The RNT750 profile is different to the 750PK profile used in section 6.2.1 because it remains close to the peak temperature for longer. It is believed that by maintaining the peak temperature for longer the film will have greater adhesion to the substrate compared to those fired with the 750PK profile.

8.2.2 Experimental process

Each experiment was conducted using the optimised PZT powder combination described in section 7.13 with 10% glass content by weight. In addition, this study will evaluate a new glass binder, Ferro EG2928, as a possible alternative to the standard Ferro CF7575 glass used previously. This was mixed in to the paste as described previously in section 3.3.1.

The substrates were screen-printed and dried using the standard processes described in section 3.3. Subsequently, one substrate was fired in the belt furnace for each of the firing profiles listed in table 8-2. Once fired, an ESL 1110-s silver polymer was screen-printed as a top electrode before the substrates were removed from the clean room for poling. One column from each substrate was removed in the clean room for observation in the SEM.

8.2.3 Results

The devices were poled for 30 minutes at 150°C with a poling field of 4MV/m to reduce losses due to dielectric breakdown. The $d_{33,f}$ values were measured using the PM35 piezometer and an average over 6 devices was recorded. These results are shown in figure 8.1.

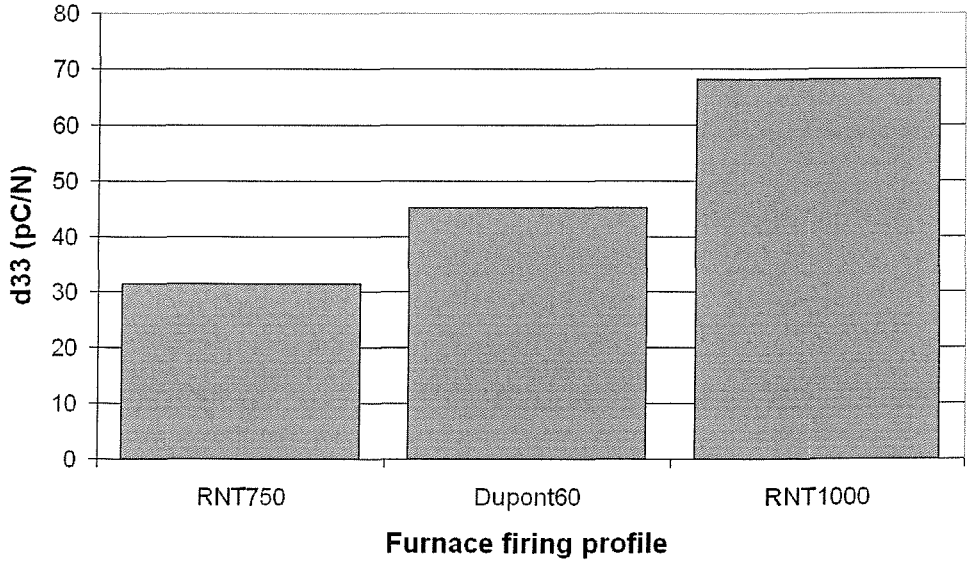

Figure 8.1: Furnace profile study results using EG2928 glass.

The SEM micrographs shown in figure 8.2, 8.3 and 8.4 are cross-sectional views of the PZT layer for RNT750, Dupont60 and RNT1000 respectively.

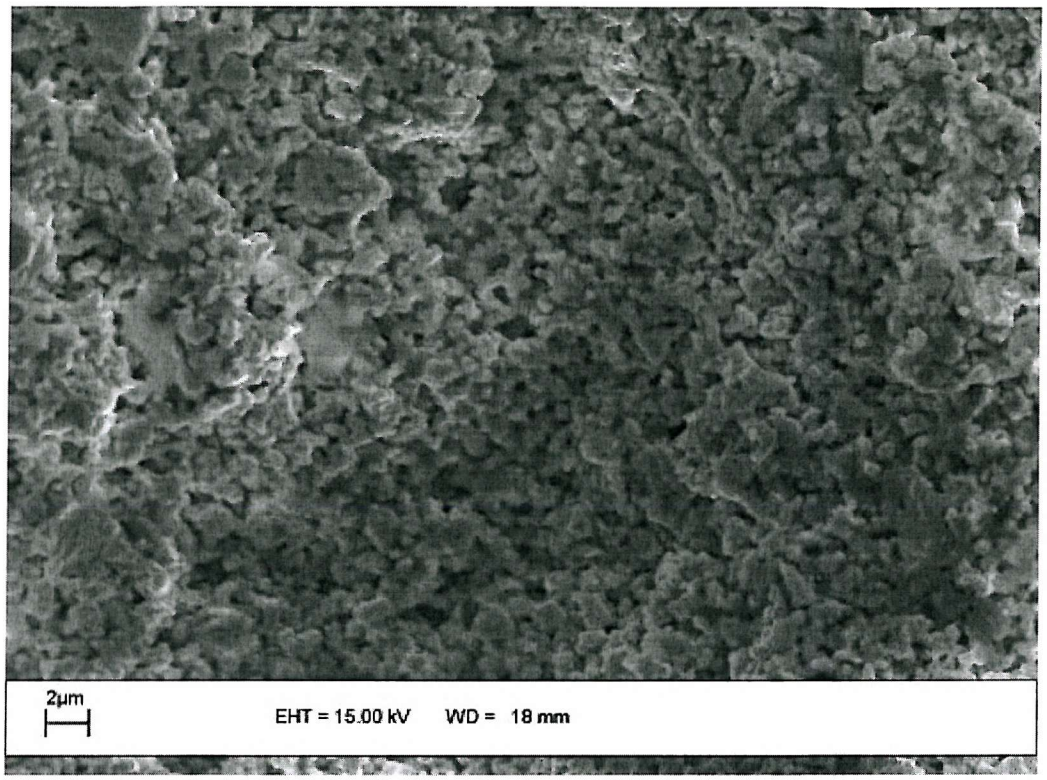

Figure 8.2: SEM micrograph of PZT layer fired using the RNT750 profile.

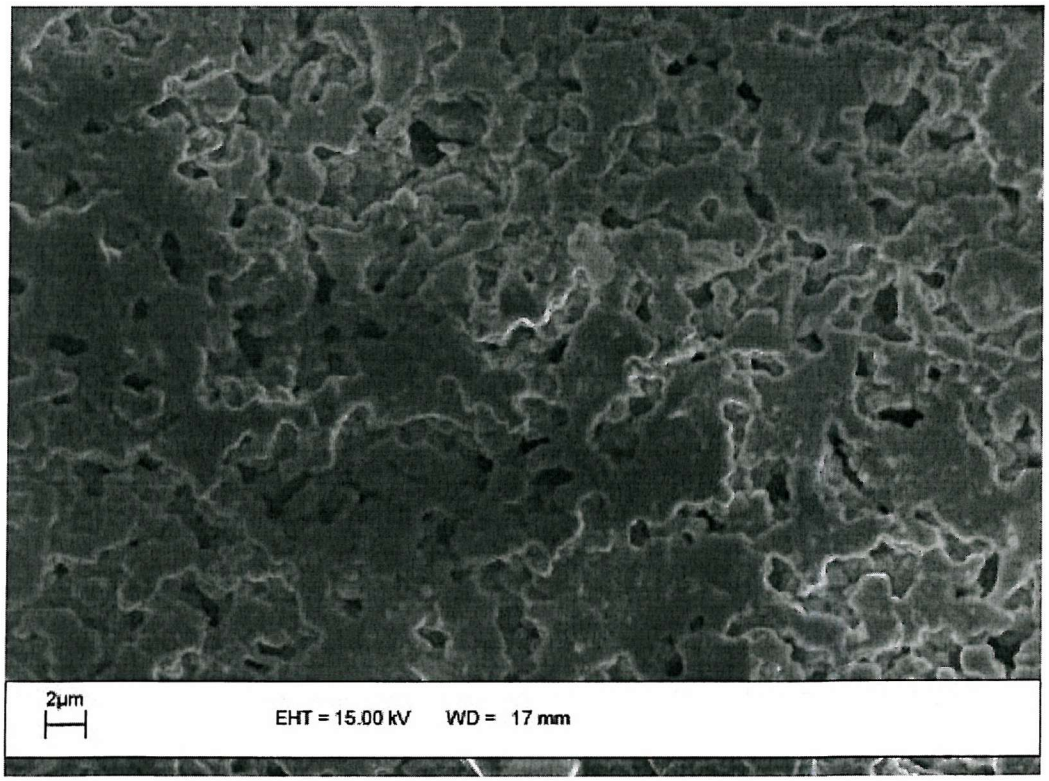

Figure 8.3: SEM micrograph of PZT layer fired using the Dupont60 profile.

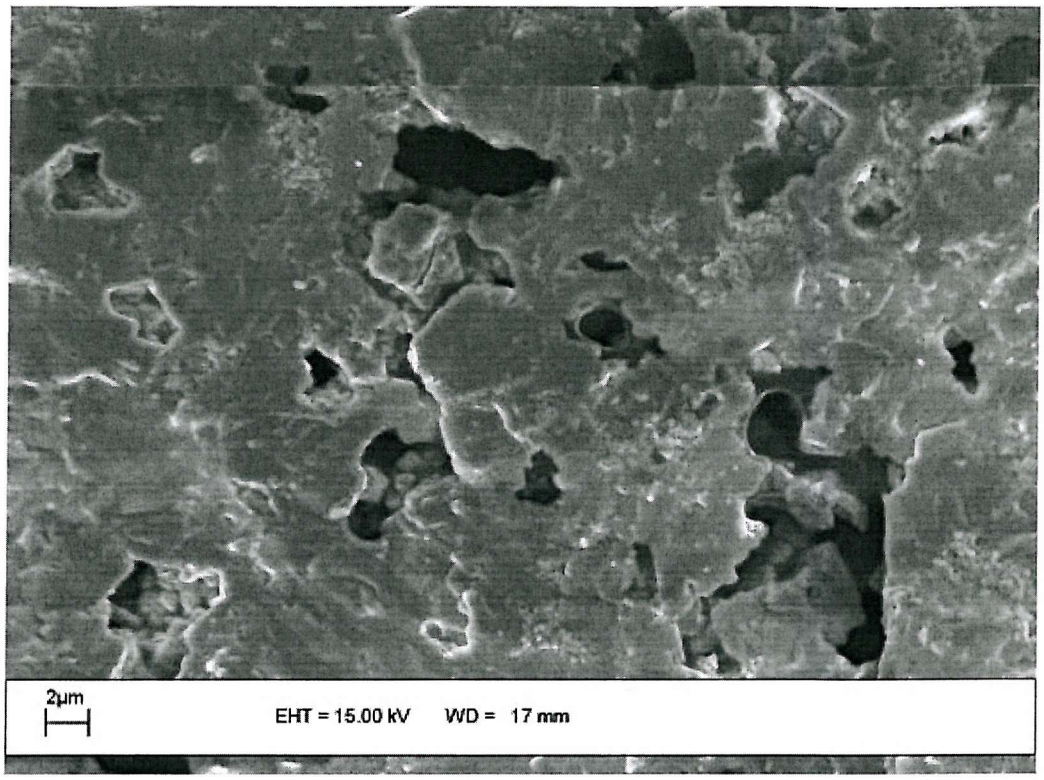

Figure 8.4: SEM micrograph of PZT layer fired using the RNT1000 profile.

The level of sintering with the EG2928 glass compares well to that seen in section 7.11.2 with CF7575. It can clearly be seen that the level of sintering increases with the firing temperature.

8.2.4 Discussion of results

The results obtained in figure 8.1 show that there is a significant increase in measured $d_{33,f}$ value when the firing temperature is increased. There is an approximately 30% increase in $d_{33,f}$ value between the Dupont60 and RNT1000 profile. The SEM micrographs show the level of sintering is comparable to that seen with CF7575 using the Dupont60 firing profile. Figure 8.4 shows a significant increase in sintering of the glass binder when the RNT1000 profile is used. This increase in piezoelectric activity and sintering would suggest that the increased firing temperature results in a greater bond between the PZT and glass. In addition, the results suggest that the stoichiometry of the PZT layer is changing and is closer to the intended optimum for PZT-5H.

The PZT layer fired using the RNT750 furnace profile showed a reasonable level of sintering. The PZT layer exhibited a higher level of adhesion than films produced with 750PK following the scratch and tape tests, described in section 3.2.6. However, the measured $d_{33,f}$ values are lower than those obtained using the Dupont60 furnace profile.

8.2.5 Conclusions

The optimum firing process is the RNT1000 furnace profile, it provides a 30% increase in $d_{33,f}$ values compared to the standard Dupont60 process used previously. This increase is considered to be due to the increased lead lost at this temperature due to evaporation, resulting in a change in the chemical composition of the thick film layer. When the PZT composition is decided upon for a commercial product, the firing process is accounted for with additional levels of material to compensate for evaporation. There is an optimum stoichiometric balance between the Lead and Zirconate in the PZT composition and it is this which changes during the firing process. It is believed that the RNT1000 firing profile brings the thick film closer to this optimum. This can only be speculated at this stage because the information is proprietary to Morgan Electro Ceramics Ltd.

The sintering levels for the EG2928 glass have proved to be sufficient compared with CF7575. However, the measured $d_{33,f}$ values have been slightly lower than the equivalent Dupont60 fired samples from section 7.11.2. However, the results are close enough to suggest that the same improvements between the Dupont60 and RNT1000 profiles could be achieve for a paste composition containing CF7575.

8.3 Co-Firing furnace profile study

Following the firing profile study, it was decided to investigate the possibility of co-firing the PZT layer and top electrodes. The study was conducted using the three firing profiles in table 8-2. Each substrate had pre-fired bottom and

underside silver/palladium electrodes. A PZT layer using the same composition as those described in section 8.2.2 was printed and dried using the standard process. Subsequently, ESL 8836 gold electrodes were printed on the dried PZT layer and then dried using the same IR drier settings. The two dried layers were then fired in the belt furnace, one substrate for each firing profile.

8.3.1 Results

The three substrates all fired correctly. The Dupont60 and RNT1000 profiles produced fired films with good adhesion levels. However, the devices fired using the RNT750 profile exhibited very weak top electrode that could be removed with a small amount of force. All the devices were poled at 4MV/m for 30 minutes at 150°C. The $d_{33,f}$ values were measured using the PM35 piezometer with an average recorded over six samples. The results are shown in figure 8.5.

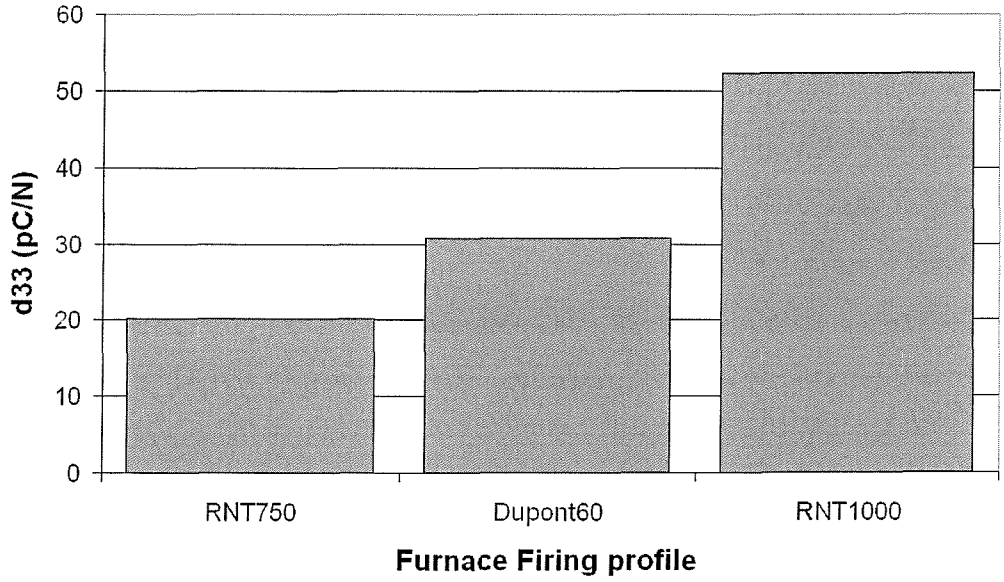

Figure 8.5: Co-firing results for different furnace profiles.

8.3.2 Discussion of results

Figure 8.5 shows that co-firing of PZT and a top electrode layer has a slightly negative effect on the $d_{33,f}$ value compared to results obtained using a polymer top electrode. However, the polymer top electrode has been shown to add 10-20pC/N per sample compared to a cermet top electrode. This suggests that the co-fired samples provide the same $d_{33,f}$ value as a normal single fired film would produce.

8.3.3 Conclusions

The results have shown that it is possible to co-fire gold electrodes using the RNT1000 furnace profile and achieve $d_{33,f}$ levels higher than those for the current Dupont60 standard furnace profile used.

This means that further devices can be fired using this new profile to further optimise the piezoelectric properties of the PZT thick-film devices. In addition, the results will allow for a reduction in the overall processing time and a reduction in the firing cycles that the PZT layer must sustain.

Comparisons with devices using a polymer top electrode suggest that in situations where a polymer is not a viable design option, co-firing is a useful alternative.

8.4 Firing profile combinations

The results of the firing profile study have shown that increasing the amount of lead evaporation can achieve higher piezoelectric activity. However, the results from the polymer electrode study in section 6.2 suggested that the use of polymer electrodes reduced the amount of lead evaporation. This reduction led to increased piezoelectric activity. Therefore, it is assumed that the optimum profile lies between the firing of the PZT layer once and twice. Firing the PZT layer twice using the Dupont60 profile, once for the PZT layer and once for the

top electrode, produces greater lead evaporation than when the PZT layer is fired just once using the RNT1000 profile.

Following these conclusions, it was important to observe the effects on piezoelectric activity when combinations of firing profiles were used. In addition, the standard devices utilise silver/palladium electrodes. Therefore, it was important to investigate the effects these have upon the firing profile study.

8.4.1 Experimental plan

The experimental plan considers the effects of combining the Dupont60 and RNT1000 furnace profiles for the PZT and top electrode layer. The experimental plan and substrate labelling is shown in table 8-3.

Substrate label	PZT layer firing profile	Silver/Palladium top electrode firing profile
d6d6	Dupont60	Dupont60
thd6	RNT1000	Dupont60
d6th	Dupont60	RNT1000
thth	RNT1000	RNT1000

Table 8-3: Firing profile combinations

A set of four substrates were printed with bottom and underside silver/palladium electrodes fired using the Dupont60 profile. Subsequently, the optimum thick-film paste formulation, using CF7575 for the glass, was printed, dried and fired using the standard process. Once fired, a silver/palladium top electrode was printed, dried and fired on the fired PZT layer using the standard process.

8.4.2 Results

The four substrates were fired in the sequences shown in table 8-3. The devices were then poled with a 4MV/m field at 150°C for 30minutes. The $d_{33,f}$ values

were measured using the PM35 piezometer with an average recorded over 6 devices. The measured results are shown in figure 8.6.

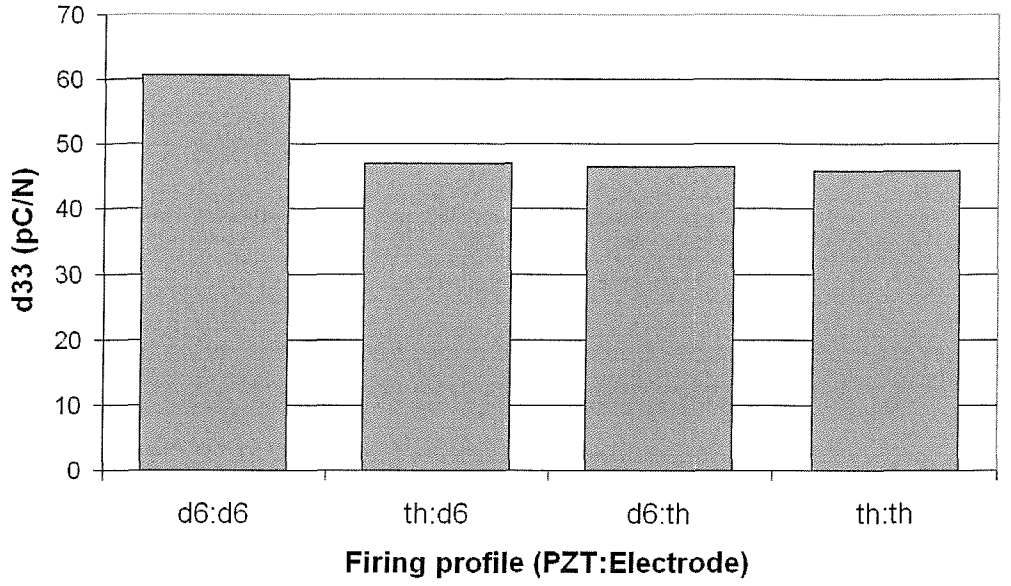

Figure 8.6: Firing profile combination results.

In addition to the results in figure 8.6 it was observed that the changes in PZT thickness for each of the firing profiles were significant, these are shown in table 8-4.

Device Batch	Average thickness
d6d6	78μm
thd6	63μm
d6th	61μm
thth	51μm

Table 8-4: PZT thickness per batch

8.4.3 Discussion of results

The results show that firing the PZT layer with the RNT1000 profile, either twice or in combination with the Dupont60 profile, reduces the piezoelectric activity of the material. The reasons for this reduction could be the increased

lead evaporation changing the stoichiometry of the PZT layer beyond the optimum Lead/Zirconate ratio for PZT-5H. In addition, it is possible that the higher temperatures are causing further electrode migration into the device and therefore reducing the effectiveness of the poling process. However, there were no problems observed during the poling process compared to those with two Dupont60 firings so this is unlikely to be the case.

The results from table 8-4 show that the PZT layer thickness changes for each of the profile combinations. This result shows that the higher temperatures have an effect on the densification of the film. This shrinkage is due to a greater amount of material burn off during the firing process and improved glass sintering forming a tighter bonding matrix.

8.4.4 Conclusions

The results have shown that if the RNT1000 profile is used to fire the PZT layer then it will be necessary to use either a polymer top electrode or a co-fired top electrode. This removes the need for the PZT layer to sustain another firing cycle which will reduce the piezoelectric activity of the film. The result confirms the hypothesis that the piezoelectric activity is at an optimum between a single and double firing at Dupont60. Thus, the RNT1000 profile provides sufficient lead evaporation and film density to achieve higher piezoelectric activity compared to two firings at Dupont60.

There is an approximate 22% reduction in $d_{33,f}$ when the RNT1000 profile is used twice or in conjunction with the Dupont60 profile. There is also a 15μm reduction in film thickness when the RNT1000 profile is used.

The results confirm that the electrode material is a critical part of the fabrication process. Therefore, to achieve the optimum piezoelectric activity for a chosen application it is essential to match the electrode material with the desired process.

8.5 Co-firing with a silver/palladium top electrode

Following the co-firing with gold electrodes it was important to conduct the same study with silver/palladium electrodes. The optimised PZT paste using CF7575 glass was mixed and printed on to a pre-fired silver/palladium bottom electrode and then dried in the IR drier. A silver/palladium top electrode was subsequently printed and dried on top of the dried PZT layer using the standard process. Once dried, the substrate was cleaved in half. The two halves of the substrate were subsequently fired using the Dupont60 and RNT1000 profiles.

8.5.1 Results and Conclusion

Both substrate halves failed to co-fire correctly. The silver/palladium top electrode peeled away from the PZT layer around the edges. The remainder of the electrode can easily be removed from the PZT layer with minimal force.

This study shows that silver/palladium is not suitable for co-firing using these firing profiles. The peeling is due to thermal coefficient of expansion mismatching between the PZT layer and electrode layer. This mismatch means the silver/palladium layer contracts faster than the PZT layer and the electrode layer comes away.

8.6 Poling parameter optimisation

The poling field investigation in section 6.4.1 showed that increasing the applied poling field will increase the measured $d_{33,f}$ of the PZT film. Building on this work, a study of the effects of poling time and temperature on the $d_{33,f}$ coefficient was conducted. A device from the 4:1poly batch, described in section 7.11, was chosen to be used for all the poling experiments. The device consisted of silver/palladium bottom electrode, silver polymer top electrode and the optimised PZT paste layer.

It is believed that the longer poling time allows the electric dipoles within the PZT layer greater time in which to align with the poling field. In addition, it is believed that an increase in temperature will provide more energy to the PZT layer to allow the dipoles to realign more easily.

8.6.1 Poling time study

The aim of this study is to observe the effects of poling temperature on the $d_{33,f}$ value. The selected device was de-poled to begin with and then poled over a range of times between 3 minutes and 24 hours. The device was de-poled by placing it on a hot plate for 4 minutes at 200°C. The de-poling procedure was conducted between each stage of the study. Subsequent measurements of the $d_{33,f}$ value were made after each poling cycle.

The poling field was maintained at 4MV/m for each stage of the study, with a poling temperature of 150°C. The poling field was maintained for a set time, once this time had elapsed the device would be cooled for 5 minutes. The cooling was performed with the aid of a fan to reduce the temperature to approximately 80°C. The poling field was maintained throughout this cooling period. The device would then be removed from the hot plate and the $d_{33,f}$ coefficient was measured using the PM35 piezometer along with a reference sample to ensure consistency. The $d_{33,f}$ value was recorded over an average of five measurements, the results are shown in figure 8.7 below.

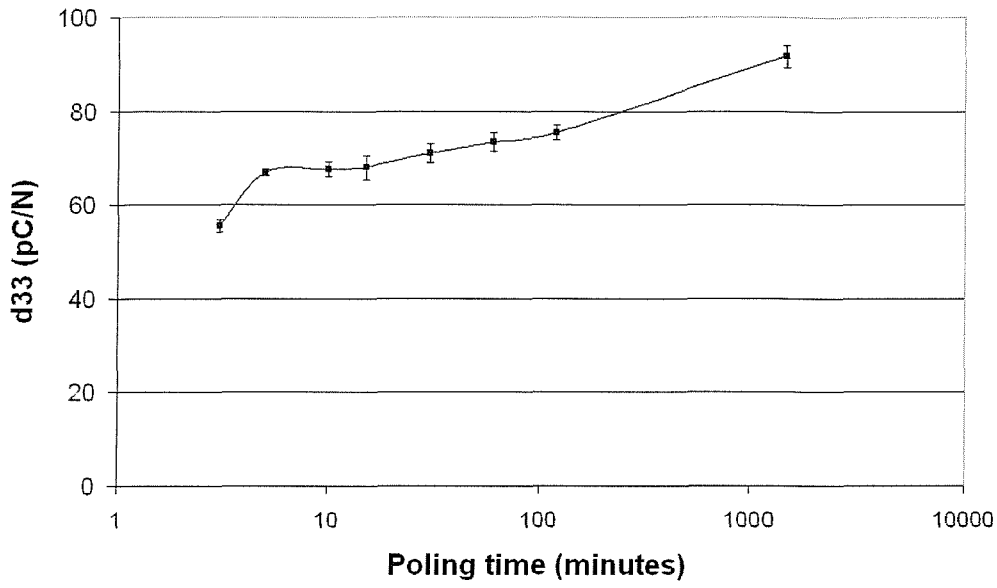

Figure 8.7: Poling time study, 4MV/m applied at 150°C.

8.6.2 Discussion of results

The poling time study has shown increasing the poling time will increase the piezoelectric activity of the material. Figure 8.7 shows that the difference between 5 minutes and 2 hours poling time is not as significant as the difference between 3 minutes and 5 minutes. The standard poling process used throughout this thesis uses a poling time of 30 minutes. The results of this study show that there is only a slight reduction, ~6%, in the piezoelectric properties if a 5 minute poling time is used. Therefore, it was decided that the next stage of the poling study would use a 5 minute poling time to obtain the final results more swiftly.

8.6.3 Poling temperature study

The aim of this stage of the study is to observe the effect of poling temperature on the piezoelectric activity of the device. A range of temperatures from 50°C to 250°C were investigated. As before, the device was de-poled and then poled with each temperature in sequence.

The results from section 8.6.2 showed that a 5 minute poling time would be a more efficient use of time. Therefore, the 4MV/m poling field was applied to the device for 5 minutes and maintained for a further 5 minutes whilst a fan cooled the device as described previously. The $d_{33,f}$ coefficient of the device was measured using the PM35 piezometer along with a reference sample for consistency. The $d_{33,f}$ value was recorded as an average from five readings, the results are shown in figure 8.8.

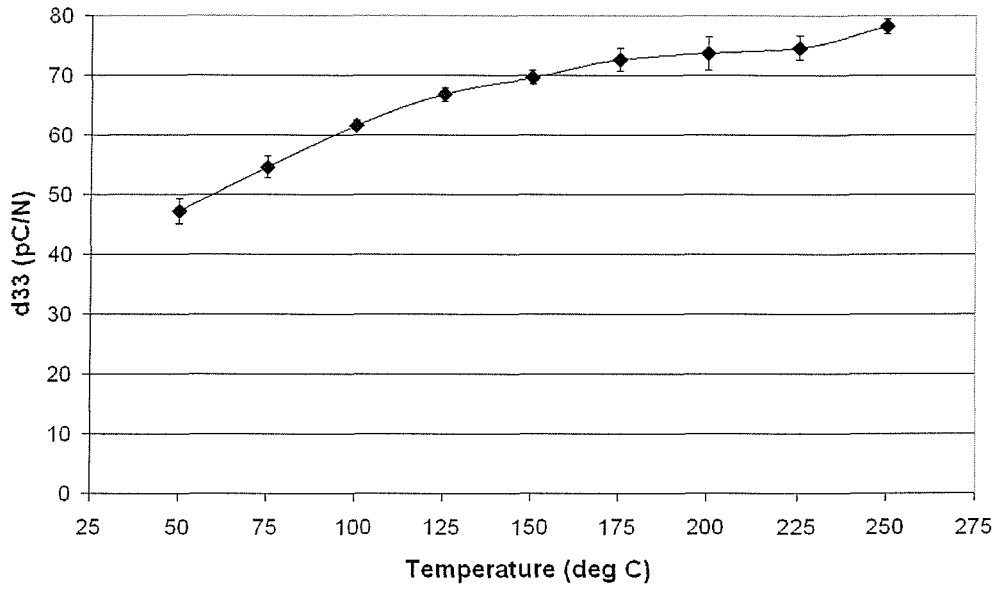

Figure 8.8: Poling temperature study, 4MV/m applied for 5 minutes.

8.6.4 Discussion of results

The results from figure 8.8 show that there is a steady increase in piezoelectric response as the poling temperature is increased. The $d_{33,f}$ value begins to remain consistent beyond 175-200°C. Beyond 250°C the solder and wires attached to the device began to melt and the poling process was made more difficult above this point. The results confirm that an increase in poling temperature leads to an increase in piezoelectric activity for the film.

8.6.5 Combination of poling time and temperature

For a commercial process, the optimum poling parameters must produce the highest piezoelectric responses in the shortest times. This study has shown that the longer a material is poled, and the higher the poling temperature, the greater the piezoelectric response from the device. Following this work, a compromise between time and temperature was studied to achieve the same results as the current process of 30 minutes at 150°C.

It is essential to develop a poling process that is practical and can be sustained by the existing devices. The results from section 8.6.4 showed that beyond 250°C the devices were difficult to pole. Therefore, a poling temperature of 225°C was selected to reduce the potential deterioration in the electrodes connection and electrode material of the device.

The poling time study was repeated between 3 minutes and 1 hour at 225°C using a poling field of 4MV/m. At each stage, the average $d_{33,f}$ value was recorded using the PM35 piezometer. The results are shown in figure 8.9. Figure 8.9 also contains the original poling time results from section 8.6.1.

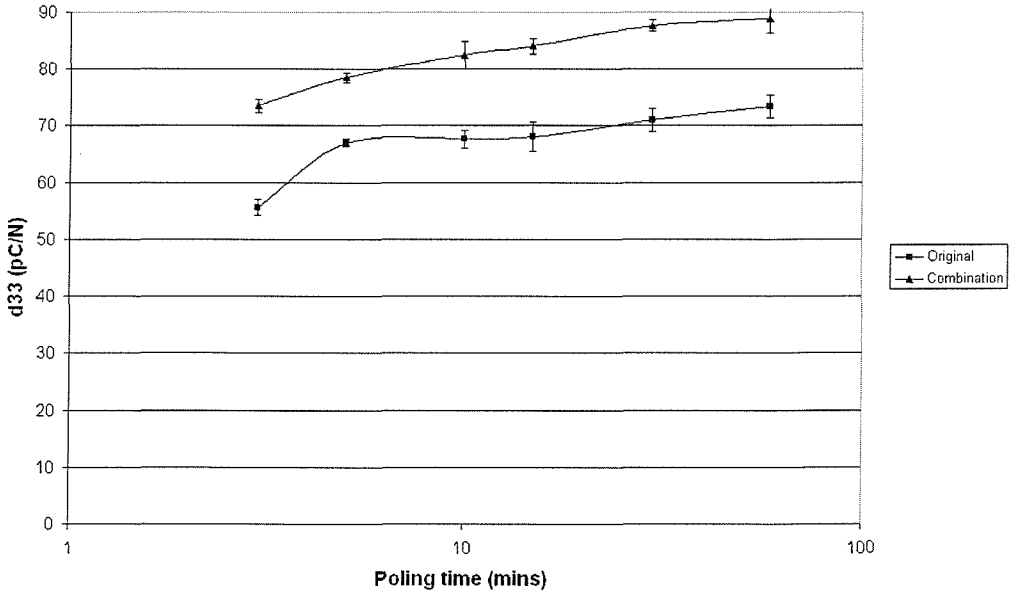

Figure 8.9: Optimum combination of poling time and temperature.

8.6.6 Discussion of results

Figure 8.9 shows that the increased poling temperature has generated an increase in measured $d_{33,f}$ value at each point in the poling time studied. This follows both sets of results from figure 8.7 and 8.8 and confirms the hypothesis that the piezoelectric activity in the film is optimised when the highest poling temperature and longest poling time are used.

8.6.7 Conclusions

The combination of 225°C poling temperature and 5 minutes poling time provide a balance between an optimum $d_{33,f}$ value and a reduction in the poling time. The standard poling parameters using a poling time of 30 minutes at a temperature of 150°C produced a $d_{33,f}$ value of 77pC/N. The combination of a 5 minute poling time with a poling temperature of 225°C produces a $d_{33,f}$ value of 78.5pC/N.

The reduced poling time produces similar $d_{33,f}$ values using a poling time that is more suitable for a high volume commercial process. Therefore, subsequent poling processes will use these new values, unless otherwise stated.

8.7 Optimum PZT thick-film paste formulation

Following the results from the previous sections the final paste formulation and firing profile was decided. A paste composition of 18wt.% attritor3, 72wt.% ball and 10wt.% CF7575 powder produces the optimum level of piezoelectric activity.

To further optimise the piezoelectric activity a gold bottom electrode was used for the final devices. This removes any possibility of silver migration into the PZT layer during the firing process.

8.7.1 Processing

A standard substrate was screen-printed with ESL 8836 gold cermet bottom electrodes and subsequently fired using the RNT1000 furnace profile. The optimum thick-film PZT paste was printed and dried on the substrate using the standard printing process. For comparative purposes, one half of the substrate was fired using the Dupont60 furnace profile with the other half fired using the RNT1000 furnace profile. Once fired, a silver polymer top electrode was printed and dried using the standard process described in section 6.2.1.

8.7.2 Results

Once fired, the devices were poled with an applied field of 4MV/m at 225°C for 5 minutes. However, the poling temperature was reduced to 200°C because the solder was melting and burning off sections of the polymer electrode. The $d_{33,f}$ values were measured using the PM35 piezometer with an average $d_{33,f}$ value recorded over six samples. The results are shown in figure 8.10 below.

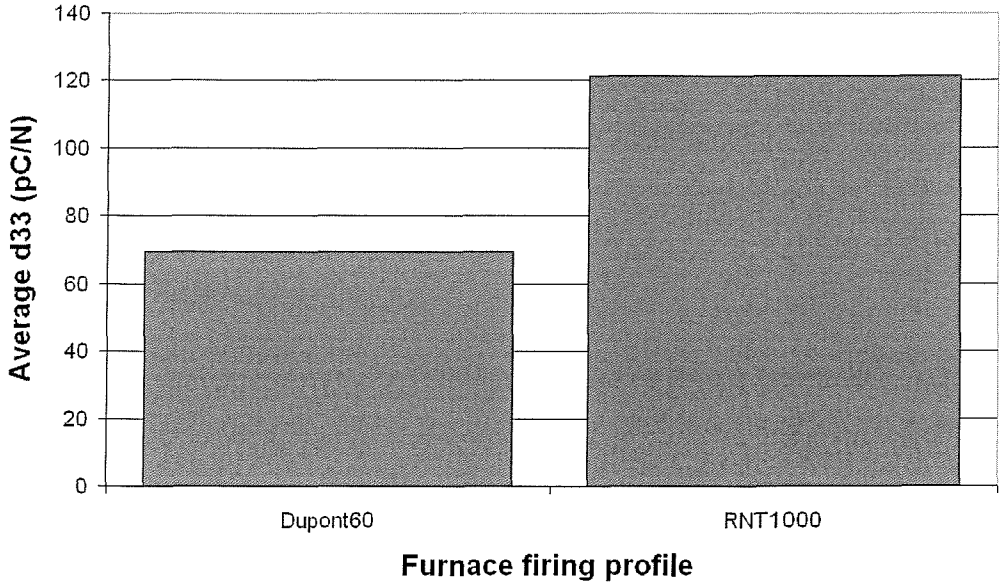

Figure 8.10: Average $d_{33,f}$ values for optimum PZT paste

A device was removed from the substrate fired using the RNT1000 profile for viewing with the SEM. The SEM micrograph shown in figure 8.11 is a cross sectional view of the fired PZT layer.

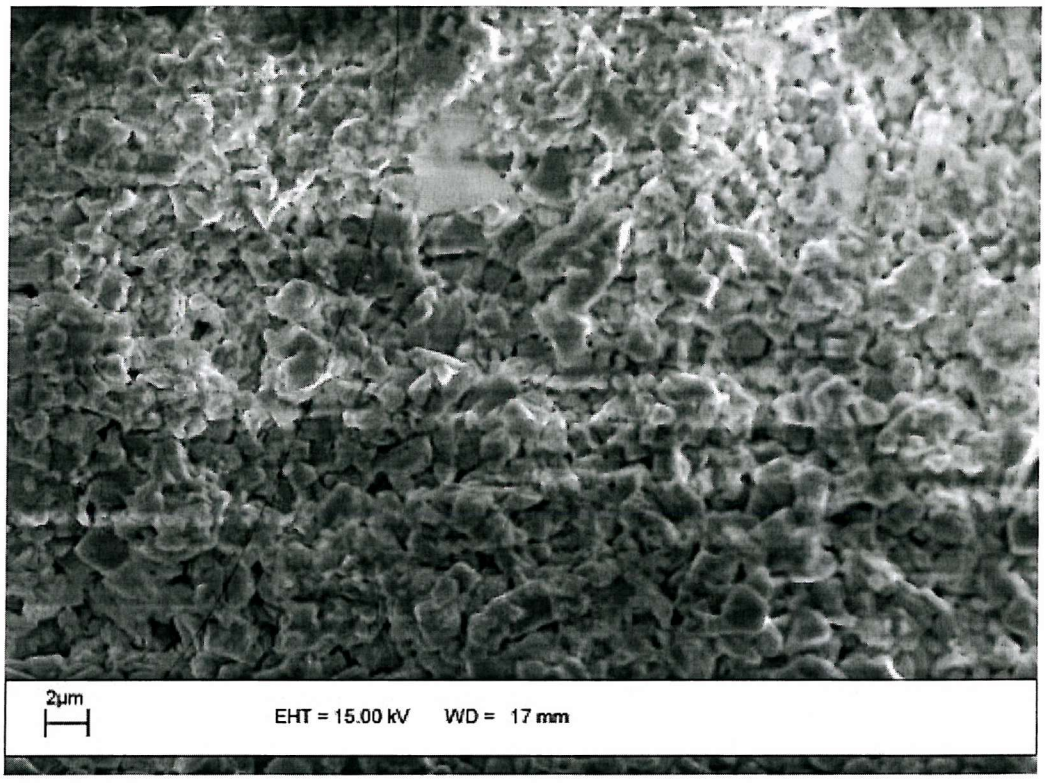

Figure 8.11: SEM micrograph of the optimised PZT paste fired using the RNT1000 profile.

8.7.3 Discussion of results and conclusions

Figure 8.10 shows that using the RNT1000 firing profile and the optimised poling process increases the measured $d_{33,f}$ value to 121pC/N. The device was re-poled using the poling time of 30minutes used previously but maintaining the increased poling temperature of 200°C. This produced a measured $d_{33,f}$ value of 131pC/N.

The SEM micrograph shown in Figure 8.11 shows the density of the film has increased compared to the same material fired using the Dupont60 profile. The increased density is due to the higher temperature generating a greater amount of sintering between the glass and the PZT and potentially between the smaller PZT particles within the film.

8.8 Conclusions

The results from this chapter have seen further optimisations of the PZT-5H thick-film. A final paste composition of 18wt.% attritor3, 72wt.% ball and 10wt.% CF7575 powder has been shown to produce the optimum piezoelectric response.

Alternative firing profile and electrode combinations have been evaluated. The highest piezoelectric activity was generated when a firing profile with a peak temperature of 1000°C was used. This higher firing temperature has increased the density of the fired film and therefore increased the mechanical coupling of the film. When combined with an ESL 8836 gold bottom electrode and an ESL-1110-S silver polymer top electrode a $d_{33,f}$ value of 121pC/N was achieved. Part of this process included a study of the poling time and poling temperature. A reduction in poling time to 5 minutes with a temperature of 225°C was shown to produce the same piezoelectric activity as the previously used 30 minutes at 150°C.

The work in this chapter has contributed towards an increase in measured $d_{33,f}$ value from 18.5pC/N for the original thick-film PZT-5H paste to a current highest measured $d_{33,f}$ value of 131pC/N.

9 Material properties of the optimised paste formulation

9.1 Introduction

This chapter covers the details of a range of measurements taken to provide the characteristic values for the optimised PZT films from chapter 8. Where necessary a description of each of the theory, measurement techniques and experiments is given. The chapter ends with a table of material properties for the optimum PZT paste.

9.2 Main characteristics of the thick-film

A number of the main characteristic properties of the thick-film devices can be determined from simple experimental, measurement and arithmetic means [5]. A sample from the optimum devices (10% CF7575, 18% att3 PZT, 72% ball PZT, gold bottom electrode, rnt1000 firing profile, silver polymer top electrode) was used to obtain characteristics for the final PZT film.

The piezoelectric constant, $d_{33,f}$, capacitance, C and the dielectric loss tangent, tan δ were measured using the Take-Control PM35 piezometer. The thickness of the PZT layer was measured using a Mitutoyo293 micrometer, the electrode area was determined from the screen design. Using these measurements it was possible to calculate the dielectric constant, K^T_{33}, the permittivity of the film, ε^T_{33}, and the piezoelectric voltage constant, g_{33}, using equations 9.1, 9.2 and 9.3 respectively, where ε_0 is the permittivity of free space, 8.85×10^{-12} F/m.

$$K^T_{33} = \frac{\text{PZTthickness} \bullet C}{\text{electrode area} \bullet \varepsilon_0} \qquad [9.1]$$

$$\varepsilon^T_{33} = K^T_{33} \bullet \varepsilon_0 \qquad [9.2]$$

$$g_{33} = \frac{d_{33}}{\varepsilon^T_{33}} \qquad [9.3]$$

The measured and calculated values are given in table 9-1 below.

Description	Symbol	Value
Piezoelectric strain constant	d_{33}	131pC/N
Piezoelectric voltage constant	g_{33}	$14.05x10^{-3}$Vm/N
PZT thickness	t	72μm
Electrode area	A	$81x10^{-6}m^2$
Capacitance	C	8973pF
Dielectric loss	Tan δ	0.0104
Relative dielectric constant	K^T_{33}	901.2
Relative permittivity	ε^T_{33}	$7.97x10^{-9}$F/m

Table 9-1: Characteristics of the optimum PZT thick-film material.

In addition to these basic characteristics it is possible to obtain the Young's modulus and the film density. However, these measurements require a more complex approach.

9.3 Young's modulus

It is possible to determine the Young's modulus of a PZT film printed on a substrate using a number of complex stress and strain formulae [98]. However, these formulae require a number of variables that are difficult to obtain and complex mathematics to solve. A simple method to determine the Young's modulus was devised by N. Grabham at the University of Southampton [99]. The technique uses a combination of experimental and computer modelling. ANSYS finite-element (FE) modelling tool is used to determine the expected deflection of a bimorph beam and the results are compared to the practically measured deflection of the beam under load. Using this data, the Young's modulus of the film can be determined by an iteration process.

9.3.1 Experimental method

Six PZT strips were printed on to a 96% alumina substrate scored to provide six bimorph strips with a pattern shown in figure 9.1.

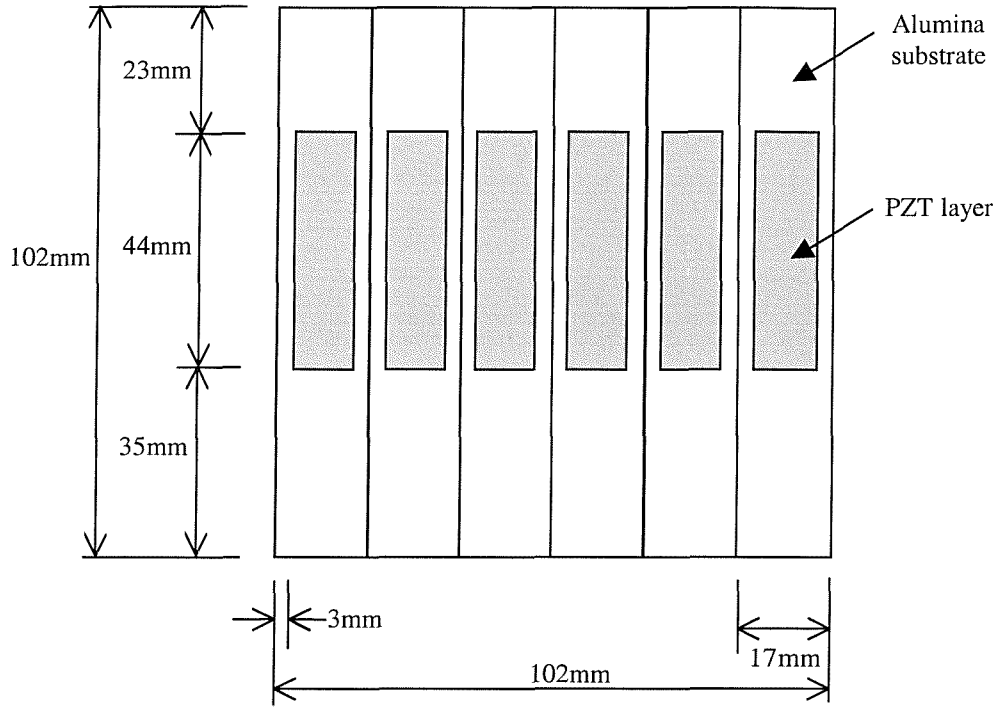

Figure 9.1: Substrate layout for Young's Modulus experiment

The optimum PZT paste was printed directly on to the substrate using the standard screen-printing process. The substrate was dried using an IR drier, 140°C for 10 minutes, then fired on a belt furnace using the rnt1000 furnace profile. Once fired, the 6 individual strips were separated and numbered for measuring.

The test equipment used to measure the Young's modulus consisted of: a clamp to hold the substrate in place, a micrometer to measure the deflection of the beam, and a piece of wire suspending the weights from the substrate to induce the deflection. This equipment is shown in figure 9.2.

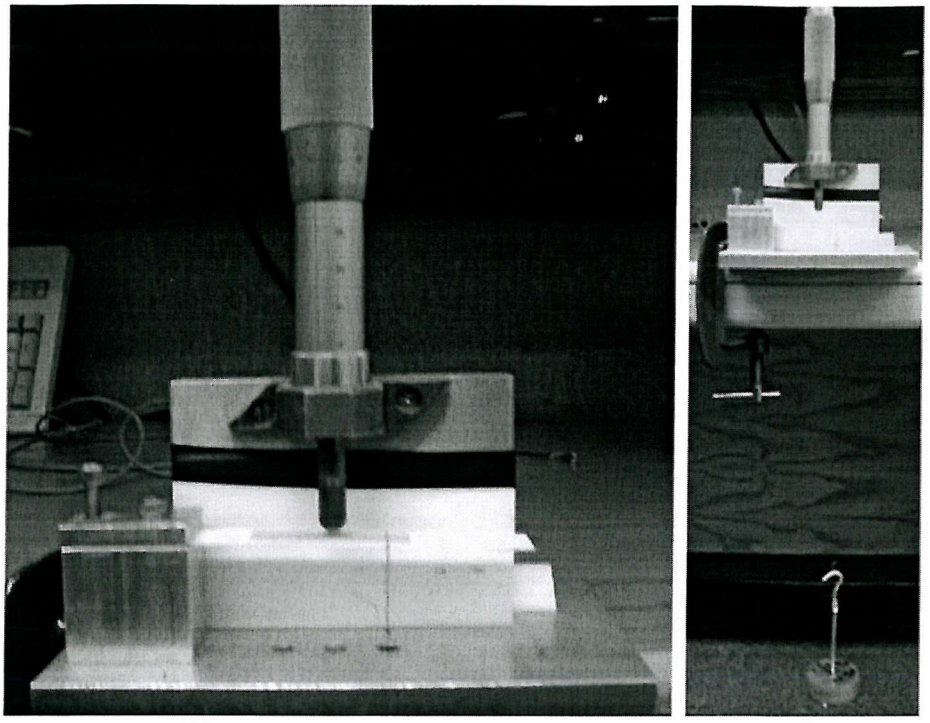

Figure 9.2: Photograph of test equipment used to measure deflection of a bimorph.

A set of 50g and 100g masses were used to apply a weight to the clamped substrate, each mass was measured using a Precisa 1600C electronic weighing scales to determine the exact mass and it is these values that were used in subsequent graphs and equations. The deflection of the beam was measured with steps of 50g mass applied, the results were recorded and plotted using the Excel spreadsheet software and a line of best fit was determined from these values.

The equation of the line was set with an intercept at zero rather than a straight line of best fit because there would be zero deflection with zero mass applied. In addition to the 6 bimorphs, an alumina strip from a substrate of the same thickness was also measured to determine the Young's modulus of the substrate.

It was discovered that the initial readings showed greater deflection than expected when the PZT layer was applied compared to the bare substrate. The reason for this discrepancy was that the substrate sample had not been fired. The firing process has a stiffening effect on the substrate. Therefore, the bare substrate sample was fired using the same rnt1000 furnace profile as the PZT

samples and measured again. Figure 9.3 and 9.4 give an example of these measurement plots for the alumina strip and for sample 1 respectively.

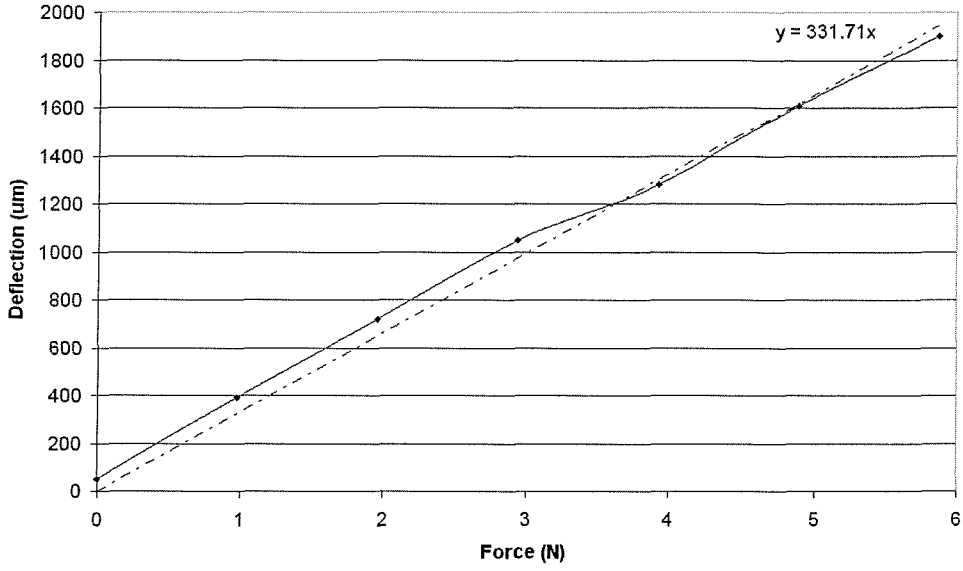

Figure 9.3: Substrate fired with no PZT using rnt1000 firing profile.

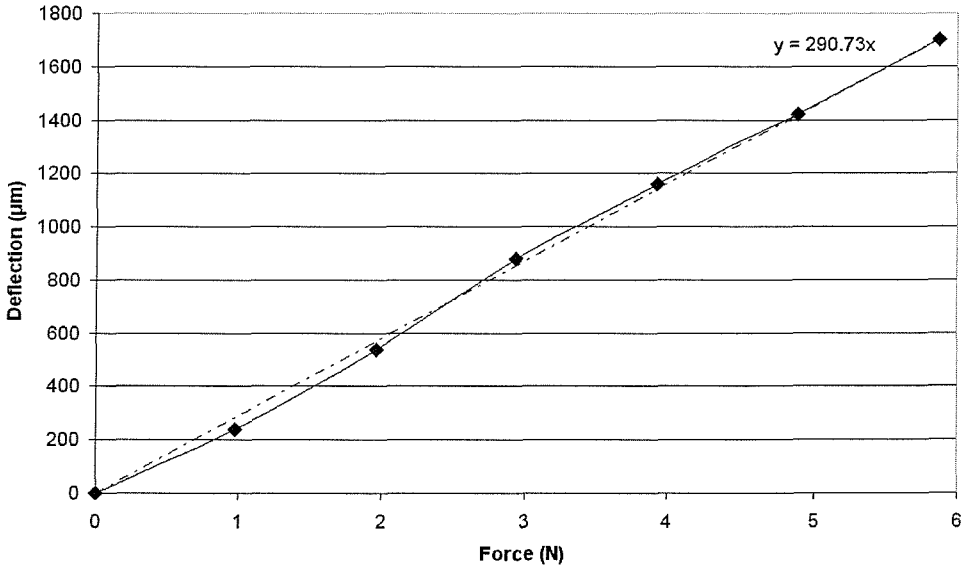

Figure 9.4: Sample 1, PZT bimorph fired using rnt1000 furnace profile.

Figures 9.3 and 9.4 show that when a PZT layer is printed on to the substrate the deflection of the beam is reduced as expected. Using these plots in conjunction with the line of best fit, the expected deflection for a 4N applied load was calculated. The average deflection from the 6 samples was subsequently used to determine the desired deflection for the ANSYS FE model.

In addition, it was necessary to determine the density of the film. The mass of the substrate with and without the PZT layer was measured after firing. Using the volume of each film an average density for the PZT layer and the substrate were calculated, ρ_{ave}=4810kg/m^3 and the ρ_{sub}=4480kg/m^3 respectively. The value for Poisson's ratio is σ=0.31 as a standard value for piezoceramics [11] and σ=0.25 for the alumina substrate [78].

9.3.2 Modelling the bimorph

The ANSYS model, given in appendix C, is a representation of the bimorph beam. The model has the load applied in an equivalent position to that of the actual sample and produces a set of deflection results for a given applied load.

The values calculated above for the Poisson's ratio and density were entered into the ANSYS model. The PZT layer was removed from the model leaving only the substrate. A value for the Young's modulus was subsequently entered and iterated until the model deflection corresponded with that of the measured deflection shown in figure 9.3. The Young's modulus was determined to be 254Gpa for the substrate. The PZT layer was then reintroduced to the model. The Young's modulus for the substrate was added to the model. Following the same iterative process, the Young's modulus of the PZT layer was determined to be 26Gpa.

9.4 Curie Temperature

A piezoceramic experiences a crystallographic phase change as it is heated beyond a specific temperature known as the Curie temperature. This phase change results in a loss of piezoelectric activity in the material. Therefore, it is important to determine the Curie temperature of a material to establish the working temperature range of a material. This is discussed in more detail in section 2.2.1.

9.4.1 Experimental method and results

The same optimised PZT device from section 9.2 was used for this experiment. The device was re-poled at 200°C for 5 minutes with an applied field of 4MV/m. The PM35 piezometer was used to measure the $d_{33,f}$ value and a hotplate was then used to heat the device over a range of temperatures from 50-240°C. The device was heated for 4 minutes at each stage to ensure sufficient transfer of heat through the PZT layer. The $d_{33,f}$ value was measured at each temperature step and an average value was recorded. These values are shown in figure 9.5 below.

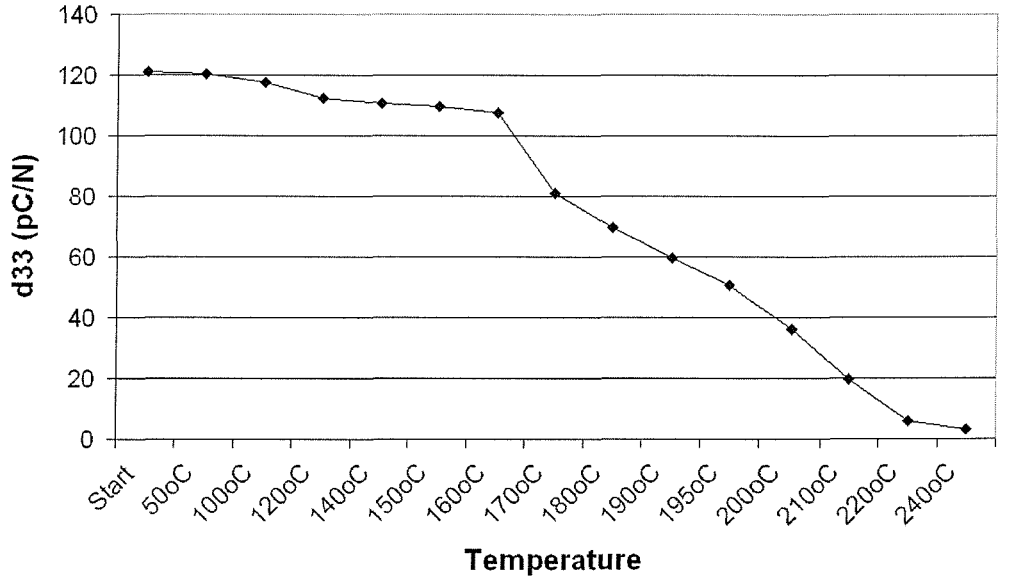

Figure 9.5: Graph of $d_{33,f}$ versus temperature for optimised PZT-5H thick-film paste.

The results in figure 9.5 show a decline in the piezoelectric activity as the temperature is increased. The measured $d_{33,f}$ values are fairly consistent until 160-190°C where they begin to decline at a faster rate. It was therefore judged that the Curie temperature for the optimised PZT thick-film is similar to the bulk PZT-5H equivalent. An alternative method may obtain a definite Curie temperature by observing the changes in dielectric constant. The dielectric constant should reach a maximum at the thermal transition point.

9.5 Characteristic values for the final thick-film

Table 9-2 is an extension of table 9-1 which includes the data from the Young's modulus and Curie temperature experiments. The characteristic values for the optimised PZT-5H thick-film are compared to an equivalent pressed bulk PZT-5H device [11].

Description	Symbol	Value: Bulk 5H	Value: Thick-film 5H
Piezoelectric strain constant	$d_{33}/d_{33,f}$	593pC/N	131pC/N
Piezoelectric voltage constant	g_{33}	$19.7x10^{-3}$Vm/N	$14.05x10^{-3}$Vm/N
PZT thickness	t	220μm	72μm
Electrode area	A	$72.4x10^{-6}m^2$	$81x10^{-6}m^2$
Capacitance	C	9902pF	8973pF
Dielectric loss	Tan δ	0.025	0.0104
Relative dielectric constant	K^T_{33}	3400	901.2
Relative permittivity	ε^T_{33}	$30.1x10^{-9}$F/m	$7.97x10^{-9}$F/m
Young's Modulus	Y	71GPa	26GPa
Density	ρ	7450kg/m^3	4810kg/m^3
Curie Temperature	T_c	195°C	195°C

Table 9-2: Final value comparison between bulk and thick-film 5H

9.6 Discussion of results

The results from table 9-2 show that the values for the screen-printed thick-film PZT-5H material compares favourably with the equivalent pressed bulk material. The most significant result that this research is concerned with is the piezoelectric strain constant, $d_{33,f}$. Table 9-2 shows a significant difference between the high bulk value of 593pC/N and the maximum thick-film value of 131pC/N. However, the clamping investigation showed that the value of the bulk device was significantly reduced, with the results in section 4.3 giving a clamped $d_{33,f}$ of 138pC/N [100]. This result was achieved with a bulk device clamped to an alumina substrate thus indicating that the thick-film is as effective as the bulk equivalent. The dielectric loss, permittivity and dielectric constant compare well to the bulk material and show that the thick-film material is well suited to the high frequency applications where these characteristics are important [5].

The structural characteristics defined by the Young's modulus and density show that the thick-film material still has a significant area of improvement which could lead to further improvements in $d_{33,f}$. This is confirmed by the results on film densification, chapter 7 [101], which showed a significant improvement in piezoelectric activity with improved film density. The PZT layer is anisotropic and therefore the Young's modulus of the film changes depending on the measurement and poling direction. The Young's modulus measured is equivalent to the open circuit elastic constant in the 1 axis, Y^{D}_{11}, because there were no electrodes on the samples and only the lateral strain was measured.

The Curie temperature experiment showed that the Curie temperature for the optimised thick-film was only slightly below that of the bulk PZT-5H, 170°C and 195°C respectively. This reduction in Curie temperature is believed to be because of the changes in the stoichiometry of the film during the firing process. Because the stoichiometry is not the same as the bulk device, characteristics such as the Curie temperature and piezoelectric activity will be different.

9.7 Conclusions

The series of optimisations throughout this thesis have resulted in a significant increase in measured $d_{33,f}$ for the thick-film PZT-5H material. The subsequent measuring of the final characteristic values for the thick-film samples has also compared favourably with the existing bulk equivalent. A maximum $d_{33,f}$ of 131pC/N has been measured for a thick-film device poled for 30 minutes at 200°C which compares well to the value of a bulk device clamped to the same alumina substrate with a d_{33} of 138pC/N. This value represents a significant improvement from the original 18.5pC/N measured for thick-film PZT-5H devices and shows the significant steps made in improving the $d_{33,f}$ value during the course of this research. The values in table 9-2 also indicate the applications that the thick-film devices would be suited to, the low dielectric loss, permittivity and dielectric constant are advantageous in many high frequency applications such as ultrasonic sensors and transmitters and the low frequency area of sonar applications. The density and young's modulus of the films are reduced compared to the bulk material. These characteristics could be improved by further research into improving the density of the film both in terms of particle distribution and bonding matrix but also compression of the film during drying and firing. Improvements in the density of the film should lead to improvements in the rigidity of the films and also the mechanical properties improving a number of the film characteristics such as $d_{33,f}$. The value of 26GPa for the thick-film Young's modulus compares favourably with the value of 18GPa obtained by P. Glynne-Jones in previous experiments with the original non-optimised PZT-5H thick-films [102].

10 Multilayer structures using thick-film PZT

10.1 Introduction

This chapter describes the application of the optimised paste and processing conditions to a multi-layer structural approach to further improve upon the measured thick-film $d_{33,f}$. The methodology involved in the screen design and the experimental plan and process are covered with a discussion of the results achieved and their implications for future applications.

10.2 Principle of multi-layer structures

The effective d_{33} of a device can be increased in many ways; one of the simplest methods is to increase the number of PZT layers in the device. If these layers are connected in series, the charge or strain generated by each layer is summated, thus increasing the overall measured $d_{33,f}$ of the device. This multi-layer structure does not increase the piezoelectric activity of the PZT layer itself so the d_{33} values are quoted as the multilayer d_{33}, $d_{33,m}$.

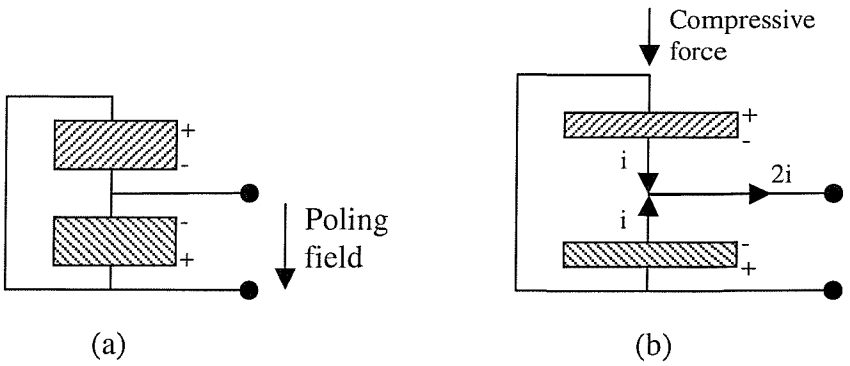

Figure 10.1: Two PZT layer structure (a) applying a poling field (b) applying a compressive force.

Figure 10.1 shows the concept of the multilayer structure for two PZT layers. Figure 10.1(a) shows the polarity and electrode connection for the two PZT layers when a poling field is applied. Figure 10.1(b) shows the charge generated

from each of the PZT layers as they are compressed. The poling direction determines the polarity of the charge generated, which is then summated at the output to produce twice the charge of a single PZT layer.

Work by Zhu et al. has shown that the introduction of multiple piezoelectric actuators in a series structure increases the effective piezoelectric properties of the test structure [103,104]. Figure 10.2(a) shows the principle of the multi-layer structure with the arrangement of electrode and piezoelectric layers. Figure 10.2(b) shows the direction of the poling field on each piezoelectric layer and the direction of the driving electric field, both of which result in a summation effect of the piezoelectric properties.

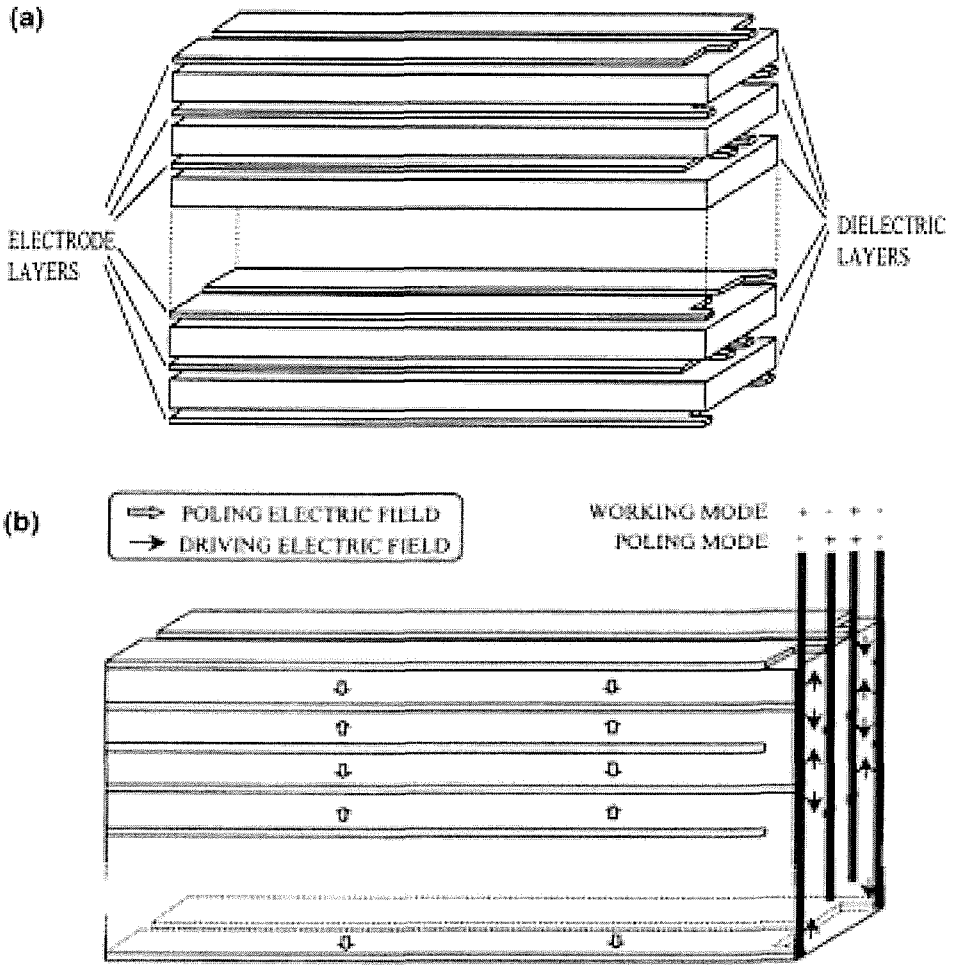

Figure 10.2: Schematic illustration for the multilayer structure: (a) orientation of electrode and piezoelectric layers (b) poling and driving field orientations. Zhu et al. [103].

The study by Zhu was conducted using 95% PZT with a 5% lead oxide binder and an alumina substrate. An organic film was deposited on the substrate using the spin coating method. Spin coating involves a fixed amount of organic vehicle deposited on to the substrate, which is then spun. This spinning uses the centrifugal effect to disperse the film across the substrate producing a homogeneous film. The electrode layers were printed using an ESL 6955 silver palladium paste. Each of the electrode and PZT layers were printed and dried in turn. Samples with 7-15 piezoelectric layers were fabricated. The organic film on the substrate was burnt off at 575°C which allowed for the multilayer structure to be released from the substrate. These structures were then fired at a peak temperature of 1130°C. The fired electrode and piezoelectric layers were 5 and 30-60 microns respectively. The overall thickness was dependant on the amount of layers and the thickness of the PZT layers. The authors do not report which PZT material they use or the bulk properties. However, they do report that the piezoelectric values obtained with the multilayer structure are still lower than those of the bulk.

This work has shown that it is possible to print and co-fire multiple stacks of piezoelectric and conductive layers. The paper is unclear on the piezoelectric benefits provided by the number of layers except to say that the structure provides a significant displacement that is suitable for future hard drive actuator applications. Therefore, it is beneficial to investigate a multilayer structure using the optimised paste to observe if the summation theory is correct.

10.3 Screen design

When developing a multilayer structure using thick-film technology, it is important to consider that as each layer is added, the step distance between the substrate and other layers is increased. This increase in step size can lead to difficulties in printing further layers as the printer requires more print strokes in order to fully cover the intended design. This leads to a build up of material on the raised parts of the design or a smearing of the overall pattern. To avoid these

problems, it is important to reduce the step size between each layer that is covered by the print pass.

The design for this multilayer study is based on the standard prototype design covered in section 3.3.3. Because the design has relatively large electrode areas the print step problem has a reduced effect. However, the screen was designed to have a progressive step between the second, third and subsequent electrode layers. This was possible with the introduction of an additional tab in line with where the next electrode will be; this is also included on the PZT layer. Figure 10.3 shows the screen design for each layer; only one device is shown but the actual screens provide 16 evenly distributed devices per substrate. The PZT layer is 10mm by 6mm.

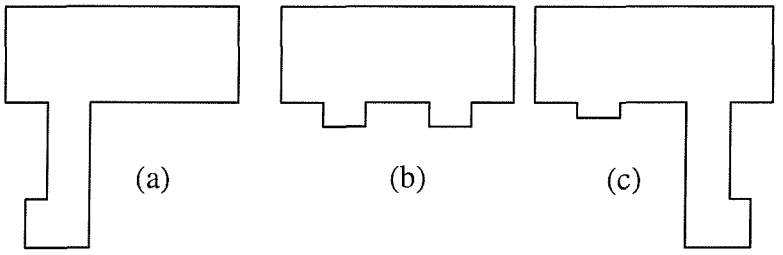

Figure 10.3: Multilayer screen design, (a) bottom electrode (b) PZT layer (c) top electrode.

Figure 10.3 illustrates the use of tabs to reduce the step size for the PZT layer and the top electrode thus aiding the printing process. In addition, the design in figure 10.3(a) was printed on the underside of the substrate to make the design compatible with the PM35 piezometer as discussed in section 3.3.3.

10.4 Experimental procedure

A related issue with multilayer structures is that the piezoelectric properties of certain PZT material types decline for each firing cycle the PZT layer endures. The proposed multilayer structure will involve the PZT layer being fired 2-6 times depending on the number of layers. Therefore, the bottom PZT layers could suffer from depreciation in $d_{33,f}$ value compared to the top layers. This

would reduce the overall $d_{33,m}$ of the structure. This problem was noted in the firing profile experiment, see section 8.4, when an electrode layer was fired on top of the fired PZT layer, causing a reduction over its co-fired counterpart. Following on from this work, it was decided to attempt a number of co-fired layers to determine if they would fire effectively together and if it resulted in an increase in $d_{33,m}$.

The PZT paste used was '4:1 Att3:Ball' milled powder with 10% CF7575 lead borosilicate glass, chapter 7 [101]. An ESL 8836 gold cermet paste was used for all the electrode layers.

The experimental plan is shown in table 10-1 below. Each substrate followed a sequence of print and fire stages to obtain a full range of possible results. One substrate had a single layer printed and co-fired on it to use as a reference sample. With the exception of substrate 5, all the substrates had a fired bottom electrode before the rest of the structure was printed.

Substrate	Bottom Electrode	Fire	PZT1 Elect2	Fire	PZT2 Elect3	Fire	PZT3 Elect4	Fire
1	Yes	Yes	Yes	Yes	N/A	N/A	N/A	N/A
2	Yes	Yes	Yes	Yes	Yes	Yes	N/A	N/A
3	Yes	Yes	Yes	Yes	Yes	Yes*	Yes	Yes
4	Yes	Yes	Yes	No	Yes	No	Yes	Yes
5	Yes	No	Yes	No	Yes	No	Yes	Yes
Notes:	*One row of substrate was removed for measurements							

Table 10-1: Printing and firing sequences for each substrate.

At each stage, a combination of PZT layer and electrode layer were printed and dried respectively using the standard process described in this thesis. Subsequently, depending on the substrate number, the printed layers were then co-fired or another combination of electrode and PZT layers printed on top. The RNT1000 furnace profile, table 8-2, was used for each firing step given in table

10-1. The printing, drying and firing stages were all conducted inside the University of Southampton clean room facility.

Once fired, the devices were removed from the clean room for poling. The multilayer structure makes it difficult to determine the thickness of the individual PZT layers. To obtain the required poling field it was assumed that each PZT layer would be the same thickness and each electrode layer was as thick as the underside electrode. Therefore, the PZT thickness was obtained by measuring the overall thickness of the structure then subtracting the thickness of the electrode layers and dividing the result by the number of PZT layers. To reduce the chances of dielectric breakdown a poling field of 4MV/m was chosen for all the devices. This voltage was maintained for 5minutes with the substrate placed on a hotplate at 200°C. After 5 minutes the substrate was cooled to room temperature. The $d_{33,m}$ for each device was then measured using the PM35 piezometer.

10.5 Results

Figure 10.4 shows the results obtained from the experiments in table 10-1. The results show that the increased number of layers does increase the $d_{33,m}$ dramatically, from 77pC/N for one layer to 325pC/N for three layers.

A number of devices were lost during the poling processes due to problems attaching solder to the gold electrodes. The increased thickness of the gold electrodes and the gold layer being burnt off due to the high soldering temperatures made it difficult to attach the wires necessary for poling.

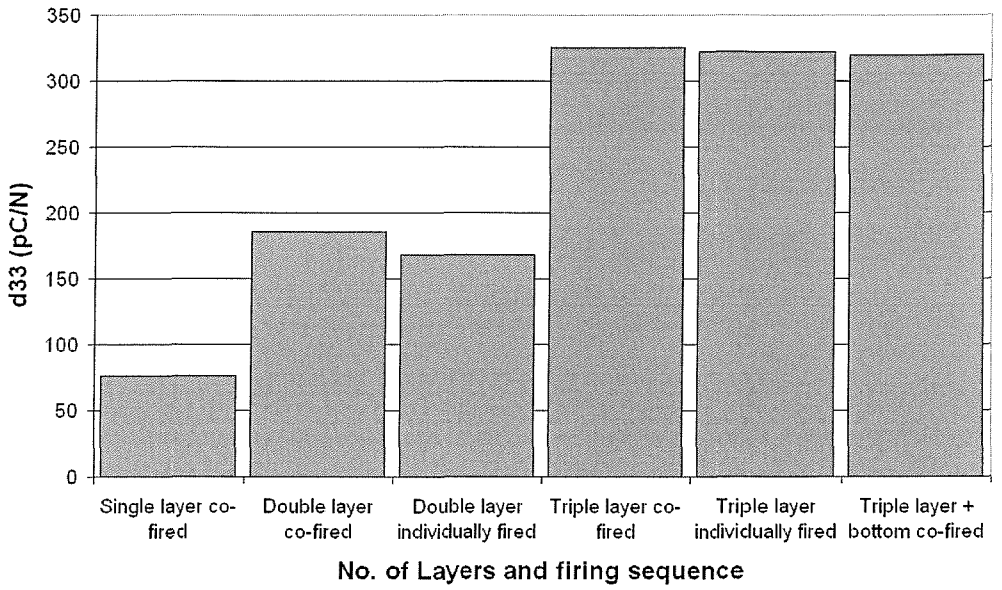

Figure 10.4: Multilayer structure experimental results

The results from figure 10.4 show that there is no direct linear relationship between the number of layers and the improvement in $d_{33,m}$, for three PZT layers it would indicate a slightly exponential increase. However, the results do show that each additional PZT layer does add to the overall piezoelectric properties of the structure.

Figure 10.4 also shows that there is little difference between the individually fired and the co-fired devices when three PZT layers are used compared to two layers. This difference could be due to a reduced print quality for the co-fired devices compared to the individually fired devices. This would imply that any advantage gained from co-firing was negated by the quality of the print. This result shows that there is no significant detrimental effect in co-firing 3 PZT layers.

10.6 Discussion of results

The results have shown that it is possible to co-fire three PZT layers and their associated electrodes. However, the structure itself could be improved as the print quality was not as high as a single layer device. The increased structural

height became harder to print beyond two PZT layers due to the step down to the substrate surface. The print quality could be improved with development of an optimised screen design for a multilayer structure.

Problems with soldering wires to the electrode pads were evident with the increase in layer numbers, this could be improved with the introduction of a final silver/palladium electrode layer to cover the pads as this material is better suited to the soldering process.

The results have shown a non-linear increase between one and three PZT layers. It is clear from the co-firing results that this non-linear result is not due to a reduction in firing cycles for the top and bottom PZT layers. It is proposed that the increase in $d_{33,m}$ is due to a reduction in the clamping effects of the substrate as the structure thickness increases.

Finally, the results show that there is no significant reduction in performance when co-firing compared to individually firing the PZT layers. In addition, with three PZT layers a slight improvement was observed with the co-fired devices compared to the individually fired devices.

10.7 Conclusions

The investigation has confirmed that the introduction of additional stacked devices connected in series will increase the overall $d_{33,m}$ of the device. The optimum $d_{33,m}$ achieved by co-firing 3 PZT layers was 325pC/N and is the highest $d_{33,m}$ achieved so far in this research. This work shows that dramatic improvements in piezoelectric responses can be achieved in applications where a multilayer structure is a viable design option. Multilayer structures provide improvements for both sensor and actuator applications.

Future work could consider the development of a technique based on the double-paste printing technique developed by Moilanen et al. [105]. This technique works on the principle of dividing the printer blade in two and rotating the

substrate so that each print prints a different material layer, it is described in more detail in section 2.4.1.

The results have shown that there are no significant problems when co-firing gold electrodes and the optimised PZT paste. Therefore, combining the co-firing with a faster printing method, such as the double-paste printing technique, will be considered valuable in reducing the printing time and costs of any future applications.

The study by Zhu used silver palladium electrodes but the results in section 8.5 show that this is not possible with the ESL 9633B silver palladium. Further work should consider an alternative silver palladium material. This could solve the problem of soldering to the electrode layers and further reduce the costs involved in potential applications.

11 Applications

11.1 Introduction

This section describes a number of applications that the optimised PZT paste is currently being developed or used in. The author has prepared the screen-printable pastes in all the applications and has performed the printing where stated. These applications are: the triple beam resonator [106], ultrasonic sensors for fluid separation [107], a multi-degree of freedom ultrasonic motor [67] and a robotic manipulator [108]. Benefits provided by the optimised PZT paste for each of these applications are discussed in detail.

11.2 Triple beam resonator

Resonant structures have a wide range of applications in the sensors field [109]. Typically a resonant sensor has a structure that has a vibrating element that will change frequency as a function of the desired measurement characteristic, usually physical or chemical. The first application the optimised paste contributed to was a triple beam resonator developed by Yan et al. [106]. The screen-printed PZT film is used as both the actuator and sensor element of the device. The resonator structure consists of three parallel beams joined at each end to a decoupling zone which is then connected to the rest of the structure. Figure 11.1 shows the plan view of a single device.

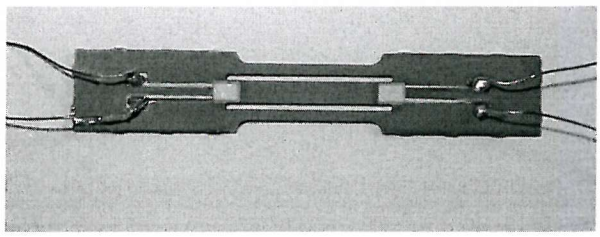

Figure 11.1: Photograph of the metallic resonator.

The structure was designed using finite element (FE) modelling and from this the modal behaviour of the structure was determined. Using this information the maximum stress points in the structure were also obtained and the PZT elements placed at these points along the central beam. The position of the PZT elements maximises the mechanical coupling between the PZT and the structure thus maximising both the actuation and detection signals. The PZT element at one end drives the beam into the correct mode whilst the PZT element on the opposite end detects the vibrations. The structure has three fundamental vibration modes. In mode 1, the three beams oscillate in phase. In mode 2 the central beam remains still whilst the outer beams oscillate 180° out of phase with respect to each other. In mode 3, the central beam oscillates in anti-phase with the outer beams. The third mode gives the optimum operating conditions for the device to work as a resonate sensor, giving it the highest Q factor. The high Q factor is a result of the design being dynamically balanced; the two outer beams moving in the opposite direction balance the stress exerted on the ends of the structure by the central beam.

The main structure of the resonator was fabricated from a 0.5mm thick 430S17 stainless steel wafer using photochemical etching. A dielectric layer was printed on the substrate at the predefined sensing and actuating points to electrically isolate the PZT devices from the steel. On top of this dielectric layer, a gold bottom electrode, PZT layer and gold top electrode were then deposited, dried and fired. The PZT elements were subsequently poled with a 4MV/m electric field and then tested in air with a spectrum analyser.

The third resonance mode was determined to be 6.2kHz and was shown to give the highest amplitude response and a measured Q factor of 3100. This Q factor is a vast improvement on similar work developed by Fabula et al with a silicon triple beam resonator recording a Q factor of 400 [110].

Whilst a high $d_{33,f}$ value is not as essential in this application it still allows for a better signal response and actuation of the resonant structure. The high $d_{33,f}$ of the optimised paste will allow for simpler electronic circuitry in the feedback

control loop necessary for the device to operate. In addition, it has been shown that early attempts to use polymer based PZT films have provided high enough signals to be detected by the spectrum analyser but not sufficient for use in a practical system, improving the $d_{33,f}$ of these using the techniques described in this thesis will allow for further development of the sensor design. The good frequency qualities, low dielectric loss, of the film and the repeatability between samples improve the overall quality of this application.

11.3 Ultrasonic micro-fluidic separator

Work by Harris et al. [107,111] has been concerned with using ultrasonic waves to provide continuous flow filtration on a micro fluidic scale. The aim of this work is to fabricate devices that are compatible with existing micro-fluidic systems and to potentially replace the existing centrifugal separation techniques for analysing on a micro-fluidic scale.

Ultrasonic standing waves can be used to generate small forces on particles within the acoustic field. This has the effect of moving the particles to a particular point within a fluid where the pressure forms a node or anti-node. This effect can be used to aggregate particles in a specific area, manipulate and fractionate particular particles or to separate groups of particles from the carrying fluid. A simple design for a micro-fluidic separator is shown in figure 11.2.

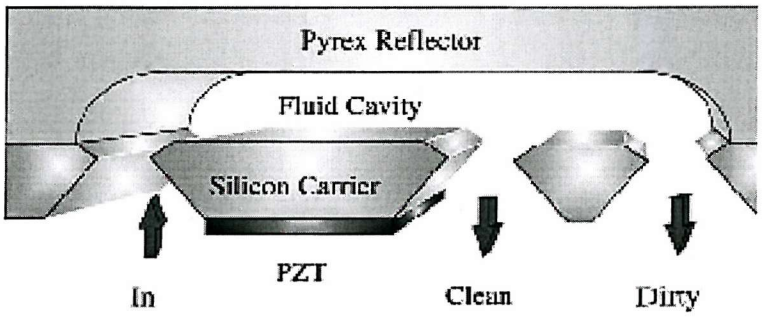

Figure 11.2: Schematic cross-section of a micro-fluidic separator. Harris et al [107].

The device, shown in figure 11.2, is fabricated from Pyrex and silicon wafers. The wafers are etched and then anodically bonded, a bulk PZT plate was then bonded to the device using an epoxy resin. Mathematical modelling was used to obtain the dimension sizes for the device. The dimensions are essential to produce the desired resonant responses required to set up the standing waves within the fluid cavity. In order for the fluid to pass in and out of the device an aluminium manifold was constructed and the seal between them was achieved using a custom silicon O-ring, the full device is shown in figure 11.3.

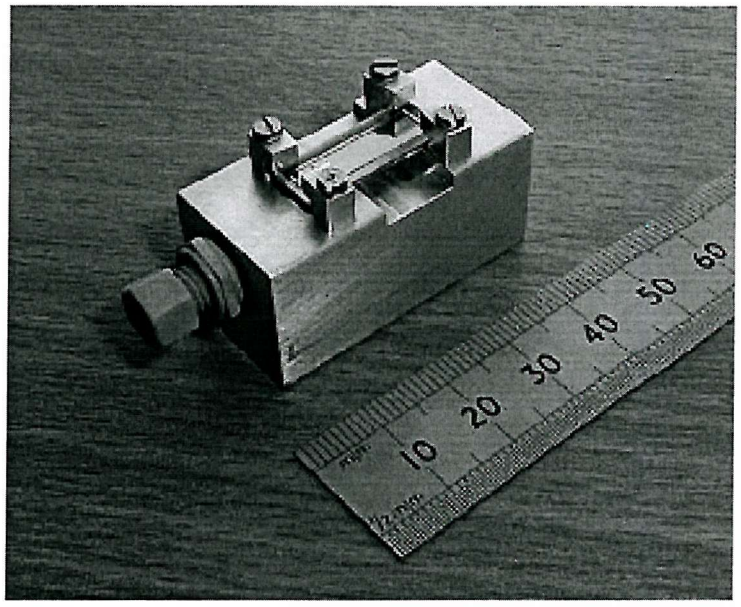

Figure 11.3: The micro-fluidic separator on the aluminium manifold, Harris et al [107].

Four frequency modes for the device were identified: mode 1 provides a pressure maximum at the silicon boundary, mode 2 provides a pressure maximum at the reflector boundary and modes 3 and 4 provide a pressure maximum at the centre of the cavity. The prototype was constructed and then tested with the use of a yeast solution to identify the particle movements. A Frequency Synthesiser was used to drive the device via a fixed gain RF amplifier (50dB). The frequency was adjusted to obtain the correct resonant modes within the chamber. The modes were measured at 1.71, 2.27, 3.44 and 4.1MHz for modes 1 to 4 respectively. The results showed that each mode performed correctly and the yeast particles could be seen to be separated from the fluid flow.

The design currently uses a bulk PZT plate bonded to the structure but current work is investigated the integration of screen-printed PZT layers. The optimised PZT paste developed in this thesis will provide an essential component to the new designs, enabling an integration of silicon microfabrication processes for integrated electronics and the use of screen-printed layers to reduce costs and fabrication time. The high $d_{33,f}$ values will reduce the complexity of the required electronics and provide greater control of the fluid flow due to the improved signal strength. Current work is developing a double-layered screen-printed structure on a silicon substrate using the co-firing technique described in section 8.3. The author of this thesis has printed the electrode and PZT layers successful and the devices are awaiting testing.

11.4 High temperature powders

The successful optimisation of the PZT-5H paste has lead to interest in the improvement of other powder types. Certain applications, such as the oil and gas applications discussed in section 11.5, require piezoelectric layers with a higher Curie temperature. A detailed study is beyond the scope of this thesis but it was decided to investigate a set of high temperature powders to assess their potential for further use and compare the results to the optimised 5H-type films.

11.4.1 High temperature paste compositions

An initial study of four high temperature powders has been conducted. The powders used were Morgan Electro Ceramics PZT-5A, Sigma Aldrich Ltd. Lithium Tantalate ($LiTaO_3$), Lithium Niobate ($LiNbO_3$) and Ferro Electronic Materials Bismuth Titanate ($Bi_4Ti_3O_{12}$). The powders were identified as piezoelectric materials that are used in high temperature applications in their bulk form and could be developed as thick-film materials. The piezoelectric values for each of these materials are given in table 11-1 [89,112], the values for PZT-5H are included for comparison.

Material	Piezoelectric Coefficients		Relative Permittivity		Curie temperature
	d_{33} (pC/N)	d_{31} (pC/N)	ε_{11} (F/m)	ε_{33} (F/m)	(°C)
$LiNbO_3$	8	-1	84	30	1210
$LiTaO_3$	8	-2	51	45	660
$Bi_4Ti_3O_{12}$	190	-78	1450	1700	650
PZT-5A	374	-171	1730	1700	365
PZT-5H	593	-274	-	3400	195

Table 11-1: Bulk properties of high temperature piezoelectric materials [89,112].

Each powder was mixed with 10% by weight of CF7575 Lead Borosilicate glass binder. These powders were mixed into a thixotropic paste using an appropriate quantity of ESL-400 pine oil solvent. Table 11-2 shows the composition of each paste.

Powder type	Label	Percentage powder	Percentage 7575 glass	ESL-400 Solvent (ml)
PZT-5A	5A	90%	10%	4.8ml
$LiNbO_3$	LN	90%	10%	5.9ml
$LiTaO_3$	LT	90%	10%	6ml
$Bi_4Ti_3O_{12}$	BT	90%	10%	3.3ml

Table 11-2: High temperature paste compositions.

11.4.2 Paste processing

The pastes were mixed in the percentages shown in table 11-2, these were then passed through a triple roll mill to disperse the powders evenly throughout the paste. The screen designs used were the standard designs used throughout this thesis. An ESL-8836 Gold cermet conductor was printed on to a 96% Alumina substrate as a bottom electrode and fired on a belt furnace with a 1000°C peak

profile. Once fired, the piezoelectric pastes were printed in two layers upon the bottom electrodes. Each paste layer was dried in a DEK 1209 IR drier at 140°C for 10 minutes then fired with the same 1000°C furnace profile. Once the piezoelectric layer was fired a gold top electrode was printed, dried and subsequently fired using an 850°C peak profile. This lower profile for the top electrode was used to reduce the effects of continued firing on the piezoelectric layers. It is considered that prolonged exposure to high firing temperatures can have a negative effect on the stoichiometry of the material.

Each of the piezoelectric layers completed the firing process, with two substrates per paste. Elementary tests on the quality of the prints were conducted; these include the tape and scratch test described in chapter 3.3.4. All the layers gave satisfactory results except for the Lithium-Niobate samples that were damaged with only a small amount of effort during the scratch test. Despite this, the Lithium-Niobate samples were robust enough to be used in the poling and measuring process.

11.4.3 Poling procedure

The poling voltage for each material was determined by applying the voltage to one sample until dielectric breakdown occurred. The remaining samples were poled at 90% of this breakdown poling voltage thus reducing the chance of breakdown but maintaining a sufficient poling field. This meant that a different voltage was used for each sample. This was considered acceptable because the aim of the study is to determine the effect of temperature on $d_{33,f}$ not the optimum $d_{33,f}$ value. Therefore, consistency between the samples with respect to poling parameters is not so important. Table 11-3 gives the poling conditions for each material type.

Powder type	Active layer thickness (μm)	Poling temperature (°C)	Poling voltage (volts)	Poling time
5A-type PZT	95	200	280	30 minutes
Lithium-Niobate	60	200	300	24 hours
Lithium-Tantalate	155	200	250	24 hours
Bismuth-Titanate	85	200	260	30 minutes

Table 11-3: Poling conditions.

It was discovered that for the Lithium Niobate and Lithium Tantalate samples, 30 minutes poling time was not sufficient to observe piezoelectric behaviour. Therefore, they were poled for 24 hours, which was found to produce measurable levels of piezoelectric behaviour.

Testing each substrate for short circuit devices has shown that a large proportion of the PZT-5A and Lithium Tantalate samples are short-circuited. A small number of the Bismuth Titanate and the Lithium Niobate are also short-circuited. It is unclear why the 5A samples should result in so many short-circuits. The average thickness is 95μm, this is typically sufficient to prevent breakdown in thick-film device. The samples were also constructed using the two PZT layer print and dry technique therefore any voids in the film should have been filled.

11.4.4 Results

After poling, the $d_{33,f}$ coefficient of each of the samples was measured using the Take-Control PM35 Piezometer. Five readings were taken per sample and averaged across two samples per material type. These measurements were taken one month after poling to take into account the natural ageing effect associated with the poling process. The results are shown in table 11-4.

Sample Label	Piezoelectric coefficient $d_{33,f}$ (pC/N)
5A	64
LN	1.7
LT	1.5
BT	2.9

Table 11-4: Measured values of $d_{33,f}$, one month after poling.

Following these results, the temperature behaviour of the samples was determined. The remainder of this study was conducted by Dr Grabham from the University of Southampton. The samples were placed in an Elite Thermal Systems Box Furnace with a Eurotherm 2216 temperature controller and cycled up to 800°C in 50°C steps with a 30 minute dwell time at each temperature. The $d_{33,f}$ readings were recorded after each stage as before. The results for PZT-5A were significantly higher than the other materials so for clarity they are shown separately in figure 11.4. Figure 11.5 shows the results for the Lithium Niobate, Lithium Tantalate and Bismuth Titanate samples.

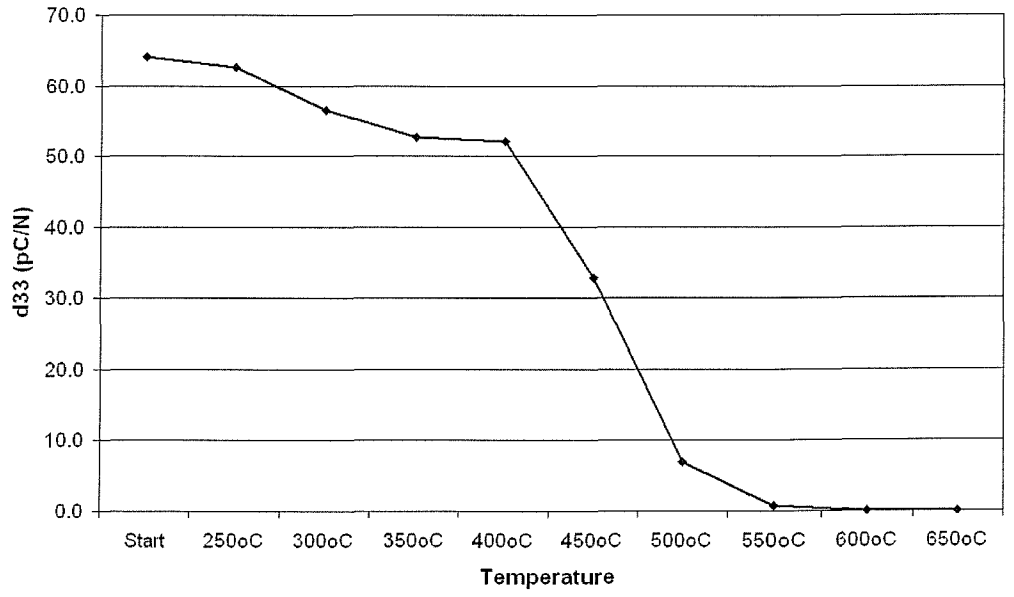

Figure 11.4: Graph showing $d_{33,f}$ versus temperature PZT-5A.

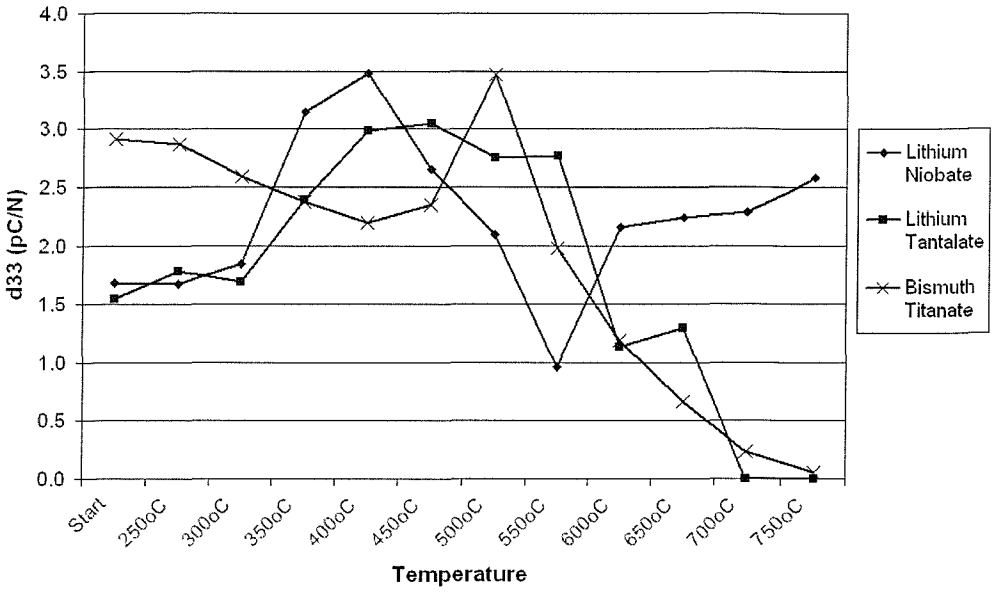

Figure 11.5: Graph showing $d_{33,f}$ versus temperature for Lithium Niobate, Lithium Tantalate and Bismuth Titanate.

11.4.5 Discussion of results and conclusion

The results confirm the four materials resistance to high temperatures with the piezoelectric behaviour only falling away as the temperature approaches the reported Curie temperatures. The results suggest the maximum practical operating temperatures of the films are 350°C, 650°C and 750°C for the PZT-5A, lithium tantalate, bismuth titanate and lithium niobate films respectively. The lithium niobate samples delaminated from the substrate at 800°C but had displayed sufficient piezoelectric activity up to that point. This delamination is thought to occur due to thermal expansion coefficient mismatching between the electrodes, piezoelectric layer and the substrate. It is likely that the mismatching is also responsible for the variation in observed $d_{33,f}$ values across the temperature range.

The low $d_{33,f}$ values seen in figure 11.4 and 11.5 compared to the bulk values given in table 11-1 are due to a combination of factors. The clamping effects due to the substrate, described in section 4.3, the dilution of the active material by the use of a glass binder, increased porosity of the thick-films compared to bulk

devices and the change of material stoichiometry due to the firing process. Further work is required to determine the degree of influence each of these factors has on the final piezoelectric properties of the films.

In conclusion, the piezoelectric activity exhibited is lower than that observed in bulk devices but could be sufficient for some applications. However, this thesis provides details of the factors that can be modified with these high temperature powders to improve the piezoelectric properties. These factors include the powder milling, powder size, glass content, firing and poling parameters. In addition, the use of multi-layer structures can be used to further enhance the practical application of these high temperature powders.

11.5 Oil and Gas extraction applications

When crude oil is extracted from the ground it is in a mixture that contains water, gas and particulates. In order for the oil to be in a suitable state for refining it must be separated from this mixture. This separation is performed inside a separator vessel that allows the mixture to settle into the various phases. The problems associated with this are that it is often very high temperature and pressure (150° and 15MPa respectively) and there are currently no instruments that identify where the phase interfaces lie. This is partly because of the environment being harsh but also because the interfaces themselves are not clear. There is a gradual separation between the phases between the emulsion of oil and water and the foam of oil and gas. Research by Hale et al. has considered the use of thick-film technology in solving this problem in cooperation with the University of Southampton [113].

The initial measurement system incorporated a column of capacitive sensors but it was discovered that this was insufficient to completely characterise the phase interfaces. Further testing indicated that ultrasound would provide the necessary additional measurement characteristics. In addition, it was discovered that prolonged exposure to the mixture resulted in the sensor being fouled with oil residues; it was therefore decided to attempt to introduce an additional high-

power ultrasonic cleaning element to the sensor design. Figure 11.6 shows the layout for the sensor design.

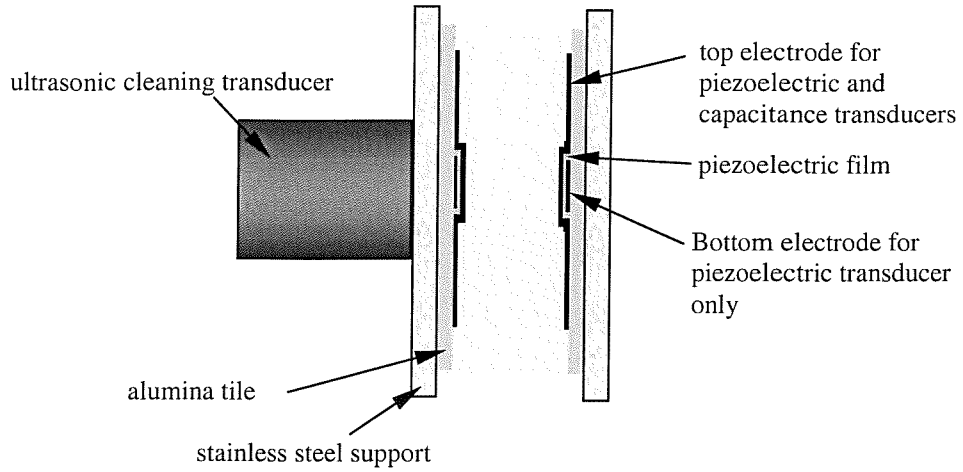

Figure 11.6: Advanced dipstick probe: schematic representation of one sensor location, Hale et al [113].

The capacitance and ultrasonic transducers are constructed using a standard thick-film screen-printing process, with gold electrodes printed on to an alumina substrate. The transducer pairs face each other across a 20mm gap through which the process fluid flows. The high-power ultrasonic transducer is used to excite the adjacent sensor tile, which then propagates the signal through the fluid to the other sensor tile. This configuration allows both tiles to be cleaned by the use of a single transducer.

Initial testing has been conducted in water at a temperature of 150°C with a pressure of 15MPa, as these closely match the most severe phase change within the separator. Because this temperature is close to the Curie temperature of the PZT-5H paste developed in this thesis, an alternative high temperature 5A paste was printed with ESL-8836 gold electrodes [114]. This was prepared in the same optimised process procedures as the 5H-type paste. The sensor measures the speed of sound through the liquid, which is then related to the volume fraction to determine the composition of the mixture. The results indicate that these materials are suitable for the design and can sustain the effects of the harsh environment. Further developments involving 5H and 5A could lead to an

integrated thick-film sensor and cleaner to remove the requirement of an external bulk transducer.

11.6 Ultrasonic motor

The ultrasonic motor designed by Aoyagi et al [67] uses a PZT actuator to induce specific resonant modes into a substrate. These resonant modes (B_{22}, B_{30} and B_{03}) are induced in different directions according to the electrode design, these modes can then be combined to vibrate the substrate. On the top side of the substrate is a ceramic column that is moved according to the applied resonant modes and rotates a ball bearing applied to the top of the column, thus allowing the ball bearing freedom of movement in all directions. The principles of this movement are shown in figure 11.7.

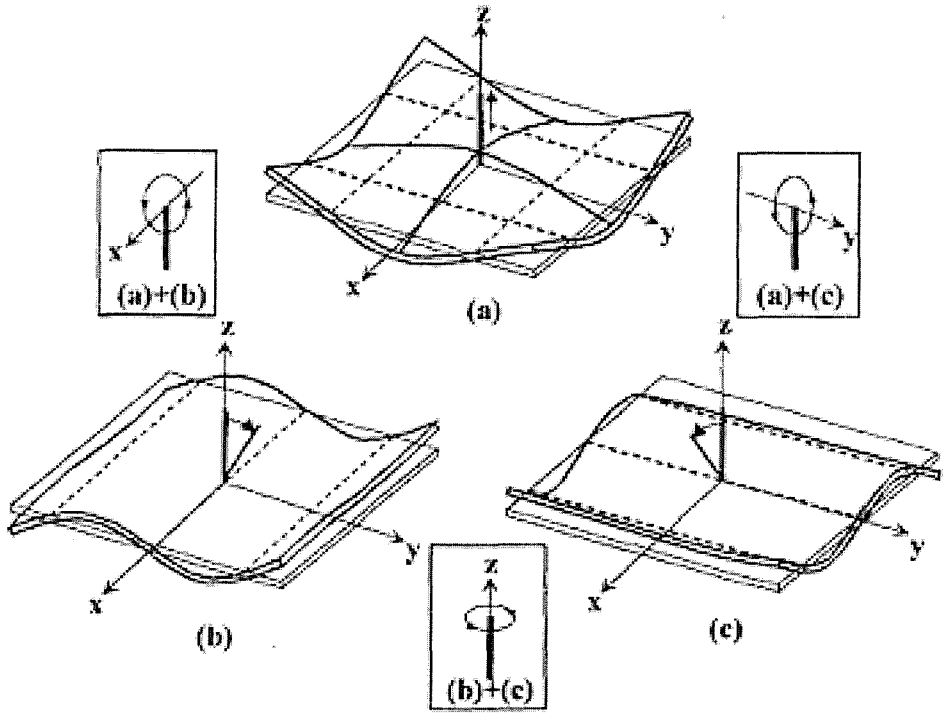

Figure 11.7: Resonant modes B_{22}, B_{30} and B_{03} respectively and their associated displacements, Aoyagi et al [67].

The motor design was successfully demonstrated, however, one of the desired improvements was the use of a ceramic collar to surround the motor. The collar has the effect of mechanically isolating the motor within its boundary, thus

allowing the motor to operate whilst held in place and potentially at any angle. In practice, when the collar was applied to the design the piezoelectric actuation was damped to the extent that the motor could no longer function correctly. Therefore, an increase in the piezoelectric properties of the PZT layer would allow for the use of the collar and thus improve the functionality of the design. The improved piezoelectric properties will allow for improved response in the B_{22} mode in particular which the paper suggests will improve the overall effectiveness of the design.

11.6.1 Finite element modelling

The operating frequencies quoted by Aoyagi do not included the influence of the PZT and electrode layers, it was therefore necessary to consider their effects when designing the control circuitry. To determine the frequency of the three resonant modes it was necessary to us the ANSYS finite element analysis software package. The model was created using a basic wire frame technique whereby the key points for the corners of the object for one layer are entered and then projected for each subsequent layer of the structure. Once all the key points are entered it is possible to create volumes for specific nodes in the design and create a complete 3-dimensional structure. The ANSYS software is a solid-modelling technique and requires that 8 key points define each volume. Because the ultrasonic motor in this case is a symmetrical design, it was possible to plot the key points for a quarter of the design and then use functions in ANSYS to mirror the nodes for the other three quarters. The PZT and electrode layers were added to the model but were left as simple circular models to reduce complexity. It was considered that the extra electrode tabs in the screen designs would have little effect on the resonant frequency of the substrate because they are small and connected with only thin strips of electrode layer.

The model was built in stages to aid in the programming process; the final model is shown in appendix C. The values for the Young's modulus, Poisson's ratio, density alumina substrate, gold electrode and PZT layer are taken from the relevant data sheets and are shown in the model. The PZT thickness and

electrode thickness were set to 60μm and 7μm respectively. These were chosen as typical thickness values for their respective screen-printed layers.

Using the dynamic view settings in ANSYS it is possible to observe the range of resonant frequencies the motor design has, from here it is possible to see the frequency at which the desired bending modes, shown in figure 11.7, occur.

The model produces modal frequencies for b_{22}, b_{30} and b_{03} of 19.13kHz, 16.74kHz and 16.74kHz respectively. This compares to the results quoted in the paper for b_{22}, b_{30} and b_{03} of 16.49kHz, 14.47kHz and 14.47kHz. The difference between the individual values in each model is very similar but the model used in this thesis has suggested higher modal frequencies. It is believed that the reason for the higher resonant frequency is that the material characteristics used in the models are slightly different.

The model provides a reasonable response. For ease of circuit design it is desired that the three modes have identical frequency, where this is not possible then they must be as close as possible. The results from the model provide an indication of the frequency that the motor controller circuit must be able to operate at and therefore aids in the circuit construction process.

11.6.2 Printing and processing the motor

The ultrasonic motor is screen printed with the same process as previously described in this thesis. The screen design for each of the material layers is shown in figure 11.8.

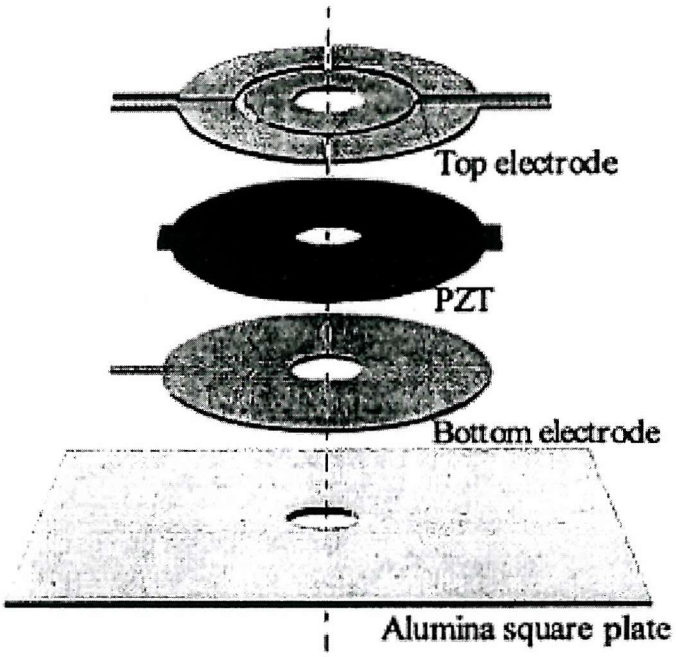

Figure 11.8: Screen design for ultrasonic motor: bottom electrode, PZT layer and top electrode respectively, Aoyagi et al [67].

The bottom electrode layer is printed using ESL 8836B gold cermet paste, fired using the rnt1000 furnace profile. Because the top electrode will use the same gold cermet paste it was decided to co-fire the PZT layer and the gold top electrode to improve the piezoelectric properties of the film. The PZT layer used the optimum '4:1 Ball:Att3' paste and was dried using the DEK 1209 IR drier at 140°C for 10 minutes. Once dried, the gold top electrode was printed on top and then subsequently dried using the same settings, the substrate was then placed on the belt furnace using the rnt1000 firing profile.

Following the results achieved in chapter 10 a multilayer approach was considered for the existing motor design. The existing screen design is easily adapted to a multilayer approach, a second PZT layer is printed on top of the existing top electrode and then the bottom electrode screen is printed on top of this. The second bottom electrode screen use is aligned with the previous bottom electrode print thus the entire structure connects the two PZT layers in series thereby creating a stacked actuator and improving the $d_{33,m}$ of the device.

Once printed and fired, the motors were poled with a 4MV/m field for 30 minutes using two power supplies in order to pole the different sections at the same time using the configuration shown in figure 11.9.

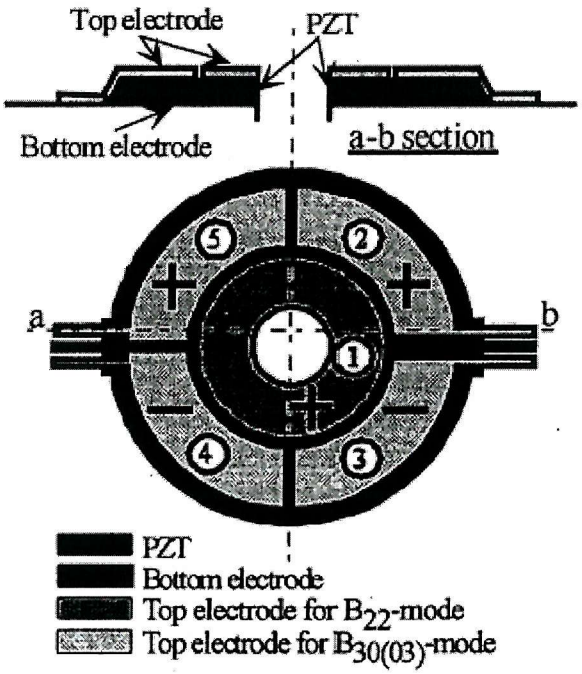

Figure 11.9: Polarisation direction for each of the electrode connections, Aoyagi et al [67].

This polarisation configuration allows each section of the device to be driven into a different resonant mode depending on the applied signal.

11.6.3 Motor controller

To control the three resonance modes it is necessary to have three independent control signals applied to the motor. Previous work on the construction of a motor controller has shown that it is possible to construct a circuit using one signal generator source and performing signal processing on the output to obtain three independent signals for the motor [115]. The block diagram for the motor controller system is shown in figure 11.10.

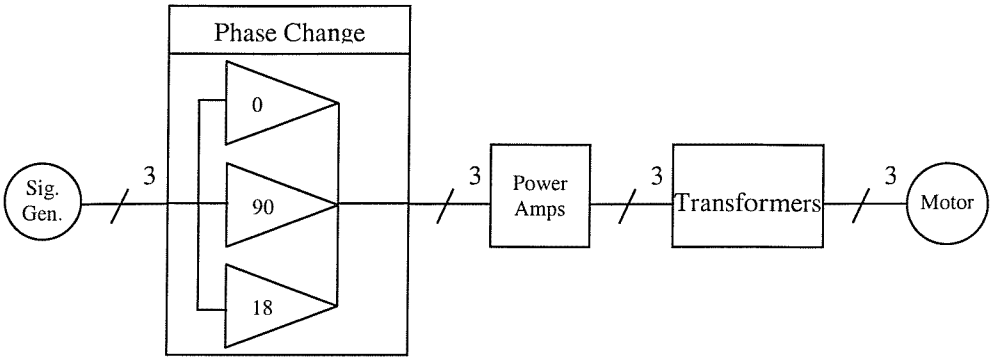

Figure 11.10: Block diagram of the motor controller system.

Figure 11.10 gives the main system blocks for the motor controller design. The phase change section will split the signal generator signal into three output signals to the power amplifier stage but each output signal could be one of three phases (0°, 90° and 180°) depending on the direction and type of movement desired in the ultrasonic motor. The power amplifier and transformer stages boost the signal to drive the motor which requires 150-200V per signal to drive it into the required resonance mode. Further details are contained within the relevant references.

11.6.4 Results and conclusion

Due to time constraints it was not possible to achieve a fully working motor-controller. The main components of the system including the splitting of the input signal and the selection of individual phase on the three channels was achieved. However, a connection between the transformer and motor stage could not be reliably achieved. The reasons for the unreliability require a more detailed study of the frequency response and power constraints of the system is required.

The problems associated with the driver circuit did not allow for a full demonstration of the improvements in the design. However, the results given in this thesis show that in principle the motor functions will be improved by the optimised paste formulation and processing parameters as Aoyagi had previously

used material with a highest $d_{33,f}$ of 33pC/N. The design could be further improved with the introduction of the second layer which can easily be incorporated into the existing design as described in section 11.6.2.

The design itself could be improved by enlarging the central electrodes thus giving a larger actuator area to increase the displacement for the B_{22} mode. Also, a redesign to incorporate more than two layers would require a greater distance between the electrode tabs. This will ensure the printing process is less problematic by reducing the effects of material accumulation.

11.7 University of Southampton Prosthetic Hand

Increased miniaturisation of mechanical and electrical systems has expanded the operating potential of prosthetic limbs. A major problem with current prosthetic devices is the inability of the user to obtain feedback control. For example, with a prosthetic hand, when the user grasps an object there is no possibility of evaluating the level of grip required, the fragility of the object or the temperature of the object other than visual assessment. If the grip level is insufficient then the object could slip from the prosthetic grasp before the user has a chance to react or could damage the object in attempting to respond. The problem with temperature is that the prosthetic or the user could be damaged or harmed if they are unaware how hot or cold the object is. Work by Cranny et al. [108] has considered combining piezoresistive (static) and piezoelectric (dynamic) sensors, for measurement of grip for a prosthetic hand. In addition, a number of thermistors are proposed for temperature measurement.

The Southampton hand, developed by Light et al. [116], is a prototype myoelectrically driven prosthetic, shown in figure 11.11. The work described here is a further development of this existing system.

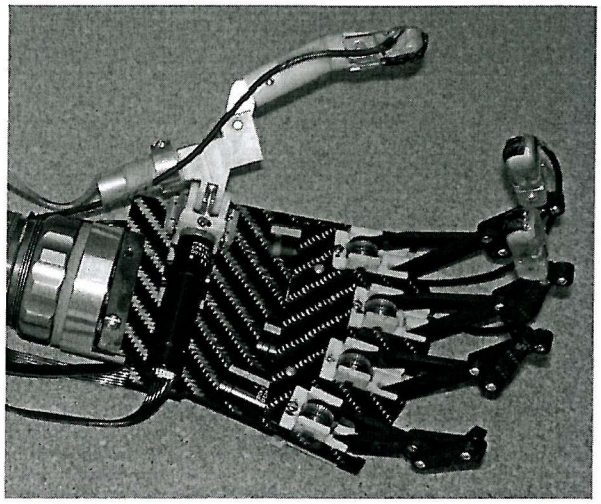

Figure 11.11: The Southampton-Remedi prosthetic hand, Chappell et al [116].

The flexing of muscles in the arm to create electrical control signals operates the hand. A micro controller interprets the signals, which moves the digits of the hand into specific positions such as hold, squeeze, grip and release and a number of other common hand postures. To perform these functions, each digit has an individual motor, which allows independent movement in each digit. The thumb has two degrees of freedom provided by two motors. The thumb and digits combine to allow a number of natural grip postures to be adopted.

To detect the grip on an object and to allow the micro-controller to intervene if the object being held begins to slip, it is necessary to use both static and dynamic force sensors. The static force sensor continually measures the force applied to an object. If the object begins to slip, the dynamic force sensor detects the vibration and the controller will activate the motors to tighten the grip.

It was decided that the optimum position for these sensors would be the fingertip. The design incorporates a single static sensor, a dynamic force sensor and a single temperature sensor, mounted on each of the four digits. The cantilever beam was decided to be the best mechanical structure with which to implement the sensor arrangement. This would be mounted along the central long axis of the finger so as to reduce force measurement errors from shear effects.

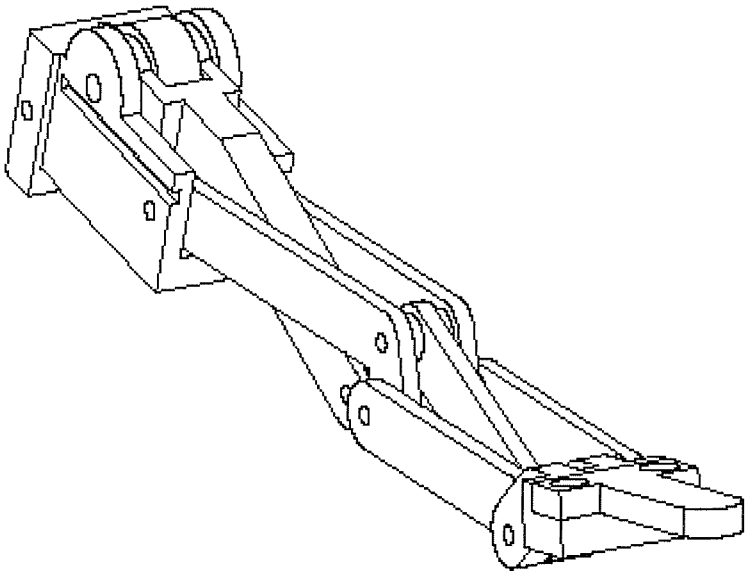

Figure 11.12: Modified finger link system. The knuckle block containing the drive wheel assembly is shown on the left of the diagram and the cantilever finger tip is shown on the right. Cranny et al [108].

Figure 11.12 shows the modified design for the finger link system for mounting the cantilever sensors. Figure 11.13 shows the top view of the cantilever with the sensor layout. The left side of the cantilever contains the static force sensors; these are screen-printed using a piezoresistive paste in a standard bridge configuration. As a force is applied, the sensors resistance changes and this can be measured using a differential amplifier. The right side of the cantilever contains the dynamic force sensor. This is screen-printed using the optimised PZT paste. The dynamic force sensor covers a larger proportion of the cantilever area and will detect any sudden variations in the force over the fingertip area which could indicate a grasped object is slipping. The temperature of any grasped object can be obtained from a screen-printed thermistor shown between the static and dynamic sensors in figure 11.13.

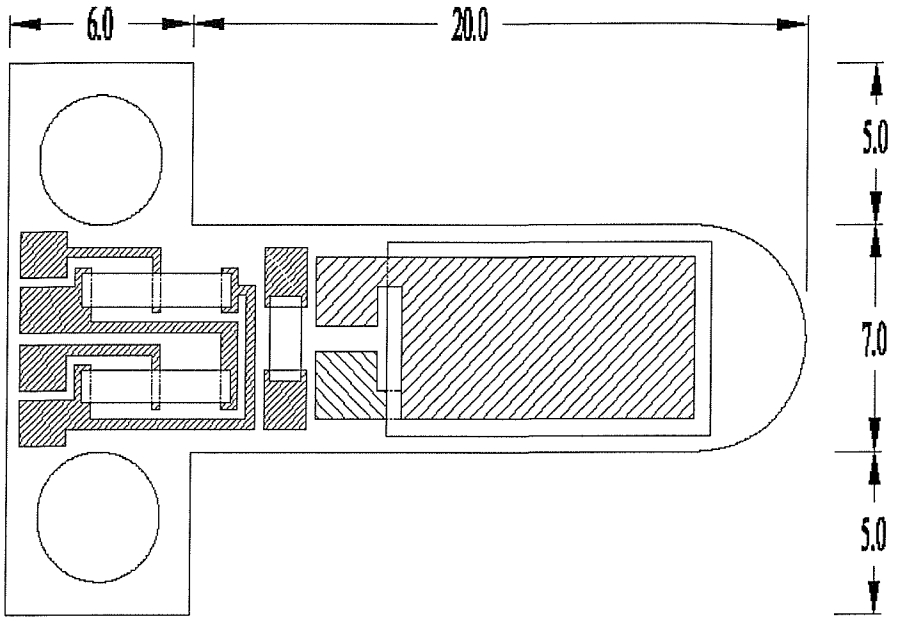

Figure 11.13: Dimensions of finger tip cantilever (mm) and location of sensors. The patterned areas represent different thick film layers. Cranny et al [108].

An insulating screen-printable dielectric layer is printed on to the fingertip with the rest of the sensor designs being printed on the top of this. The design is improved by the high $d_{33,f}$ levels of the optimised paste in a number of areas. The high $d_{33,f}$ value provides greater sensitivity and reduces the amount of detection and control electronics required, thus reducing the overall weight and power requirements of the prosthetic. In addition, future designs will look to achieve multiple stacked sensor layers following the results achieved in chapter 10.

11.8 Conclusions

This chapter has demonstrated the direct application of the optimised paste and provided details of further work, in combination with the work presented in this thesis, to further develop a varied set of applications. The improvements made in each application related to the work contained within this thesis have been discussed in detail. Further improvements that could be made to their design and operation by continued development of enhanced piezoelectric and mechanical properties of thick-film PZT have also been highlighted.

The repeatability of the paste allows for improvements and consistency in the applications which increases their commercial viability. The high piezoelectric activity and good high frequency qualities of the optimised film improve the sensitivity of the applications. In addition, these improved properties potentially reduce the amount of external circuitry required which reduces the size, complexity and cost of the final application.

The results of the high temperature powder investigation have shown potential for further optimisation. The results offer opportunities to combine the materials, particularly the PZT-5A, with existing applications such as the prosthetic hand to prevent damage to sensors on the hand when in contact with high temperature objects.

12 Conclusions and Further work

12.1 Conclusions

The piezoelectric properties of thick-film PZT-5H layers fabricated using the screen-printing technique have been studied. The results throughout the thesis have shown that the level of piezoelectric activity for the final thick-film layer is dependant on the paste composition and the subsequent processing involved. The piezoelectric constant $d_{33,f}$ has been identified as an important characteristic to determine the quality of the thick-film layer and has been used throughout the study to measure any improvements made.

12.1.1 Measurement method

The Take-Control PM35 piezometer was determined to be the best available method for measuring the $d_{33,f}$ value of the thick-film devices. This method was chosen because it was quick and simple to use with a lower standard deviation between measurements compared with the existing University of Southampton measurement system. Using the PM35 piezometer allowed for direct comparison between the results. Therefore, the task of observing trends in the results was easier. In addition, the ease of operation allowed for a greater number of samples to be measured in a shorter time. These factors aid the optimisation process by allowing a broader range of samples to be measured. This reinforces any conclusions made by reducing the statistical effect of anomalies such as unusually high or low samples.

12.1.2 Glass content and powder milling type

The firing temperatures used to form thick-film piezoceramics are not sufficiently high to enable sintering between the PZT particles. Therefore, thick-film materials require an additional binder material to form a bonding matrix

during firing. The study showed that the combination of 10% by weight of CF7575 lead borosilicate glass with 90% ball milled PZT-5H powder gave the optimum $d_{33,f}$ values with an average of 51.5pC/N. The lowest standard deviation between devices was achieved using 5% glass and 95% PZT-5H powder attritor milled 3 times, 2.1%. These two characteristics are due to the size and distribution of the respective milling processes. The ball milling produces large particles, 2μm diameter, which results in increased piezoelectric activity but less isotropic films. The attritor3 process produces smaller particles, 1μm diameter, which form less porous and more uniform films giving a greater consistency between devices.

12.1.3 Particle size combinations

The results show that the porosity of the film affects the $d_{33,f}$ but that a large particle size is also desired for greater piezoelectric activity, section 5.7 [117]. Therefore, combining the properties of ball milled and attritor3 powders provides a further increase in $d_{33,f}$ and a reduction in the deviation of measured $d_{33,f}$ between devices.

The original paste formulation was improved by combining 72% by weight of ball milled PZT, 18% of attritor3 milled PZT and 10% CF7575 glass. This combination improved the $d_{33,f}$ to an average of 63.5pC/N, which was further increased to 77pC/N with the introduction of a silver polymer top electrode. The deviation between devices was also reduced compared to the ball milled, 6.1% to 3.9% respectively, which brings the consistency closer to that of the attritor3 devices.

12.1.4 Parameter optimisation

Having established the optimum thick-film paste formulation, it was necessary to optimise the subsequent process parameters. The parameters studied were the furnace profile used to form the fired film and the poling parameters used to induce the piezoelectric effect in the thick-film device. The optimum furnace

profile was determined to have a peak temperature of 1000°C and is given in table 8-2. This higher temperature provided an improved level of glass sintering to increase the bonding between the PZT particles

12.1.5 Multilayer structure

The introduction of secondary and tertiary thick-film layers connected in series has been shown to increase the overall $d_{33,m}$ of the structure. The level of improvement is approximately a summation of the individual $d_{33,f}$ values for each PZT layer. Combining the optimised paste and parameters with multilayer printing techniques leads to a $d_{33,f}$ of 325pC/N for a three PZT layer structure at a height of 219.5μm from the substrate.

12.2 Summary

This work has shown that 10wt.% CF7575 glass, combined with of 18wt.% PZT-5H Attritor3 particles and 72wt.% PZT-5H Ball milled particles, with diameters of 1μm and 2μm respectively, is the optimum paste formulation achieved. The introduction of a gold bottom electrode and a silver polymer top electrode combined with a peak firing temperature of 1000°C and poling parameters of 5minutes, 200°C provide a maximum achieved $d_{33,f}$ of 131pC/N for a single PZT layer. The introduction of subsequent thick-film PZT layers connected in series gave a proportionate increase in $d_{33,m}$ to the maximum achieved for 3 layers, 325pC/N.

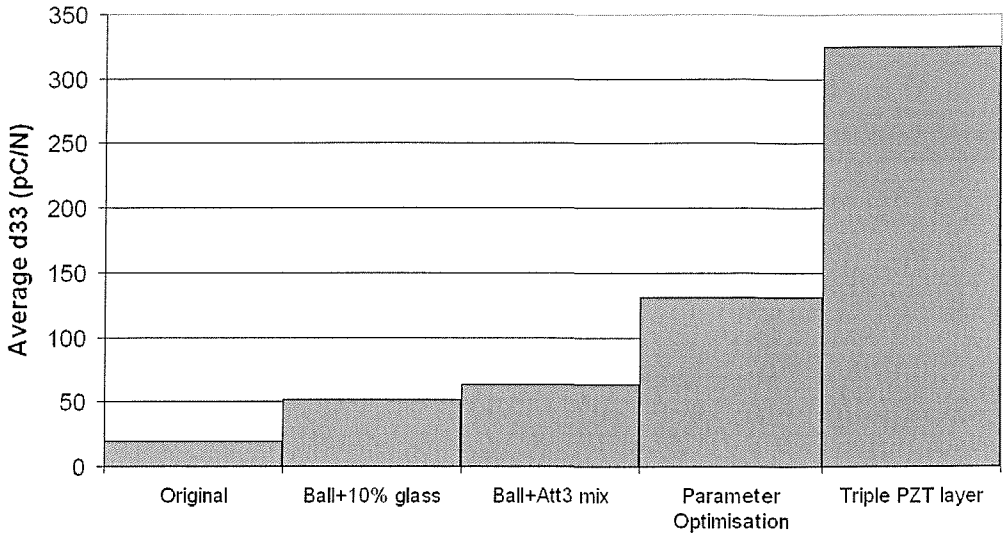

Figure 12.1: Summary showing progression of average d_{33} at each stage

Figure 12.1 shows the progression made in the results throughout the study. For a single thick-film PZT-5H layer, the average $d_{33,f}$ has been increased from 18.5pC/n to 131pC/N, which is an over 6-fold increase.

The value of 131pC/N compares favourably with the values for the bulk PZT-5H devices that were attached to substrates in the clamping effect study, 121pCN in section 4.3 [100].

12.3 Further work

As discussed in section 12.2, there are still potential areas for improvement in the piezoelectric properties of the thick-film. This section highlights the main areas where it is believed the most significant improvements could still be made and outlines a path to achieving these. In addition to the details given in chapter 11 detailing the current and future applications of the optimised PZT paste, a brief description of the most immediate applications that can be improved upon are given.

12.3.1 Stoichiometry of the powder

The main limiting factor in any further improvement in the $d_{33,f}$ value is the PZT powder composition. The PZT-5H powder stoichiometry is optimised for the high temperature lead atmosphere firing process of the Morgan Electro Ceramics factory. Therefore, the commercially fired powder has a crystal phase that lies along the morphotropic phase boundary giving the optimum d_{33}. The firing process used at the University of Southampton cannot match these conditions and therefore the thick-film PZT-5H layer will not match the tight stoichiometric balance of the bulk PZT-5H. Further work should involve either developing a PZT composition that is balanced for our firing profile or, attempting to recreate similar conditions within our furnace to that of the factory process.

An alternative option is to sinter the PZT-5H powder to alter the stoichiometry of the material before mixing into a screen-printable paste. It would require a set of experiments to observe the effects of pre-sintering the powder and at a temperature low enough that sintering between the powder particles does not occur. Once this heat treatment has been performed, the powder can then be mixed into a thixotropic paste, printed, dried and fired using the previously described methods. This method has the potential to provide the benefits in material stoichiometry of firing at high temperatures, whilst allowing the compatibility of lower sintering temperatures with other technologies such as silicon.

12.3.2 Improved density of the thick-film layer

The introduction of isostatic pressing or vacuum drying/firing could also increase the film density. This will improve the mechanical density of the film and provide higher and more consistent $d_{33,f}$ values. This study could be combined with a more complex 3D model of the PZT layer structure. Potentially a model could be developed to combine more than two powder sizes and focus more on the percentage weights of each powder type. In addition to this, it could be possible to combine the current optimised paste with the work by Corker et al.

[24] in coating the thick-film layer in a Sol-Gel layer to improve the density of the entire structure whilst maintaining the larger thickness associated with thick-film layers.

12.3.3 High temperature powders

The initial results given in section 11.4 suggest that a similar optimisation process for PZT-5A could lead to improved $d_{33,f}$ values with the additional high temperature characteristics. Obtaining the PZT-5A powders with the same particle size as the optimised PZT-5H paste and a study of the effects of poling parameters would potentially broaden the applications of thick-film PZT still further.

12.3.4 Further Applications

The most immediate application to benefit from the improvements in the thick-film paste development and processing is the ultrasonic motor, described in chapter 11.6. Achieving a fully working system for the ultrasonic motor controller would be desirable to demonstrate a working improvement in the optimised process compared to the original paste.

The prosthetic hand can benefit from any possible improvements in the use of polymer binders and piezoelectric materials, combining this with the possibility of pre-sintering the powders could lead to further advances in this field.

An additional area of study would be further improvement of the self-powered systems developed by Glynn-Jones et al. [118] at the University of Southampton. The self-powered system relies heavily on the amount of charge that can be generated by the piezoelectric element of the design. The optimised paste will improve the design by providing more power due to the increased piezoelectric response. Alternatively, the generator design could be further miniaturised because a smaller design using the optimised paste could provide the same power as the current design.

Appendix A – Substrate clamping effect on d_{33}

From Young's modulus, Y, the mechanical strain can be related to the compliance of the material and the applied stress.

$$S = \text{mechanical strain} = \frac{1}{Y} \text{x Strain} \rightarrow S = sT$$

The electrical strain can be related to the piezoelectric constant d, which is defined as the change in dimension related to the applied electric field.

$$S = \text{electrical strain} = \frac{\text{change in length}}{\text{Field}} \text{x Field} \rightarrow S = dE$$

As the piezoelectric crystal is defined by a matrix equation the strains combine to form equation 3.2 in tensor form.

The piezoelectric constant d can be defined by the ratio of short circuit charge density to the applied stress; from this it is possible to derive the charge due to the piezoelectric effect.

$$D = \text{electric displacement} = \frac{\text{charge density}}{\text{Stress}} \text{x Stress} \rightarrow D = dT$$

The construction of the piezoceramic device produces a capacitive structure and therefore a proportion of the charge generated will be due to the capacitive effect.

$$Q = CV \rightarrow \sigma = \frac{CV}{A} \rightarrow \sigma = \varepsilon E \rightarrow D = \varepsilon E$$

The electric displacements due to the piezoelectric and capacitive effects combine in tensor notation to form equation 3.3.

Matrix equations

Equations 3.2 and 3.3 define the response of a crystal in tensor form, these equations cane be determined in matrix form as shown below and expanded out to:

$$\begin{bmatrix} s_{11} & s_{12} & s_{13} & 0 & 0 & 0 \\ s_{21} & s_{11} & s_{13} & 0 & 0 & 0 \\ s_{31} & s_{13} & s_{33} & 0 & 0 & 0 \\ 0 & 0 & 0 & s_{44} & 0 & 0 \\ 0 & 0 & 0 & 0 & s_{44} & 0 \\ 0 & 0 & 0 & 0 & 0 & 2(s_{11}-s_{12}) \end{bmatrix} \qquad \begin{bmatrix} 0 & 0 & 0 & 0 & d_{15} & 0 \\ 0 & 0 & 0 & d_{24} & 0 & 0 \\ d_{31} & d_{32} & d_{33} & 0 & 0 & 0 \end{bmatrix}$$

Where: $s_{12}=s_{21}$, $s_{31}=s_{13}$, $s_{44} = s_{55}$, $d_{32} = d_{31}$, $d_{24} = d_{15}$

The matrix equations can be expanded to give the following strain equations:

$$S_1 = s_{11}^E T_1 + s_{12}^E T_2 + s_{13}^E T_3 + d_{31} E_3 \quad [A1.1]$$
$$S_2 = s_{11}^E T_2 + s_{12}^E T_1 + s_{13}^E T_3 + d_{31} E_3 \quad [A1.2]$$
$$S_3 = s_{13}^E (T_1 + T_2) + s_{33}^E T_3 + d_{33} E_3 \quad [A1.3]$$
$$S_4 = s_{44}^E T_4 + d_{15} E_2 \quad [A1.4]$$
$$S_5 = s_{44}^E T_5 + d_{15} E_1 \quad [A1.5]$$
$$S_6 = s_{66}^E T_6 \quad [A1.6]$$

And for the electric displacement:

$$D_1 = \varepsilon_1^T E_1 + d_{15} T_5 \quad [A1.7]$$
$$D_2 = \varepsilon_1^T E_2 + d_{15} T_4 \quad [A1.8]$$
$$D_3 = \varepsilon_3^T E_3 + d_{31}(T_1 + T_2) + d_{33} T_3 \quad [A1.9]$$

Inverse effect

For the inverse effect, applying an electric field and measuring the change in dimensions, S_3 is used as we look for the relation to d_{33}.

With no applied stress $T_3= 0$, writing the change in length Δl as a ratio to the applied voltage V can be related to the strain and applied field.

$$\frac{\Delta l}{V} = \frac{S_3}{E_3} = \frac{d_{33} E_3}{E_3} + \frac{s_{13}^E (T_1 + T_2)}{E_3} + \frac{s_{33} T_3}{E_3} \rightarrow \frac{\Delta l}{V} = d_{33} + \frac{s_{13}^E (T_1 + T_2)}{E_3} \quad [A1.10]$$

We are only concerned with ceramics that are mounted on a substrate, therefore it is necessary to consider the clamping effects of the substrate on the piezoceramic as it attempts to change dimensions in axis 1 and 2. Assuming the substrate has greater rigidity than the ceramic allows us to treat the displacement

in axis 1 and 2 as zero and therefore the strain $S_1=S_2=0$. We also assume the substrate and the ceramic are isotropic and therefore $T_1=T_2=T$.

Using equations A1.1 and A1.2 it is possible to formulate d_{33} independent of T.

$$S_1 = s_{11}^E T_1 + s_{12}^E T_2 + s_{13}^E T_3 + d_{31} E_3$$

$$\therefore -d_{31}E_3 = (s_{11}^E + s_{12}^E)T \rightarrow \quad \frac{T_3}{E_3} = \frac{-d_{31}}{(s_{11}+s_{12})}$$

$$\therefore \left(\frac{\Delta l}{V}\right)_T = d_{33} - 2d_{31}\frac{s_{13}^E}{(s_{11}^E + s_{12}^E)} \quad [A1.11]$$

Thus equation A1.11 can be written to give the effective d_{33} value, $d_{33,f}$, that could be measured, from this the real d_{33} value can be inferred.

$$d_{33,f} = d_{33} - 2d_{31}\frac{s_{13}^E}{(s_{11}^E + s_{12}^E)} \quad [A1.12]$$

Direct effect

The direct effect looks at the amount of charge generated when a force is applied to the ceramic.

If a bar is subjected to a stress it will expand and contract in its axis depending on the type of stress. It was found that the lateral strain is proportional to the longitudinal strain, the constant of proportionality is called Poisson's ratio ν.

Lateral strain = -ν x direct strain (due to stress) [A1.13]

For the purposes of the piezoceramic equations this result means the lateral strains in the device are related to the stress applied in axis 3, T_3. Assuming an isotropic substrate and ceramic, the lateral strain is the same in each direction and that they have a Young's modulus and a Poisson's ratio.

$$S_1 = S_2 = -\nu \times \text{direct strain} \qquad \text{direct strain} = \frac{\text{direct stress}}{\text{Youngs modulus}}$$

$$\therefore S_1 = S_2 = -\left(\frac{\nu}{Y}\right)T_3 \qquad [A1.14]$$

The piezoelectric constant d in axis 3 is defined as the charge generated, q, as a ratio of the applied force, F, for the direct effect, therefore we can equate this to the applied stress and the electric displacement.

$$\frac{q}{F_3} = \left(\frac{D_3}{T_3}\right)_E \qquad [A1.15]$$

Using equation A1.9, assuming $S_1 = S_2$ and the stress $T_1 = T_2 = T$ due to the substrates clamping effects gives the following:

$$-\left(\frac{\nu}{Y}\right)T_3 = (s_{11}^E + s_{12}^E)T + s_{13}^E T_3 + d_{31}E_3 \quad [A1.16]$$

For the short circuit condition, $E_3 = 0$ and therefore combining equation A1.9, A1.15 and A1.16 gives:

$$\left(\frac{D_3}{T_3}\right)_E = \left(\frac{2d_{31}T + d_{33}T_3}{T_3}\right)_E \qquad [A1.17]$$

Re-arranging equation A1.16 and substituting into equation A1.17 gives the effective d_{33}; therefore equation A1.18 gives $d_{33,f}$ for the direct effect.

$$\left(\frac{D_3}{T_3}\right)_E = d_{33,f} = d_{33} + 2d_{31}\left(\frac{-\left(\frac{\nu}{Y}\right) - s_{13}^E}{(s_{11}^E + s_{12}^E)}\right) \qquad [A1.18]$$

Using values obtained by Morgan Electro Ceramics and efunda.com it is possible to obtain the values for the constants in typical bulk 5H material. We have assumed a clamped film and therefore the Poisson's ratio and Young's modulus for the alumina substrate will be used, these were obtained from Hybrid Laser-tech.

$$\nu = 0.25,\ Y = 331\text{GPa},\ s_{11}^E = 16.4\text{x}10^{-12},\ s_{12}^E = -4.78\text{x}10^{-12},\ s_{13}^E = -8.45\text{x}10^{-12}$$

Substituting these values into equation A1.18 gives:

$$d_{33,f} = d_{33} + 1.33d_{31} \qquad [A1.19]$$

From the Morgan Electro Ceramics data book, the typical values for d_{33} and d_{31} are 593pC/N and –274pC/N respectively. Therefore the typical measured $d_{33,f}$ values for thick film PZT-5H devices should be in the order of 227.76pC/N, a reduction of 62% from the bulk value.

Appendix B – Experimental data

Additional results from chapter 5:

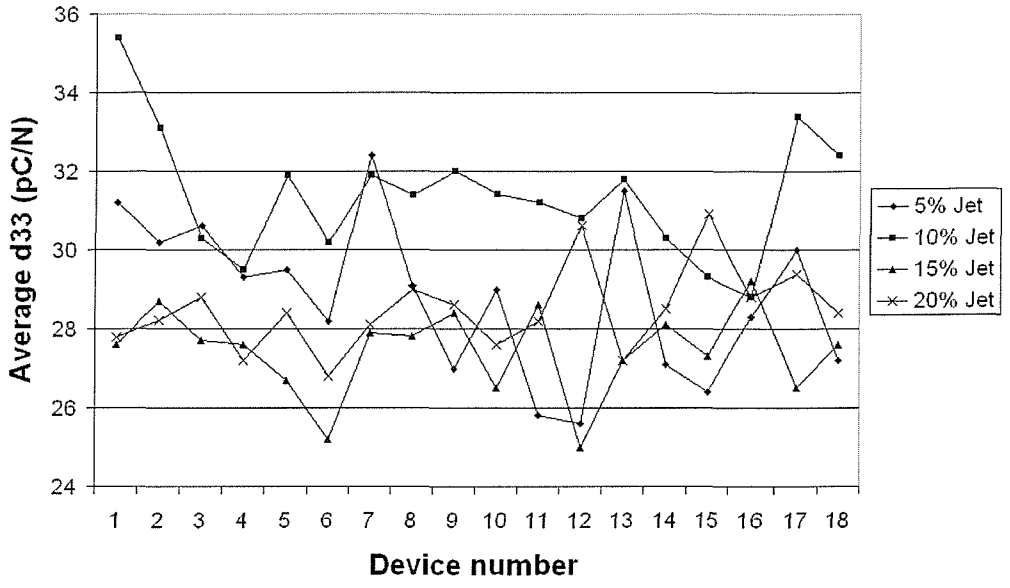

Figure B1: Average $d_{33,f}$ for jet milled powder with different percentages of glass frit.

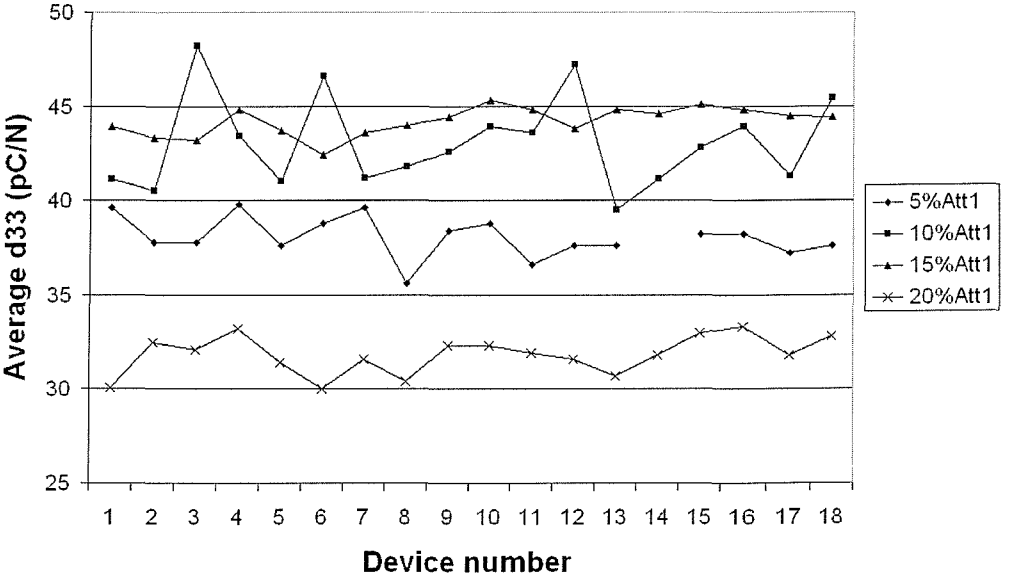

Figure B2: Average $d_{33,f}$ for Att1 milled powder with different percentages of glass frit.

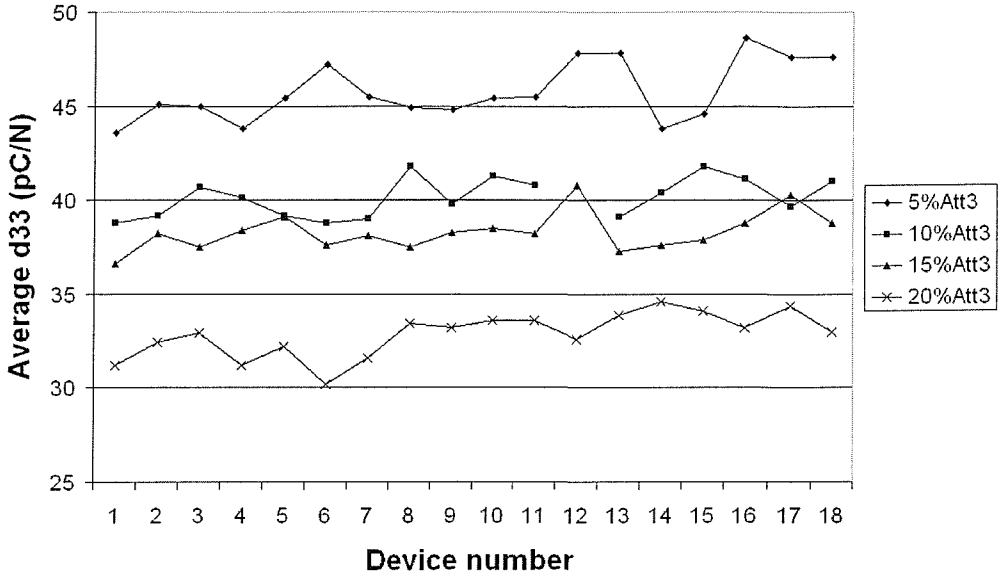

Figure B3: Average $d_{33,f}$ for Att3 milled powder with different percentages of glass frit.

Appendix C – ANSYS models

ANSYS model for determination of Young's modulus by iteration of the optimised PZT-5H thick-film on alumina cantilever beam

```
! Model Of PZT Thick-Film Cantilever

finish
/clear,start

/PREP7

/TITLE, PZT Youngs Modulus

! Dimensional parameters
alt=635e-6          ! Alumina thickness
filmt=848e-6          ! film thickness + Al thickness
l1=94e-3              ! Total cantilever length
l2=39e-3              ! Distance at which deflection is measured
l3=54e-3              ! Point at which load is applied
l4=59e-3              ! Length of the film
l5=16e-3              ! film indent from fixed end
w1=14e-3              ! Film width + border
w2=3e-3                     ! border
w3=17e-3              ! Beam width

load=4                ! In Newtons

epzt=26e9             ! Youngs modulus for PZT film

! Material properties

! Alumina - material 1
mat,1
ET,1,45

MP,DENS,1,4480
MP,NUXY,1,0.25
mp,ex,1,254e9

! PZT material properties
mat,2
et,2,45

MP,DENS,2,4810
```

```
MP,NUXY,2,0.31
mp,ex,2,epzt


! Build model
k,1
k,2,w2
k,3,,alt
k,4,w2,alt
k,5,w1
k,6,w1,alt
k,7,w3
k,8,w3,alt
k,9,w2,filmt
k,10,w1,filmt

kgen,2,all,,,,,l5,50
ksel,s,loc,z,l5
kgen,2,all,,,,,l2-l5,50
ksel,s,loc,z,l2
kgen,2,all,,,,,l3-l2,100
ksel,s,loc,z,l3
kgen,2,all,,,,,l4-l3,100
ksel,s,loc,z,l4
kgen,2,all,,,,,l1-l4,100
ksel,all

! Cantilever volumes
v,1,2,4,3,51,52,54,53
v,2,5,6,4,52,55,56,54
v,5,7,8,6,55,57,58,56

v,51,52,54,53,101,102,104,103
v,52,55,56,54,102,105,106,104
v,55,57,58,56,105,107,108,106
v,54,56,60,59,104,106,110,109

v,101,102,104,103,201,202,204,203
v,102,105,106,104,202,205,206,204
v,105,107,108,106,205,207,208,206
v,104,106,110,109,204,206,210,209

v,201,202,204,203,301,302,304,303
v,202,205,206,204,302,305,306,304
v,205,207,208,206,305,307,308,306
v,204,206,210,209,304,306,310,309

v,301,302,304,303,401,402,404,403
v,302,305,306,304,402,405,406,404
v,305,307,308,306,405,407,408,406
```

```
! Selecting materials
vsel,s,loc,y,0,alt
vatt,1,,1
vsel,s,loc,y,alt,filmt
vatt,2,,2
vsel,all

esize,500e-6
vmesh,all

! Apply Load
nsel,s,loc,y,0
nsel,r,loc,z,l3
nsel,r,loc,x,w3/2
f,all,fy,-load
nsel,all

! Define master degrees of freedom
total,100,1

! Merge coincidences and reduce wavefront
numm,all,1e-6
waves

nsel,s,loc,z,0
d,all,all
nsel,all

/view,1,1,1,1
/pbc,all,1
eplo

fini
/solu
antype,static
solve

fini
/post1
!plns,si

! select nodes at displacement measuring point
nsel,s,loc,z,l2
prdi,all    ! LOOK AT UY RESULT!!!!
```

ANSYS model for Aoyagi Multi-degree of freedom ultrasonic motor with electrode and PZT layers

```
! Model for an ultrasonic motor with PZT layers

finish
/clear,start


/prep7

/TITLE, Aoyagi MDOF USM +PZT

!----------

! Dimensions

lr1=1.5e-3          ! large radius          (mm)
sr1=1e-3            ! small radius          (mm)
t1=3e-3                     ! thickness of circle    (mm)

subt1=250e-6        ! substrate thickness   (mm)
subw1=10e-3         ! 1/2 substrate width   (mm)
subl1=10e-3         ! 1/2 substrate length  (mm)

pztth=95e-6         ! pzt thickness         (mm)
pztr=4.5e-3         ! pzt radius            (mm)

elth=7e-6           ! electrode thickness   (mm)

voltage=500         ! applied voltage       (volts)

!----------

! MATERIAL PROPERTIES

!substrate - material 1

mat,1               ! material number 1
ET,1,45             ! type of material used "solid45"

MP,DENS,1,3750      ! density of material 1
MP,NUXY,1,0.21      ! poissons ratio for material 1
MP,ex,1,303.4e9     ! youngs modulus for material 1
```

```
! MATERIAL PROPERTIES

!PZT - material 2

mat,2
ET,2,45

MP,DENS,2,7450      ! density of material 2
MP,NUXY,2,0.31      ! poissons ratio for material 2
mp,ex,2,96.5e9      ! youngs mod from petes thesis for thick film
!MP,ex,2,11.1e10    ! youngs modulus for material 2
!MP,ex,2,4.8e10 ! alternative youngs mod for mat 2

! MATERIAL PROPERTIES

!gold electrode - material 3

mat,3
ET,3,45

MP,DENS,3,1932      ! density of material 3
MP,NUXY,3,0.42      ! poissons ratio for material 3
MP,ex,3,79e9  ! youngs modulus for material 3

!--------------------

! MODEL COORDINATES

*afun,deg       ! sets mode degrees

k,1,            ! bottom layer
k,2,sr1
k,3,lr1
k,4,subw1

k,5,(cos(45))*sr1,(sin(45))*sr1
k,6,,sr1
k,7,(cos(45))*lr1,(sin(45))*lr1
k,8,,lr1

k,9,,subl1
k,10,subw1,subl1

! pzt circle
k,11,pztr
k,12,(cos(45))*pztr,(sin(45))*pztr
k,13,,pztr
```

```
! generate further coordinates automatically
kgen,2,all,,,,,subt1,100          ! gens kps at top of substrate
ksel,s,loc,z,subt1
kgen,2,all,,,,,t1,100             ! gens kps at top of PZT
ksel,s,loc,z,0
kgen,2,all,,,,,-elth,300 ! key points 300
ksel,s,loc,z,-elth
kgen,2,all,,,,,-pztth,100         ! key points 400
ksel,s,loc,z,-(elth+pztth)
kgen,2,all,,,,,-elth,100 ! key points 500
ksel,s,loc,z,-(elth+pztth+elth)
kgen,2,all,,,,,-pztth,100         ! key points 600
ksel,s,loc,z,-(elth+pztth+elth+pztth)
kgen,2,all,,,,,-elth,100 ! key points 700

ksel,all

! generate arcs

larc,2,5,1,sr1
larc,5,6,1,sr1                    ! generates substrate arc
larc,3,7,1,lr1                    ! for column
larc,7,8,1,lr1                    !

larc,11,12,1,pztr                 ! generates substrate arc
larc,12,13,1,pztr                 ! for pzt layer
larc,111,112,101,pztr             !
larc,112,113,101,pztr             !

larc,302,305,301,sr1              !
larc,305,306,301,sr1              ! generates PZT arcs
larc,303,307,301,lr1              !
larc,307,308,301,lr1              !
larc,311,312,301,pztr             !
larc,312,313,301,pztr             !

larc,402,405,401,sr1              !
larc,405,406,401,sr1              ! generates top electrode arcs
larc,403,407,401,lr1              !
larc,407,408,401,lr1              !
larc,411,412,401,pztr             !
larc,412,413,401,pztr             !

larc,502,505,501,sr1              !
larc,505,506,501,sr1              ! generates top electrode arcs
larc,503,507,501,lr1              !
larc,507,508,501,lr1              !
larc,511,512,501,pztr             !
larc,512,513,501,pztr             !
```

```
larc,602,605,601,sr1          !
larc,605,606,601,sr1          ! generates PZT 2 arcs
larc,603,607,601,lr1          !
larc,607,608,601,lr1          !
larc,611,612,601,pztr         !
larc,612,613,601,pztr         !

larc,702,705,701,sr1          !
larc,705,706,701,sr1          ! generates top electrode arcs
larc,703,707,701,lr1          !
larc,707,708,701,lr1          !
larc,711,712,701,pztr         !
larc,712,713,701,pztr         !

larc,102,105,101,sr1          !
larc,105,106,101,sr1          ! generates inner arc
larc,202,205,201,sr1          ! for column
larc,205,206,201,sr1          !

larc,103,107,101,lr1          !
larc,107,108,101,lr1          ! generates outer arc
larc,203,207,201,lr1          ! for column
larc,207,208,201,lr1          !

!--------------------

! VOLUMES


!!v,1,2,5,6,101,102,105,106          ! hole
v,2,3,7,5,102,103,107,105           ! substrate layer
v,5,7,8,6,105,107,108,106           !
v,3,11,12,7,103,111,112,107         !
v,7,12,13,8,107,112,113,108         !
v,11,4,10,12,111,104,110,112                !
v,12,10,9,13,112,110,109,113                !

v,2,3,7,5,302,303,307,305           !
v,5,7,8,6,305,307,308,306           ! bottom electrode
v,3,11,12,7,303,311,312,307         !
v,7,12,13,8,307,312,313,308         !

v,302,303,307,305,402,403,407,405   !
v,305,307,308,306,405,407,408,406   ! PZT layer
v,303,311,312,307,403,411,412,407   !
v,307,312,313,308,407,412,413,408   !

v,402,403,407,405,502,503,507,505   !
v,405,407,408,406,505,507,508,506   ! top electrode
v,403,411,412,407,503,511,512,507   !
```

```
v,407,412,413,408,507,512,513,508  !

v,502,503,507,505,602,603,607,605  !
v,505,507,508,506,605,607,608,606  ! PZT 2nd layer
v,503,511,512,507,603,611,612,607  !
v,507,512,513,508,607,612,613,608  !

v,602,603,607,605,702,703,707,705  !
v,605,607,608,606,705,707,708,706  ! top electrode
v,603,611,612,607,703,711,712,707  !
v,607,612,613,608,707,712,713,708  !


v,102,103,107,105,202,203,207,205  ! column
v,105,107,108,106,205,207,208,206  !

vsel,all
vsymm,y,all,,,,,,
vsel,all
vsymm,x,all,,,,,,


! selecting materials

vsel,s,loc,z,0,subt1+t1          ! select all volumes in the z direction
vatt,1,,1                        ! attribute these volumes with material 1 and
element 1

vsel,s,loc,z,0,-(pztth+elth+elth) ! select electrodes
vsel,u,loc,z,-elth,-(pztth+elth)
vsel,u,loc,z,-(pztth+elth+elth),-(pztth+elth+elth+pztth)
vatt,3,,3

vsel,s,loc,z,-elth,-(pztth+elth+pztth) ! select all volumes in the z direction below
substrate
vsel,u,loc,z,-(pztth+elth),-(pztth+elth+elth)
vatt,2,,2                        ! attribute this volume with material 2 and element
2

vsel,all                 ! selects all volumes

numm,all,0.5e-6
waves

esize,2e-3                       ! quickest whilst still being accurate
!!esize,500e-6                   ! optimum
vmesh,all
nsel,all
```

```
/view ,1,1,1,1
/pbc ,all,1
eplot


! modal solution

finish
/solu
antype ,modal
modopt ,lanb,40,8e3,35e3
mxpand,,8e3,35e3
solve
```

Publications

Reviewed Journals and Conferences:

Influence of milling process and powder preparation on the d_{33} coefficient of thick-film piezoelectric layers
Torah.R.N, Beeby.S.P and White N.M.,
Proceedings of Ferroelectrics UK Leeds, pp.58, 2002.

A study of the effect of powder preparation and milling process on the piezoelectric properties of thick-film PZT
Torah.R.N, Beeby.S.P and White N.M.
Proceedings of Eurosensors XVI 1, Prague, pp 93-94, 2002.

Screen printed PZT thick films using composite film technology
R.A.Dorey, R.W. Whatmore, S.P. Beeby, R.N. Torah, N.M. White
15th International Symposium on Integrated Ferroelectrics, 2003, Colorado, USA.

A study of powder size combinations for improving piezoelectric properties of PZT thick-film devices
Torah.R.N, Beeby.S.P and White N.M.,
Eurosensors XXVII Portugal 2003 Conf. Proc., 360-361.

Improving the piezoelectric properties of thick-film PZT: the influence of paste composition, powder milling process and electrode material
Torah.R.N, Beeby.S.P and White N.M.
Sensors and Actuators A, Vol. 110 (1-3), pp 378-384, 2004.

Experimental investigation into the effect of substrate clamping on the piezoelectric behaviour of thick-film PZT elements
Torah.R.N, Beeby.S.P and White N.M.
Journal of Physics D: Applied Physics, Vol. 37, pp. 1074-1078, April 2004.

Screen printed PZT thick films using composite technology

Dorey RA, Whatmore RW, Beeby SP, Torah RN, White NM

Integrated Ferroelectrics, Vol. 54, pp. 651-658, 2003.

An improved thick-film piezoelectric material by powder blending and enhanced processing parameters

R. Torah, S.P. Beeby, N.M.White,

Submitted to IEEE Ultrasonics, Ferroelectric and Frequency Control.

INSTITUTE OF PHYSICS PUBLISHING JOURNAL OF PHYSICS D: APPLIED PHYSICS
J. Phys. D: Appl. Phys. 37 (2004) 1074–1078 PII: S0022-3727(04)71423-0

Experimental investigation into the effect of substrate clamping on the piezoelectric behaviour of thick-film PZT elements

R N Torah, S P Beeby and N M White

Department of Electronics and Computer Science, University of Southampton, SO17 1BJ, UK

Received 4 November 2003
Published 17 March 2004
Online at stacks.iop.org/JPhysD/37/1074 (DOI: 10.1088/0022-3727/37/7/019)

Abstract

This paper details an experimental investigation of the clamping effect associated with thick-film piezoelectric elements printed on a substrate. The clamping effect reduces the measured piezoelectric coefficient, d_{33}, of the film. This reduction is due to the influence of the d_{31} component in the film when a deformation of the structure occurs, by either the direct or indirect piezoelectric effect. Theoretical analysis shows a reduction in the measured d_{33} of 62%, i.e. a standard bulk lead zirconate titanate (PZT)-5H sample with a manufacturer specified d_{33} of 593pC/N would fall to 227.8pC/N. To confirm this effect, the d_{33} coefficients of five thin bulk PZT-5H samples of 220 μm thickness were measured before and after their attachment to a metallized 96% alumina substrate. The experimental results show a reduction in d_{33} of 74% from 529pC/N to 139pC/N. The theoretical analysis was then applied to existing University of Southampton thick-film devices. It is estimated that the measured d_{33} value of 131pC/N of the thick-film devices is the equivalent of an unconstrained d_{33} of 345pC/N.

1. Introduction

Bulk lead zirconate titanate (PZT) piezoceramics have many applications as both sensors and actuators [1] but are of limited use in micro-electro-mechanical systems (MEMS) because they are generally not compatible in terms of size or processing methods. Thin-film PZT layers are an alternative, but they are limited by the complexity of the deposition processes and the need to pattern the films afterwards. Screen printable piezoceramics, first reported by Baudry [2], allow relatively thick piezoceramic layers to be deposited directly onto the device. The thick-film process is additive, and hence the piezoceramic layers can be printed to a desired pattern without the need for subsequent etching. However, this process can introduce problems because the printed layer requires high temperature firing, 600–1000°C, to form a sintered piezoceramic layer. Other drawbacks include the limits of the resolution of the screen, typically 100 μm, and the ability of the device to withstand an applied printing pressure.

The boundary conditions applied to a piezoelectric element also influence piezoelectric behaviour. Optimum piezoelectric behaviour is obtained when the piezoceramic is unconstrained in all directions. Thick-film piezoelectric elements, however, are rigidly clamped on one face to a substrate. This constraint limits the movement of the PZT layer as it attempts to expand or contract when a force or voltage is applied. Previous work [3, 4] has investigated the internal stresses and boundary conditions for thin-film ferroelectrics but has not related these effects to bulk devices and the reduction in piezoelectric properties observed. This paper presents, for the first time, an experimental comparison of both constrained and unconstrained bulk PZT-5H samples and relates the analysis to thick-film piezoelectric layers. The results are compared with theoretical analysis presented in [5–7] and applied to thick-film devices to determine the amount by which the clamping effect reduces the effective d_{33} coefficient of the printed PZT layer.

2. Theoretical evaluation of the clamping effect

The direct and indirect methods of measuring the piezoelectric coefficient are obtained from the relationships between charge,

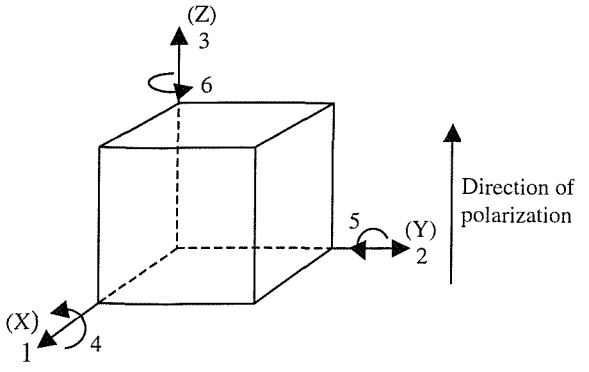

Figure 1. Notation of crystal axes with polarization direction.

induced strain and induced stress on the piezoceramic [8]. Equations (1) and (2) are defined as the piezoelectric constitutive equations:

$$S_\alpha = s^{\mathrm{E}}_{\alpha\beta} T_\beta + d_{i\alpha} E_i \tag{1}$$

$$D_i = d_{i\alpha} T_\alpha + \varepsilon^{\mathrm{T}}_{ij} E_j \tag{2}$$

$$\alpha, \beta = 1, 2, \ldots, 6 \qquad i, j = 1, 2, 3$$

where S, T, D and E are the strain, stress ($\mathrm{N\,m^{-2}}$), electric displacement ($\mathrm{C\,m^{-2}}$) and electric field ($\mathrm{V\,m^{-1}}$), and s, d and ε are the compliance ($\mathrm{m^2\,N^{-1}}$), piezoelectric constant ($\mathrm{C\,m^{-1}}$) and dielectric constant ($\mathrm{F\,m^{-1}}$), respectively. The superscripts E and T indicate a constant electric field and constant stress, respectively. Figure 1 shows the orientation of the ceramic defined by α, β, i and j.

Equations (3), (4) and (5) are obtained from expanding the tensor notation.

$$S_1 = s^{\mathrm{E}}_{11} T_1 + s^{\mathrm{E}}_{12} T_2 + s^{\mathrm{E}}_{13} T_3 + d_{31} E_3 \tag{3}$$

$$S_3 = s^{\mathrm{E}}_{13}(T_1 + T_2) + s^{\mathrm{E}}_{33} T_3 + d_{33} E_3 \tag{4}$$

$$D_3 = \varepsilon^{\mathrm{T}}_3 E_3 + d_{31}(T_1 + T_2) + d_{33} T_3 \tag{5}$$

2.1. Inverse effect

The inverse effect relates the piezoelectric coefficient, d_{33}, to the change in dimensions of a piezoceramic due to an applied field. The strain, S_3, can be used to obtain the relation to d_{33}.

With no applied stress, $T_3 = 0$, the ratio of change in length (Δl) to the applied voltage (V) can be related to the strain and applied field.

$$\frac{\Delta l}{V} = \frac{S_3}{E_3} = \frac{d_{33}E_3}{E_3} + \frac{s^{\mathrm{E}}_{13}(T_1 + T_2)}{E_3} + \frac{s_{33}T_3}{E_3}$$

$$\rightarrow \frac{\Delta l}{V} = d_{33} + \frac{s^{\mathrm{E}}_{13}(T_1 + T_2)}{E_3} \tag{6}$$

We are only concerned with piezoceramics that are mounted on a substrate; therefore it is necessary to consider the clamping effects on the piezoceramic as it attempts to change dimensions in axes 1 and 2. Assuming that the substrate has greater rigidity and relative thickness than the piezoceramic allows the assumption that the displacement in axes 1 and 2 is negligible and therefore the strain $S_1 = S_2 = 0$. We also assume that the substrate is the dominant element and that it is isotropic and therefore $T_1 = T_2 = T$. Using equations (3) and (4), it is possible to express d_{33} independent of T.

$$S_1 = s^{\mathrm{E}}_{11} T_1 + s^{\mathrm{E}}_{12} T_2 + s^{\mathrm{E}}_{13} T_3 + d_{31} E_3$$

$$\therefore -d_{31} E_3 = (s^{\mathrm{E}}_{11} + s^{\mathrm{E}}_{12}) T \rightarrow \frac{T}{E_3} = \frac{-d_{31}}{(s^{\mathrm{E}}_{11} + s^{\mathrm{E}}_{12})} \tag{7}$$

$$\therefore \left(\frac{\Delta l}{V}\right)_{\mathrm{T}} = d_{33(\mathrm{eff})} = d_{33} - 2d_{31}\frac{s^{\mathrm{E}}_{13}}{(s^{\mathrm{E}}_{11} + s^{\mathrm{E}}_{12})}$$

Thus equation (7) gives the effective d_{33} value that is measured. From this, the unconstrained d_{33} value can be determined.

2.2. Direct effect

The direct effect concerns the amount of charge generated when a force is applied to the piezoceramic. If a bar is subjected to a stress, it will expand and contract along its axes depending on the direction of the stress. The lateral strains in the device are related to the stress applied along axis 3, denoted as T_3. Assuming an isotropic substrate that dominates the piezoceramic, the lateral strain is the same in each direction and therefore $S_1 = S_2$ and the stress $T_1 = T_2 = T$ due to the substrate clamping. This is different from the indirect effect because the applied stress is transferred via the film to the substrate. Thus, the values of S_1 and S_2 must be determined as a function of T_3 using Hooke's law, shown in equation (8), where ν_{sub} and Y_{sub} are Poisson's ratio and Young's modulus of the substrate, respectively.

$$S_1 = S_2 = -\left(\frac{\nu_{\mathrm{sub}}}{Y_{\mathrm{sub}}}\right) T_3 \tag{8}$$

Relating the strain and the ratio of the charge generated to the applied force and combining this with equations (3), (4) and (8) gives equation (9).

$$-\left(\frac{\nu_{\mathrm{sub}}}{Y_{\mathrm{sub}}}\right) T_3 = (s^{\mathrm{E}}_{11} + s^{\mathrm{E}}_{12}) T + s^{\mathrm{E}}_{13} T_3 + d_{31} E_3 \tag{9}$$

For the short circuit condition, $E_3 = 0$, the assumptions made concerning the direct effect can be combined with equations (5) and (9) to obtain equation (10).

$$\left(\frac{D_3}{T_3}\right)_{\mathrm{E}} = \left(\frac{2d_{31}T + d_{33}T_3}{T_3}\right)_{\mathrm{E}} \tag{10}$$

Re-arranging equation (9) and substituting into equation (10) gives the effective d_{33}, denoted $d_{33(\mathrm{eff})}$ for the direct effect (as shown in equation (11)).

$$\left(\frac{D_3}{T_3}\right)_{\mathrm{E}} = d_{33(\mathrm{eff})} = d_{33} + 2d_{31}\left(\frac{-(\nu_{\mathrm{sub}}/Y_{\mathrm{sub}}) - s^{\mathrm{E}}_{13}}{s^{\mathrm{E}}_{11} + s^{\mathrm{E}}_{12}}\right) \tag{11}$$

The values for PZT-5H type materials were obtained from Morgan Electro Ceramics [1] and Efunda [9]. We have assumed a clamped film on a 96% pure alumina substrate, and therefore the Poisson's ratio and Young's modulus values for

the substrate will be used; these values were obtained from Hybrid Laser Tech [10].

$$\nu_{sub} = 0.25 \qquad Y_{sub} = 331\,\text{GPa}$$
$$s_{11}^{E} = 16.4 \times 10^{-12}\,\text{m}^2\,\text{N}^{-1}$$
$$s_{12}^{E} = -4.78 \times 10^{-12}\,\text{m}^2\,\text{N}^{-1}$$
$$s_{13}^{E} = -8.45 \times 10^{-12}\,\text{m}^2\,\text{N}^{-1}$$

Substituting these values into equation (11) gives equation (12):

$$d_{33(\text{eff})} = d_{33} + 1.33d_{31} \tag{12}$$

From the Morgan Electro Ceramics data book, typical values for d_{33} and d_{31} are 593pC/N and −274pC/N, respectively. Therefore, using equation (12), the measured d_{33} values for clamped thick-film 5H-type PZT devices have a theoretical maximum of 227.8pC/N, a reduction of 61% from the bulk value. This formula shows that the actual d_{33} of the material remains the same but the effective measurement of that d_{33} is reduced.

3. Practical measurement of the clamping effect

Thick-film samples cannot be used to demonstrate equation (11) because it is impractical to remove the devices from the substrate for direct measurement of d_{33}. Therefore, thin bulk samples from the Morgan Electro Ceramics product range were attached to a substrate to observe the effects on d_{33}.

Five metallized bulk 5H-type PZT discs, average thickness 220 μm and diameter 9.6 mm, were obtained from Morgan Electro Ceramics and their d_{33} coefficient measured. These were fully processed bulk piezoceramics that had been previously fired and poled by Morgan Electro Ceramics. The five discs were de-poled by heating them above the Curie temperature on a belt furnace and then re-poled at the Morgan Electro Ceramics factory using a proprietary manufacturing process. The piezoelectric coefficient, d_{33}, was then measured for each disc as a reference point for the unclamped disc. The bulk samples were then bonded on 0.64 mm thick 96% alumina substrate. An ESL 9633B silver–palladium electrode was printed on the substrates and the bulk discs placed on the wet printed pastes. The samples were dried in a DEK 1209 IR drier and fired with an 890°C peak temperature furnace profile. The plane view of the assembled samples is shown in figure 2. The silver–palladium film provides an electrical connection to the bulk piezoceramic whilst simultaneously rigidly bonding it to the substrate. Because the furnace temperature is above the Curie temperature of 5H-type PZT, it was necessary to re-pole the discs once fired. The samples were re-poled at the Morgan Electro Ceramics factory with parameters identical to those used before firing to ensure consistency with the poling level and decay time, thereby enabling a direct comparison between the unclamped and clamped d_{33}. In addition, it ensured that any reduction in d_{33} would be known to be due to the clamping effects rather than the device not obtaining polarization saturation, which would also result in a lower d_{33}. The d_{33} values before and after clamping were measured using a Take Control PM35 piezometer; five measurements were taken for each sample with a frequency setting of 97 Hz.

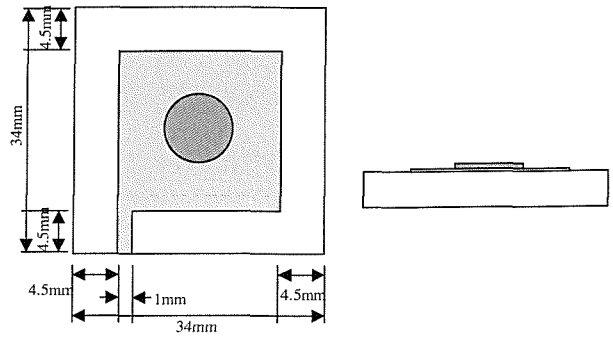

Figure 2. Sample design layout for substrate, electrode and PZT disc.

4. Experimental results

The values used for d_{31} in equation (11) were calculated as a ratio of the data sheet value for d_{31} compared with the measured value of d_{33}. This assumes that the d_{33} and d_{31} values change proportionally. These values were used to calculate the theoretical value of $d_{33(\text{eff})}$ using equation (12).

Figure 3 shows a comparison between the unclamped bulk devices, theoretical values given by equation (12) and the measured values once the disc was attached to the substrate and re-poled. These results show an average unclamped d_{33} of 529pC/N and an average clamped value of 138pC/N, giving a reduction of 74%.

5. Discussion of results

Figure 3 indicates that clamping a piezoceramic to a substrate reduces the measured d_{33}. The clamped 5H samples have ~32% lower measured d_{33} values than the theoretical values obtained from equation (12). This further reduction in d_{33} could be attributed to the lead loss experienced by the PZT layer when fired in the belt furnace. However, the firing temperature was only slightly above that at which lead migration occurs and therefore unlikely to have a large influence on the stoichiometry of the bulk device. This would indicate that any change in the domain structure of the bulk device would be minimal but could be a factor in the extra reduction observed.

Another contributing factor is that, despite the poling parameters before and after clamping being identical, the effect of the applied poling field after clamping is reduced. The electric dipoles within the ceramic cannot align to the same degree as an unclamped bulk ceramic when the poling field is applied because the associated deformation of the device is restricted by the substrate. This effect means that the polarization saturation point in the bulk device is reduced, thus causing an overall reduction in the piezoelectric activity. Another possible source for error is that the theoretical calculation ignores the shear effects within the film structure, which in practice could be introducing a further negative effect on the measured piezoelectric activity. Reductions in d_{33} due to grain size or size related domain structure transitions [11,12] can be ignored because the bulk disc was already fully sintered before being clamped to the substrate, as evidenced by the high d_{33} measurements before clamping.

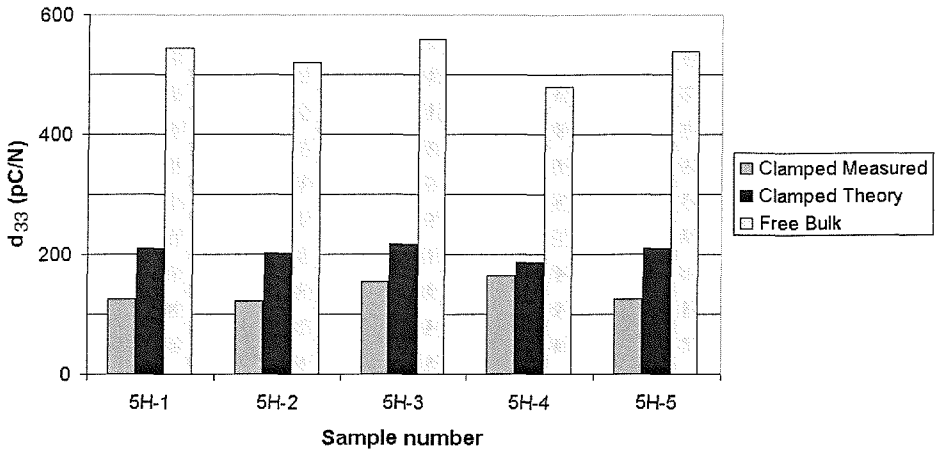

Figure 3. Comparison of theoretical and measured values of clamped d_{33}.

5.1. Thick-film samples

Using these results, it is possible to estimate the unconstrained d_{33} value from the $d_{33(\text{eff})}$ value measured for the University of Southampton thick-film devices, 131pC/N, using equation (12). These devices represent a continuation of the optimization work concerning 5H-type PZT thick-film devices conducted at the University of Southampton [13]; they consist of a blend of ball and attritor milled PZT powders with a lead borosilicate binder fired at a peak temperature of 1000°C and with optimized poling parameters. The device comprises a square of PZT ($1.1 \times 1.1\,\text{cm}^2$) of $60\,\mu\text{m}$ thickness printed on a standard 96% alumina substrate. It is not possible to measure the unclamped d_{31} for these devices, and therefore this is assumed to be the ratio of bulk d_{33} and d_{31}. A d_{31} value of −274pC/N can be used in equation (12) to produce a theoretical estimate of 345pC/N.

$$\begin{aligned} &\frac{d_{33}}{d_{31}} = \frac{593}{-274} \quad \rightarrow \quad d_{31} = -\frac{d_{33}}{2.16} \\ &d_{33(\text{eff})} = d_{33} - 1.33\left(\frac{d_{33}}{2.16}\right) \\ &d_{33} = 2.63 d_{33(\text{eff})} \\ &d_{33} = 2.63(131\text{pC/N}) = 345\text{pC/N} \end{aligned} \tag{13}$$

This is still less than the equivalent bulk 5H-type device with a d_{33} of 593pC/N; this discrepancy will be due to the different domain and structural effects that the thick-film device is subject to as a result of its manufacture [11, 12].

6. Conclusions

This paper has confirmed that the addition of a substrate to a piezoceramic has significant effects on the measured d_{33} value. The clamping effect equation [5], given in equation (12), has been shown to be valid with the measured results showing a significant reduction in d_{33} as predicted. For the bulk 5H devices, a reduction of average values from 529pC/N to 139pC/N was observed. This was found to be an approximately 74% reduction in the measured d_{33} value.

This result is significant because it provides an indication of the maximum achievable d_{33} for a particular PZT type and substrate combination. This is important when considering which powder and process combinations to use when designing devices for a particular application. This is of direct relevance to work on thick-film devices, where the measured d_{33} value is considerably lower than that of bulk devices. These results give an estimation of the proportion of the reduction due to the clamping effect and that due to processing and material differences between bulk and thick-film devices.

Further work will investigate the effect of the top electrode on the overall clamping of the piezoceramic and how this effect can be reduced with the use of alternative electrode materials.

Acknowledgments

The authors would like to thank Morgan Electro Ceramics Ltd for their continued support and assistance.

References

[1] Morgan Electroceramics Ltd *Piezoelectric Ceramics Data Book for Designers*
[2] Baudry H 1987 Screen-printing piezoelectric devices *6th European Microelec. Conf. Proc.* pp 456–63
[3] Pertsev N A, Zembilgotov A G and Tagentsev A K 1998 Effect of mechanical boundary conditions on phase diagrams of epitaxial ferroelectric thin films *Phys. Rev. Lett.* **80** 1988–91
[4] Shafer J D, Nafe H and Aldinger F 1999 Macro- and microstress analysis in sol–gel derived $Pb(Zr_xTi_{1-x})O_3$ thin films *J. Appl. Phys.* **85** 8023–31
[5] Lefki K and Dormans G J M 1994 Measurement of piezoelectric coefficients of ferroelectric thin films *J. Appl. Phys.* **76** 1764–7
[6] Nemirovsky Y, Nemirovsky A, Muralt P and Setter N 1996 Design of a novel thin-film piezoelectric accelerometer *Sensors Actuators* A **56** 239–49
[7] Dubois M-A and Muralt P 1999 Measurement of effective transverse piezoelectric coefficient $e_{31,f}$ of AlN and $Pb(Zr_x, Ti_{1-x})O_3$ thin films *Sensors Actuators* A **77** 106–12

[8] Jaffe B and Cook W R 1971 *Piezoelectric Ceramics* (New York: Academic)
[9] Efunda Engineering Fundamentals, http://www.efunda.com
[10] Hybrid Laser Tech Ltd, http://www.hlt.co.uk/
[11] Ren S B, Lu C J, Liu J S, Shen H M and Wang Y N 1996 Size related ferroelectric-domain-structure transition in a polycrystalline $PbTiO_3$ thin film *Phys. Rev.* B **54** 14337–40
[12] Arlt G, Hennings D and de With G 1985 Dielectric properties of fine-grained barium titanate ceramics *J. Appl. Phys.* **58** 1619–25
[13] Torah R N, Beeby S P and White N M 2003 A study of powder size combinations for improving piezoelectric properties of PZT thick-film devices *Eurosensors 27th Portugal 2003 Conf. Proc.* pp 360–1

A study of powder size combinations for improving piezoelectric properties of PZT thick-film devices

R.N.Torah, S.P.Beeby and N.M.White

Department of Electronics and Computer Science, University of Southampton, UK
Email: rnt00r@ecs.soton.ac.uk http://www.ecs.soton.ac.uk

Summary: This paper details investigations into the effects of different powder size ratios on the d_{33} coefficient of thick-film PZT layers. The two powders used were 5H type PZT supplied by Morgan Electro Ceramics Ltd. These were prepared using ball milling for the large particles, ~2um, and attritor milling for the small particles, ~1um. These powders were mixed with 10% by weight of Ferro CF7575 lead borosilicate glass and an appropriate quantity of ESL 400 solvent to formulate a screen printable paste. The results show the optimum powder combination obtained and a final formulation for a practical thick-film paste. The highest d_{33} value, 63.5pC/N, was obtained with the 4:1 ball to attritor powder by weight paste formulation.

Keywords: piezoelectric, thick-film, d_{33}
Category: 2 (Materials and Technology)

1 Introduction

Screen printable piezoelectric materials were first reported in 1987 [1] and have since found use in many applications; including motors [2] and micromachined silicon devices [3]. Studies have shown however, that the thick-film PZT samples have lower d_{33} coefficients than their bulk counterparts [4,5] due to differences in processing, composition and the influence of the substrate the film is printed on [6].

Piezoelectric thick-film pastes are produced by mixing milled piezoelectric powders with a suitable binder and organic vehicle. Both cermet pastes utilizing glass binders [7] and polymer pastes with the active material held within a polymer matrix [8] have been demonstrated. The most commonly used piezoelectric material used in the paste preparation is lead zirconium titanate ($PbZr_xTi_{1-x}O_3$ or PZT). Several milling processes can be used to form the powder [9]. The physical nature of the PZT powder, i.e. particle size, distribution and shape are determined by the processing techniques used in its preparation.

Ball milling involves the PZT powder being mixed in a slurry with a suitably abrasive milling media in a horizontally rotating mill. This process results in smooth particles, the extent of this smoothness is determined by the speed of the process and the milling media used. Attritor milling is similar and often uses powder that has already been ball milled. The powder passes through a vertical mill with a rotating central shaft resulting in a more uniform size distribution. It is standard practice to feed the resultant milled powder back into the mill to further tighten the distribution. The powder is then defined by the number of times it has passed through the mill, i.e. attritor one, attritor three for one and three passes respectively.

Previous work has shown that the large particle size, ~2um, of ball milled powder produces the highest d_{33} values, whilst the smaller, more evenly distributed, particles of the attritor milled powders, ~1um, produce the most consistent d_{33} values [9]. This paper presents details of the next stage in the paste development; the combination of ball and attritor milled powders and determining their optimum ratios.

2 Theory

The larger particle size associated with the ball milled powder results in increased piezoelectric responses. Therefore, it was important to maintain the ball milled particle as the dominant particle within any powder combination. The smaller attritor milled particles can be used to fill the interstice between the ball milled particles. The increased mechanical density of the film improves both the mechanical coupling and subsequent piezoelectric properties of the film. Hence, it was anticipated that by blending these two powders we would obtain a compromise between the high d_{33} values associated with ball milled powder and the consistency achieved with the attritor3 powders [9].

The attritor particles used in this investigation were milled 3 consecutive times and have been denoted attritor3. The combined ball milled and attritor3 milled powders were mixed with Ferro CF7575 lead borosilicate glass, which forms the binding matrix when fired.

3 Calculations

The initial calculations for the ratio of ball milled to attritor milled powders used a basic 2D model shown in figure 1.

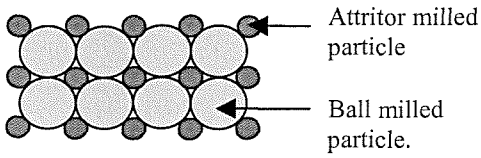

Fig 1: Ideal 2D model for particle distribution.

A ball milled particle is the central particle in the lattice and the interstice between these are filled with smaller attritor milled PZT particles.

The limitations associated with this model are that it is a 2D representation of a 3D problem and it assumes the particles are spherical. The model also assumes the glass binder will melt in the processing and form an ideal bonding matrix surrounding the particles. In addition, it assumes that the optimum solution completely fills the interstice surrounding the central particle with attritor particles and glass binding matrix. The particle sizes used in the model are obtained from the size distributions identified in figure 2.

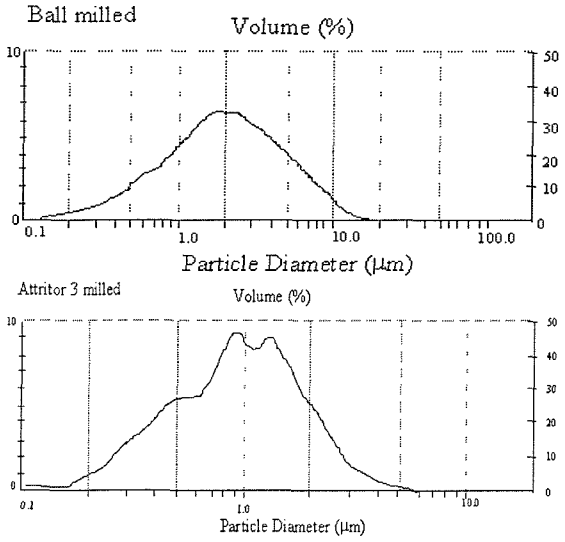

Fig 2: Particle size distributions for ball and attritor3 milled powders respectively.

The average particle size was used in the calculations but clearly in practice there are a range of particle sizes. The particle layout shown in figure 1 was used in the model since the remaining interstice closely matches the average particle size of the attritor3 powder when the ball milled powder is used as the dominant particle in the lattice.

Using the average ball milled particle diameter of 2μm, the largest particle size that will fit the interstice between the particles is 0.83μm. Using this value, the total area between the ball particles was calculated. This configuration fills 92% of the area, which is the maximum achievable with two particle sizes. A ratio of attritor particles to ball particles required to fill the total area was then calculated based on the assumption the ideal result would be obtained when the remaining interstice was filled. The weight ratio of powders can be calculated using the density of PZT-5H [4], this gives an optimum powder ratio of 8.8:1 ball milled to attritor milled powder by weight.

In practice the attritor3 powder has an average particle size of 1μm, slightly above the ideal. This practical powder size produces a new optimum powder ratio of 7.4:1 ball milled to attritor milled powder by weight. The closest integer number of particles in the lattice of figure 1 to this would give an optimum weight ratio of 4:1. Given this, and allowing for the other assumptions described above and using an integer number of particles in the model, a range of powder ratios from 8:1 to 2:1 by weight were investigated. The calculated percentages of powders for each paste are shown in table 1. The percentage of glass binder remained constant since 10% has previously been identified as the optimum [9].

Table 1. Percentages of Att3 and Ball powders

Paste	Attritor3 percentage weight	Ball percentage weight	CF7575 percentage weight
8:1	10%	80%	10%
4:1	18%	72%	10%
2.6:1	25%	65%	10%
2:1	30%	60%	10%

4 Processing

The four powder combinations in table 1 were mixed with ESL 400 solvent to create thixotropic screen printable pastes. These pastes were then mixed using a triple roll mill, which disperses the powders evenly throughout the paste. The pastes were printed on a 96% alumina substrate using standard thick-film screen-printing process with a DEK 1200 printer. The substrates were dried in a DEK 1209 IR drier at 140°C and then fired on a belt furnace with a firing profile shown in table 2.

Table 2: Furnace firing profiles for Dupont60 and rnt1000.

Stage	1	2	3	4	5	6
Temp (°C)	350	600	885	883	890	870

The screen-printed layers formed a capacitor structure arrangement, with ESL 9936B low migration AgPd

bottom and top electrodes fired with the same firing profile as the PZT layer, figure 3.

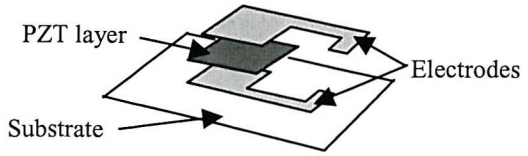

Fig 3: Capacitive structure for the piezoelectric device

This entire process took place within the University of Southampton Microelectronics Centre clean room facility to further reduce any possible sources of contamination in the pastes. Samples from each batch were viewed in a Scanning Electron Microscope (SEM).

Once fired, each sample was poled at 150°C with field strength of $4MVm^{-1}$ for 30 minutes and then allowed to cool to room temperature with a continuously applied electric field [4]. The d_{33} values were measured using a Take Control PM35 piezometer. This measurement method provides consistent and repeatable results but the measured results are limited by the clamping effect of the substrate. This clamping effect increases the influence of the d_{31} coefficient thereby reducing the effective d_{33} [6]. The bending moments generated by the substrate must be carefully controlled as the increased stress within the device can amplify the effective d_{33} and if not accounted for correctly can lead to artificially high results being reported.

5 Results

Five d_{33} measurements were taken on between 8 and 24 devices with the average value recorded and the standard deviation calculated. Figure 4 and 5 show the average measured d_{33} values and standard deviations for each of the powder combinations respectively. Included are the previous results for ball and attritor3 milled powder for comparison [9].

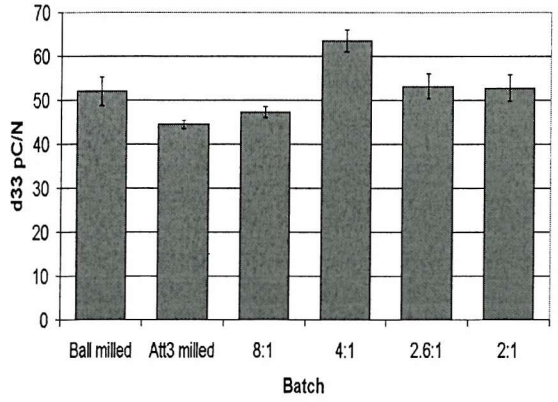

Fig 4: Average measured d_{33} value for each powder combination.

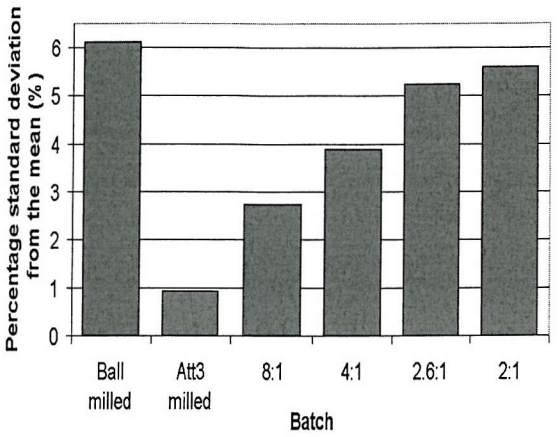

Fig 5: Percentage standard deviation for the measured d_{33} value of each powder combination.

Figure 6 shows a SEM micrograph of the 4:1 ball to attritor PZT layer. It appears that the level of sintering between the PZT particles is low but that the glass bonding matrix and the combination of powders has produced a relatively dense film with reduced interstices.

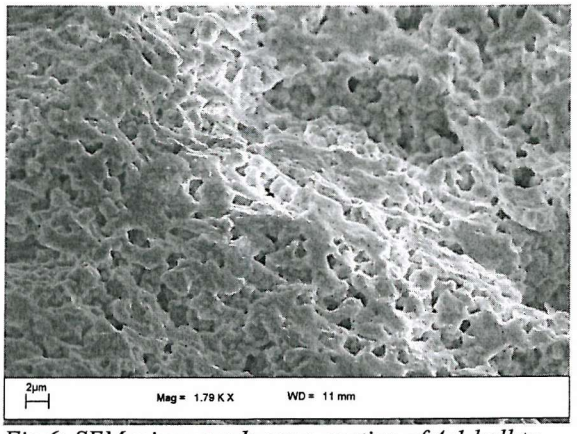

Fig 6: SEM micrograph cross-section of 4:1 ball to attritor PZT layer.

The results show that there is a clear improvement in the d_{33} value obtained by combining powder types together. In addition, there is an optimum ratio of powders which occurs at a ratio of 4:1 by weight. This gives a d_{33} value of 63.5pC/n and also shows an improved standard deviation when compared to the original ball milled paste.

6 Discussion of results

The combination of 4:1 by weight of ball milled to attritor milled powder (18% attritor3, 72% ball and 10% CF7575 powders) produces the highest d_{33} coefficient with an average measured value of 63.5pC/N. Figure 4 shows that the number of smaller particles added to the paste indicates a saturating effect past ratios of 2.6:1 as the interstice gaps within

the matrix have been already filled. This result agrees reasonably closely with the basic 2D model.

The previous optimum paste, obtained from purely ball milled powder, had a d_{33} coefficient of 52pC/N. The new 4:1 paste has resulted in an increase in piezoelectric activity of over 20%. The results also show that the percentage of deviation has decreased from 6.2% to 3.9% from the previous ball milled paste. This indicates the optimum paste not only produces a more active film, but also results in a more repeatable material.

7 Conclusions

This paper has demonstrated that the blending of ~2μm and ~1μm diameter ball and attritor3 milled PZT powders with a respective weight ratio of 4:1 results in improved piezoelectric thick-film behaviour. Increasing from a previous high of 52pC/N to 63.5pC/N, a 20% improvement, with an almost 50% increase in consistency.

Further work will develop a 3D model to seek further optimisation and confirmation of the experimental work. Once confirmed, a further investigation into improving the process parameters for the film will be conducted, specifically, the firing temperature and poling parameters. In addition, the use of multilayer structures in combination with this new paste formulation will be investigated to further increase the effective d_{33} coefficient.

8 Acknowledgements

The authors wish to thank the support and assistance given to us by Morgan Electro Ceramics Ltd.

9 References

[1] H.Baudry, Screen-printing piezoelectric devices, 6th European Microelec. Cont. Proc, p456-463, 1987.
[2] J.Dargahi, A piezoelectric tactile sensor with three sensing elements for robotic, endoscopic and prosthetic applications, Sensors and Actuators A, 80 (2000) 23-30.
[3] S.P.Beeby, N.M.White, Silicon micromechanical resonator with thick-film printed vibration excitation and detection mechanisms, Sensors and Actuators A, 88 (2001) 189-197.
[4] P.Dargie, R.Sion, J.Atkinson, N.White, An investigation of the effect of poling conditions on the characteristics of screen-printed piezoceramics, Microelectronics International, 15/2 (1998) 6-10.
[5] Morgan Electroceramics Ltd.: Piezoelectric Ceramics Data Book for Designers.
[6] K.Lefki, G.J.M.Dormans, Measurement of piezoelectric coefficients of ferroelectric thin films, Journal of applied physics, vol. 76, pp 1764,1767, 1994.
[7] P.Glynne-Jones, S.P.Beeby, P.Dargie, T Papakostas, N.M.White: An investigation into the effect of modified firing profiles on the piezoelectric properties of thick-film PZT layers on silicon, Meas. Sci. Technol., Vol. 11, pp 526-531, 2000.
[8] Piezoelectric thick-film polymer pastes, T.Papakostas, N.R.Harris, S.P.Beeby, N.M.White, Eurosensors XII, pp. 461-464, 1998
[9] R.N.Torah, S.P.Beeby, N.M.White, A study of the effect of powder preparation and milling process on the piezoelectric properties of thick-film PZT, Eurosensors XVI Proc., Prague, 2002.

Bibliography and websites

Texts:

Morgan Electro Ceramics: Transducer Products Division "Excellence in Piezoelectric Technology".

B.Jaffe, W.R.Cook (1971). "Piezoelectric ceramics". Academic press.

W.G.Cady. (1964). "Piezoelectricity: An introduction to the theory and applications of electromechanical phenomena in crystals" 2nd ed. Dover publications.

J.F.Nye (1957), "Physical properties of crystals", Oxford University press.

Philips Components: "Piezoelectric ceramics: properties and applications"

Websites:

http://www.piezoceramics.co.uk/
http://www.piezo-kinetics.com
http://www.apc.thomasregister.com
http://www.ndt.net
http://www.piezo.com
http://www.physikinstrumente.com/tutorial/

References

[1] "Piezoelectricity: An introduction to the theory and applications of electromechanical phenomena in crystals", W.G.Cady , 1st ed. Mcgraw- Hill, 1946. 2nd ed. Dover publications, 1964.

[2] Titanium Alloy Mfg. Co. Electrical Report No. 8, (Sept. 17, 1942) Wainer. E, Salomon, A.N.

[3] Piezoelectric properties of lead zirconate-lead titanate solid-solution ceramics, B. Jaffe, R.S. Roth, S. Marzullo, J. Appl. Phys. , Vol. 25, pp. 809-810, 1954.

[4] Piezoceramic Thick Films – Technology and Applications, State of the Art in Europe, W.W. Wolny, Proc. ISAF 2000, pp. 257-262, 2000.

[5] Morgan Electro Ceramics: Transducer Products Division "Excellence in Piezoelectric Technology".

[6] National Physics Laboratory: http://www.npl.co.uk/npl/cmmt/functional/tutorial.html

[7] Piezoelectric crystals and their application to ultrasonics, W.P. Mason, D. Van Nostrand Company Inc., 1950.

[8] Domain process in lead zirconate titanate and barium titanate ceramics, Journal of applied physics, D. Berlincourt, H. Krueger Vol. 30, No. 11, pp. 1804-1810, 1959.

[9] "Physical properties of crystals", J.F.Nye, Oxford University Press, 1957.

[10] "Piezoelectric Ceramics", B. Jaffe, W.R. Cook, Academic press, pp. 289-290, 1971

[11] Morgan Electro Ceramics: Transducer Products Division "Excellence in Piezoelectric Technology". Table 3. Typical Values of Lead Zirconate Titanate Materials.

[12] Dependance of electric properties of $Pb(Zr_xTi_{1-x})O_3$ solid solutions on their composition, J.Dudek, Z. Wrobel, Ferroelectrics, Vol. 18, pp. 161-164, 1978.

[13] Intrinsic and Extrinsic size effects in fine-grained morphotropic-phase-boundary lead zirconate titanate ceramics, C.A.Randall, N. Kim, J-P. Kucera, W. Cao, T.R. Shrout, J. Am. Ceram. Soc., Vol. 81, No. 3, pp. 677-688, 1998.

[14] Effect of calcium on the piezoelectric and dielectric properties of Sm-modified $PbTiO_3$ ceramics, S.Y.Chu, C.H.Chen, Sensors and Actuators A, Vol.89, pp. 210-214, 2001.

[15] Piezoelectric thick-film materials and sensors, M.Prudenziati, B. Morten, G. De Cicco, Microelectronics International, No. 38, pp. 5-11, 1995.

[16] PZT thin films for microsensors and actuators: Where do we stand?, P. Muralt, IEEE Trans. On Ultrasonics, Ferroelectrics and Freq. Ctrl., Vol. 47, No. 4, pp. 903-915, 2000.

[17] Liquid-phase sintering of PZT ceramics, D.L. Corker, R.W. Whatmore, E. Ringgaard, W.W. Wolny, Journal of the European Ceramic Society, Vol. 20, pp. 2-39-2045, 2000.

[18] Screen-printing piezoelectric devices, H.Baudry, 6th European Microelec. Conf. Proc, p456-463, 1987.

[19] Ultrasonic & Acoustic Transducer Group: Production of Piezoceramics, UK, Morgan Electro Ceramics internal publication.

[20] Miniature sensors using high density screen printing, C.Robertson, R.D.Shipton, D.R.Gray, Sensor Review, Vol. 19, No. 1, pp. 33-36, 1999.

[21] Fabrication of piezoelectric thick-film low-voltage multilayer actuators using a new double-paste printing technique, H. Moilanen, S Leppavuori, A. Uusimaki, Sensors and Actuators A, Vol. 37-38, pp. 106-111, 1993.

[22] Sol Gel process website: http://www.chemat.com/html/solgel.html

[23] Densification Method of Screen Printed PZT(52/48) Thick Films, Y.B.Kim, T.S.Kim, K.S.Choi, D.J.Choi, Integrated Ferroelectrics, Vol.35, pp. 199-208, 2001.

[24] PZT 'composite' ferroelectric thick films, D.L.Corker, Q.Zhang, R.W.Whatmore, C.Perrin, J. Eur. Ceram. Soc., Vol. 22, pp. 383-390, 2002.

[25] Microstereolithography of lead ziconate titanate thick film on silicon substrate, X.N Jiang, C.Sun, X. Zhang, B. Xu, Y.H. Ye, Sensors and Actuators A, Vol.87, pp. 72-77, 2000.

[26] Anodic bonding of lead zirconate titanate ceramics to silicon with intermediate glass layer, K.Tanaka, E.Takata, K. Ohwada, Sensors and Actuators A, Vol.69, pp. 199-203, 1998.

[27] Preparation of lead zirconate titanate thin film by hydrothermal method, K. Shimomura, T. Tsurumi, Y. Obha, M. Daimon, Jpn. J. Appl. Phys., Vol. 30 (9B) 2174-2177, 1991.

[28] A cylindrical shaped micro ultrasonic motor utilizing PZT thin film (1.4mm in diameter and 5.0mm long stator transducer), T. Morita, M. Kurosawam T. Higuchi, Sensors and Actuators A, Vol. 83, pp. 225-230, 2000.

[29] RF planar magnetron sputtering and characterisation of ferroelectric $Pb(Zr,Ti)O_3$ films, S.B. Krupanidhi, N. Maffei, M. Sayer, K. El-Assal, J. Appl. Phys., Vol. 54, No. 11, pp. 6601–6609, 1983.

[30] Silicon micro mechanical resonator with thick-film printed vibration excitation and detection mechanisms, S.P.Beeby, N.M.White, Sensors and Actuators A, Vol 88, pp. 189-197, 2001.

[31] Preparation of ferroelectric thick film actuator on silicon substrate by screen-printing, T. Futakuchi, H. Yamano, M. Adachi, Japanese Journal of Applied Physics, Vol 40, pp. 5687-5689, 2001.

[32] A piezoelectric tactile sensor with three sensing elements for robotic, endoscopic and prosthetic applications, J.Dargahi, Sensors and Actuators A, Vol.80, pp. 23-30, 2000.

[33] Thick-film printing of PZT onto silicon, R. Maas, M. Koch, N. Harris, N.M. White, A. Evans, Materials Letters, Vol. 31, pp. 109-112, 1997.

[34] Dielectric, ferroelectric and piezoelectric properties of lead Zirconate Titanate thick films on silicon substrates, H.D.Chen, K.R.Udayakumar, L.E.Cross, J.Appl.Phys, Vol77, pp. 3349-3353, April 1995.

[35] A novel approach for hybrid optoelectronic circuits: thick-film on glass (TOG), A.Kohler,P.Dullenkopf, Microelectronics International, Vol. 17/3, pp. 7-10, 2000.

[36] Acoustic wave technology sensors, B. Drafts, Sensors Magazine, Vol. 17, No.10, October 2000.

[37] Study of injection moulding pressure sensor with low cost and small probe, J. Huang, S. Cheng, Sensors and Actuators A, Vol. 101, pp. 269-274, 2002.

[38] Polymer films in sensor applications: a review of present uses and future possibilities, G.Harsanyi, Sensor Review, Vol.20, pp. 98-105, 2000.

[39] The preparation of piezoceramic-polymer thick films and their application as micro mechanical actuators, W.W.Clegg, D.F.L.Jenkins, M.J.Cunningham, Sensors and Actuators A, Vol. 58, pp. 173-177, 1997.

[40] PVDF piezoelectric polymer, P.Uebershlag, Sensor Review, Vol. 21, pp. 118-125, 2001.

[41] Piezoelectric thick-film polymer pastes, T.Papakostas, N.R.Harris, S.P.Beeby, N.M.White, Eurosensors XII, pp. 461-464, 1998.

[42] Piezoelectric paints as one approach to smart structural materials with health-monitoring capabilities, S.Egusi, N.Iwasawa, Smart Mater. Struct., Vol. 7, pp. 438-445, 1998.

[43] A novel thick-film strain transducer using piezoelectric paint, J.M. Hale, J. Tuck, Proc. Instn. Mech. Engrs, Vol 213 part C, pp. 613-622, 1999.

[44] The role of piezocomposites in ultrasonic transducers, W.A. Smith, IEEE Ultrasonics Symposium Proceedings, pp. 755-766, 1989.

[45] Novel piezoelectric ceramics and composites for sensor and actuator applications, A. Safari, Mat. Res. Innovat., Vol. 2, pp. 263-269, 1999.

[46] First Quartz Clock: http://www.britannica.com/clockworks/t_quartz.html

[47] Piezoceramic manufacturer:
http://www.alphapiezo.com/sonar_projection.htm

[48] Trends in accelerometer design for military and aerospace applications, P.L.Walter, Sensors Magazine, Vol. 16, No.3, March 1999.

[49] Low frequency underwater piezoceramic transducer, Irinela Chilibon, Sensors and Actuators A, vol. 85, pp. 292-295, 2000.

[50] Thick-Film acoustic wave sensor structure, N.M.White, V.T.K. Ko, Electronics Letters, Vol. 29, No. 20, pp. 1807-1808, Sept. 1993.

[51] Large bandwidth and thermal compensated piezoelectric thick-film acceleration transducer, D.Crescini, D.Marioli, E.Sardini, A.Taroni, Sensors and Actuators A, Vol.87, pp.131-138, 2001.

[52] Design and fabrication of a micromachined silicon accelerometer with thick-film printed PZT sensors, S.P.Beeby, J.N.Ross, N.M.White, J.Micromech. Microeng., Vol. 10, pp. 322-328, 2000.

[53] Micromachined accelerometer with microprocessor self-test procedure, S.P.Beeby, N.J.Grabham, N.M. White, Sensor Review, Vol. 21, No. 1, pp. 33-37, 2001.

[54] Development of new capacitive strain sensors based on thick film polymer and cermet technologies, K.I.Arshak, D. McDonough, M.A.Duncan, Sensors and Actuators A, Vol 79, pp. 102-114, 2000.

[55] Durham Instruments, Showa strain gauge:
http://www.disensors.com/showa.html

[56] Piezoelectric ceramic bimorph coupled to thin metal plate as cooling fan for electronic devices, J.H.Yoo, J.H.Hong, W.Cao, Sensors and Actuators A, Vol. 79, pp. 8-12, 2000.

[57] A piezoelectric linear actuator formed from a multitude of bimorphs, J.Friend, A.Umeshima, T.Ishii, K.Nakamura, S.Ueha, Sensors and Actuators A, Vol 109, pp. 242-251, 2004.

[58] Rotary Ultrasonic Motors Actuated By Travelling Flexural Waves, Y. Bar-Cohen, X. Bao, W. Grandia, Proc of SPIE's 6th Annual Symp. On Smart Structures and Materials, Paper no. 3668-63, March 1999.

[59] A 1.6mm Metal Tube Ultrasonic Motor, S. Cagatay, B. Koc, K. Uchino, IEEE Trans. On Ultrasonics, Ferroelectrics and Frequency Control, Vol. 50, No. 7, pp. 782-786, July 2003.

[60] Micro machined Piezoelectric Travelling Wave Micromotors for Intelligent Systems, J. Zhang, T. Gong, D. Shen, W. Wang, Proc. 3rd World Cong. Intelligent Control and Automation, pp. 1454-1457, July 2000.

[61] A piezoelectric spherical motor with two degree-of-freedom, M.Hu, H.Du,S-F.Ling, J-K.Teo, Sensors and Actuators A, Vol. 94, pp. 113-116, 2001.

[62] An analysis of a noncontact ultrasonic motor with an ultrasonically levitated rotor, J. Hu, K. Nakamura, S. Ueha, Ultrasonics 35, pp. 459-467, 1997.

[63] Development of a Master-Slave System for Active Endoscope Using a Multi-DOF Ultrasonic Motor, K.Takemura, D.Harada, T.Maeno, IEEE Trans. On Control, Automation and Systems Engineering, Vol. 4, No.1, pp. 17-22, March 2002.

[64] Investigation of stator transducer for a column-shaped ultrasonic motor, M.Kurosawa, H.Inagaki, T.Higuchi, Ultrasonics, Vol. 34, pp. 271-274, 1996.

[65] A cylindrical micro ultrasonic motor using PZT thin film deposited by single process hydrothermal method (ϕ 2.4mm, L = 10mm stator transducer), T. Morita, M. Kurosawa, T. Higuchi, IEEE UFFC, Vol. 45, No.5, pp. 1178-1186, Sept 1998.

[66] Simplified equivalent circuit of an ultrasonic motor and its application, M. Aoyagi, Y. Tomikawa, T. Takano, Ultrasonics, Vol. 34, pp. 275-278, 1996.

[67] M.Aoyagi, S.P.Beeby and N.M.White: A novel multi-degree-of-freedom thick-film ultrasonic motor, IEEE Transactions on Ultrasonics, Ferroelectrics, and Frequency Control, Vol.49, No.2, pp. 151-158, 2002.

[68] Improved preparation procedure and properties for a multilayer piezoelectric thick-film actuator, K.Yao, W. Zhu, Sensors and Actuators A, Vol. 71, pp. 139-143, 1998.

[69] Design and fabrication of a novel piezoelectric multilayer actuator by thick-film screen printing technology, W.Zhu, K.Yao, Z.Zhang, Sensors and Actuators A, Vol.86, pp. 149-153, 2000.

[70] A novel micro pump design with thick-film piezoelectric actuation, M.Koch, N.Harris, R.Maas, A.G.R.Evans, N.M.White, A. Brunnschweiler, Meas. Sci. Technol. Vol.8, pp. 49-57, 1997.

[71] Ultrasonic PZT gas sensor using thick-film technology, S.Gwirc, H.Gomez, C.Negreira, L.Malatto, IEEE ultrasonics symposium, pp. 427-431, 1997.

[72] Thick-film sensors: Past, present and future, N. M. White, J. Turner, Measurement Science and Technology, 8, pp. 1-20, 1997.

[73] Lead Zirconate Titanate Particle Dispersion in Thick-Film Ink Formulations, E.S. Thiele, N Setter, J.Am.Ceram.Soc., Vol. 83, pp. 1407-12, 2000.

[74] Low temperature firing of PZT thick films prepared by screen printing method, B. Lee, C. Cheon, J.S Kim, K, Bang, J.C Kim, H. Lee, Materials Letters, Vol. 56, pp. 518-521, 2002.

[75] An investigation into the effect of modified firing profiles on the piezoelectric properties of thick-film PZT layers on silicon, P.Glynne-Jones, S.P.Beeby, P.Dargie, T.Papakostas, N.White, Meas. Sci. Technol., Vol. 11, pp. 526-531, 2000.

[76] An investigation of the effect of poling conditions on the characteristics of screen-printed piezoceramics, P.Dargie, R.Sion, J.Atkinson, N.White, Microelectronics International, Vol. 15/2, pp. 6-10, 1998.

[77] Piezoelectric Ceramics: Bulk components, Ferroperm, http://www.amroh-electronics.de/bulk.pdf

[78] Hybrid Laser Tech Ltd.: http://www.hlt.co.uk/

[79] Laser interferometric measurement of displacement-field characteristics of piezoelectric actuators and actuator materials, H. Moilanen, S. Leppavuori, Sensors and Actuators A, Vol. 92, pp. 326-334, 2001.

[80] Take-Control Piezometer: http://www.take-control.demon.co.uk

[81] "Design of a system to measure the d_{33} coefficient of piezoelectric ceramics", P.G.Jones, 3rd year project, Dept. of Electronics & Computer Science, Univ. of Southampton, 1998.

[82] $e_{31,f}$ determination for PZT films using a conventional 'd_{33}' meter, J.E. Southin, S.A.Wilson, D.Schmitt, R.W.Whatmore, J. Phys. D: Appl. Phys, Vol. 34, pp. 1456-1460, 2001.

[83] Effect of mechanical boundary conditions on phase diagrams of epitaxial ferroelectric thin films, N.A.Pertsev, A.G.Zembilgotov, A.K.Tagentsev, Physical review letters, 80, pp. 1988-1991, March 1998.

[84] Macro- and microstress analysis in sol-gel derived $Pb(Zr_xTi_{1-x})O_3$ thin films. J.D.Shafer, H.Nafe, F.Aldinger, Journal of Applied Physics, 85, pp. 8023-8031, 1999.

[85] Apparent reduction in the value of d_{33} piezoelectric coefficient in PZT thick films, Dorey, RA, Whatmore RW, Integrated Ferroelectrics, Vol. 50, pp. 111-119, 2002.

[86] Measurement of piezoelectric coefficients of ferroelectric thin films, K.Lefki, G.J.M.Dormans, Journal of applied physics, vol. 76, pp. 1764-1767, 1994.

[87] Design of a novel thin-film piezoelectric accelerometer, Y.Nemirovsky, A.Nemirovsky, P.Muralt, N.Setter, Sensors and Actuators A, 56, pp. 239-249, 1996.

[88]Measurement of effective transverse piezoelectric coefficient $e_{31,f}$ of AlN and $Pb(Zr_x,Ti_{1-x})O_3$ thin films, M.-A.Dubois, P.Muralt, Sensors and Actuators A, 77, pp.106-112, 1999.

[89] Efunda engineering fundamentals: http://www.efunda.com/materials/piezo/material_data/

[90] Size related ferroelectric-domain-structure transition in a polycrystalline $PbTiO_3$ thin film, S.B.Ren, C.J.Lu, J.S.Liu, H.M.Shen, Y.N.Wang, Physics Review B, 54, pp. 14337-14340, Nov 1996.

[91] Dielectric properties of fine-grained barium titanate ceramics, G.Arlt, D.Hennings, G.de With, J. Appl. Phys., pp. 1619-1625, 1985.

[92] Manufacturer of processing equipment: http://www.frigmaires.com/

[93] Malvern Instruments website:
http://www.malvern.co.uk/Laboratory/laser.htm

[94] Preparation of piezoelectric $Pb(Zr,Ti)O_3$-$Pb(Zn_{1/3}Nb_{2/3})O_3$ thick films on ZrO_2 substrates using low-temperature firing, K.Tanaka, T.Kubota, Y.Sakabe, Sensors and Actuators A, Vol. 96, pp. 179-183, 2002.

[95] Effect of sintering aid and repeated sol infiltrations on the dielectric and piezoelectric properties of a PZT composite thick-film. R.A.Dorey, S.B. Stringfellow, R.W. Whatmore, Journal of the European Ceramic Society, Vol. 22, pp. 2921-2926, 2002.

[96] Influence of milling process and powder preparation on the d_{33} coefficient of thick-film piezoelectric layers. Torah.R.N, Beeby.S.P, White N.M., Proceedings of Ferroelectrics UK Leeds, pp. 58, 2002.

[97] A study of the effect of powder preparation and milling process on the piezoelectric properties of thick-film PZT, Torah.R.N, Beeby.S.P, White N.M., Proceedings of Eurosensors XVI 1, Prague, pp. 93-94, 2002.

[98] "Formulas for stress and strain", 5^{th} edition, R.J. Roark, W.C. Young, New York, McGraw-Hill, pp. 112-113, 1975.

[99] Development of a thick-film magnetostrictive material: Formulation and characterisation, N.J.Grabham, PhD Thesis, University of Southampton, 2002.

[100] Experimental investigation into the effect of substrate clamping on the piezoelectric behaviour of thick-film PZT elements, Torah.R.N, Beeby.S.P, White N.M., Journal of Physics D: Applied Physics, Vol. 37, pp. 1074-1078, April 2004.

[101] A study of powder size combinations for improving piezoelectric properties of PZT thick-film devices, Torah.R.N, Beeby.S.P, White N.M., Eurosensors XXVII Portugal Conf. Proc., 360-361, 2003.

[102] Vibration powdered generators for self-powered microsystems, P. Glynne-Jones, University of Southampton PhD Thesis, 2001.

[103] Design and fabrication of a novel piezoelectric multilayer actuator by thick-film screen printing technology, W. Zhu, K. Yao, Z. Zhang, Sensors and Actuators A, Vol. 86, pp. 149-153, 2000.

[104] Deflection characteristics of a trapezoidal multilayer in-plane bending piezoelectric actuator, Z. Wang, W. Zhu, C. Zhao, X. Yao, IEEE Trans. On Ultrasonics, ferroelectrics and frequency control, Vol. 48, No. 4, July 2001.

[105] Development of piezoelectric micromovement actuator fabrication using a thick-film double-paste printing method, H. Moilanen, J. Lappalainen, S. Leppavuori. Sensors and Actuators A, Vol. 43, pp. 357-365, 1994.

[106] T.Yan, B.E.Jones, R.T.Rakowski, M.J.Tudor, S.P.Beeby, N.M.White, Metallic triple beam resonator with thick-film printed drive and pickup, Eurosensors XXVII Portugal Conf. Proc., pp. 8-9, 2003

[107] A dual frequency, ultrasonic, microengineered particle manipulator, N. Harris, M. Hill, Y. Shen, R. Townsend, S. Beeby, N. White. Ultrasonics, Vol. 42, pp. 139-144, 2004.

[108] Improving the functionality of a prosthetic hand through the use of thick-film force sensors, Cranny AWJ, Chappell PH, Beeby SP and White NM, Proc. Eurosensors XVII, Portugal, 2003.

[109] Resonant Silicon Sensors, G. Stemme, Micromech. Microeng. Vol. 1, pp. 113-125, 1991.

[110] Triple-beam resonant force sensor based on piezoelectric thin films. Th.Fabula, H.-J.Wagner, B.Schmidt. Sensors and Actuators A, 41-42, pp. 375-380, 1990.

[111] A micro fabricated ultrasonic particle manipulator with frequency selectable nodal planes, M. Hill, N. Harris, R. Townsend, N. White, S. Beeby. WCU 2003 Paris, pp. 1647-1650, 2003.

[112] Lithium Niobate: summary of physical properties and crystal structure, RS Weis and TK Gaylord, Applied Physics A, 37, pp. 191-203, 1985.

[113] A Sensor System for Oil-Water Separators: Materials Considerations. T. Dyakowski, N. Harris, N. White, J. Hale, A. Jaworski. Proc. of Sensors and their Applications XII, Limerick, pp. 71-76, 2003.

[114] Characterisation of heterogeneous mixtures by using thick-film ultrasonic transducers. Dyakowski, T., Hale, J., Jaworski, A., White, N. M., Harris, N. and Nowakowski, A. Proc. of 3rd World Congress in Industrial Process Tomography (in press), Alberta, Canada, 2003.

[115] Design and build of a digital control system for a multi-degree of freedom ultrasonic motor, Mark Warrick, University of Southampton BEng Project, 2002.

[116] Development of a lightweight and adaptable multiple-axis hand prosthesis, Medical Engineering and Physics, C. Light, P. Chappell, Vol. 22, pp. 679-684, 2000.

[117] Improving the piezoelectric properties of thick-film PZT: the influence of paste composition, powder milling process and electrode material. Torah.R.N, Beeby.S.P, White N.M., Sensors and Actuators A, Vol. 110 (1-3), pp. 378-384, 2004.

[118] An electromagnetic, vibration-powered generator for intelligent sensor systems. Glynne-Jones, P., Tudor, M. J., Beeby, S. P. and White, N. M. Sensors and Actuators A, Vol. 110, pp. 344-349, 2004.